

Chemistry, Functionalization, and Applications of Recent Monoelemental Two-Dimensional Materials and Their Heterostructures

Zhongjian Xie,[†] Bin Zhang,[†] Yanqi Ge,[†] Yao Zhu,[†] Guohui Nie,[†] YuFeng Song,[†] Chang-Keun Lim,[†] Han Zhang,^{*} and Paras N. Prasad^{*}



Cite This: <https://doi.org/10.1021/acs.chemrev.1c00165>



Read Online

ACCESS |

Metrics & More

Article Recommendations

ABSTRACT: The past decades have witnessed a rapid expansion in investigations of two-dimensional (2D) monoelemental materials (Xenes), which are promising materials in various fields, including applications in optoelectronic devices, biomedicine, catalysis, and energy storage. Apart from graphene and phosphorene, recently emerging 2D Xenes, specifically graphdiyne, borophene, arsenene, antimonene, bismuthene, and tellurene, have attracted considerable interest due to their unique optical, electrical, and catalytic properties, endowing them a broader range of intriguing applications. In this review, the structures and properties of these emerging Xenes are summarized based on theoretical and experimental results. The synthetic approaches for their fabrication, mainly bottom-up and top-down, are presented. Surface modification strategies are also shown. The wide applications of these emerging Xenes in nonlinear optical devices, optoelectronics, catalysis, biomedicine, and energy application are further discussed. Finally, this review concludes with an assessment of the current status, a description of existing scientific and application challenges, and a discussion of possible directions to advance this fertile field.



CONTENTS

1. Introduction	B	2.4.4. Optical and Nonlinear Optical Properties	P
2. Structure, Properties, and Theory of Xenes and Their Heterojunctions	C	2.4.5. van der Waals Heterostructures	S
2.1. Graphdiyne	C	3. Fabrication and Surface Modification of Xenes	S
2.1.1. Molecular Structure and Chemical Properties	D	3.1. Graphdiyne	S
2.1.2. Electronic Properties	E	3.2. Borophene	V
2.1.3. Optical and Nonlinear Optical Properties	E	3.3. Group V: Arsenene, Antimonene, and Bismuthene	W
2.1.4. Heterojunctions	G	3.4. Tellurene	Z
2.2. Borophene	H	3.5. Heterojunctions	Z
2.2.1. Structures	H	4. Applications of Xenes and Their Heterostructures	AA
2.2.2. Chemical Properties	H	4.1. Optical Devices	AA
2.2.3. Electronic Properties	H	4.1.1. GDY	AA
2.2.4. Optical Properties	I	4.1.2. Arsenene, Antimonene, and Bismuthene	AB
2.2.5. Heterojunctions	J	4.1.2.3. Bismuthene	AC
2.3. Arsenene, Antimonene, and Bismuthene	J	4.1.3. Tellurene	AD
2.3.1. Structures	J	4.2. Optoelectronics	AE
2.3.2. Chemical Properties	L	4.2.1. GDY	AE
2.3.3. Electronic Properties	L	4.2.2. Borophene	AE
2.3.4. Optical and Nonlinear Optical Properties	M		
2.3.5. van der Waals Heterostructures	N		
2.4. Tellurene	O		
2.4.1. Structural Phase Transition	O		
2.4.2. Chemical Property	P		
2.4.3. Electronic Property	P		

Received: February 26, 2021

4.2.3. Group V: Arsenene, Antimonene, and Bismuthene	AE
4.2.4. Tellurene	AG
4.3. Catalysis	AH
4.3.1. GDY	AH
4.3.2. Group V: Arsenene, Antimonene, and Bismuthene	AK
4.4. Sensors	AM
4.4.1. GDY	AM
4.4.2. Borophene	AN
4.4.3. Group V: Arsenene, Antimonene, and Bismuthene	AN
4.4.4. Tellurene	AQ
4.5. Biomedical Applications	AQ
4.5.1. Phototherapy	AQ
4.5.2. Bioimaging	BA
4.5.3. Biosafety	BC
4.6. Energy Application	BD
4.6.1. GDY	BD
4.6.2. Borophene	BI
4.6.3. Group V: Arsenene, Antimonene, and Bismuthene	BJ
4.6.4. Tellurene	BK
5. Conclusions and Perspectives	BM
5.1. Challenges	BM
5.1.1. Synthesis, Fabrication, and Characterization	BM
5.1.2. Database for Opto-Electro-Magnetic-Biomedical Properties	BM
5.2. Opportunities	BN
5.2.1. Multiscale Modeling and Materials Informatics	BN
5.2.2. Photonic Structures	BN
5.2.3. Magnetic 2-D Xenes	BN
5.2.4. Phase Change Materials, ENZ Materials, Quantum Materials, and Metasurfaces	BN
5.2.5. Organic–Inorganic Hybrid Heterostructures	BO
5.2.6. Biomedical Applications	BO
Author Information	BO
Corresponding Authors	BO
Authors	BO
Author Contributions	BP
Notes	BP
Biographies	BP
Acknowledgments	BQ
References	BQ

1. INTRODUCTION

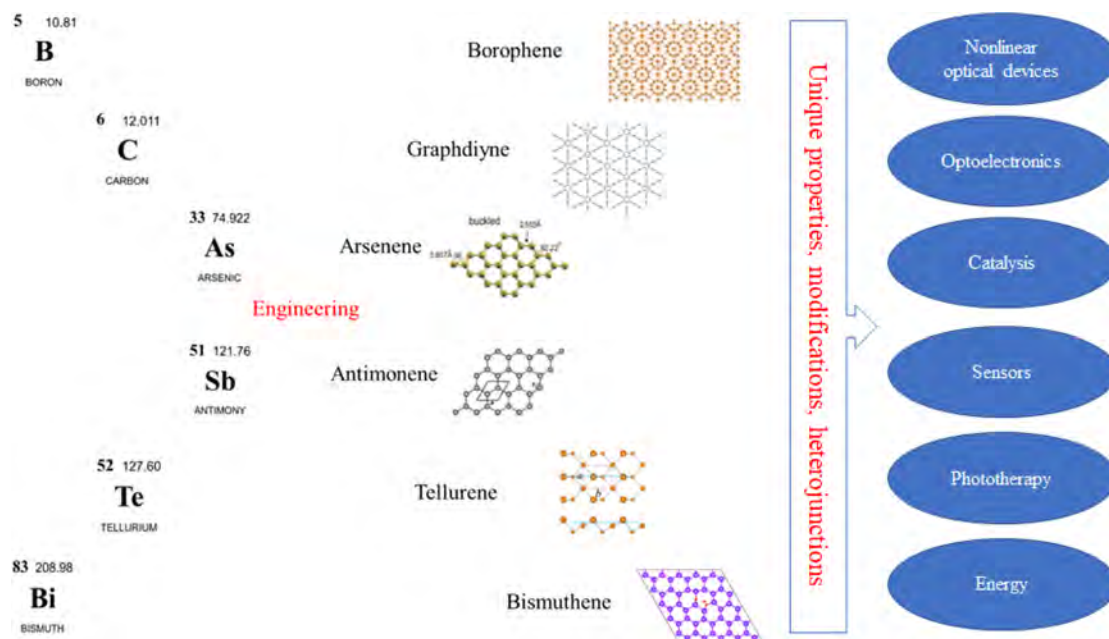
Successful exfoliation of graphene has inspired intensive research on 2D materials with unique characteristics and functions. 2D materials show great promise in tackling many social issues in energy, electronics, and health care. The emerging monoelemental 2D Xenes materials have recently become new favorites in the 2D material family. Xenes mainly include semimetallic group IVA Xenes^{1–4} and group V Xenes,^{5–11} as well as metallic group IIIA Xenes.^{12,13,22,14–21} Their unique physical properties are derived from their ultrathin 2D structures. Each Xene possesses specific elemental composition, atomic structure, and interlayer coupling, resulting in versatile optical, electronic, and chemical properties.

The emerging 2D Xenes show promising potential in opening unexploited application fields of other 2D materials.^{23,24} The low carrier mobility of transition-metal dichalcogenides (TMDs) prevents their applications for a biosensor. The graphene of zero-bandgap and the MXenes with limited bandgaps hinder their applications in field-effect transistor (FET) and optical sensing, even though they have high carrier mobility. The insulating properties make h-BN unsuitable to be used in electronics. In contrast, 2D Xenes have shown layer-dependent bandgaps, which are expected to fill up space among TMDs (large-bandgaps), MXenes (limited bandgaps), graphene (zero-bandgap), and h-BN (insulator). Therefore, the interactions between Xenes and electromagnetic waves covering from the ultraviolet to the near-infrared (NIR) spectral region can be realized. Chemically, Xenes are the most chemically active materials in the 2D material family. Therefore, they possess unique advantages in biological metabolism and degradability compared with multielemental materials. Each of Xene nanostructures has unique merits and functionalities suitable for specific applications in optoelectronics, sensing and biomedical diagnostics and therapy. This comprehensive review focuses selectively on emerging Xenes, including graphdiyne, borophene, arsenene, antimonene, bismuthene, and tellurene.

Baughman *et al.* predicted for the first time that graphdiyne (GDY) was a stable crystalline carbon allotrope in 1987.²⁵ But it was successfully synthesized for the first time in 2010 by Li *et al.* via the in situ cross-coupling reaction of phenylethynyl precursors.²⁶ Since then, it has attracted more and more interest. It has a new 2D carbon nanostructure, with benzene rings bridged with diacetylene bonds, which endows GDY with significantly different properties from graphene. The 2D GDY framework constructed by sp- and sp²-hybridized carbon atoms provides tunable electronic properties, high π -conjugation, and uniformly distributed pores for further applications.

A study on boron dated back to two centuries ago.²⁷ At that time, it had only existed in compounds before the preparation of pure boron (bulk g-B106) was reported first by Sands *et al.* in 1957.²⁸ As boron locates nearest to carbon in the periodic table, the computational work of Boustani in 1996 predicted that the quasi planner cluster of borons has excellent performance similar to the graphite.²⁹ Borophene is the lightest 2D material ever discovered. Because bulk boron is composed of complex three-dimensional spatial structures, the production of borophene remains challenging. In 2015, borophene was first synthesized by Andrew *et al.* on a silver substrate under an ultrahigh vacuum, and it appeared to be metallic.³⁰ Since then, numerous theoretical and experimental investigations on the properties and applications of borophene have been reported.³¹

In addition to the emerging monoelemental 2D materials in group IIIA and IVA, there have been tremendous studies on Xenes from group VA, including phosphorene, arsenene, antimonene, and bismuthene.⁶ Among them, extensive investigations on 2D phosphorene have been conducted since 2014, and these works have been thoroughly summarized in many review articles^{10,24,32} and, hence, will not be discussed here. Three other Xenes from group VA have also attracted substantial interest and are more intriguing than phosphorene due to their higher stability under ambient conditions.⁶ Distinct from the ones in IIIA and IVA group, Xenes from the VA group usually form similar honeycomb monolayer puckered structures and are electronically enriched on the surface. Arsenene, antimonene, and bismuthene had been explored decades ago, but the research has not become a hot topic until recent

Scheme 1. Emerging 2D Monoelemental Xenos^a

^aReproduced with permission from ref 41. Copyright 2015 American Physical Society. Reproduced with permission from ref 35. Copyright 2016 American Physical Society. Reproduced with permission from ref 42. Copyright 2017 American Physical Society. Reproduced with permission from ref 43. Copyright 2015 Wiley-VCH Verlag GmbH & Co. KGaA, Weinheim. Reproduced with permission from ref 44. Copyright 2019 the Royal Society of Chemistry. Reproduced with permission from ref 45. Copyright 2019 the Royal Society of Chemistry.

researchers applied them in gas-sensing, biosensing, catalysis, and biomedicines.³³ For arsenene and antimonene, their bandgaps can transform from original indirect to direct one via a rational modification or stimulation, and studies before 2018 were generally based on theoretical calculations and simulation.³⁴ Since then, intriguing potential for versatile applications in optoelectronics, chemical sensing, catalysis, and biomedicines has been demonstrated. For antimonene, its applications in nonlinear photonics, electrocatalysis, and antitumor agents are emphasized in this review. Notably, the antimonene substituent can selectively exist in stable Sb(III) and Sb(V) oxidation states depending on its environment, with the former being highly toxic and the latter being nontoxic. Bismuthene, consisting of the heaviest and the only metallic element in group VA, differs from other VA group Xenos. In 1997, bismuthene was synthesized over a Bi(111) surface, but the topological properties are still under discussion due to inconsistent results from different groups.³⁵ Although the confliction limits its applications, bismuthene is reviewed here due to its attractive features. It possesses a large X-ray/ Γ -ray capture cross-section and can be used as a contrast agent for medical imaging and radiotherapy. Besides such highlights, this review also presents a comprehensive description of bismuthene and summaries of recent research on it.

Bulk tellurium is composed of stacked helical chains of Te atoms through weak bonding. In the last two decades, various morphologies of Te nanostructures have been synthesized through different methods. The structural anisotropy of tellurium endows the production of 1D Te nanomaterials, like nanowires, nanotubes, and nanobelts, with a large yield.⁶ Much less work has been reported on 2D Te nanostructures, *i.e.*, tellurene. The existence of a few-layer tellurene has been reported recently by theoretical predictions³⁶ and experimental work.^{37,38}

This review only focuses on these recently emerging 2D Xenos materials, which have not been systematically reviewed before, but their explosive development has been witnessed (Scheme 1). Other Xenos with mature technology such as graphene, silicene, germanene, stanene, and phosphorene have already been widely reviewed.^{23,39,40} Thus, they are not in the scope of this review. The molecular structures of these newly emerging Xenos and the theoretical calculations of their electronic band structures are first introduced. Then, their specific characteristics, including chemical, electronic, optical and nonlinear properties, are summarized. Synthetic strategies to realize both the bottom-up growth and top-down exfoliation are concluded. The applications in diverse fields, including optical devices, optoelectronics, catalysis, sensors, biomedicine and energy, are systematically presented. Finally, the challenges of Xenos for further applications are put forward along with a discussion of their future opportunities.

2. STRUCTURE, PROPERTIES, AND THEORY OF XENES AND THEIR HETEROJUNCTIONS

2.1. Graphdiyne

Graphdiyne is an emerging 2D carbon material of growing interest, which possesses a special structure and numerous unique properties superior to traditional carbon materials. It comprises aromatic rings of sp^2 -hybridized carbon atoms linked with butadiyne linkers of sp -hybridized carbon atoms. The unique structure endows graphdiyne with a high π -conjugation, uniformly distributed in-plane cavities and uneven surface charge distribution. Graphdiyne is predicted to be a semiconductor naturally. It shows superior electronic, optical, and mechanical properties and promising potential in catalysis and energy storage applications. In this review, graphdiyne's structure, properties, heterojunctions, and application are reviewed in parallel with other monoelemental Xenos. Graph-

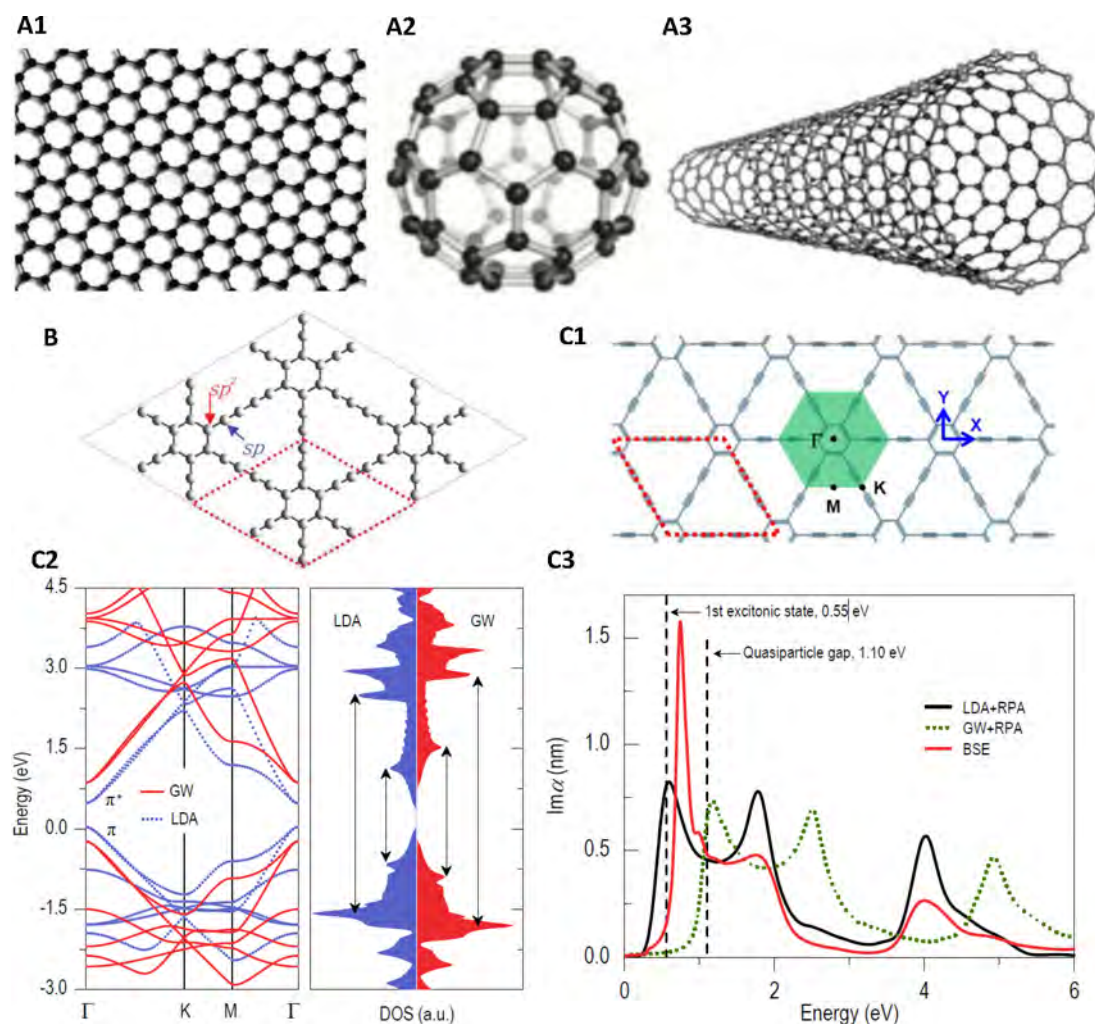


Figure 1. (A) Different carbon materials based on graphene. (A1) 2D graphene, (A2) 0D fullerene, (A3) carbon nanotube. Reproduced with permission from ref 57. Copyright 2020 Elsevier, Inc. (B) Atomic structure of a supercell of GDY crystal. Reproduced with permission from ref 56. Copyright 2012 American Chemical Society. (C1) First Brillouin zone (green hexagon) of GDY. (C2) The band structure (left) and DOS (right) of GDY calculated through the DFT within the LDA. (C3) The imaginary part of polarizability obtained from the GW + random-phase approximation (RPA) (green dotted line), LDA + RPA (solid black line), and Bethe Salpeter equation (BSE, solid red line) approach. Reproduced with permission from ref 58. Copyright 2011 American Physical Society.

diyne, solely, has been intensively reviewed on its chemical and physical properties and applications.^{46–49}

2.1.1. Molecular Structure and Chemical Properties.

Graphite, a typical carbon elemental form, is in a hexagonal crystalline structure. It is a naturally occurring structure and is stable under standard conditions. In the past several decades, three other carbon forms, fullerenes (Figure 1A2),⁵⁰ carbon nanotubes (Figure 1A3),⁵¹ and graphene (Figure 1A1),⁵² have generated extensive research. In graphene, the first discovered 2D material, the individual layers consist of carbon atoms bonded in a hexagonal lattice. A carbon nanotube can be regarded as wrapping a graphene nanosheet into a seamless cylinder. Different from the graphene with a zero band gap, carbon nanotubes can be either semiconducting or metallic.⁵³ Compared with graphene and its allotropes with sp^2 hybridization, the sp - and sp^2 -hybridized carbon atoms in GDY (Figure 1B,C1), and the related bonds make it more flexible. Thus, GDY is able to form curved structures where its mechanical stiffness is weakened. Moreover, the acetylene linkages in GDY make its stability decreased.⁵⁴ It was presumed that the formation energy of GDY was low, but higher than graphite.⁵⁵ Baughman *et al.*

predicted for the first time that the stability GDY was good even at high temperature.²⁵

Like the hexagonal symmetry ($p6m$) for graphene, GDY consists of benzene rings linked by acetylenic groups. Its sp - and sp^2 -hybridized carbon atoms have a combined effect, as the single C–C bonds are shrunk due to weak π -conjugation between the alkynyl units and the aromatic ring moieties (Figure 1B). In GDY, different bonds have different lengths. The lengths of the C_{sp^2} – C_{sp} bond in between the nearby $C\equiv C$ triple and $C=C$ double bonds, C_{sp^2} – C_{sp^2} bonds in benzene rings, single C_{sp} – C_{sp} bonds and triple C_{sp} – C_{sp} bonds are 1.40, 1.41, 1.33, and 1.24 Å, respectively.⁵⁶

The extended π -conjugated structure of GDY endows them strong visible light absorption capacity and the ability to accelerate charge separation during the charge transfer process. Moreover, owing to the highly porous plane of GDY, the reactive sites increase for chemical reactions and offer a dispersion network at atomic-level for other reactions with high efficiency. These characteristics make GDY and its derivatives suitable for catalysis applications such as photocatalyst,^{59–62} electrocatalyst,^{63–67} photoelectrochemical water splitting,^{68–70} and

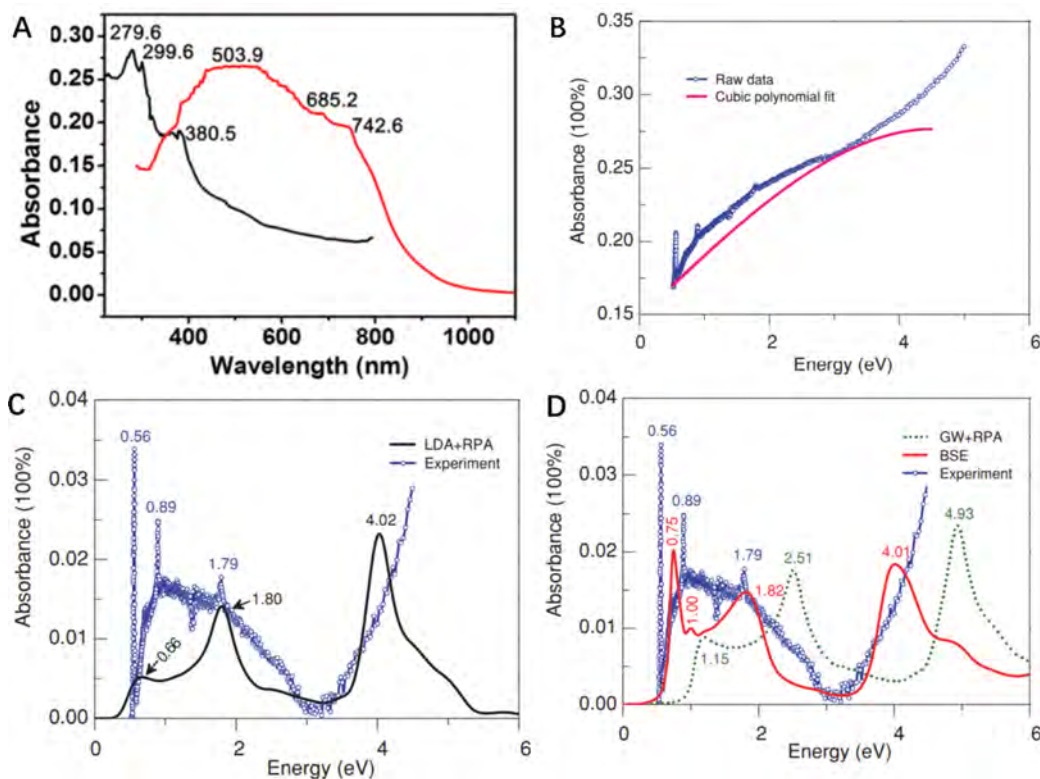


Figure 2. (A) UV-vis spectra of GDY nanowalls. Reproduced from ref 99. Copyright 2015 American Chemical Society. (B) Absorbance of the GDY film (Blue line is experimental data; red line shows cubic polynomial fit for its background). (C) Absorbance of the GDY film (Blue line shows experimental data; red line shows LDA+RPA absorbance of GDY). (D) Absorbance of the GDY film (Blue line is experimental data; the green line shows absorbance at the GW + RPA; the solid red line represents the BSE level of GDY.) Reproduced with permission from ref 58. Copyright 2015 American Physical Society.

supporters for catalysts.^{71,72} Meanwhile, the pores structured by diacetylene bonds in GDY provide sufficient storage space for metal atoms, ion diffusion passageways, and performance enhancement of an electrode used in rechargeable lithium-ion^{73–77} and sodium-ion^{78–81} storage. Even for the sodium ions which are larger than the lithium ions, GDY provides them a diffusion channel with a low energy barrier (see section 4.6.1.2). GDY enhances charge transport due to the highly π -conjugated structure. After GDY forms compounds with P3CT-K, PCBM, ZnO, and PbI₂/MAL, a high-efficiency percolation channel can be formed in the active layer. More interestingly, the Pt and the triple bonds of GDY are more prone to chemical reactions, causing them to form unique “p–n” junction with higher catalytic activity and superb electron transport capabilities. These features show that GDY has great potential for photovoltaic devices.^{82–84} Moreover, the highly reactive diacetylene groups, the unique conjugated structure and good biocompatibility of GDY enable it to be used for biomedical applications.^{85–89}

2.1.2. Electronic Properties. Thanks to the sound foundation for modern band-structure simulation for self-energy,⁹⁰ the bandgap of GDY has been calculated. It is 0.44 eV, calculated through the density functional theory (DFT) in the local density approximation (LDA), while it increases to 1.10 eV via the GW many-body theory. It is attributed to the reduced dimensionality of GDY and thus enhanced Coulomb interaction (Figure 1C1,C2).⁵⁸ The density of states (DOS) of GDY was also calculated. Both the valence band maximum (VBM) and the conduction band minimum (CBM) are degenerate at the Γ point. The excitonic effects dominate its optical absorption, with

an electron–hole binding energy larger than 0.55 eV (Figure 1C3). The optical absorption spectrum of GDY, defined by the imaginary part of polarizability, shows three peaks, calculated by combining the LDA and the random-phase approximation (RPA) models. The first peak defines the transition around the bandgap, and the other two peaks originate from the transitions around the Van Hove singularities of the K and M points, respectively. The Bethe–Salpeter equation (BSE) is used to describe electron–hole interaction (excitonic effects) in a two-particle formalism. Figure 1B shows the redistribution of the BSE spectrum and the enhanced peak at a specific energy.

On the basis of the first-principles theoretical analysis, GDY was proved as the first real example of a 2D second-order topological insulator (SOTI), with topological 0D corner states. In the scanning tunneling spectroscopy measurement, sharp peaks appear when the tip moves close to the corner, indicating the occurrence of the corner states.⁹¹ The high-quality GDY films prepared by the vapor–liquid–solid (VLS) growth process can produce electrical conductivity of 2800 S cm⁻¹.⁹² GDY nanowires can also be fabricated by VLS methods, with diameters of 20–50 nm and lengths of 0.6–1.8 mm. They possess a mobility of 7.1×10^2 cm² V⁻¹ s⁻¹⁹³ and a conductivity of 1.9×10^3 S m⁻¹, even higher than those of the GDY film. It indicates that GDY is highly suitable for application in electronics.

2.1.3. Optical and Nonlinear Optical Properties. Unlike graphene with a zero bandgap or crystalline silicon with an indirect bandgap, GDY is characterized by a natural direct bandgap, which is tunable in accordance with the size, layer number, stacking arrangement, chemical doping, strain, and

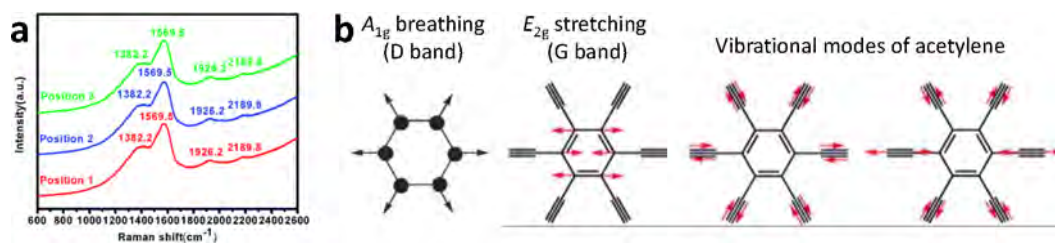


Figure 3. (A) Raman spectra of three different positions on a GDY film. Reproduced with permission from ref 26. Copyright 2010 Royal Society of Chemistry. (B) Atomic motions of Raman-active modes. The red arrows indicate the main motion directions. Reproduced with permission from refs 104 and 105. Copyright 2016 American Chemical Society and Copyright 2016 Wiley-VCH Verlag GmbH and Co. KGaA, Weinheim.

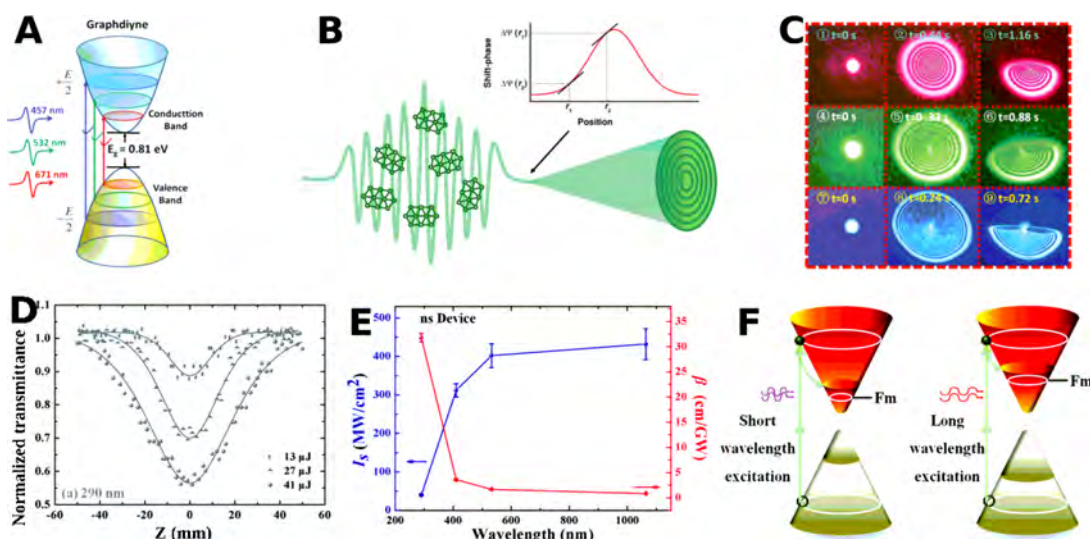


Figure 4. (A) Schematic of the incident light interacting with GDY. (B) Nonlinear optical response of GDY is shown as diffraction rings in the SSPM experiment. (C) Patterns of diffraction rings of GDY obtained at $\lambda = 671$ (red), 532 (green), and 457 (blue) nm. Reproduced with permission from ref 106. Copyright 2019 Wiley-VCH Verlag GmbH and Co. KGaA, Weinheim. (D) TPA results of GDY NSs in the ns open-aperture Z-scan setup upon 290 nm excitation. (E) Relationship between the saturable intensity (I_s), TPA coefficient (β) of GDY, and the nanosecond laser wavelengths. (F) TPA mechanism of GDY NSs upon light excitation with different wavelengths. Reproduced with permission from ref 108. Copyright 2020 Royal Society of Chemistry.

electric field.^{45,47,94–98} Meanwhile, similar to graphene, GDY has a Dirac-cone-shaped band structure, which locates in its Brillouin zone (the green hexagon in Figure 1C1).^{45,47} This unique band structure leads to exceptional nonlinear optical properties. There have been several review papers summarizing linear optical properties of GDY.^{45,47,94} In this section, the nonlinear optical properties of GDY is also reviewed to provide fundamentals for the nonlinear optical devices in section 4.1.1.

The UV–vis absorption measurement showed a broadband absorption in the UV to Vis range, indicating electron delocalization is enhanced by an extended π -conjugation system (in Figure 2A).⁹⁹ Luo *et al.* measured the absorption spectra of GDY films from NIR to UV.⁵⁸ Smooth cubic polynomials were used to remove the experimental background (in Figure 2B). Then the observed absorbance was compared to the calculated ones at the LDA + RPA (in Figure 2C), GW + RPA, and BSE levels (in Figure 2D). The BSE level result was most similar to the experiment outcomes: three observed absorption peaks match the BSE excitonic peaks well. An intense absorption depression behavior was seen between 2 and 3.5 eV in both the experimental and theoretical studies. The first two measured energy peaks were both smaller than the corresponding ones of BSE prediction. Such a difference is mainly caused by the 2D nature of the GDY flake measured in the experiment, with the reduced Coulomb interaction as the dimensionality increases.

The energy of photoexcited electrons in GDY can be released radiatively (resulting in luminescence) or nonradiatively. The natural direct bandgap of GDY elicits its strong potential as a luminophore.⁴⁷ However, the photoluminescence (PL) properties of pristine GDYs have not been explored comprehensively so far. It has only been reported that GDY quantum dots of 3 nm conjugated with pyrene exhibited a high PL quantum yield (42.82%), with a superior water dispersibility. Meanwhile, the nonradiative decay pathway of photoexcited electrons in GDY leads to other desirable optical properties such as (i) strong resonance Raman scattering by the suppression of seriously interfering photoluminescence (PL) background signal;¹⁰⁰ (ii) photothermal property induced by nonradiative phonon relaxation;¹⁰¹ (iii) PL quenching of adjacent fluorophores,¹⁰² which provides strong potential for analytical and biomedical applications.

The Raman spectra of a bulk GDY (Figure 3A) exhibit two major (a D band at about 1380 cm^{-1} and a G band at about 1570 cm^{-1}) and two minor (at about 1925 and 2190 cm^{-1}) characteristic peaks upon excitation by an argon ion laser at the 514.5 nm line.²³ The D and G bands are typical Raman vibrations for 2D carbon materials such as graphene, graphyne, and GDY. The D band shows the A_{1g} breathing vibration of the sp^2 carbon–carbon (C–C) bonds in the aromatic ring, which is forbidden in perfect carbon 2D materials, and only activated in

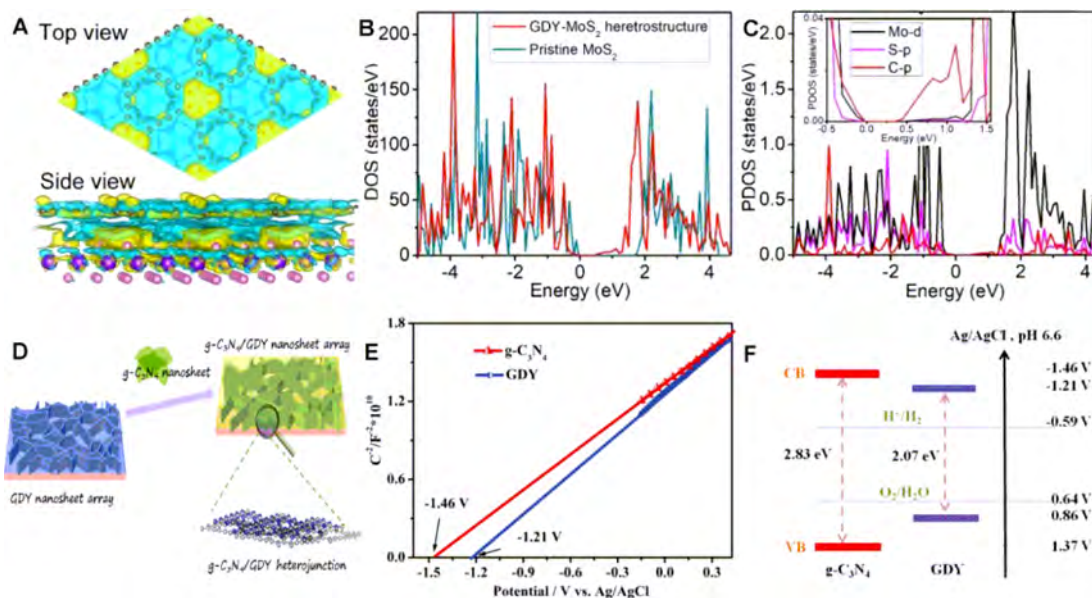


Figure 5. GDY-MoS₂ heterostructure: (A) charge density difference maps; (B) DOS; (C) projected DOS. Reproduced with permission from ref 117. Copyright 2019 Elsevier, Inc. Graphitic carbon nitride (g-C₃N₄/GDY) heterojunction: (D) construction schematic; (E) Mott–Schottky plots; (F) band structures. Reproduced with permission from ref 69. Copyright 2018 Wiley-VCH Verlag GmbH and Co. KGaA, Weinheim.

the presence of disorder;¹⁰³ the G band corresponds to first-order scattering from the E_{2g} symmetric stretching vibration mode for aromatic C–C bonds (Figure 3B). A higher ratio of the D to G bands (I_D/I_G) suggests that GDY is produced with a higher density of sp^2 defects in the 2D carbon material. The minor peaks are assigned as the vibration of acetylene linkages ($-C\equiv C-C\equiv C-$) (Figure 3).

Large conjugated frameworks and holes to accommodate dopant on the atomic layers make GDY promising candidates for organic nonlinear optical (NLO) materials. For the pristine GDYs, the optical Kerr effect induced by an intensity-dependent change in the real part of the refractive index, together with intensity-dependent saturable two-photon absorption (TPA) and absorption (SA), has been reported. Wu *et al.* demonstrated a large Kerr nonlinearity from the GDY-PMMA film, with a large nonlinear refractive index ($n_2 \approx 10^{-5} \text{ cm}^2 \text{ W}^{-1}$). It is two orders higher than that of graphene, evaluated with the spatial self-phase modulation (SSPM) experiment (see Figure 4A–C).¹⁰⁶ The application of the Kerr nonlinearity of GDY will be discussed in section 4.1.1. Zhao *et al.* reported the SA property of GDY and its application to erbium-doped mode-lock fiber lasers.¹⁰⁷ GDY has two different Dirac cones, facilitating to reach the SA state. The smaller volume of energy states in the conical band structure, especially near the bandgap, can easily cause full excitation of electrons in the valence band or full occupation of all available states in the conduction band. Then, there is no transition of electrons due to the Pauli Exclusion Principle, thus leading to absorption saturation. The application of SA in GDY will also be discussed in section 4.1.1. Zhang *et al.* observed strong TPA (TPA cross-section of $8.7 \times 10^{-44} \text{ cm}^4 \text{ s}$ and TPA coefficient of 31.8 cm GW^{-1} upon illumination by a 290 nm pulse laser with the pulse width of 6 ns) using a GDY nanosheet (Figure 4D–F).¹⁰⁸ In this study, a higher TPA performance was achieved with the laser of a shorter wavelength (290 nm), which is also attributable to the cone-like band structure of GDY (Figure 4E,F). The smaller volume at a lower level of the cone of the conduction band can be saturated easily (Figure 4E,F). Thus, the excitation of electrons to a higher level of the cone

with a laser of shorter wavelength (higher energy) can provide a higher probability of filling a larger volume in the conduction band. The strong TPA of ultraviolet (UV) light can facilitate applying GDY as an optical limiting (OL) material.

The susceptibility for the second-order nonlinear optical property (e.g., second-harmonic generation (SHG)) of π -conjugated organic materials, bridging electron donor and acceptor groups by a conjugated segment, is proportional to the first hyperpolarizability that requires non-centrosymmetry.^{109,110} Generally, the hyperpolarizability can be improved with increasing the electron donating/accepting strength and is enhanced by increasing the length of the π -conjugated bridge. GDY has an ordered anisotropic arrangement of π -conjugated 18-membered ring units, which can adsorb electron-accepting dopants such as alkali-metal (Li, Na, K) and super alkali compounds. Therefore, the nonlinear optical susceptibility can be dramatically improved by charge transfer between GDY (electron donor) and the dopants (electron acceptor). It has been explored theoretically to enhance the static hyperpolarizabilities of $AM_3@GDY$ (dopant: alkali-metal (AM)),^{111,112} $Li_3NM@GDY$ (dopant: tetrahedral alkali-metal (M) nitride),¹¹³ $M_3F@GDY$ (dopant: alkali-metal fluoride),¹¹⁴ and $AM_3O@GDY$ (dopant: trialkali-metal oxide).¹¹⁵

2.1.4. Heterojunctions. As the only 2D carbon materials that can directly grow on an arbitrary substrate, GDY is promising to form various hybrids with other 1D, 2D, and 3D materials.^{69,70,116,117} Among them, a common type of 2D heterojunction is synthesized via either van der Waals force or covalent bonding with another 2D material.

Figure 5 depicts two examples of GDY-based heterojunctions: GDY-MoS₂ (Figure 5A–C) and g-C₃N₄/GDY (Figure 5D–F). Examining the DOS and projected DOS of GDY-MoS₂ heterostructures, it was found that the two 2D materials were connected via chemical bonds (Figure 5A). It resulted in the conduction band minimum position shifted to the Fermi level due to the critical contribution of carbon 2p orbitals in GDY.¹¹⁷ Unlike the heterojunctions GDY-MoS₂ formed with chemical bonding, Lu *et al.* fabricated a van der Waals g-C₃N₄/GDY

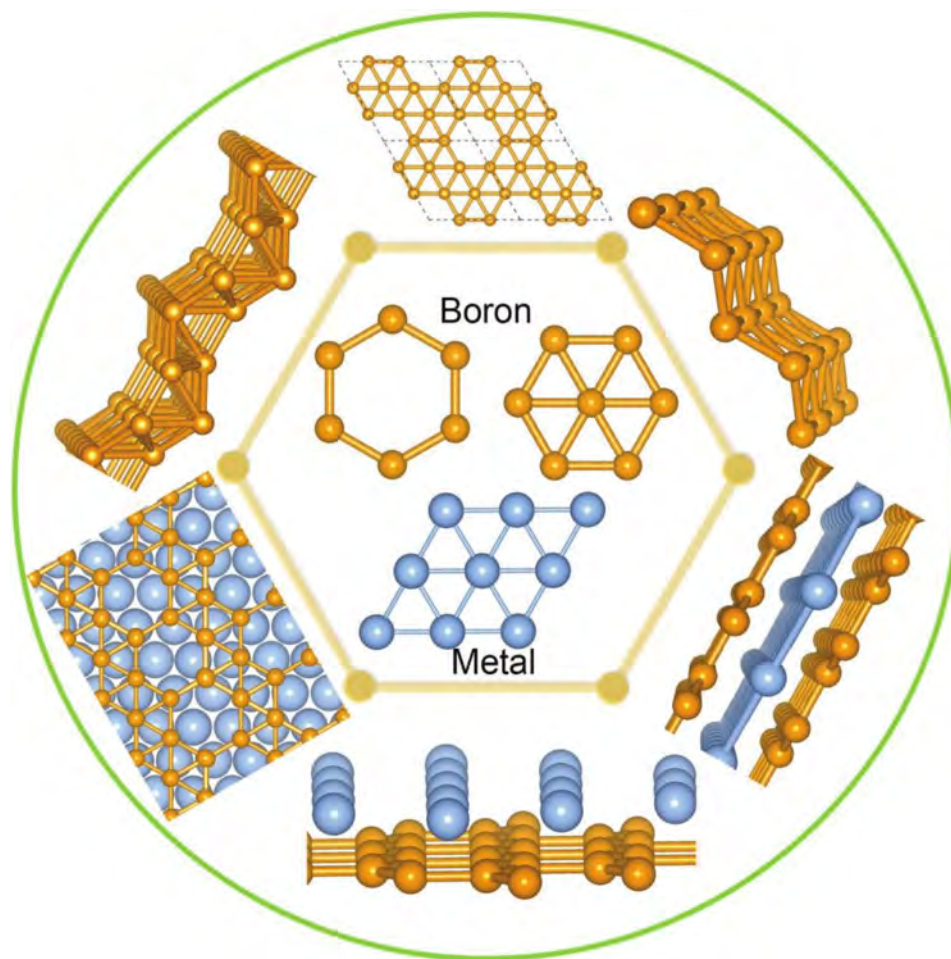


Figure 6. Borophene structures. Borophene exhibits polymorphism and structural anisotropy. Reproduced with permission from ref 127. Copyright 2019 Wiley-VCH Verlag GmbH and Co. KGaA, Weinheim.

heterostructure (Figure 5D) and employed a series of characterization techniques to analyze its band structures (Figure 5E,F). As can be seen, the holes generated upon illumination underwent a transfer from $g\text{-C}_3\text{N}_4$ toward GDY's valence band.

2.2. Borophene

2.2.1. Structures. Different from the honeycomb structure of graphene, the unique character of 2D boron layers is a triangular grid with a hollow hexagons (HHs) layout (Figure 6). The HH pattern is highly variable with concentration and distribution, with numerous crystal lattices near the ground-state energy line, leading to polymorphism.¹¹⁸ 2D boron possesses higher energy than its bulk forms, remarkably different from other known 2D materials. Therefore, assembling the boron atoms into a metastable 2D layer remains a challenge and needs further experimental efforts.

Until the year of 2015, borophene was synthesized under ultrahigh vacuum for the first time.³⁰ Compared with graphene, borophene is more robust, lighter, and more flexible,^{119,120} which has attracted rising attention recently. It possesses unique properties, such as strong electron–phonon coupling^{121,122} and optical transparency,¹²³ attributed to its polymorphism and anisotropic structure (Figure 6).^{118,124,125} Different phases of borophene can be a metal or a semiconductor. The metallicity makes borophene promising as an optically transparent electrode,¹²³ which is predicted to result in phonon-induced

superconductivity.^{121,122} The $\gamma\text{-B28}$ monolayer presents prominent semiconducting property with a direct bandgap of 2.25 eV, leading to a strong photoluminescence emission at ~ 626 nm.⁴³ Moreover, high phonon velocities can be obtained through the coupling of the low mass of borophene and its small bending stiffness, resulting in efficient thermal transport.¹²⁶

2.2.2. Chemical Properties. Borophene has low environmental stability, making it easily contaminated in ambient conditions.³⁰ Oxidation occurs when borophene is exposed to air. It was found to occur at the edges of borophene nanosheets owing to the chemically active edge effect. On the contrary, the regions with an intact lattice keep almost unoxidized, even as it is exposed in a high oxygen concentration. Moreover, it is predicted that borophene on metal substrate can catalyze the hydrogen evolution reaction.¹²⁸ This chemical property is unique among 2D materials and could be used to achieve varying functionalities via reaction with different chemical species.¹²⁹ However, considering practical applications, it is necessary to explore encapsulation methods for air-stability. For instance, the borophene NSs could be protected from the air through capping with a protection layer. Guisinger et al. reported that borophene nanosheets could be significantly protected from oxidation by covering with a silicon/silicon oxide layer.³⁰

2.2.3. Electronic Properties. Although bulk boron is an insulator, some of borophene polymorphs are metallic.^{118,130} The metallicity of most borophene polymorphs originates from the $2p_z$ state, which is highly delocalized around the Fermi level.

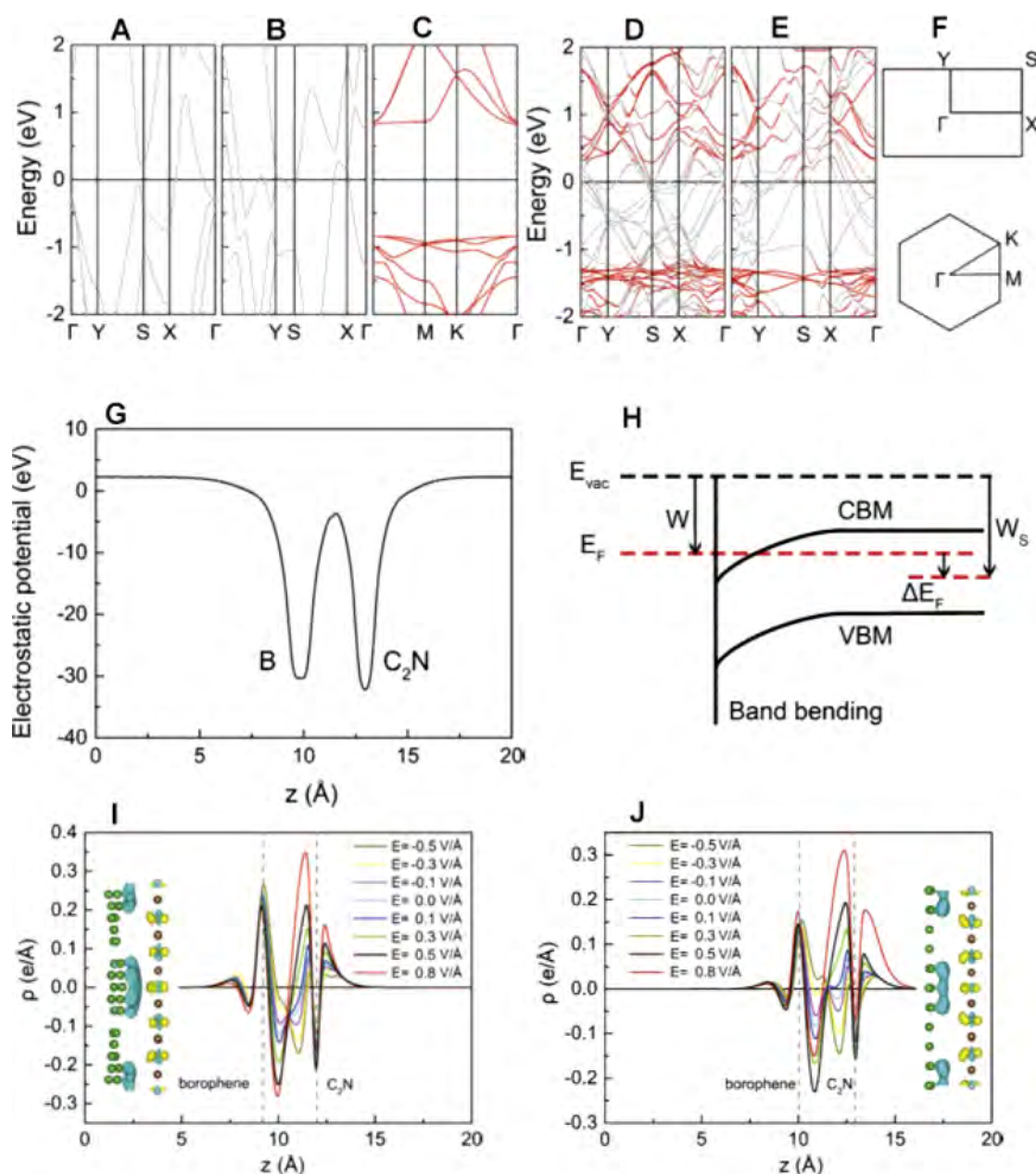


Figure 7. (A–E) Band structures of pure borophene and their heterostructures: (A) β_{12} borophene, (B) χ_3 borophene; (C) g-C₂N, (D) β_{12} borophene/C₂N vdW heterostructure, (E) χ_3 borophene/C₂N vdW heterostructure. (F) Brillouin zone and the high symmetry points. (G) plane-averaged electrostatic potential of the borophene/C₂N vdW heterostructure. (H) Schematic 2D electronic device model where the borophene/C₂N contact is connected to the g-C₂N channel. Different plane-averaged charge density with the different electric field in (I) β_{12} borophene/C₂N and (J) χ_3 borophene/C₂N heterostructures. Reproduced with permission from ref 139. Copyright 2018 Elsevier, Inc.

Significantly, for the $\nu_{1/5}$ sheet, its metallic state is partly attributed to the $2p_x$ and $2p_y$ states, which are located around the Fermi level in the borophene nanosheets with $\nu = 10$ –15%.¹¹⁸ Recently, the metallicity of borophene was experimentally confirmed.^{131–133} In 2016, Feng et al. conducted a systematic analysis of the electronic characteristics of the S1 borophene phase ($\nu_{1/6}$ sheet) on the Ag(111) surface through angle-resolved photoemission spectroscopy.¹³¹ They observed the metallic bands of the S1 borophene phase and demonstrated its Fermi surface composition on the Ag (111) surface with one electron pocket (B₁) and a pair of electron pockets (B₂ and B₂') at the \bar{S} point and near the \bar{X} point, respectively.

2.2.4. Optical Properties. Borophene, except the γ -B28 monolayer, shows extremely low photoconductivity owing to the absence of intermediate bands. The computed optical conductivity anisotropy was also reported. Borophene remains optically inactive up to 6.5 eV under the electric field with orientation along the main conductive direction (along nonbuckled B lines). The transmittance of borophene depends on the disorder, with the value possibly reaching 100% in the visible range.¹³⁴ Upon oxidation, the reflectance and the optical conductivity of borophene in the NIR region increase, while its reflectance in the visible region remains relatively low, and the optical transparency is reduced. Oxidized borophene remains metallic. These make borophene suitable as a transparent

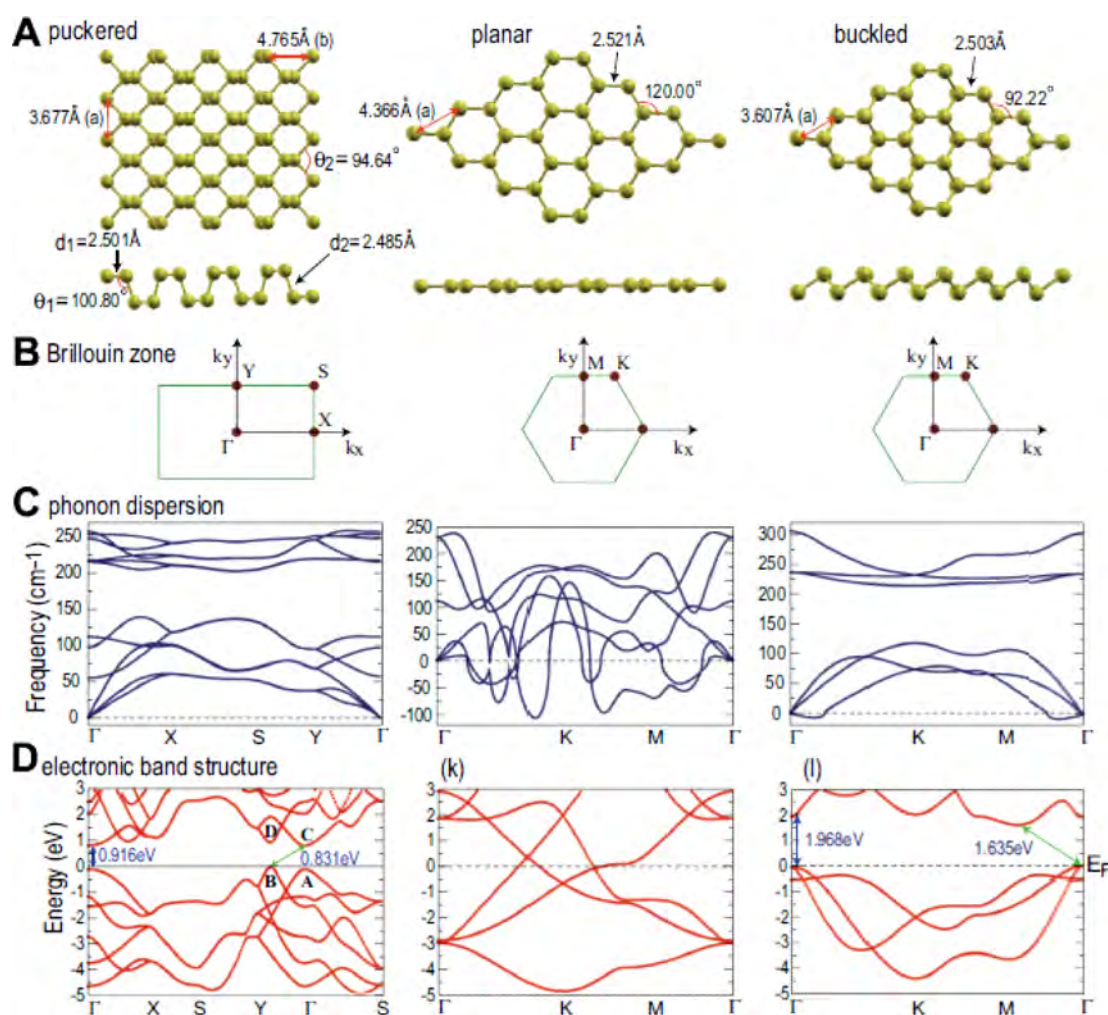


Figure 8. DFT calculation results for puckered, planar, and buckled arsenene: (A) simulated structural parameters; (B) Brillouin zones; (C) phonon dispersion results; (D) calculated electronic band structures. Reproduced with permission from ref 41. Copyright 2015 American Physical Society.

conductive material.¹³⁵ Different adsorption sites have been taken into account. It was found that the preferred one was in between adjacent B lines. However, from the computed electronic structure, it was anticipated that the degradation of dc conductivity is because the disorder decreases the velocities as it increases the effective masses.

2.2.5. Heterojunctions. Recently, constructing van der Waals heterostructures or lateral heterojunctions of borophene with another 2D material or compound has attracted increasing interest in theoretical and experimental research.^{136–139}

Taking the borophene- C_2N (a type of carbon nitride) van der Waals structure as an example, the band structure and electronic structure take advantage of both borophene and C_2N (Figure 7), which provides an opportunity for rationally tuning the properties accordingly.¹³⁹ Specifically, Figures 7A–F clearly show that both the β_{12} B/ C_2N vdW heterojunction and χ_3 B/ C_2N vdW heterojunction form n-type Schottky contacts and show metallic properties, while preserving the band structures of the C_2N layer. The work functions and charge density values unambiguously demonstrated charge transfer between the two constituents. In Figure 7G, the electrostatic potential of C_2N was more negative than that of borophene. The calculations based on the electronic device model further proved charge transfers from the contact to C_2N , forming an n-type contact. More interestingly, it was shown in Figure 7I,J that the external

electronic field could effectively modulate the energy level of borophene by promoting charge transfer. It leads to achieving tunable contacts from n-type Schottky to Ohmic ones. This suggested a good theoretical foundation for designing electronic devices.

2.3. Arsenene, Antimonene, and Bismuthene

Arsenene,^{41,140–142} antimonene,^{6,143–145} and bismuthene,^{146,147} located in the same group with phosphorene, have become new research favorites and are developing vigorously. Arsenene and antimonene were first predicted with a wide bandgap by Zhang et al.¹⁴⁰ More theoretical and experimental work were further exploited.^{5–8} Antimonene is more stable than phosphorene,^{145,148} and some excellent qualities are predicted theoretically, such as high carrier mobility,¹⁴⁹ size-dependent thermal conductivity,¹⁵⁰ size-induced semiconductor–semi-metal transition, strain-induced direct–indirect bandgap transition,¹⁴⁰ and spin–orbit coupling.¹⁵¹ Successful fabrication approaches for antimonene include liquid-phase exfoliation,¹⁵² mechanical isolation,¹⁵³ and epitaxial growth.^{154,155} Broad interests is aroused for their potential applications in energy storage,¹⁵⁶ electrocatalysis,¹⁵⁷ supercapacitors,¹⁵⁸ and optoelectronics.^{143,154}

2.3.1. Structures. **2.3.1.1. Arsenene.** In 2015, Kamal and co-workers employed DFT calculations to examine arsenene with a

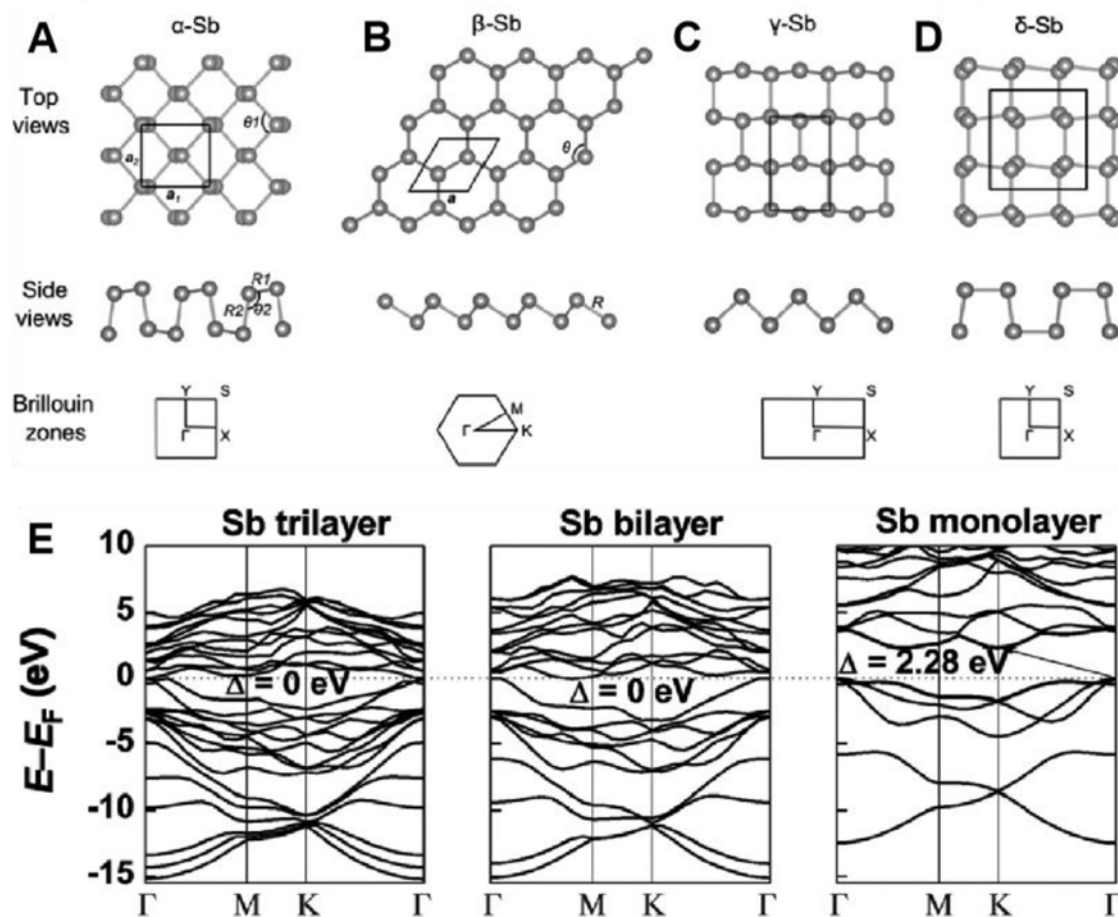


Figure 9. (A–D) Calculated configurations of four allotropes of Sb. Reproduced from ref 162. Copyright 2015 American Chemical Society. (E) Layer-dependent electronic structures of Sb. Reproduced with permission from ref 166. Copyright 2015 Wiley-VCH Verlag GmbH and Co. KGaA, Weinheim.

honeycomb structure. They showed that wrinkle structures were the steadiest forms.⁴¹ Among the three structures depicted in Figure 8A,B, buckled arsenene is the most stable configuration due to its lowest energy. Its cohesive energy is similar to that of a puckered structure, with a difference close to the thermal energy under ambient conditions.¹⁵⁹ They are similar to the cohesive energy of bulk arsenic, while that of the planar arsenene is calculated to be the least. The perspective of energy consideration explains why puckered and buckled structures are more favorable and stable (Figure 8C). However, recent studies have illustrated that 2D pnictogens are unstable when in contact with water and oxygen, where oxidative structural degradation would happen. Theoretical calculation offers predictive guidelines for Xenes, but the results might not be consistent with the real case. Therefore, experimentally convincing evidence on the structures and properties of Xenes is in demand to evaluate a theoretical model.¹⁶⁰ Unlike the 2D black phosphorus (BP), the 2D arsenene is defined as a semiconducting material because of its indirect bandgap from 0.3 to 2.0 eV. The simulation results elucidated that at the Γ point and along the Γ –Y direction, the conduction band and the valence band possess maximum and minimum values, respectively. Also, Figure 8D displays that the energy difference between the two valence band edges around the Fermi level is smaller than 85 meV for puckered arsenene, while the value is higher than 500 meV for puckered BP.^{41,161}

2.3.1.2. Antimonene. Compared with BP and As, antimonene is another pnictogen with a heavier mass and higher stability toward water and oxygen. Figure 9A–D depicts four antimonene phases. First principle theoretical studies demonstrate that the β -type phase with a curved atomic layer is the most stable configuration from the thermodynamic perspective.¹⁶² It is well accepted that a monolayer antimonene has an indirect bandgap from 0.76 to 2.28 eV, depending on the selected configured allotropes (five typical honeycomb and four nonhoneycomb structures).¹⁶³ Such antimonene has low lattice thermal conductivity¹⁶⁴ as well as modulated electronic structures. Theoretical calculations also predicted that ultrathin antimonene with a few-layer has a zero bandgap.⁶ Therefore, practical applications of antimonene might be inhibited, especially in the field of optoelectronic semiconductor devices. The major tackle for making the best of antimonene is through band engineering via site point defects/dopants or fabricating heterostructures with graphene and carbon nitride. Notably, antimonene oxide is a direct-bandgap semiconductor whose bandgap tuned from 0 to 2.28 eV.¹⁶⁵ Figure 9E displayed the layer number-dependent electronic structures of antimonene. As can be seen, the trilayers and bilayers showed metallic states with the VB top and CB bottom crossing the Fermi level, while monolayered Sb demonstrated a wide band gap of 2.28 eV.¹⁶⁶ Therefore, band engineering via surface modification serves as

an important strategy that optimizes the structures and performance of pristine antimonene.

2.3.1.3. Bismuthene. Parts A and C of Figure 10 depict the molecular structures of 3D and 2D Bi. The energetic parameters

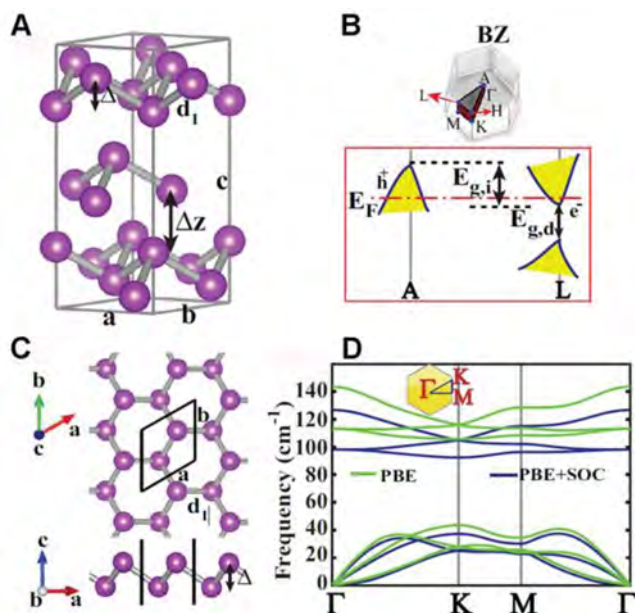


Figure 10. (A) Hexagonal unit cell of bulk Bi crystal structure and (B) relevant structure parameters of Bi crystal. (C) Single layer of the buckled honeycomb structure of Bi, b-Bi. (D) Phonon dispersion curves are calculated with and without spin–orbit coupling (SOC). Reproduced with permission from ref 35. Copyright 2016 American Physical Society.

of corresponding structures are also shown in Figure 10B,D.³⁵ According to DFT calculations, bismuthene with a rhombohedral structure is the only thermodynamically stable one. Among the pnictogens, Bi is the only metallic element in Group V and owns the greatest mass fraction, distinguishing it from others. Because of its large molar weight and prominent spin–orbit coupling, bismuth is regarded to be a common component in nontrivial topological systems. One recent work reported that bismuthene could serve as an insulator, with a 2D topological structure, but it is still under debate.¹⁶⁷ For a deeper understanding of its electronic nature, it is of high significance to test the electron transmission properties of Bi with isolated buckled structure. It helps in profound insights on the contribution of spatial confinement to the electrical properties. The transformation from semimetal/metal into semiconductor during exfoliation of heavy pnictogens is accompanied by electron transfer and bandgap transition. Notably, reducing the thickness of Bi might lead to unique properties like 2D topological insulation, which is not available in bulk Bi. Hence, bismuthene has broad application prospects.

2.3.2. Chemical Properties. Some 2D materials with coordinatively unsaturated atoms are attracting increasing interest for engineering functionalized 2D surfaces.^{168,169} The bandgap energy and terminating configuration have been reported to change dramatically after coordinative surface modification. Considering phosphorene, the affinity of unpaired electrons in phosphorus to the functional groups is not very strong, such that its surface modifications are usually performed by electrostatic attraction.^{170,171} Although the affinity toward organic functionalities might not be strong, these materials are

attractive for anchoring metal species. The diameters of arsenic, antimony, and bismuth are 0.30, 0.32, and 0.34 nm, respectively. They are larger than those of nonmetal elements but close to the noble metals, making these 2D materials possible for anchoring metal atoms on the surface and for heteroatom doping via a chemical exchange process.^{34,172} Despite the above properties, the stability issues of these 2D materials are worth noting, as the materials suffer from decomposition in the presence of O₂ and H₂O.^{44,173}

Owing to the nonmetallic nature of arsenene and the coordinatively unsaturated arsenic atoms, heteroatom dopants are usually introduced to endow the pristine arsenene with valuable chemical properties such as a strong bond formation with polar molecules and catalytically favored energy level configuration.¹⁶⁸ Antimonene also has potential for poisonous gas sensing because antimonene is reported to have a strong affinity toward NO₂ and form a covalent bond with such gas but only has physical interaction with water molecules. By embedding different adatoms into the antimonene, the chemical properties are adjusted as desired, broadening the chemical applications of antimonene.¹⁴³ As discussed in previous sections, the conductivity and metallic properties of bismuthene are layer-dependent. In terms of chemical properties, the unpaired electrons of bismuthene are more accessible to lose than arsenene and antimonene, making it more suitable for sensing NO, NO₂ and NH₃ by forming a strong metal–nitrogen covalent bond. The metallic nature of bismuthene make it ready to achieve controllable exfoliation with less energy consumption compared to nonmetallic Xenes.³⁵

2.3.3. Electronic Properties. Previous research has demonstrated that Group-V 2D materials may exhibit structure-dependent metallic or semiconductor-like properties. The bandgaps of puckered and buckled arsenenes were determined to be indirect, with the values of 0.831 and 1.635 eV, respectively. Thus, 2D arsenene is the most stable indirect bandgap semiconductor. As to the electronic structures and bandgap structures, theoretical studies have illustrated the partial density of states (PDOS) of buckled and puckered arsenene. It was found that the *s* and the *p* orbitals have an enormous influence on the states around the Fermi level. What should not be ignored is that the *s* orbitals contribute much less than the *p* orbitals for the total DOS.¹⁷⁴ Unlike black phosphorus, which has a direct bandgap,^{24,175} the indirect-gap semiconducting character makes puckered arsenene distinctly different. The indirect semiconducting characteristics of arsenene originate from a competition between the energies of the conduction band edge and the valence band edge, where the VBM and the CBM occur along the Γ -Y direction and at the Γ point, respectively. Bi is determined to have prominent spin–orbit coupling within its structures. Existing as a hexagonal crystalline structure, 3D Bi has a narrow direct bandgap and inverted indirect bandgap. It suggests that 3D Bi shows a topological insulating behavior when imposing additional strain. However, bismuthene is topologically nontrivial from the simulated spin–orbit coupling calculations.¹⁷⁶ As a significant indicator of electronic properties, carrier transport properties of As, Sb, and Bi have been explored by the deformation potential technique,^{166,177} with the values reaching thousands of cm² V⁻¹ s⁻¹. Interestingly, the spin–orbit coupling (SOC) effects seem not to be a key factor in modulating arsenic and bismuth conduction bands. However, it altered the topmost valence band, resulting in variations of effective masses and deformation

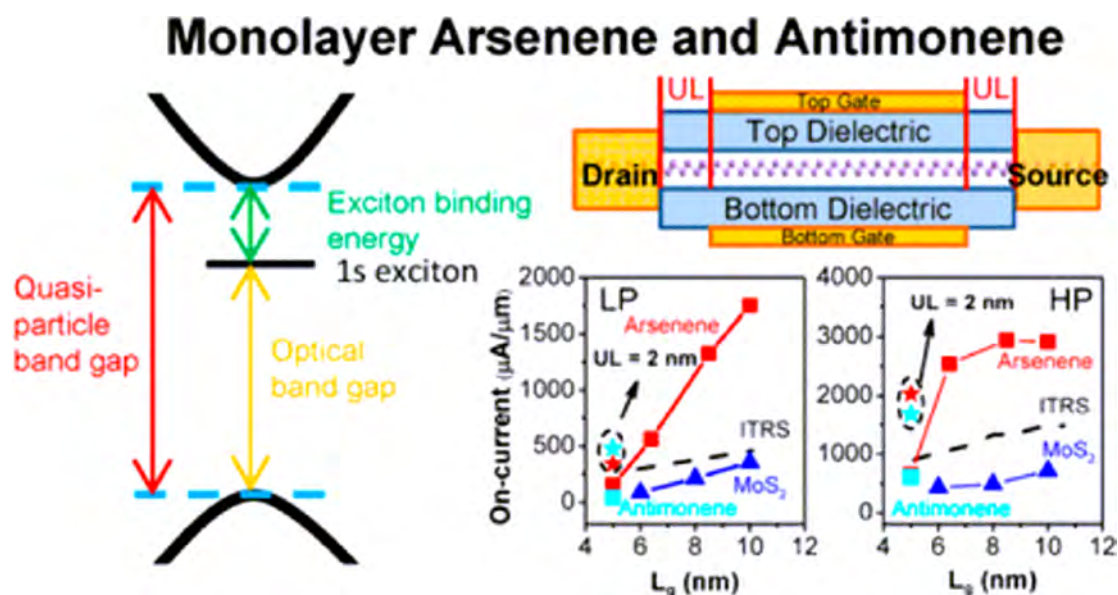


Figure 11. Schematic description for the optical properties of monolayer arsenene and antimonene. Reproduced from ref 177. Copyright 2017 American Chemical Society.

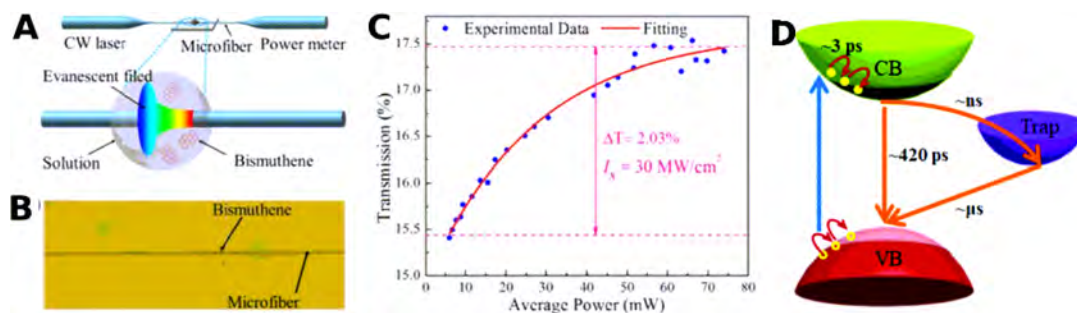


Figure 12. (A) Scheme for illustrating the deposition process of bismuthene. (B) Morphology of the as-synthesized bismuthene based SA. (C) Relationship curve between transmission and average power. Reproduced with permission from ref 182. Copyright 2018 Wiley-VCH Verlag GmbH and Co. KGaA, Weinheim. (D) Schematic of carrier dynamics in a few-layer bismuthene. Reproduced with permission from ref 183. Copyright 2018 Royal Society of Chemistry.

potentials and increasing the holes mobilities: 25% for arsenene and 84% for bismuthene.

The tunable electronic properties of VA group Xenes provide an attractive prospect for engineering applications. Various techniques have been theoretically proposed to modulate their intrinsic characteristics, such as creating defects, chemical modifications, and introducing heteroatom dopants. In reality, defects are usually inevitable due to the synthetic methods or poor stability of these materials under oxidative conditions. For targeted characteristics modulation, defects are usually introduced artificially to the surface of 2D materials, which destroy the uniform 2D structures, further altering the electronic conductivity and carrier mobility.

2.3.4. Optical and Nonlinear Optical Properties. The optical bandgaps of arsenene, antimonene, and bismuthene are all tunable, despite the fact that As and Sb are indirect bandgap semiconductors. From calculations, monolayer arsenene possesses an optical bandgap of 1.6 eV and an exciton binding energy of 0.9 eV, while those of antimonene are 1.5 and 0.8 eV, respectively. Deeper insights into the studies manifest that the values of electron/hole mobilities reaching 150/510 and 21/66 $\text{cm}^2/\text{V}\cdot\text{s}$ for antimonene and arsenene, respectively, demonstrating that the conductivity and the carrier mobility are

relatively low for arsenene and moderate for antimonene. With the excellent detected stability under ambient conditions, monolayer As and Sb exhibit exciting prospects for practical optoelectronic applications.¹⁷⁷ Figure 11 clearly show the bandgap structures of a semiconductor (quasi-particle and optical gaps). The calculations were performed over monolayer arsenene and antimonene whose underlayer equals to 2 nm. As depicted in the left bottom of Figure 10, whether at high power (HP) and low power (LP), the results demonstrated that both Xenes have larger on-current than MoS_2 , promising for optical and electronic applications. DFT calculations of dielectric functions, absorption coefficients, and other optical parameters for antimonene were performed to elucidate its optical properties.¹⁴⁹ It was found that antimonene was promising for applications in UV nanodevices, solar energy transformation, and storage.¹⁷⁸ Noteworthy, the dielectric functions differ for different crystal structures of antimonene. They have a negative real part with the absolute value ranging from 5.1 to 9.0 eV for the α -phase and 6.9 to 8.4 eV for the β phase antimonene, suggesting that antimonene is intrinsically metallic in the ultraviolet wavelength range. Moreover, the plasmon energies of ~ 9 eV were obtained from its electron energy loss spectra, indicating metallic characteristics relating to the reflection of

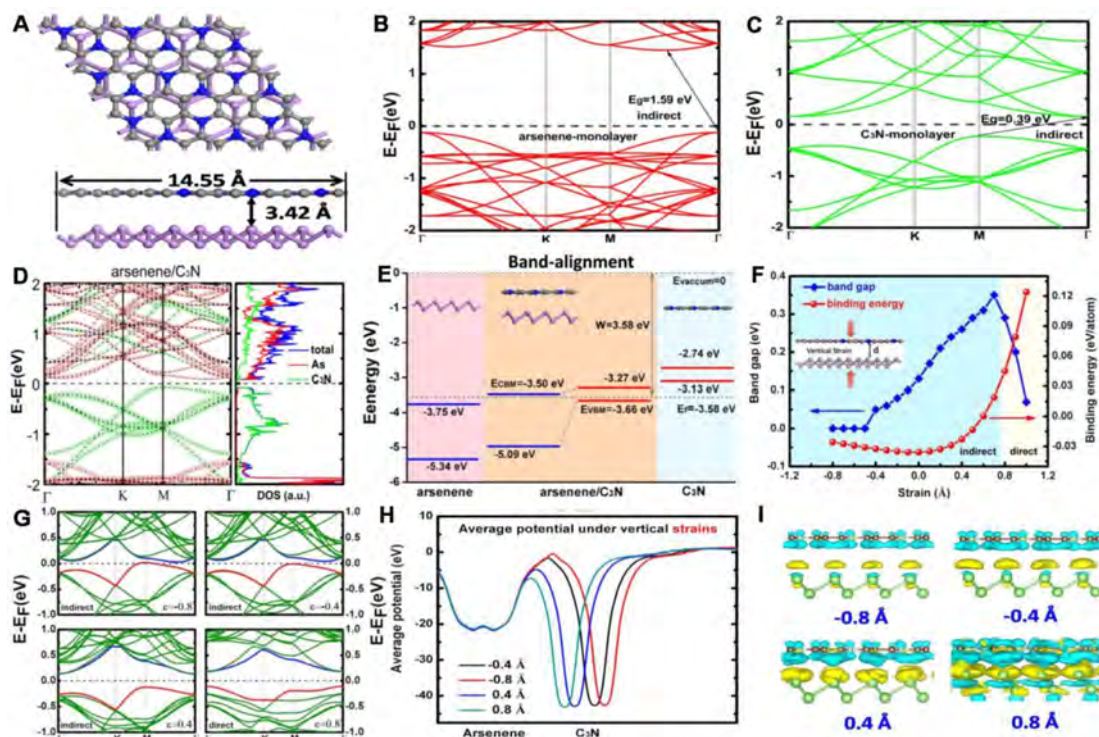


Figure 13. (A) Configuration of the optimized arsenene/ C_3N_4 heterostructure. Calculated band structures for (B) monolayer arsenene. (C) Single-layer C_3N_4 and (D) arsenene/ C_3N_4 heterostructure. (E) Theoretical band alignment deduced for arsenene/ C_3N_4 heterostructure and its (F) bandgap E_g and binding energy E_b . (G) Calculated band structures for the heterostructure at a different vertical strain. (H) Simulated average potential under vertical strain. (I) Isosurface of the differential charge density. Reproduced with permission from ref 187. Copyright 2018 IOP Publishing.

light.¹⁷⁹ Recent studies demonstrate that Sb and Bi nanosheets, whose bandgap values are in the visible to NIR spectral range, have great potential for broadband photonic and light modulator devices. On the basis of the Heyd–Scuseria–Ernzerhof (HSE) results, hexagonal buckled Sb shows obvious visible light absorption, and the absorption of hexagonal buckled Bi is in the infrared region. Notably, the optical properties related performances of these two structures are active even out of the visible light regime. Therefore, the absorption initiates in the IR region for all other phases (symmetric washboard, asymmetric washboard or square-octagon) excluding the hexagonal buckled phase.¹⁸⁰

Similar to GDY, the nonlinear optical properties of Sb and Bi, such as the optical Kerr effect and saturable absorption (SA), have been reported. Lu et al. demonstrated the optical Kerr effect from a few-layer antimonene with a high nonlinear refractive index ($10^{-5} \text{ cm}^2 \text{ W}^{-1}$) by using the SSPM experiment.¹⁴⁵ Zhang et al. observed that nonlinear absorption (NLA) was saturated in β -antimonene nanosheets at a laser power of $49.7\text{--}253.5 \text{ MW cm}^{-2}$, while the NLA was increased by TPA at a laser power over 613.1 MW cm^{-2} .¹⁸¹ Lu et al. reported the optical Kerr effect from a few-layer bismuthene, with a high nonlinear refractive index, which was obtained through the SSPM experiment. They also illustrated its SA property at 1559.18 nm , with a saturable intensity of $\sim 30 \text{ MW cm}^{-2}$ (see Figure 12A–C).¹⁸² Yang et al. demonstrated by time-resolved absorption spectroscopy that the origin of SA in a few-layer bismuthene is the superfast (fs to ps) carrier dynamics at the early stage and a trap mediated slow exciton bleaching recovery process of up to ms (see Figure 12D).¹⁸³ The bismuthene and antimonene applications in nonlinear optical devices will be discussed in section 4.1.2.

2.3.5. van der Waals Heterostructures. The interlayer interaction in the Xenex is the van der Waals force, which is much weaker than the intralayer covalent bonding. It makes possible to rearrange atomically thin layers of Xenex by using the van der Waals force among different layers composed of different 2D materials and form van der Waals heterostructures. The rearrangement would maintain the integrity of the original layer structures due to the weak interaction between the adjacent layers. Compared to traditional semiconductor heterojunctions, there is a small lattice mismatch requirement between 2D Xenex. It should be noted that the interface of the heterostructures undergoes mutations at the atomic level, which can control the stacking order between materials, thus showing unique electrical and optical properties for various applications.^{184–186}

Studies on the As, Sb, and Bi heterostructures have been mainly conducted through theoretical calculations, despite some 2D heterostructures being successfully synthesized. Combined pnictogens with other 2D materials such as metal sulfides, group-III monochalcogenide, and other mono-elemental Xenex have been reported.^{188–192} Taking the arsenene/carbon nitride (C_3N_4) heterostructure as an example, the optimized packing mode is shown in Figure 13A. Theoretical calculations were performed to illustrate the electronic band structures. It was observed from Figure 13B–D that the electronic structure of monolayer As/ C_3N_4 maintains the structures of both As and C_3N_4 . Meanwhile, the VBM and the CBM undergo drastic changes from the original As and C_3N_4 because of their mutual interactions. The simulated results via DFT calculations matched well with the results from the projected density of states, demonstrating that the as-assembly As/ C_3N_4 hybrid has an indirect bandgap of 0.16 eV . Furthermore, as indicated in

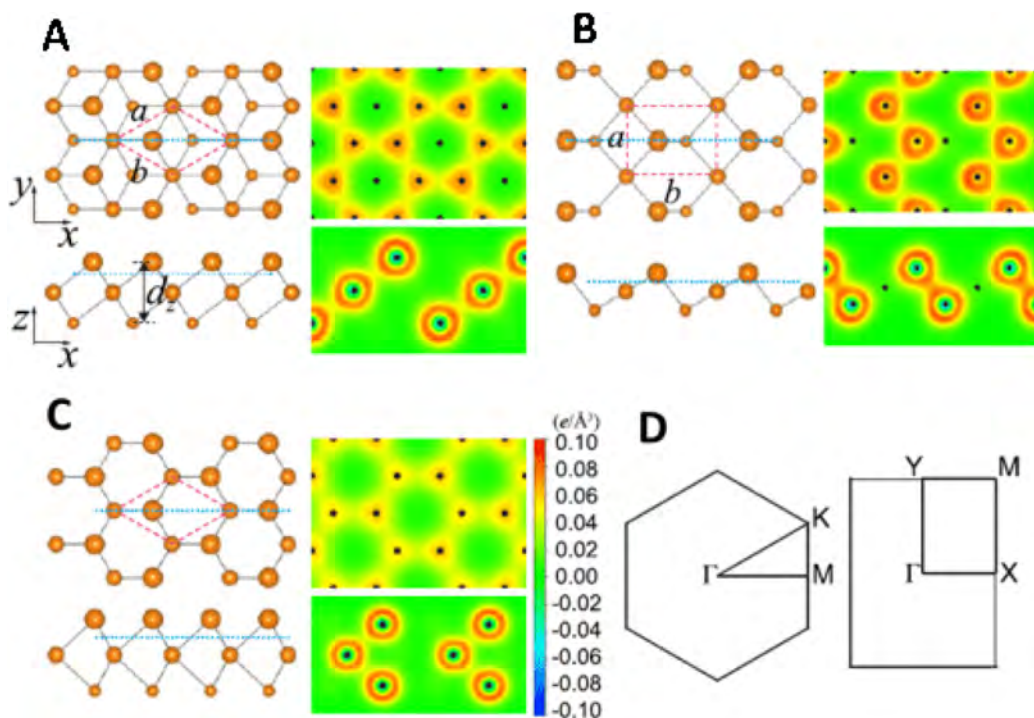


Figure 14. Tellurene structures in different phases: (A) α -Te, (B) β -Te, and (C) γ -Te. (D) Surface Brillouin zones. The unit cell of each phase is shown. Reproduced with permission from ref 42. Copyright 2017 American Physical Society.

Figure 13F–I, the interlayer van der Waals interaction plays an important role in determining the geometry and electronic characteristics. In Figure 12F, varying the vertical strains, it is observed that the bandgaps were tuned within the range from 0 to 0.35 eV. Figure 13G reveals that the VBM shifting can be controlled via vertical strain engineering, which can be attributed to a tunable van der Waals interaction between carbon nitride layers and arsenene. The enhanced interlayer coupling interaction serves as an exciting prospect.¹⁹³ Notably, the VBM contributions from As (minuend) and carbon nitride (subtrahend) would respectively go up and down with the increased dielectric constant, suggesting the influence on the monotonously enhanced bandgap. Theoretical studies have also proven that electron transfer would be more prominent with the decreased distance between the layers. It is determined that the bandgap would reach its maximum only when the energy of the CBM in arsenene is higher than that in carbon nitride.¹⁹⁴

In sharp contrast, although the vertical strain also explains the changes of the electronic structures from the perspective of band arrangement, it must be taken into account that there is decreased charge transfer between the heterostructures when ϵ reduces, which is confirmed in Figure 13I. Another point that requires attention is that the VBM in carbon nitride and CBM in As would go up and down, respectively, when the heterostructures are packed denser. Therefore, based on the properties discussed above, the As/C₃N₄ heterostructure with direct and smaller bandgaps adjusted by vertical strain are promising candidates for solar energy conversion applications.¹⁹⁵ In addition to C₃N₄, arsenene can form heterostructures with other 2D materials and metal salts. The bandgap alignment also influences the electronic band structures, conductivity, and optical properties due to the interlayer van der Waals interplay.

Besides van der Waals heterostructures, which are generally packed with vertical strain, a lateral heterostructure can be formed via covalent bonding, which is more stable than the van

der Waals heterostructures in principle.¹⁹⁶ However, these structures are more difficult to synthesize uniformly due to the strict requirement for the subtle bonding and arrangement structures.

2.4. Tellurene

Tellurium (Te), belonging to the VIA group, has a small bandgap of 0.35 eV. 2D tellurium, named tellurene, was calculated to possess multiple phases and higher carrier mobility than transition-metal dichalcogenides.³⁶ It possesses unique properties such as broadband absorption and efficient photothermal conversion.¹⁹⁷ The photothermal effect in other Te nanomaterials is also observed, which has been employed in photothermal cancer therapy.^{197,198} The research work on tellurene shows its broad applications in topological insulator,¹⁹⁹ thermoelectric,²⁰⁰ semiconducting,²⁰¹ electronic,^{202–204} optoelectronic,^{205,206} and biomedical fields.^{207–210}

2.4.1. Structural Phase Transition. Zhu et al. predicted three structures of tellurene: stable 1T-MoS₂-like structure (α -Te), 2H-MoS₂-like structure (γ -Te), and metastable tetragonal structure (β -Te) (Figure 14).⁴² Their formation mechanisms are based on the multivalent nature of the metalloid element Te, with the metallic central-layer Te, while the two outer layers are more like semiconductors (e.g., MoS₂-like structure). The α -Te phase exists in specific thicknesses divided by three layers cut along the [001] direction of the bulk Te. Both the α - and the β -Te phases possess much higher carrier mobilities than that of MoS₂. Qiao et al. found that the α -Te phase is most stable in few-layer tellurene nanosheets,²¹¹ while the tetragonal β -Te phase more likely exists in monolayer tellurene nanosheets.

Recent efforts in fabricating atomically thin tellurene also have shown versatile results. Chen et al.²¹² grew a crystalline β -phase monolayer Te film on highly oriented pyrolytic graphite substrates through van der Waals epitaxy (vdWE). Huang et al. also grew monolayer Te films on graphene layers through

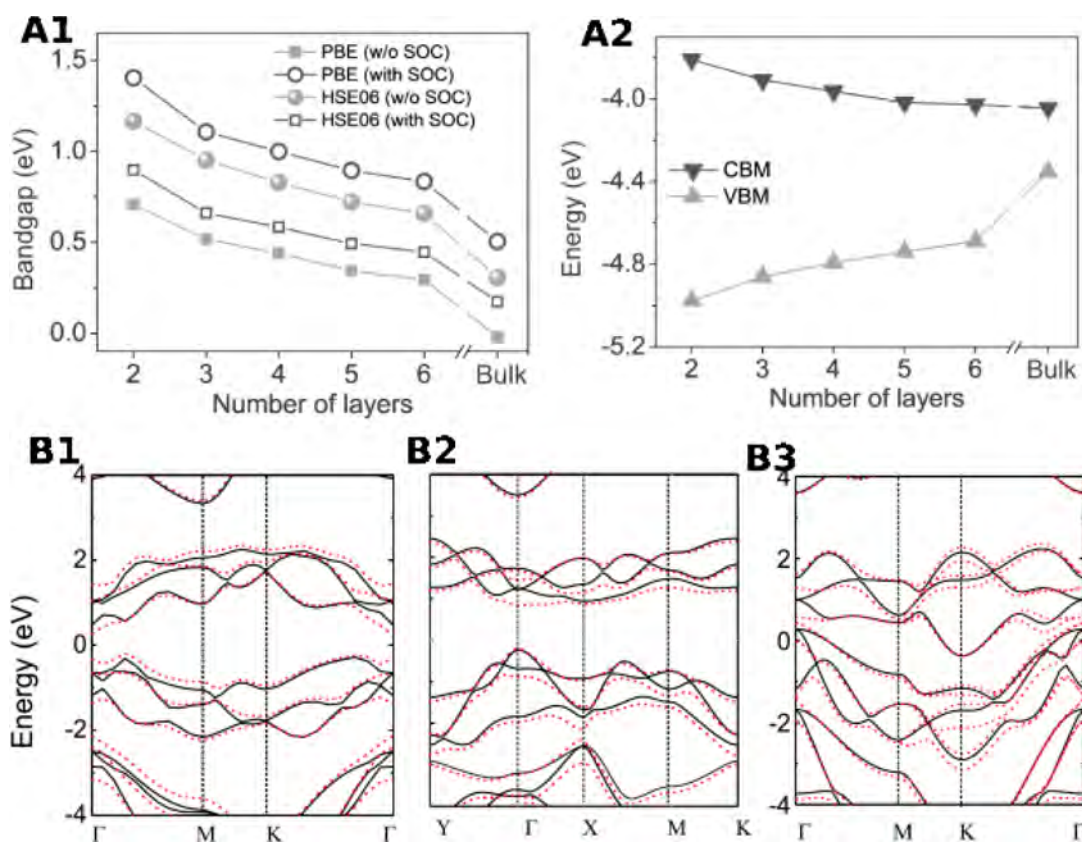


Figure 15. (A1, A2) The change in the indirect bandgaps and the positions of CBM and VBM with layer number of few-layer tellurene based on the Perdew–Burke–Ernzerhof (PBE) functional and the hybrid functional (HSE06) with and without spin–orbit coupling (SOC). Reproduced with permission from ref 211. Copyright 2018 Elsevier, Inc. Band structures of (B1) α -Te, (B2) β -Te, and (B3) γ -Te, obtained within the PBE scheme without (solid) and with (dashed) the inclusion of SOC. Reproduced with permission from ref 42. Copyright 2017 American Physical Society.

vdWE,²¹³ but with a larger lattice, which is more consistent with bulk trigonal Te. The work of Wang et al.²⁰² illustrated that the free-standing few-layer tellurene grown in the solution possesses the bulk trigonal structure, which corresponds to the prediction of Qiao et al.²¹¹

The different structures in tellurene derived from different synthesis processes show that the formation mechanisms of a monolayer or few-layer tellurene are complex. It is necessary to make theoretically and experimentally more efforts to investigate the effect of the growth process on its structural phase transition. Furthermore, the growth substrate also plays an essential role in determining the structure phase and characteristics of the as-grown tellurene.

2.4.2. Chemical Property. High air-stability of tellurene has been observed even for few-layer nanosheets. There is no obvious degradation of the electrical performance in 2D tellurene based transistors in two-month air-exposure under ambient conditions.²¹³ The stability of tellurene in solution was also investigated. For photodetection performance, after storage of tellurene nanosheets in 0.1 M KOH for 1 month, a 24% reduction of the photocurrent intensity was observed, indicating good chemical stability of tellurene NSs in KOH electrolyte.³⁸ The existence of a larger energy barrier is responsible for preventing the oxidation of few-layer tellurene nanosheets. This high environmental stability makes tellurene promising for technological realization.

2.4.3. Electronic Property. The electronic band structures of monolayer and few-layer tellurene have been studied theoretically. Qiao et al. presented that bilayer tellurene has an

indirect bandgap, with a value of 1.17 eV. When the layer number of tellurene increases, the bandgap of the few-layer tellurene is reduced (Figure 15A1),²¹¹ with their VBM varying from -4.98 eV to -4.35 eV. It is about three times the CBM, which indicates that the contact between the few-layer tellurene nanosheets and the electrodes is p-type (Figure 15A2). Zhu et al. demonstrated that α - and β -tellurene are semiconductors with the respective indirect bandgap of 0.76 and 1.17 eV (Figure 15B1, B2), while γ -Te is metallic (Figure 15B3).⁴²

The thickness-dependent electronic band structure endows tellurene as a promising candidate for many emerging applications in the mid-infrared and terahertz spectral range. Tellurene is also predicted to have large carrier mobility at room temperature, covering a large range of hundreds to thousands of $\text{cm}^2 \text{V}^{-1} \text{S}^{-1}$.^{42,211} It is much greater than that of a few-layer BP and 2D TMDCs (transition-metal dichalcogenides), which makes tellurene promising for building high-speed and energy-efficient electronics, like transistor devices.²⁰²

2.4.4. Optical and Nonlinear Optical Properties. A significant increase in absorption begins at 1.3 eV in 2L- α -Te (Figure 16A1), which shows an interband transition between the conduction band and the valence band. This absorption edge becomes smooth in thick Te nanosheets (NSs) because of greater electronic band dispersion as a result of the stronger interlayer electronic interaction (Figure 16A2).²¹¹ Therefore, light absorption in a few-layer α -Te is nearly isotropic, making it a good light absorber. Moreover, tellurene has an extraordinarily high incident light absorbance, which is linearly polarized with the in-plane directions. Figure 16A3 shows the optical

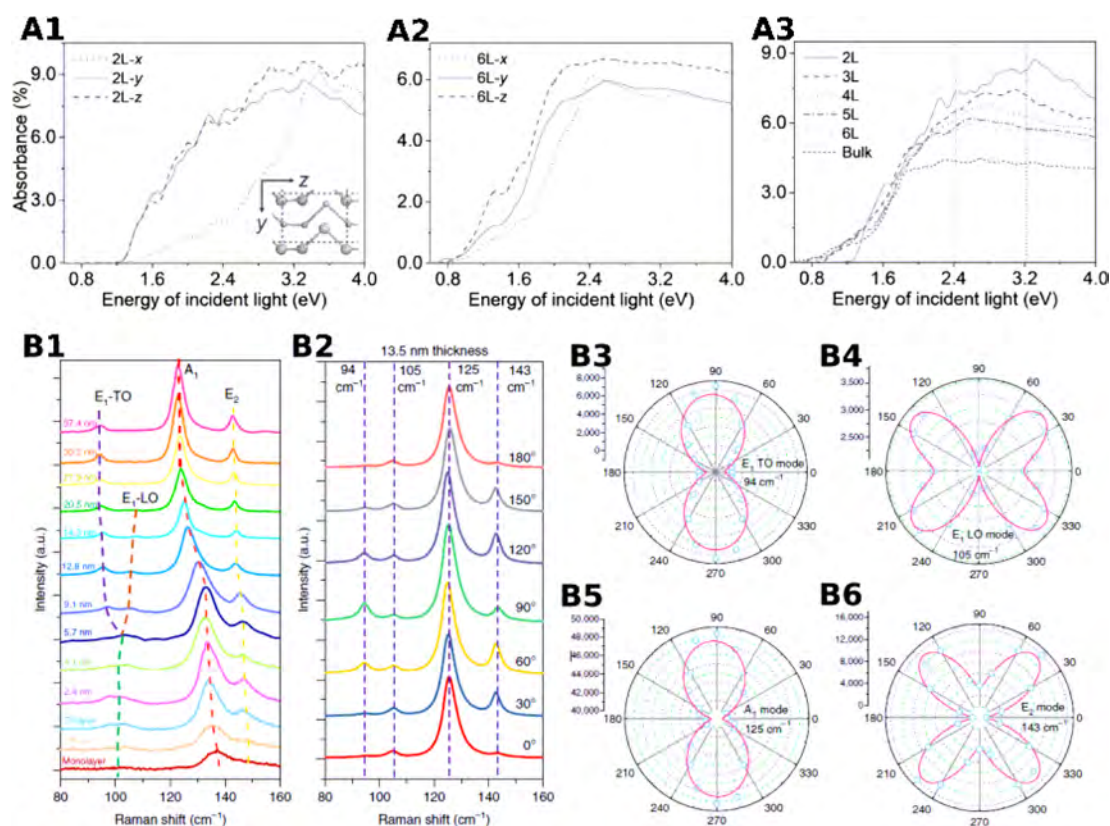


Figure 16. (A1, A2) Respective absorbance of 2L- and 6L- α -Te upon the incident light with the polarization direction along with three-dimensional directions. (A3) Absorbance of few layers α -Te upon the incident light with the polarization direction along y -axis. Reproduced with permission from ref 211. Copyright 2018 Elsevier, Inc. (B) Thickness-dependent angle-resolved Raman spectra. (B1) Thicknesses-dependent Raman spectra. (B2–B6) Angle-resolved Raman spectra for different modes with different angles between the incident laser polarization and the crystal orientation. Reproduced with permission from ref 202. Copyright 2018 Springer Nature.

absorbance of bulk α -Te and a few-layer (from two layers to six layers) α -Te when light is linearly polarized with the noncovalent direction (y -axis). It can be seen that the absorption edge energy of tellurene is nearly 0.2 eV larger than its bandgap energy.

For the first time, Wang et al. studied the optical properties of the as-prepared tellurene with thickness from monolayer to 37.4 nm at room temperature, applying angle-resolved polarized Raman spectroscopy.²⁰² With the light entering along the [1010] direction and polarized along the [0001] helical chain, the Raman spectra of tellurene with different thicknesses were recorded (Figure 16B1). There are three prominent peaks, corresponding to three phonon modes: one A-mode corresponding to chain expansion in the basal plane and two E-modes of E1 and E2 characters, which respectively correspond to bond bending around [1210] direction, and asymmetric stretching with the [0001] direction modes. The E1 mode includes two phonon modes; one is the transverse vibration E1(TO) at 92 cm^{-1} , and the other is longitudinal vibration E1(LO) at 105 cm^{-1} .

For tellurene thicker than 20.5 nm, the E1 (LO) mode is absent (Figure 16B1). With the thickness decreasing to 9.1 nm, the deformation potential of the crystal lattice is increased, resulting in the appearance of the E1 (LO) mode. When the thickness of tellurene is close to 9.1 nm, the E1(TO) and E1(LO) modes are degenerate with peak broadening, possibly due to a variation of the electronic band structure and the intrachain atomic displacement. Furthermore, as the thickness of tellurene decreases to a monolayer, both E₁ (shift to 136

cm^{-1}) and E₂ (shift to 149 cm^{-1}) modes blueshift significantly. The anisotropic optical properties of the tellurene nanosheets with larger thicknesses (28.5, 13.5, and 9.7 nm) were also studied. The Raman peak intensities are dependent on the polarization angle (Figure 16B2). When fitting them with a Lorentz function into the polar figures correspondingly (Figure 16B3–B6), it is found that the A1 mode in all samples is most sensitive to the relative orientation between the polarization of the excitation laser and its [0001] lattice direction. Notably, the direction of the maximum intensity in the A1 and E1(LO) modes (Figure 16B4) is thickness-dependent. It could be because of the different absorption spectral ranges in the [0001] and [1210] directions.

Nonlinear optical properties of tellurene have been reported. Wu et al. reported the optical Kerr effect from tellurene NSs and developed an all-optical switch and photonic diode with the Te NSs.²¹⁴ All-optical switching was demonstrated with a strong pump beam (671 nm) to modulate a weak probe light (532 nm) to realize on/off switching by the spatial cross-phase modulation (SXPM) method (Figure 17A–C). From an open aperture z-scan experiment of hexagonal tellurene nanosheets, Zhang et al. observed optical limiting behaviors and saturated absorption, depending on the energy (wavelength) and intensity of the illuminated laser.²¹⁵ The saturated absorption dominated upon illumination of 0.73–0.83 eV (1698–1494 nm) laser, while the optical limiting behavior by TPA dominated upon illumination of \sim 1.04–2.76 eV (1192–449 nm) laser (Figure 17D). It is attributed to the higher saturation probability near the edge of

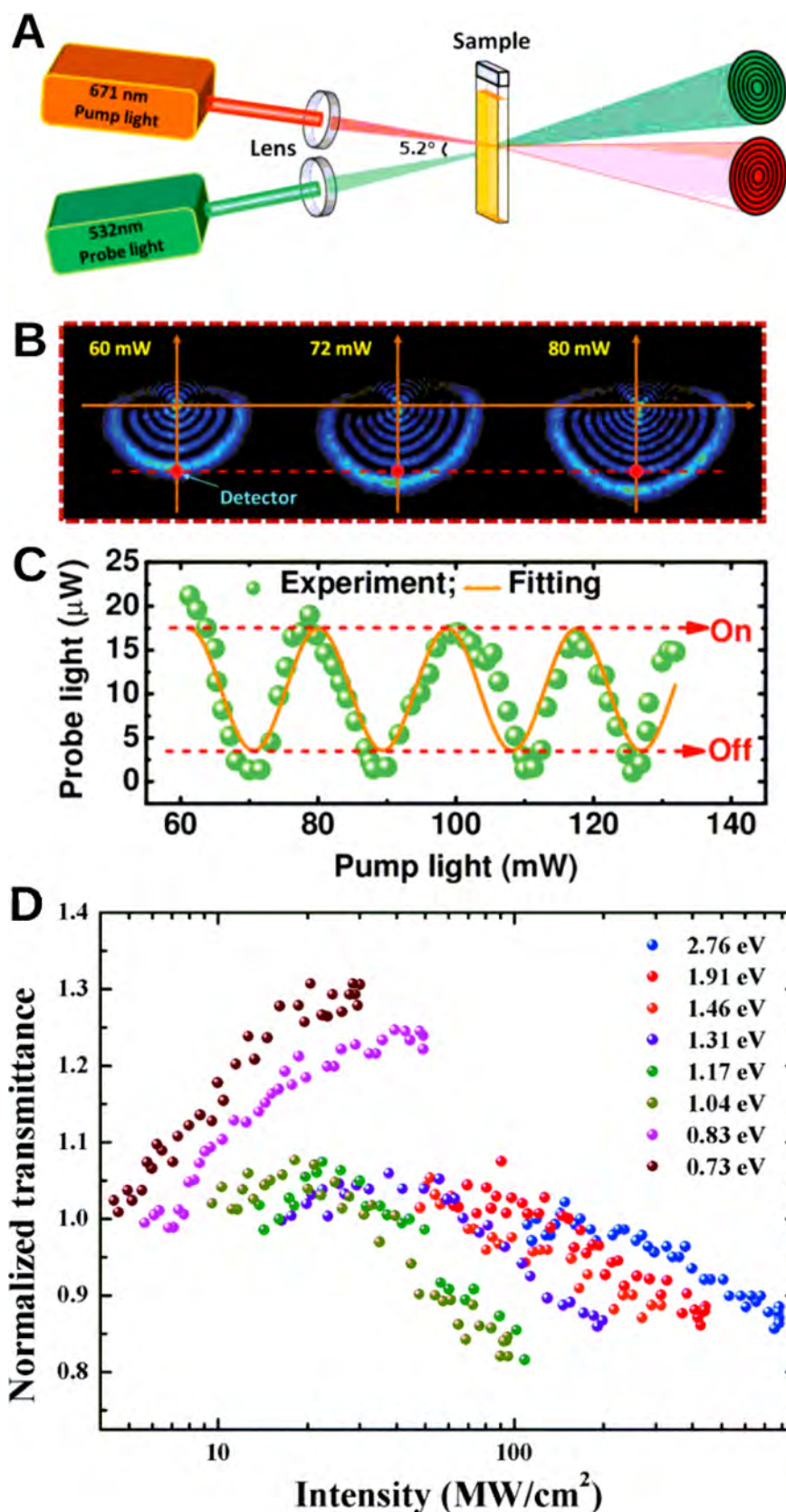


Figure 17. (A) All-optical switching system based on SXPM upon two light excitations (532 and 671 nm). (B) Diffraction rings for the probe light as a function of the power of pump light (60–80 mW) focused on 2D Te NSs dispersion. (C) All-optical switch to modulate the probe light based on 2D Te NSs by pump light. Reproduced with permission from ref 214. Copyright 2018 Wiley-VCH Verlag GmbH and Co. KGaA, Weinheim. (D) Relationship between the excitation energy density and the normalized transmittance of Te NSs at different photon energies. Reproduced with permission from ref 215. Copyright 2019 Royal Society of Chemistry.

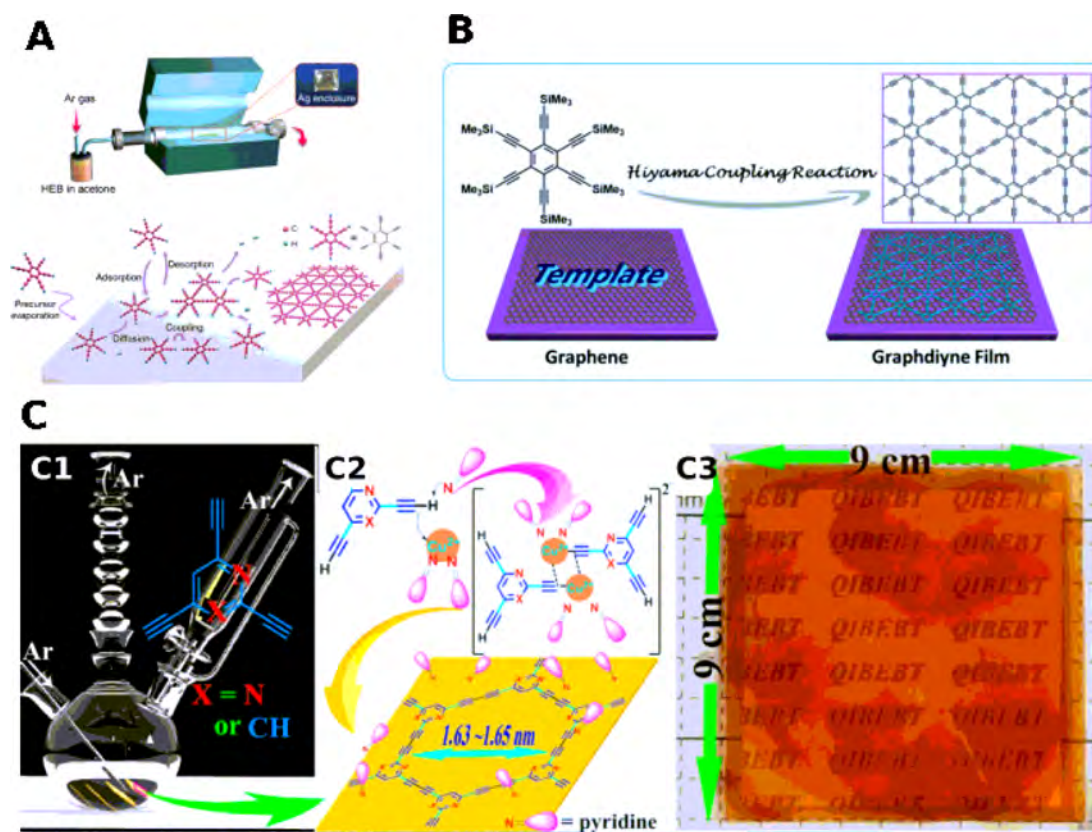


Figure 18. (A) GDY growth on a silver surface through a CVD system. Reproduced with permission from ref 223. Copyright 2017 Wiley-VCH Verlag GmbH and Co. KGaA, Weinheim. (B) Synthesis of GDY film on graphene. Reproduced from ref 224. Copyright 2018 American Chemical Society. (C1) Illustrated fabrication equipment and (C2) the reaction process for the pyridinic N-substituted GDY. (C3) Photograph of large PM-GDY film (~ 80 cm²). Reproduced from ref 225. Copyright 2018 American Chemical Society.

the Dirac cone, similar to nonlinear absorption of GDY in section 2.1.3.

2.4.5. van der Waals Heterostructures. Due to the easily tunable morphology and bandgap, Te-based heterostructures have attracted significant attention. Various kinds of Te–Se heterostructures have been prepared through the epitaxial growth procedure because Se and Te locate in the same group on the periodic table with similar anisotropic and isomorphous characteristics. Owing to the high reactivity of Te, Te in the heterostructure nanowire can degrade into telluride, which contributed to produce a variety of telluride-based heterostructures, such as Bi₂Te₃–Ag₂Te²¹⁶ and Bi₂Te₃–PbTe.²¹⁷ For the construction of tellurene/TMDs heterojunctions, the lattice mismatch remains a problem. A lattice match method was developed by Hu et al.,²¹⁸ which showed the optimal supercell model of tellurene and TMDs.

Huang et al. synthesized Te@Se heterostructures by epitaxial growth of Se on Te nanotubes and used them as working electrodes for electrochemical photodetector.²¹⁹ Compared with the telluride-based photodetectors, they showed better self-powered broadband light detection ability, enhanced photocurrent density, and stability in various water environments (NaCl, HCl, and KOH solutions). Wu et al. proved that tellurene-based heterojunction was a candidate promising for the design of solar cells with high efficiency because it has ideal photoelectric properties (*i.e.*, ideal bandgap: 1.47 eV), high carrier mobility, strong light absorption, and high stability under ambient conditions.²²⁰ These are superior to the existing 2D semiconductor for solar cells. The experimental results show

that the heterojunction structure can effectively enhance solar absorption and separate the sunlight. Particularly, the maximum energy conversion efficiency of Te/MoTe₂ and Te/WTe₂ heterojunction solar cells is 22.5% and 20.1%, respectively. The light detection performance of tellurene is poor, and its stability is relatively uncertain, which greatly limits its practical application.

3. FABRICATION AND SURFACE MODIFICATION OF XENES

Fabrication techniques for Xenes include both bottom-up and top-down strategies. In bottom-up methods, chemical vapor deposition (CVD) and molecular beam epitaxy (MBE) are two typical fabrication techniques for optoelectronic devices. In top-down techniques, liquid-phase exfoliation is a practical technique used for biomedical applications.

3.1. Graphdiyne

Since the first successful fabrication of GDY using a chemical template coupled in an organic solvent,²⁶ huge interests have been aroused to synthesize GDY. Various fabrication strategies, such as thermal coupling and two-phase reaction, and different reaction conditions in the reaction category, catalyst system, precursor structure, and selected template, have been employed. In this section, these fabrication strategies are systematically discussed.

Li et al. first demonstrated a successful strategy to prepare GDY on a copper substrate, using in situ cross-coupling reaction.²⁶ The monomer of hexaethynylbenzene (HEB) (see the chemical structure in Figure 18A) was prepared from

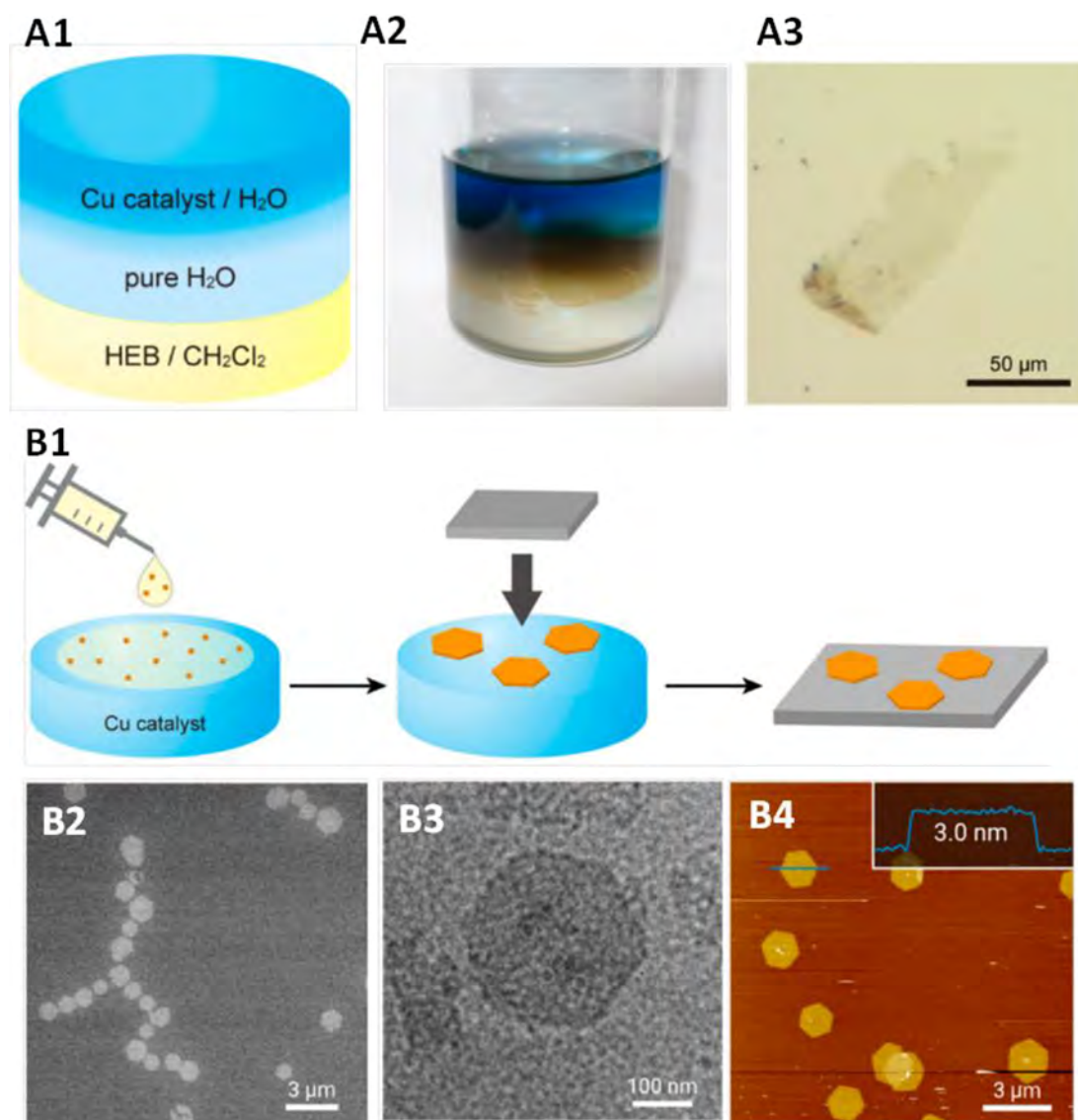


Figure 19. (A) Liquid–liquid interfacial synthesis of GDY nanosheets: (A1) illustration, (A2) synthetic setup for GDY at the liquid/liquid interface and (A3) TEM micrograph. (B) Gas/liquid interfacial synthesis: (B1) schematic synthesis process, (B2, B3) TEM micrographs, and (B4) AFM image and the height analysis. Reproduced from ref 226. Copyright 2017 American Chemical Society.

hexakis[(trimethylsilyl)ethynyl]benzene (see the chemical structure in Figure 18B) in THF solution by the addition of the tetrabutylammonium fluoride (TBAF). Then its cross-coupling reaction was catalyzed by a Cu foil, which was also used as the substrate for GDY film growth. In basic (in the presence of pyridine) solution, a small number of copper ions (Cu^{2+}) can be released from the Cu foil, which in turn catalyzes the cross-coupling reaction of the HEB monomers. They successfully obtained GDY film grown on the Cu foil and characterized it with transmission electron microscopy (TEM), X-ray diffraction (XRD), X-ray photoelectron spectroscopy (XPS), Raman spectroscopy, and atomic force microscopy (AFM).

The crystal structure of the as-prepared few-layered GDY nanosheet showed ABC stacking observed by TEM using low current density.²²¹ It is theoretically proven in the studied stacking modes of GDY, the energy of the ABC-stacked structure is the lowest.²²²

Ag can also be used as a growth substrate, but through the CVD process (Figure 18A).²²³ Compared with the CVD growth of graphene, the growth process of GDY is quite different. As

GDY is composed of two kinds of hybridized carbon atoms, GDY building blocks are molecules with alkynyl and phenyl groups, while that of graphene are sp^2 hybridized carbon atoms. The growth of GDY is completed by covalent bonding between terminal alkynes and precursor molecules. Therefore, the molecular skeleton structure plays a vital role during the growth process. A low temperature is necessary for the CVD growth of GDY, because a high temperature will damage the molecular skeleton structure of the precursors.

Template synthesis provides another effective method for GDY preparation. The cousin of GDY, graphene, is an appropriate choice as a template for GDY film synthesis. Zhou et al. successfully synthesized ultrathin GDY film on graphene (Figure 18B).²²⁴ Owing to the all-carbon and atomically flat structure of graphene, a strong interaction occurs between graphene and GDY, leading to the growth of an ultrathin flat and continuous GDY film, whose thickness is less than 3 nm.

Unlike traditional epitaxy growth requiring a strict lattice matching, van der Waals (vdW) epitaxy can relax the lattice matching condition because of the weak vdW binding between

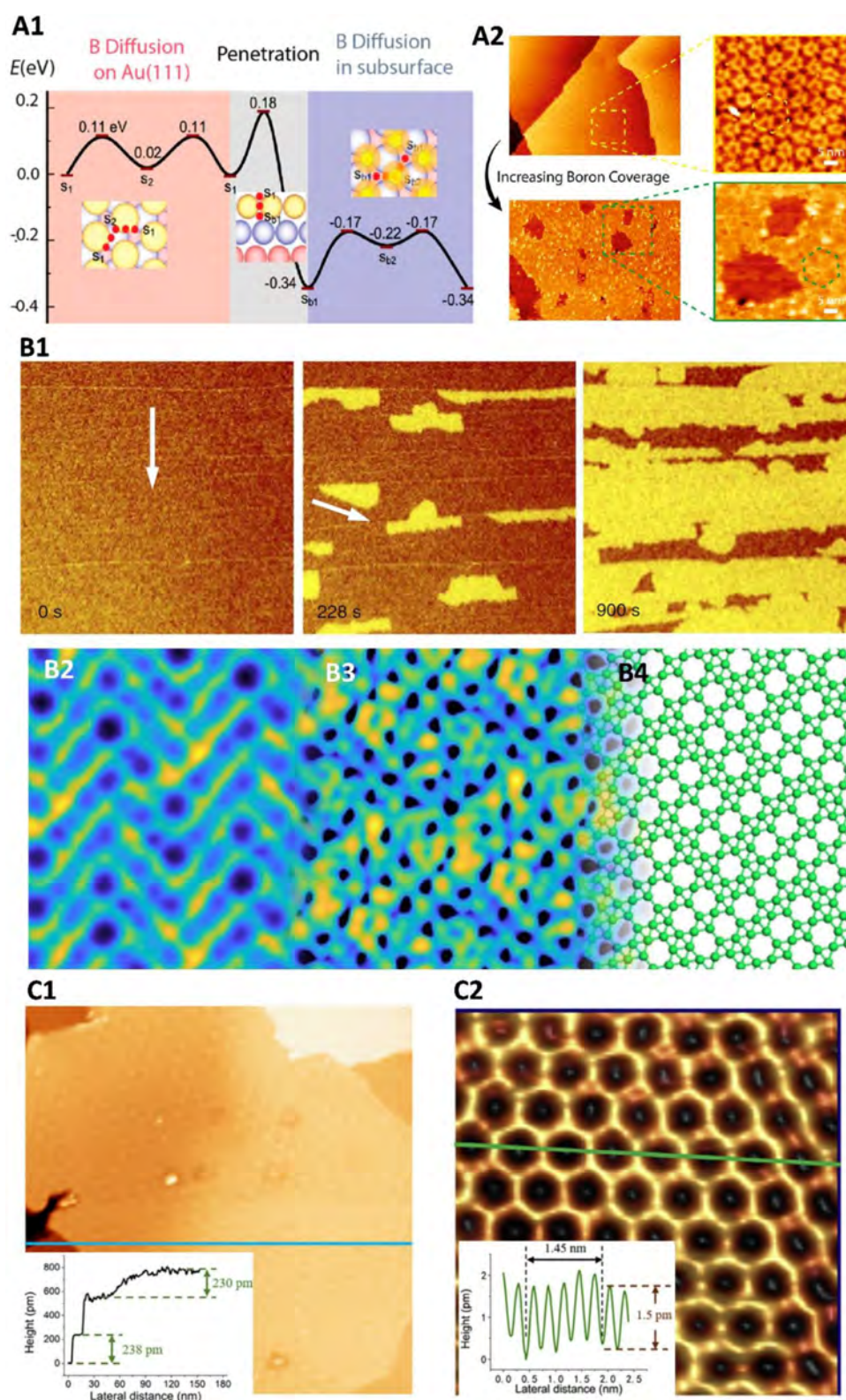


Figure 20. (A1) Minimum energy path for the diffusion of boron on Au(111) (red), penetration (gray), and diffusion (blue) into the subsurface. (A2) Higher boron dose leads to the formation of larger borophene islands. Reproduced from ref 239. Copyright 2019 American Chemical Society. (B1) Bright-field low energy electron microscopy images show that borophene islands are easy to grow on the edge of a Cu substrate. (B2) Ultrahigh-resolution STM image of borophene. (B3) DFT-simulated constant tunneling current isosurface of the proposed borophene structure. (B4) Pictorial view of the borophene structure. Reproduced with permission from ref 244. Copyright 2019 Springer Nature. (C1) Monolayer borophene NS on Al(111) substrate and (C2) its high-resolution STM image. Reproduced with permission from ref 15. Copyright 2018 Elsevier, Inc.

the substrate and the epilayer. Through a vdW epitaxial strategy, Gao et al. synthesized an ultrathin GDY film of single-

crystallinity on graphene.²²² Their lattice mismatch was alleviated by weak interaction between the substrate and the

admolecule, promoting the in-plane cross-coupling of admolecules, while the out-of-plane coupling was slow to form one- or few-layer GDY.

The nitrogen (N) atoms doping could increase electrochemically active binding sites and enhance electrochemical performance through the production of heteroatomic defects. Pyridine-like N atoms can be doped via an easy chemical synthesis technique. Porous networks of pyrimidine-GDY (PM-GDY) and pyridine-GDY (PY-GDY) films with large areas up to 80 cm² were successfully synthesized (Figure 18C).²²⁵ They are uniform, self-supported, transparent, continuous, and flexible.

A bottom-up liquid/liquid interfacial synthesis of GDY nanosheets (NSs) was applied by Matsuoka et al.²²⁶ A dichloromethane solution containing HEB was put on an aqueous layer and catalyzed by Cu at room temperature (Figure 19A1,A2). A multilayer GDY is synthesized at the interface via a continuous alkyne–alkyne homocoupling reaction (Figure 19A3). A gas/liquid interfacial preparation method was further investigated (Figure 19B1). The HEB in a mixture of toluene and dichloromethane was sprinkled onto the surface of the liquid, and the single-crystalline GDY NSs emerged, which showed regular hexagonal domains with 1.5 μm of lateral size and 3.0 nm of uniform thickness (Figure 19B2–B4).

For the other morphologies, such as nanowire, nanotube, and nanowall, the growth mechanism is almost the same, but the morphology is tunable with the selection of the template. Li et al. synthesized GDY nanotube arrays on an anodic aluminum oxide template based on an earlier cross-coupling method.²²⁷ The VLS growth process can be used to prepare GDY nanowires.⁹³ Besides Cu foil, a copper oxide (CuO) nanowire can also act as a template to grow a hierarchical structure with the CuO nanowire on the inner side and GDY on the outer side, respectively.²²⁸ Zhou et al. synthesized GDY nanowalls through a modified Glaser–Hay coupling reaction.⁹⁹

3.2. Borophene

Because of the bulk boron having covalent bonding configurations, it is a great challenge to fabricate borophene. Theoretically, a triangular lattice with periodic holes is calculated to be more stable^{229,230} and can be synthesized on metal substrates because of the metal passivation from the hybridization of sp².^{124,231} Borophene striped nanoribbon was first demonstrated experimentally by Mannix et al., through MBE growth on Ag(111) under ultrahigh-vacuum conditions.³⁰ Feng et al. also used the MBE technique to obtain borophene on Ag(111), but with a triangular lattice that is arranged with periodic holes.²³² A similar striped pattern can be obtained for both reported borophene. Moreover, Tai et al. synthesized atomically thin borophene composed of orthorhombic γ-B28 cells on Cu foils via chemical vapor deposition (CVD).⁴³ Given the recent reports on borophene fabrication, two issues need to be further addressed: the small nanometer-sized domains for device fabrication and substrate-dependent structural variation. The domains growing on Ag(111) are always at the nanoscale level for different growth conditions. By choosing a Cu(111) substrate that is less inert than Ag, a large area crystal up to 100 μm² can be obtained.²³³ Most of the reported borophenes possess a triangular lattice. Unlike these reports, Li et al. prepared a graphene-like borophene with the honeycomb structure on an Al substrate when the honeycomb boron structure can be stabilized by obtaining one electron charge from Al.²³⁴ As a contrast, there is negligible charge transfer between boron and Ag or Cu, endowing triangular lattice generation.²³⁵

Rather than these bottom-up fabrication techniques, Ji et al. employed a top-down strategy to obtain borophene through synergistic thermal oxidation etching and liquid-phase exfoliation.²³⁶ Ranjan et al. employed sonochemical exfoliation to obtain monolayer borophene using an appropriate solvent.²³⁷ These rare bottom-up fabrication reports illustrate difficult exfoliation from nonlayered bulk boron.

Although successful fabrication of borophene has been achieved, it remains a question if synthetic borophene can exist as chemically and structurally distinct layers connected by van der Waals (vdW) forces. Campbell et al. reported that ultrathin borophene nanosheets grown on a Ag(111) substrate exhibit a vdW-like structure different from the bulk allotrope.²³⁸ It is observed that the boron atoms form a single planar layer on the Ag substrate. This growth of synthetic borophene from the substrate suggests that it is possible to realize more types of 2D materials than those obtained from layered bulk crystals.

Besides the growth of borophene on Ag substrates, Kiraly et al. showed that boron atoms can diffuse into Au at high temperatures and aggregate into borophene islands on the surface as the substrate cools.²³⁹ Importantly, subsurface boron undergoes a less steric effect from the surrounding Au atoms and, in turn, can generate a strong B–Au interaction to make a more energetically favorable adsorption site (see Figure 21A1). Furthermore, strain relief and energy minimization of the Au(111) surface lead to borophene nucleation and growth. Increasing boron coverage breaks the nanoscale template and small ordered islands can thus be evolved into larger sheets (Figure 20A2). Wu et al. reported that large area crystals up to 100 μm² could also be obtained by choosing the Cu(111) substrate that is less inert than Ag (Figure 20B1).²³³ The crystal structure is composed of triangular sites and a honeycomb lattice with the exact ratio of triangular sites and honeycomb lattice sites of 5 (Figure 20B2–B4). Furthermore, a charge-transfer interaction was predicted, with less covalent bonding between the Cu substrate and borophene.

The sp² hybridization-based planar honeycomb structure in graphene endows it with great potential in numerous applications,²⁴⁰ which arouses interest in other elemental 2D-enes, such as the silicene,⁴ stanene,² and germanene.³ But the 2D-enes mentioned above easily form a buckled honeycomb structure due to the sp²–sp³ hybridization. The primary cause for this difference is their larger atomic radius than carbon. Unlike these 2D-enes, the smaller atomic radius of boron renders the possible formation of planar honeycomb borophene. Up to now, most of the fabrication reports on borophene focus on triangular borophene. The fabrication of honeycomb borophene remains a challenge owing to its electron deficiency.²³⁴ Electron charging can lead to a structural change with alternative electronic property. It is found that a stable honeycomb boron structure can exist in boride compounds (e.g., MgB₂), where the Mg atoms can provide electrons for boron atoms.²⁴¹ Inspired by this idea, Li et al. fabricated a pure honeycomb borophene on an Al(111) substrate through MBE growth.¹⁵ Monolayer honeycomb borophene was observed by scanning tunneling microscopy (STM) (Figure 20C1,C2). It is shown that the honeycomb borophene grown on the Al(111) substrate is energetically stable. The finding of honeycomb borophene is important to understand basic boron chemistry. More details can be found in a recent review paper.³¹

The honeycomb boron layer included in diborides may offer a chance to obtain honeycomb borophene through a top-down strategy.^{242,243} Unfortunately, the borophene layer is also

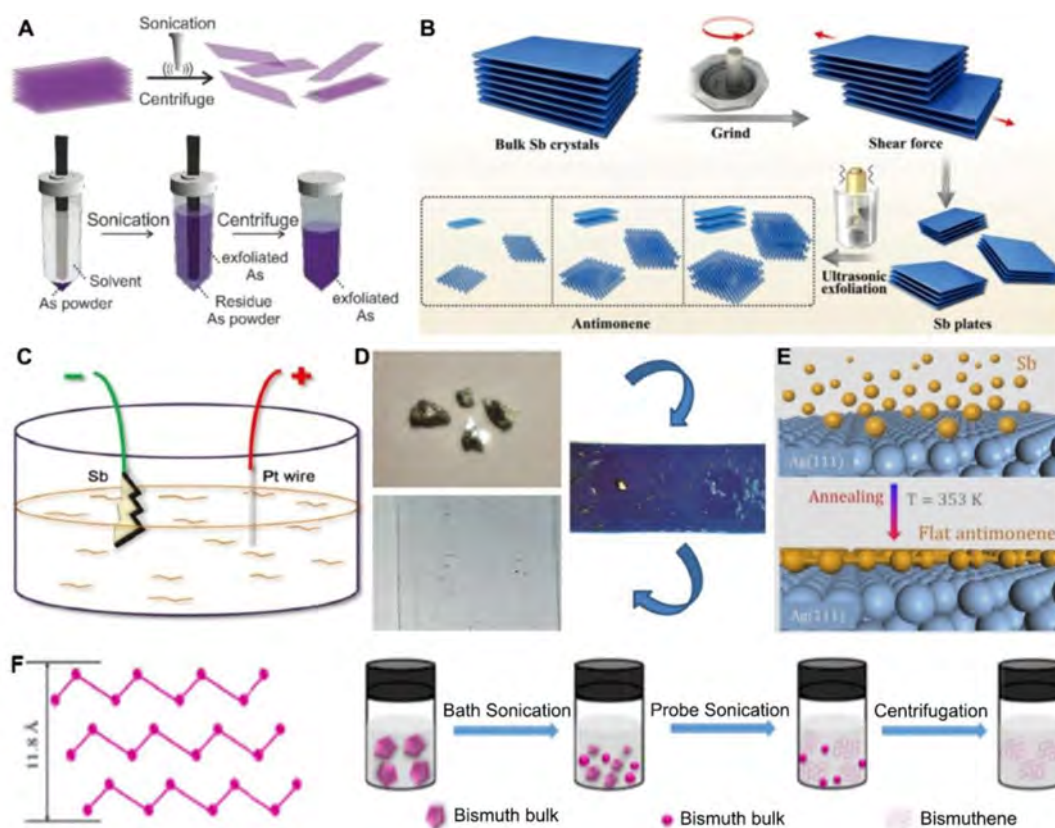


Figure 21. Selected synthetic routes for 2D As, Sb, and Bi Xenes. (A) Liquid exfoliation for As. Reproduced with permission from ref 251. Copyright 2019 Wiley-VCH Verlag GmbH and Co. KGaA, Weinheim. (B) Grinding-assisted exfoliation of Sb. Reproduced with permission from ref 246. Copyright 2018 Wiley-VCH Verlag GmbH and Co. KGaA, Weinheim. (C) Electrochemical exfoliation of Sb. Reproduced with permission from ref 253. Copyright 2017 Wiley-VCH Verlag GmbH and Co. KGaA, Weinheim. (D) Mechanical isolation of Sb. Reproduced with permission from ref 254. Copyright 2016 Wiley-VCH Verlag GmbH and Co. KGaA, Weinheim. (E) Bottom-up synthetic approach for Sb. Reproduced from ref 255. Copyright 2018 American Chemical Society. (F) Liquid exfoliation of Bi NSs. Reproduced with permission from ref 182. Copyright 2018 Wiley-VCH Verlag GmbH and Co. KGaA, Weinheim.

covalently bound with metal layers in diborides, making it challenging to directly exfoliate honeycomb borophene. Similar to the fabrication of MXene, the strategy through acid etching technique from diborides may be a useful method to obtain borophene.

3.3. Group V: Arsenene, Antimonene, and Bismuthene

Among various methods, liquid exfoliation and mechanical exfoliation approaches have been widely applied for obtaining a single layer or few-layer pnictogens.^{178,182,245–250} Different factors such as solvents screening and the size of bulk materials have been reported to have a dramatic influence on the exfoliation process.

As shown in Figure 21A, liquid exfoliation is the most widely employed “top-down” strategy for producing thin-layer Xenes. Tip ultrasonication with a higher power is usually employed to defeat the strong van der Waals force of Arsenene layers within a much shorter time than normal ultrasonication, which effectively avoids the problem of overheating.²⁵¹ Water and oxygen reactivity are general issues for 2D Xene preparation, and thus, oxygen-free organic solvents are needed to avoid the oxidation of Xene layers. Compared with water, organic solvents with heavier molecular weight and higher surface tension are demonstrated to yield more nanosheets from the bulk As, among which *N*-methyl-2-pyrrolidone (NMP) proves to be the optimized solvent. Solvents would affect not only the yield of the 2D nanosheets, but also the size and morphology. When

using toluene as the solvent to replace NMP, Arsenene nanodots were obtained.²⁴⁸ Systematic theoretical and experimental studies were performed to investigate the solvent effect, and the conclusion suggests that electronic interaction between solvents and the As surface plays a significant role in determining the surface charges over arsenene, thus providing a way to tune the van der Waals force between layers by changing solvents with different polarity.²⁴⁷ Apart from Arsenene, antimonene nanosheets were also obtained via the liquid exfoliation method. Grinding pretreatment has been utilized before ultrasonication (Figure 21B), resulting in antimonene with good quality and intact structures to enhance speed and efficiency.²⁴⁶ To further increase the efficiency, balling pretreatment of bulk Sb in the presence of polymerized ionic liquids was proved to be a solution, with stable antimonene NSs produced in high concentration.²⁵⁰ Unlike Arsenene or BP, butanol was found as an optimal solvent for antimonene, providing appropriate shear force and wetting parameters. However, the high boiling point makes it difficult for separation, which was overcome by a modified sonication method under an ice bath, with ethanol as the optimal solvent for producing concentrated atomic layer antimonene NSs.²⁵² Liquid exfoliation has also been performed to synthesize 2D bismuthene, as shown in Figure 21F.¹⁸² In addition to the ultrasonication-assisted exfoliation approach, electrochemical exfoliation offers another cost-effective way to produce NSs with regular morphology (Figure 21C).²⁵³

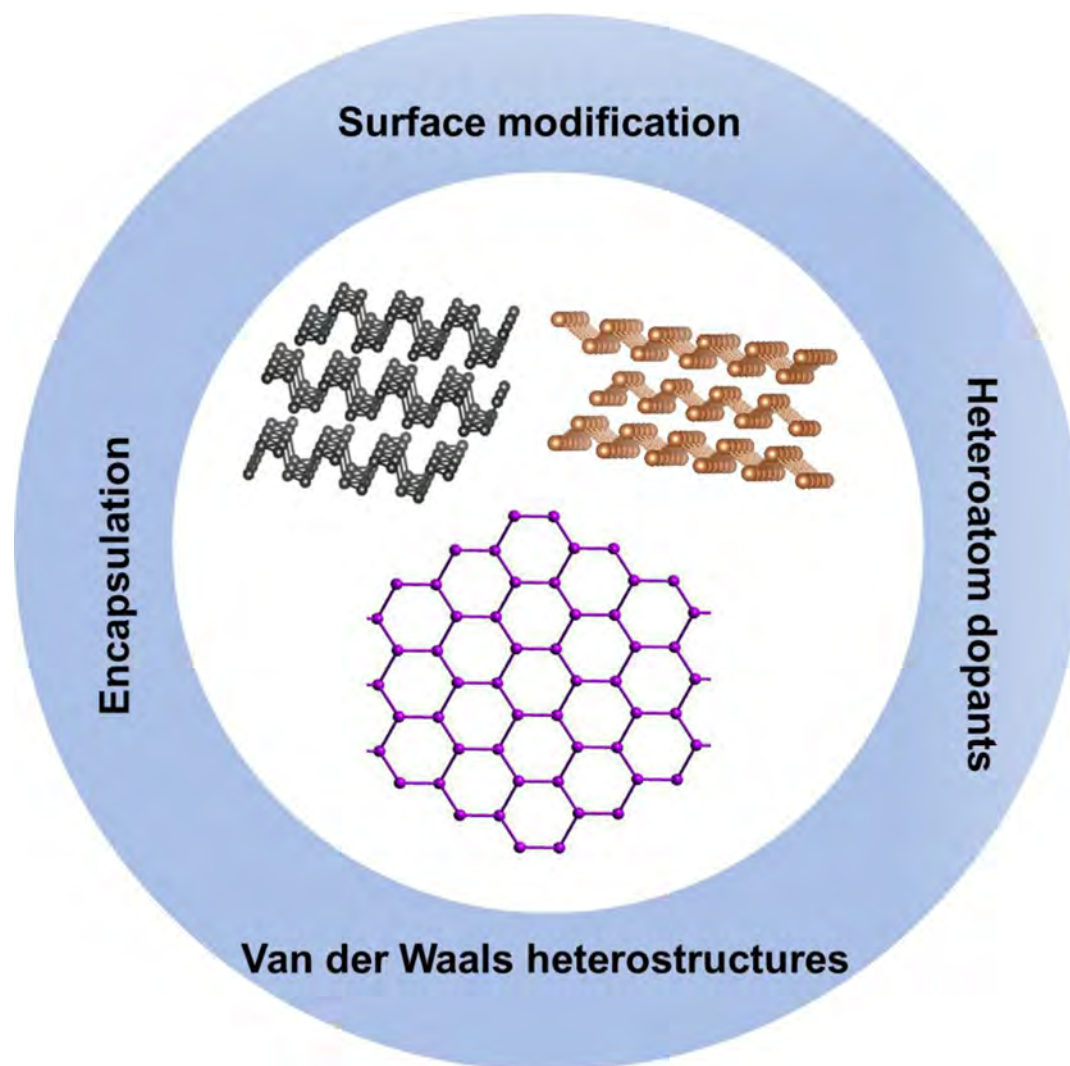


Figure 22. Common strategies for Xene modifications.

Mechanical exfoliation has been used for substrate supported Xenes. For example, to effectively load antimonene on the Si substrate, a viscoelastic stamp was mixed with bulk Sb before the exfoliation process, resulting in antimonene NSs with high resistance toward air and water as well as with a high transferring efficiency to the Si substrate (Figure 21D).²⁵⁴

Apart from these commonly employed top-down strategies, bottom-up approaches have also demonstrated their efficacy for fabricating these 2D Xenes. Figure 21E depicts an example that Sb atoms first grow on a silver crystal surface via deposition, followed by layer formation with more Sb deposition. Although this approach is more expensive than the methods mentioned above, it gains an advantage over them due to the uniform structures produced and having intrinsically high transferring efficiency to additional substrates.²⁵⁵

To fully exploit the Xenes, which generally exhibit poor solubility in biological media, post-treatment is required to further enhance their stability under ambient conditions and trigger biophotonics activities (Figure 22).⁴⁴ Common treatments, involving the encapsulation of Xenes in hydrogels or polymers (e.g., PLGA),^{256,257} surface modification via chemical (coordinating with metal species, ionic liquids, organic ligands or azides)^{258–260} or physical interaction (electrostatic adsorption),^{261,236} are generally required. These treatments increase

the resistance of Xenes against water and O₂, and modify the surface's polarity, which benefits their dispersion in blood. The guiding principles for the modifiers are that post-treatment of these 2D materials should lead to a remarkable enhancement of dispersion stability, useful lifetime during the biomedical process, and surface reactivity (for drug loading). More importantly, the modifiers must be nontoxic and degradable in vivo. Generally, the dispersion of pure Xenes in water is poor; hence, the interaction of hydrophilic modifiers with the surface would largely increase water solubility.

Moreover, the preservation of Xenes within hydrogels or polymers makes it possible to realize smart drug release control or other biomedical applications. The photothermal effect in these 2D materials is aimed to destroy the structure of hydrogels for controlled release of drugs.²⁵⁶ However, surface modification might prevent Xenes from exhibiting their full potential, which requires further study for confirmation.

In addition to the above post-treatment, surface modification of 2D Xenes via electrostatic adsorption of ions (metal salts or ionic liquids),²⁶² coordination with molecules or metal species,¹⁹¹ introduction of defects/dopants,²⁶³ as well as heterojunction construction^{188,194} have all been achieved during the past years. These modifications enhanced the stability and enriched the functionalities of the parent pnictogens, and

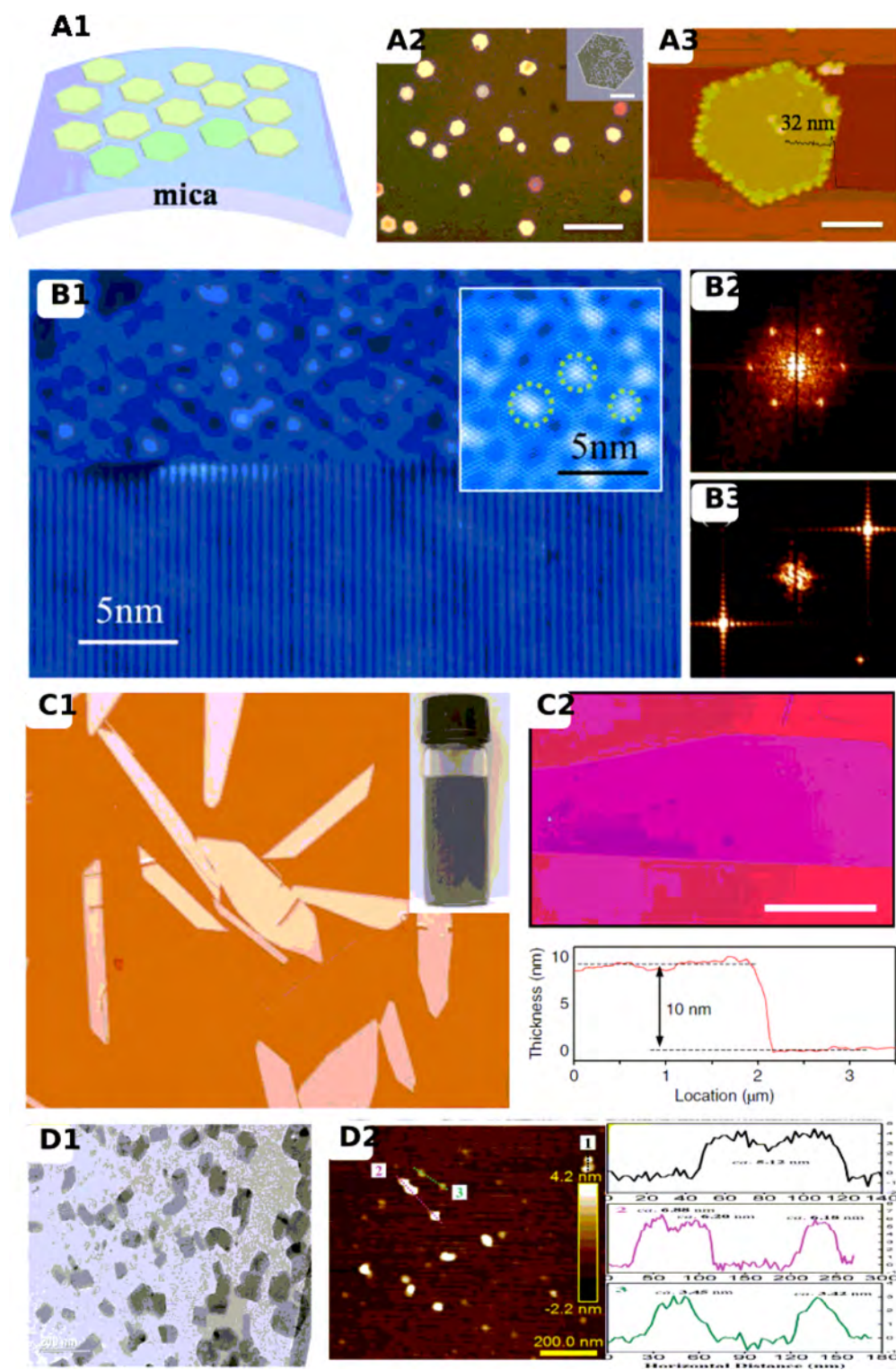


Figure 23. (A1) Schematic illustration of hexagonal tellurene NSs grown on flexible mica substrates. (A2) Typical hexagonal NSs (scale bar: $30\ \mu\text{m}$). (A3) AFM image of a hexagonal tellurene NS. Reproduced from ref 205. Copyright 2014 American Chemical Society. (B1) Growth of monolayer tellurene film on graphene; fast Fourier transform patterns of (B2) monolayer tellurene and (B3) graphene substrate shown in (B1). Reproduced from ref 213. Copyright 2017 American Chemical Society. (C1) Solution-grown Te nanoplates; (C2) AFM image of tellurene NSs. Reproduced with permission from ref 202. Copyright 2018 Springer Nature. (D1) TEM image of the morphology of tellurene NSs; (D2) AFM image illustrating thickness and the corresponding height profile. Reproduced with permission from ref 38. Copyright 2018 Wiley-VCH Verlag GmbH and Co. KGaA, Weinheim.

provided tuning of conductivity, carrier mobility, chemical potential, and free energy. For example, the As/MoS₂ and Sb/Ge heterostructures have both yielded a transition from indirect

bandgap (As, Sb) to direct band structures via precise control,^{192,264} which promotes the rational design of novel functional 2D materials.

Despite several approaches that have been developed for preparing 2D materials and their corresponding nanoplateforms, the intrinsic forms of as-prepared 2D materials are usually not uniform in structure and composition and may suffer from decomposition. Reaching a decisive conclusion for given biomedical performances based on currently available 2D material-based nanoplateforms is not easy, hindering our understanding of how light-activated biophotonic processes occur when applying these systems to diversified biological practices. The surface functionalization process is a standard pretreatment; however, it remains unclear to what extent the pristine 2D materials are influenced.

3.4. Tellurene

A chainlike structure of tellurium prefers to form one-dimensional architectures, and thus, significant progress has been made in synthesizing 1D nanostructures of Te. In contrast, much less effort has been put into synthesizing 2D Te nanostructures and studying their properties. Wang et al. fabricated hexagonal tellurene nanoplates on mica sheets via vdWE.²⁰⁵ A mica surface is chemically inert and allows a huge lattice mismatch, facilitating the migration of tellurium adatoms along the surface (Figure 23A1). This is beneficial for a lateral growth of 2D tellurene nanoplates. Typical regular hexagonal tellurene nanoplates with a lateral size from 6 to 10 μm (Figure 23A2) and thickness of mainly 30–80 nm (Figure 23A3) have been successfully achieved. Huang et al. synthesized monolayer and few-layer tellurene films by MBE on the graphene/SiC substrate (Figure 23B1).²¹³ They consist of parallel helical Te chains. Unlike the hexagonal symmetry of a graphene substrate, tellurene films present a rectangular lattice (Figure 23B2,B3). To overcome the limitations in crystal size and stability of tellurene synthesized on substrates, Wang et al. report a substrate-free solution process (Figure 23C1).²⁰² It can realize the fabrication of tellurene with a large-area and high-quality. The thickness of the obtained tellurene can range from a monolayer to tens of nanometers, with the lateral dimension being up to 100 μm (Figure 23C2). Besides these bottom-up methods, Xie et al. have adopted a liquid-phase exfoliation method to exfoliate tellurene NSs to a typical chain-like structure of layered materials.³⁸ The achieved tellurene NSs possess a large lateral dimension variation from 41.5 to 177.5 nm but a relatively uniform thickness of 5.1–6.4 nm (Figure 23D1,D2).

3.5. Heterojunctions

Apart from pure Xenes, a number of Xenes-based heterojunctions have also been successfully fabricated through various methods, many of which were similar to those of Xenes, as discussed above. The synthetic approaches are briefly summarized in Table 1. Heterojunctions are classified into different types, based on the discontinuity resulting from the alignment of bands. For heterostructures of type-I, the bandgap of one component entirely overlaps with that of the other. The potential discontinuity for the conduction band, ΔE_c , is expressed as " $\Delta E_c = E_{c1} - E_{c2} = f(E_{g1} - E_{g2}) = f\Delta E_g$ " while that for the valence band, ΔE_v , is expressed as " $\Delta E_v = E_{v1} - E_{v2} = (1 - f)(E_{g1} - E_{g2}) = (1 - f)\Delta E_g$ "; For type-II heterostructures, both the edges of conduction band and valence band for one component are lower than those of the second component.

Ren et al. designed an arsenene monolayer deposited on PtS_2 , named $\text{PtS}_2/\text{arsenene}$, using the chemical vapor deposition method.²⁶⁵ Based on the work function of arsenene being higher

Table 1. Summary of Interlayer Interactions and Preparation Methods for Selected Xenes-Based Heterojunctions

materials	interaction between compositions	method	ref
$\text{g-C}_3\text{N}_4/\text{GDY}$	$\pi-\pi$ stacking	solvothermal reaction	69
$\text{CoN}_x@\text{GDY}$	synergistic interaction	calcination to obtain CoN_x NS, followed by in-site growing GDY.	269
GDY-MoS_2	covalent bonding	growth on 3D carbon fiber networks through hydrothermal synthesis of MoS_2 NSs, followed by the in situ growth of GDY NSs on MoS_2 surface	117
borophene/ PTCDA	covalent bonding	deposition of PTCDA onto submonolayer borophene on $\text{Ag}(111)$ substrates	138
borophene– graphene	covalent bonding	bottom-up electron-beam evaporation	137
$\text{PtS}_2/\text{arsenene}$	Z-scheme heterojunction	chemical vapor deposition	265
$\text{InSe}/\text{arsenene}$	type-II heterojunction	bottom-up deposition	267
arsenene/ TCNNQ	type-II heterojunction	many-body perturbation GW method and extrapolation approach.	270
antimonene/ Bi_2Se_3	van der Waals force	bottom-up deposition	266
CNSb_x	van der Waals force	two-step procedure	268
Bi/BiOCl	Bi–O covalent bonding	hydrothermal	271
$\text{Bi}@/\text{Bi}_2\text{O}_7/\text{rGO}$	Bi–O covalent bonding	surface charge mediated self-assembly and in-site reduction	272
$\text{Bi}_4\text{MoO}_9/\text{Bi}$	Bi–O covalent bonding	a facile surface chemical reduction treatment	273
$\text{Bi}/\text{Bi}_2\text{O}_2\text{CO}_3$	Bi–O covalent bonding	solvothermal	274
$\text{Bi}/\text{Bi}_2\text{O}_3$	covalent bonding	pulsed laser deposition	275

than that of PtS_2 and the built-in electric field, the photoinduced electron of PtS_2 transfers to the valence band of arsenene to combine with the hole, while the photogenerated charges of arsenene gathered in its conduction band, thus generating a Z-scheme heterojunction where PtS_2 interacts with the arsenene monolayer by the van der Waals force. The Z-scheme heterojunction can suppress the recombination of electron–hole pairs, improving the photocatalytic performance significantly. Niu et al. used arsenene as a cocatalyst with the unique bandgap and optical properties to explore the As/tetracyano-naphthoquinodimethane (TCNNQ) photocatalyst by using many-body perturbation GW method and extrapolation approach, forming a type-II heterojunction, which can efficiently increase the mobility of charge carriers and be a good candidate for photocatalysis and photovoltaics.²⁶⁶ However, this is mostly limited to theoretical calculations; additionally, experiments are required for verification. In 2018, Xie et al. built $\text{InSe}/\text{arsenene}$ by the growth of a single layer of InSe on the surface of an arsenene NS via bottom-up deposition.²⁶⁷ The first principle calculation analysis reveals that a type-II heterostructure is formed at the interface of $\text{InSe}/\text{arsenene}$. In the same year, Barrio et al. reported the CNSb_x as a photocatalyst for pollutant degradation prepared by liquid exfoliation, where the Sb flake is closely connected with the g-CN layer with strong interaction.²⁶⁸ The Tauc plot and Mott–Schottky analytical results explain that the conductive band position (−0.91 eV) and the bandgap energy (2.22 eV) of g-CN are all higher than that of Sb, demonstrating the generation of a type-I heterojunction by the van der Waals force.

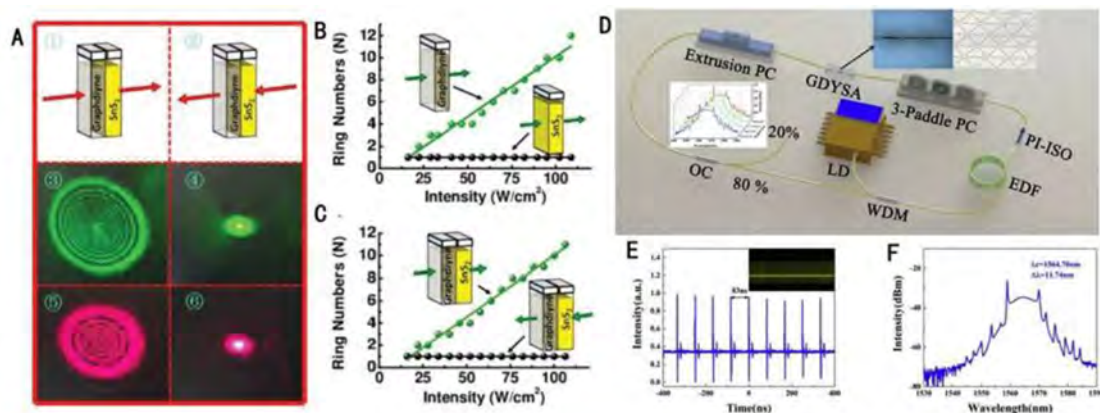


Figure 24. (A) Observation of nonreciprocal light propagation from the as-fabricated photonic diode. (B) Number of diffraction rings as light intensity increases, excited from the independent GDY dispersions (green line) and SnS₂ dispersions (black line) at $\lambda = 532$ nm. (C) Nonreciprocal light propagation with a fixed wavelength of 532 nm. Reproduced with permission from ref 106. Copyright 2019 Wiley-VCH Verlag GmbH and Co. KGaA, Weinheim. (D) Fiber laser setup with a GDY-based SA. (E) Output pulses, inset: pulse train in a 14 ms span. (F) Optical spectrum. Reproduced with permission from ref 47. Copyright 2019 Elsevier, Inc.

4. APPLICATIONS OF XENES AND THEIR HETEROSTRUCTURES

In this section, the nonlinear optical, optoelectronic, catalysis, sensors, biomedical, and energy applications of Xenes will be reviewed. Nonlinear optical applications will focus on nonlinear absorption, including saturable absorption, two-photon absorption, and spatial self-phase modulation (SSPM). Sensor applications mainly include biosensors and gas sensors. For biomedical applications, Xenes-based photothermal, photodynamic, and drug delivery systems will be discussed.

4.1. Optical Devices

Two-dimensional materials-based nonlinear optical devices have attracted wide attention since graphene was first proposed as a saturable absorber in a fiber ring laser.²⁷⁶ Light interaction with 2D materials enables nonlinear absorption in which the material absorption coefficient changes with the input laser intensity. Nonlinear effects include saturable absorption, two-photon absorption, excited-state reversed saturable absorption, and spatial self-phase modulation. In saturable absorption, the material's absorption coefficient of light gradually decreases with the increase of laser intensity, and the material eventually becomes optically transparent. In excited-state reversed saturable absorption and two-photon absorption, the opposite occurs, which means enhanced absorption and reduced transparency corresponding to increasing light intensity.

SSPM is an all-optical modulation phenomenon, which is a third-order nonlinear optical effect. SSPM refers to when a laser with high intensity interacts with a homogeneous medium, a diffraction pattern due to beam divergence can be observed at a certain distance. The phase of the light is modulated by its intensity. In recent years, SSPM based on two-dimensional material has attracted much attention. SSPM is widely used to measure the nonlinear refractive index of two-dimensional materials. However, the physical mechanism of SSPM is still controversial; the study of SSPM is still at an early stage. Many of the reported SSPM results which were obtained by using nanosecond long pulses, may be due to thermal effects rather than electronic nonlinearity. Potential applications of SSPM with two-dimensional materials include optical limiting, optical modulation, optical switching, all-optical diode, optical bistability, and dark hollow beam generation. Two-dimensional

materials that have been proposed to investigate SSPM include graphene, TMDCs, BP, topological insulators, and other 2D materials. There have been many studies on broadband SSPM, but they mostly focused on the visible light band. Broadening the research area of SSPM and developing ultrafast wideband SSPM will be a promising area.²⁷⁷

In this section, 2D materials optoelectronic applications derived from the above-mentioned nonlinear optical effects will be reviewed.

4.1.1. GDY. Modulation of the bandgap of GDY has been demonstrated with two methods. The first method is doping nitrogen and boron into the carbon networks of GDY⁵⁶ and another method is applying a homogeneous electric field perpendicular to it. It is possible to further study the regulation of the nonlinear optical response of the GDY by changing its bandgap. GDY possesses tunable bandgaps and ultrahigh carrier mobilities, which may have broader prospects for optoelectronic applications.⁴⁷ 2D GDY exhibits excellent optical properties and thus has several promising applications in nonlinear optics, such as an optical switch, optical modulator, and optical wavelength converter.²⁷⁸ However, the study of nonlinear optics of GDY is still at its initial stage, which needs further investigation.

4.1.1.1. Photonic Diode. In 2019, GDY was first designed as a photonic diode using the SSPM method.¹⁰⁶ GDY has been demonstrated to have a nonlinear intensity-dependent refractive index (Kerr nonlinearity) with the order of magnitude $\sim 10^{-5}$ cm² W⁻¹. Motivated by the strong Kerr effect of GDY, a nonlinear photonic diode composed of GDY and SnS₂ was proposed to achieve nonreciprocal light propagation. It was reported that GDY has a broadband nonlinear optical response. SnS₂ exhibits the behavior of reverse saturable absorption²⁷⁹ with a bandgap of 2.6 eV, which makes it difficult to excite diffraction rings. When GDY and SnS₂ are coupled together to form a hybrid structure, propagational symmetry-breaking occurs, which can realize unidirectional diffraction rings excitation. Corresponding experimental setup and results are shown in Figure 24. This indicates that the GDY/SnS₂ hybrid structure supports nonreciprocal light propagation, indicating that GDY can be used as a nonlinear photonic diode.

4.1.1.2. Mode-Locked Fiber Lasers. Recently, a 2D GDY decorated tapered fiber-based saturable absorber was used in a fiber laser to generate stable mode-locking pulses in the optical

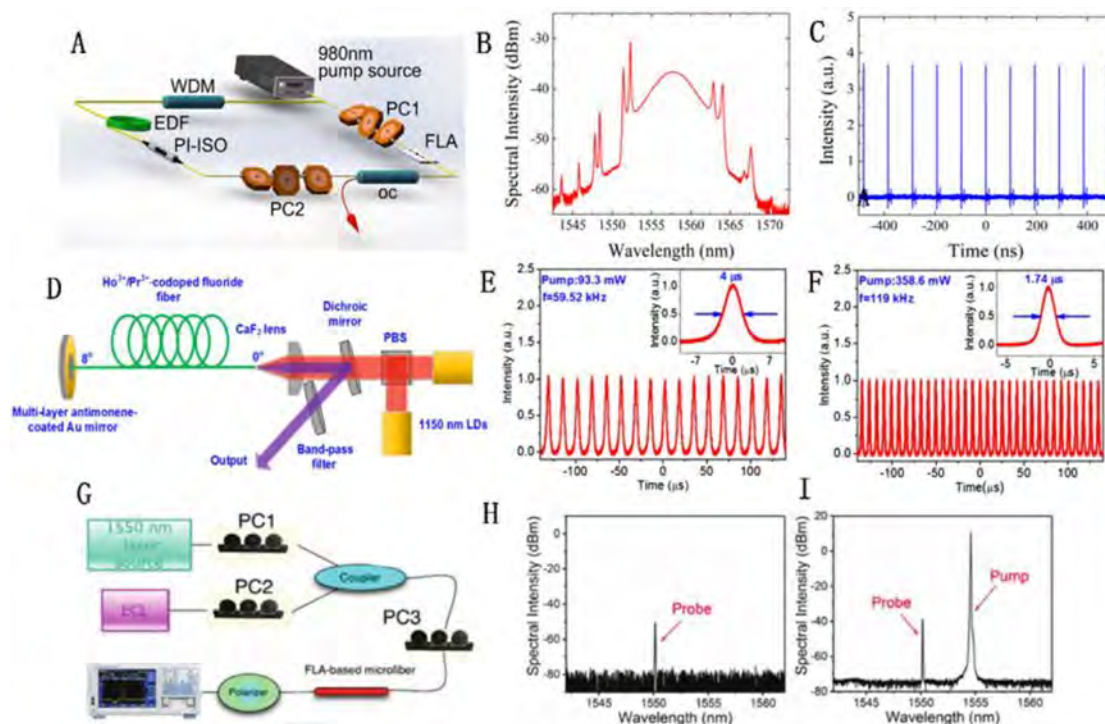


Figure 25. (A) Schematic diagram of the fiber laser including few-layer antimonene (FLA); (B) optical spectrum; (C) pulse train. Reproduced with permission from ref 281. Copyright 2017 IOP Publishing. (D) Experimental setup of a Q-switched Ho³⁺/Pr³⁺-codoped fluoride fiber laser; pulse train and single pulse (inset) at the launched pump power of (E) 93.3 mW and (F) 358.6 mW. Reproduced with permission from ref 286. Copyright 2018 The Optical Society. (G) Experimental setup illustration of antimonene-based microfiber applied as a Kerr switch; Corresponding optical spectrum of pump and probe when the switch is (H) turned off and (I) turned on. Reproduced with permission from ref 288. Copyright 2018 Wiley-VCH Verlag GmbH and Co. KGaA, Weinheim.

communication band.¹⁰⁷ The saturation intensity and modulation depth of the as-fabricated 2D GDY decorated tapered fiber-based saturable absorber were respectively measured to be 60.1 MW/cm² and calculated to be 11%. The pulse train repeats with a rate of 12.05 MHz and the pulse duration is 734 fs. Their center operating wavelength is 1564.70 nm and the 3-dB spectral bandwidth is 11.74 nm. Corresponding experimental results are shown in Figure 24D–F. This is the first report on GDY employed as a saturable absorber in a mode-locked fiber laser, demonstrating that GDY is promising for the nonlinear fiber application.

Nearly at the same time, Li et al. investigated a fiber ring laser passively mode-locked by a few-layer GDY.²⁸⁰ The hybrid mode-locked fiber laser was supported by the nonlinear polarization evolution technique and nonlinear absorption of GDY. The central wavelength, the repetition rate, and the pulse duration of mode-locking pulses were 1530.7 nm, 14.7 MHz, and 690.2 fs, respectively. Compared to using GDY as a saturable absorber or applying only a nonlinear polarization rotation technique, the output pulse duration of this hybrid passive mode-locked laser decreased more than 50 fs. Thus, GDY is demonstrated to be capable of being applied in ultrafast fiber lasers.

4.1.2. Arsenene, Antimonene, and Bismuthene.

4.1.2.1. Arsenene. Currently, arsenene-based optoelectronics devices have not been thoroughly investigated by researchers, with concrete evidence. It can be anticipated that arsenene has potential applications in laser oscillators, optical switching, and corresponding areas based on the optical properties discussed above.

4.1.2.2. Antimonene. 4.1.2.2.1. Mode-Locked Fiber Lasers.

In 2017, antimonene was first used as a saturable absorber in fiber ring lasers to generate ultrashort pulses at 1550 nm. Song et al. conducted an open-aperture Z-scan laser measurement on a few-layer antimonene, reported its nonlinear optical response, and verified the good stability for the 2D antimonene based nonlinear optical device (see Figure 25A–C).²⁸¹ After this study, a number of researchers focused on the usage of antimonene saturable absorbers in mode-locked fiber lasers. In 2018, Tian et al. demonstrated multilayer antimonene based short pulse generation at 1550 nm.²⁸² The central optical spectrum of the pulses is located at ~1545 nm, and the corresponding pump power is ~21.5 mW. The radio frequency spectrum shows a signal-to-noise ratio of ~47.5 dB. Simultaneously, a few-layer antimonene NSs with thicknesses of 3–6 nm were employed as saturable absorbers by Liu et al. to obtain dual-wavelength mode locking in an erbium-doped fiber laser.²⁸³ Stable dual-wavelength output pulses were measured at 1561.3 and 1562.7 nm.

4.1.2.2.2. Q-Switched Fiber Lasers. In 2018, antimonene was first used as a saturable absorber in solid-state lasers.²⁸⁴ Wang et al. proposed a passively Q-switched solid-state laser operating at 946, 1064, and 1342 nm using antimonene as saturable absorbers. The Q-switched pulse durations were 209, 129, and 48 ns, and their respective peak powers were 1.48, 1.77, and 28.17 W. This research showed that antimonene could be applied in a broadband nonlinear optical device in lasers, particularly NIR. Since then, Q-switched fiber lasers using antimonene SA have been developed by many researchers,²⁸⁵ particularly the application of antimonene for the mid-infrared spectral region laser has been proven for the first time. Luo et al.

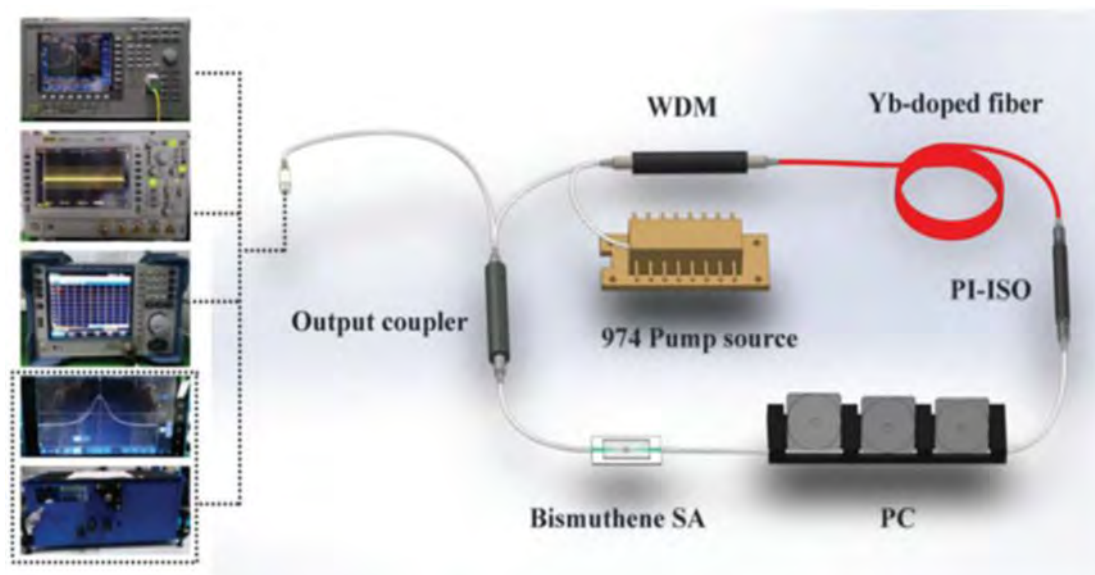


Figure 26. Schematic diagram of the fiber laser with a bismuthene decorated microfiber saturable absorber. Reproduced with permission from ref 292. Copyright 2018 Royal Society of Chemistry.

experimentally demonstrated that stable Q-switched pulses in a fluoride fiber laser codoped with Ho^{3+} and Pr^{3+} , operated at 2865.0 nm by introducing a 2D antimonene SA device into the cavity (see Figure 25D–F).²⁸⁶ The pulses generated from the laser were with 0.72 μJ pulse energy, with a largest output power of 112.3 mW. The pulse width is as short as 1.74 μs , and the fastest repetition rate was up to ~ 156.2 kHz. In 2019, fluorinated antimonene, which is a new derivative of antimonene, was proposed. Its direct bandgap can be modulated by the degree of fluorination, revealing an effective method to regulate bandgap.²⁸⁷ Fluorinated antimonene has been applied as a SA device in passive Q-switched Nd:LuAG laser by Zhanget al., which can support a stable pulse train having the pulse duration 326.7 ns and the repetition rate 733.1 kHz.

4.1.2.2.3. All-Optical Thresholding. In 2017, Song et al. used antimonene decorated microfiber for an all-optical threshold to reduce the noise of the optical pulses propagating in the optical fiber, thus improving the signal-to-noise ratio ~ 10 dB.²⁸¹ The results guide the application of 2D antimonene in all-optical threshold with long-term stability.

4.1.2.2.4. Optical Kerr Switch. An optical Kerr switch refers to a device that utilizes the effect of an intense light propagating in a nonlinear medium, which produces additional nonlinear phase shifts. Due to the nonlinear phase shift, when the input light intensity increases, the polarization of the signal light will evolve. An experimental setup of an optical Kerr switch using the antimonene decorated microfiber, designed by Song et al., is presented in Figure 25G–I.²⁸⁸ This optical Kerr switch has an extinction ratio of 12 dB. This finding indicates that a few-layer antimonene-based optical device can be potentially applied in next-generation optical communication systems.

4.1.2.2.5. All-Optical Wavelength Converter. In the field of nonlinear optics, four-wave mixing (FWM) refers to an intermodulation phenomenon. In a single-mode fiber, four-wave mixing occurring when two laser beams operating at two different wavelengths propagate along with the fiber could generate new wavelength signals; thus, it can be applied in optical wavelength conversion in the communication system. Graphene has been applied in a FWM wavelength converter.²⁸⁹

However, the efficiency of FWM cannot fulfill the current demand of the optical communication system. In 2018, Song et al. reported an antimonene based all-optical wavelength converter, which has a conversion efficiency as large as 63 dB, indicating an enhanced performance of the device.²⁸⁸

4.1.2.3. Bismuthene. **4.1.2.3.1. Ultrashort Pulse Generation.** Similar to black phosphorus, bismuthene also has a direct tunable bandgap and high carrier mobility. Thus, BP's general applications have been examined for bismuthene, such as broadband optical detectors, phase modulators, and all-optical switches.^{290,182} Compared to BP, the heavier bismuthene is intrinsically more stable in the ambient environment. Furthermore, theoretical calculations predict that the bandgap of bismuthene ranges from 0 to 0.55 eV, suggesting its potential applications within MIR and IR.²⁹¹ Recently, a few-layered bismuthene has been fabricated with an average thickness of 3 nm. Bismuthene based all-optical switching by utilizing spatial cross-phase modulation, was demonstrated in their work, which is attributed to a prominent nonlinear refraction effect in bismuthene. Later on, an erbium-doped mode-locked fiber laser with a bismuthene saturable absorber was reported.²⁹² The laser setup is shown in Figure 26.

4.1.2.3.2. Mode-Locked Fiber Lasers. In 2017, bismuthene was first investigated for nonlinear optics by diffraction ring patterns and demonstrated saturable absorption at the telecommunication waveband.¹⁸² Lu et al. fabricated a few-layer bismuthene decorated microfiber with a nonlinear absorption feature at the communication band, which was measured with a modulation depth of $\sim 2.03\%$. The as-fabricated bismuthene SA was employed in a fiber laser for ultrashort pulse generation. This was the first time that bismuthene was applied as a nonlinear optical device. In 2018, Chai et al. demonstrated a bismuthene-based dissipative soliton fiber laser operating at 1 μm .²⁹² The repetition rate of the laser-generated typical dissipative soliton pulses was 21.74 MHz and their pulse width was 30.25 ps. Later, 2D bismuthene based SA mode-locked fiber lasers were widely reported. Guo et al. successfully obtained a bismuthene-based fiber laser with a pulse duration of ~ 193 fs operating at 1561 nm.²⁹³ This finding unambiguously

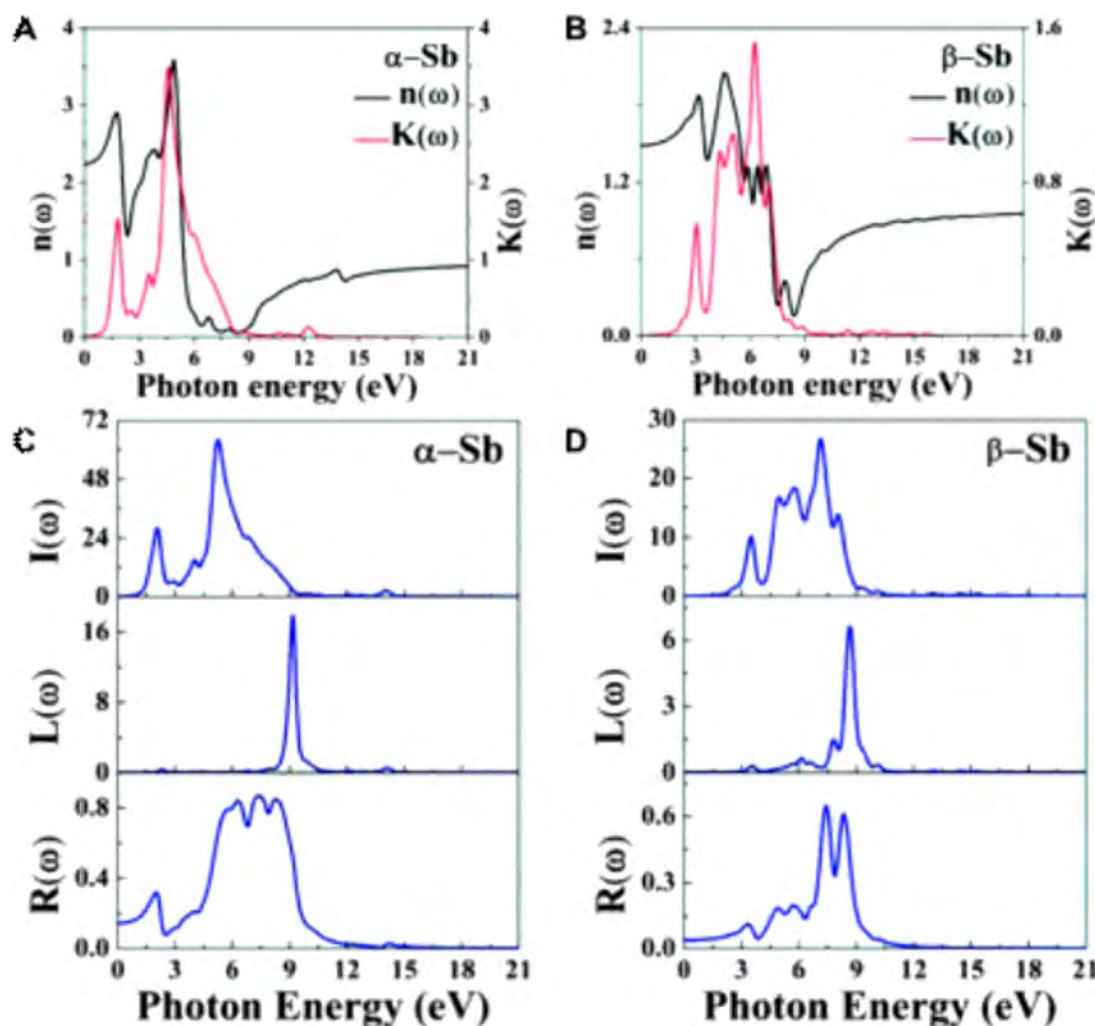


Figure 27. Refractive index $n(\omega)$ and extinction coefficient $K(\omega)$ of (A) α -Sb and (B) β -Sb monolayers obtained using hybrid functional HSE06. Absorption coefficient $I(\omega)$ (the unit of the absorption coefficient is $10^5/\text{cm}$), energy loss spectrum $L(\omega)$ and reflectivity $R(\omega)$ of (C) α -Sb and (D) β -Sb monolayers obtained using hybrid functional HSE06. Reproduced with permission from ref 294. Copyright 2016 Royal Society of Chemistry.

implied that few-layer bismuthene possesses excellent nonlinear optical properties for ultrafast photonics.

Singh et al. employed theoretical calculations within the random phase approximation for ultraviolet (UV) optical nanodevice applications of both puckered and buckled Sb configurations. The simulations of different parameters such as specific dielectric function and electron energy loss spectra (EELS) suggest that the refractive index values of the two Sb allotropes can achieve as high as 3.6 within the UV region, primarily indicating possible applications of Sb as UV absorbers. Further simulations on the dielectric function and EELS manifest that the value of plasmon energies are close to 9 eV, which corresponds to the region that Sb exhibits metallic properties upon reflection. This theoretical work guides future studies on strain engineering of antimonene, which finally contributes to antimonene photonic devices within the UV region (Figure 27).²⁹⁴ Moreover, arsenene and antimonene undergoing hydrogenation pretreatment have been simulated as magnetic and Dirac materials, further expanding optoelectronic devices' applications. Based on DFT calculations, hydrogen treatment would transform the buckle structure of NSs into a planar structure. More importantly, semihydrogenation will alter the electronic structure to metallic, while full-hydrogenation would transfer the pristine 2D Xenos to Dirac materials.²⁹⁵

Interestingly, if arsenene or antimonene is treated with oxygen forming oxides, such Xenos will be changed to be topological insulators with direct bandgaps, as evidenced by Zeng's group.¹⁶⁵

4.1.3. Tellurene. 2D Te has an optical absorption band from 200 to 2000 nm, which is suitable for fabrication of optical devices located at both infrared and visible bands.

Recently, tellurium nanostructures were discovered by Wang et al.²⁹⁶ These tellurium nanostructures have been demonstrated to have nonlinear optical properties using the open-aperture z -scan measurement over a broad wavelength range. This work achieved mode-locking pulses and Q-switching pulses based on biologically produced Te (Bio-Te) in erbium-doped fiber laser and 2 μm solid-state lasers, respectively. It is suggested that the Bio-Te has a potential for wideband photonic applications, such as mode-locked lasers and optical routing.

It is also worth mentioning that small-sized two-dimensional Se-coated Te lateral heterojunction nanomaterials were applied in ultrafast lasers by researchers from Shenzhen University. A Se-coated Te-based microfiber was fabricated as a mode-locking device in ultrafast fiber lasers at infrared. Tellurene also shows great potential for other applications, like the all-optical signal processing and optical computing.

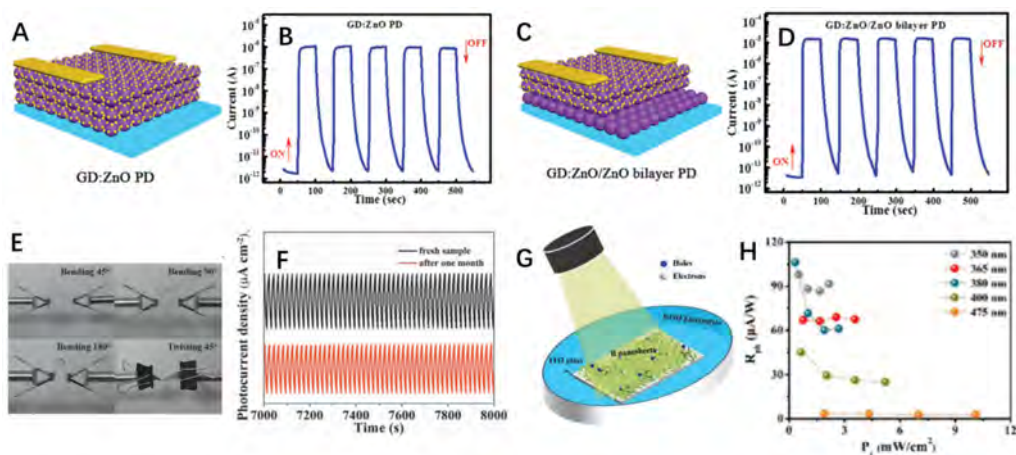


Figure 28. (A, B) Schematic diagram and ON/OFF measurement of GDY:ZnO photodetector. (C, D) Schematic diagram and ON/OFF measurement of GDY:ZnO/ZnO photodetector. Reproduced with permission from ref 298. Copyright 2016 Wiley-VCH Verlag GmbH and Co. KGaA, Weinheim. (E) Photographs of GDY-based PDs under bending (45° , 90° , and 180°) and twisting (45°); (F) The intercepted ON/OFF signals of GDY-based PDs. Reproduced with permission from ref 299. Copyright 2020 Wiley-VCH Verlag GmbH and Co. KGaA, Weinheim. (G) Schematic diagram of movement and rapid separation of photogenerated electrons and holes in boron nanosheets with excitation light. (H) Photoresponsivity of the same device as a function of different wavelengths and light power density. Reproduced with permission from ref 300. Copyright 2020 Royal Society of Chemistry.

4.2. Optoelectronics

In recent years, photodetectors based on 2D materials and their heterostructures have attracted extensive interest. Due to their unique photoelectric characteristics, two-dimensional photodetectors have made remarkable achievements for ultrasensitive optoelectronics.

4.2.1. GDY. For GDY, Li et al. reported heterojunction UV photodetectors with TiO_2 :GDY nanocomposites and MgZnO .²⁹⁷ It has a large signal-to-noise ratio of 1.5×10^5 at 254 nm, with the rise and fall times of 3.5 s and 2.7 s, respectively. Jin et al. reported GDY/ZnO nanocomposites prepared via self-assembling GDY on modified ZnO nanoparticles surface for UV photodetection as shown in Figure 28A,C.²⁹⁸ The connection between GDY-nanoparticles and ZnO nanoparticles significantly enhances the carrier exchange rate between the two nanoparticles, thus improving the optical response significantly. The fabricated device exhibited a fast rise/fall time of 6.1/2.1 s and a large response of 1260 A W^{-1} (Figure 28D). In contrast, traditional reference devices have a response of 174 A W^{-1} and a rise/fall time of 32.1/28.7 s (Figure 28B), which are significantly lower and longer. Zhang et al. demonstrated the deposition of ultrathin GDY NSs on a flexible PET substrate for PEC light detection.²⁹⁹ The flexible photodetectors of GDY nanosheets have long-term stability at 0.1 M KOH. In addition, the photodetector device maintains good light response characteristics after 1000 cycles of twisting (45°) and bending (180°) (Figure 28E,F).

4.2.2. Borophene. Ma et al. prepared a photoelectrochemical (PEC) and a field-effect transistor (FET) based on boron nanosheets, as shown in Figure 28G.³⁰⁰ The experimental results show that the PEC device has excellent self-power supply ability and has a high optical response up to $2.9\text{--}91.7 \mu\text{A W}^{-1}$ in the UV band. In addition, under the excitation light of 405 nm, the FET also shows a tunable light response range from 174 to $281.3 \mu\text{A W}^{-1}$ (Figure 28H).

4.2.3. Group V: Arsenene, Antimonene, and Bismuthene. Despite lacking experimental studies employing arsenene directly as optoelectronic devices, the unique optical and tunable electronic properties of Arsenene promote

theoretical simulation investigations on this application, which has laid a good foundation for future research.³⁰¹ In 2018, Gao et al. observed strong superconductive pairing interaction in arsenene using first-principles DFT calculations. By carefully checking the possible phonon-mediated superconductivity under electron doping, researchers simulated the superconducting transition temperature of the arsenene. As one arsenene doped with 0.2 electrons and 12% biaxial tensile strain was applied, its superconducting transition temperature was 30.8 K, which was predicted to be the highest in the electron-doped 2D Xenex.³⁰² For arsenene, the metal electrical contact is a key factor in photoresponse and charge transport processes in two-dimensional semiconductors (2DSC) devices of nanosize, with their inherent properties covered up. Lu's group has simulated the electrical contact between different electrodes and the single-layer As (Figure 29A).³⁰³ Schottky barriers are always formed from bulk metal contacts, which is ascribed to Fermi level pinning, while the hole injection in the monolayer (ML) As device is free of barrier when applying a hybrid electrode of graphene and Pt, indicating amazing performance in such an Arsenene-based device. They provide a theoretical basis to choose advantageous electrodes when designing a ML arsenene device in the future.³⁰³ Thanks to the prominent carrier mobility and resistance against oxygen and water, arsenene is promising for applications in field-effect transistors (FETs). Lu's group also simulated the performance of ML As device with the gate length of sub-5 nm by using accurate ab initio quantum transport simulation (Figure 29B,C).³⁰⁴ It was found that the optimized 2D ML Xenex metal-oxide-semiconductor FETs (MOSFETs) can meet the requirements of low power as the gate length is larger than 4 nm. When the gate length is decreased to 1 nm, the on-current the double gate (DG) ML antimonene and arsenene MOSFETs are better than that of the DG ML MoS_2 MOSFETs, indicating 2D Xenex are more suitable for ultrashort FETs.^{303,304}

Unlike As and Sb, whose energy density is closely correlated with the external environment, 2D bismuthene's Young's modulus and maximum bond length are insensitive to an external electric field.³⁰⁵ However, metal incorporation (V, Cr, Mn, Fe, etc.) would significantly alter the electronic and

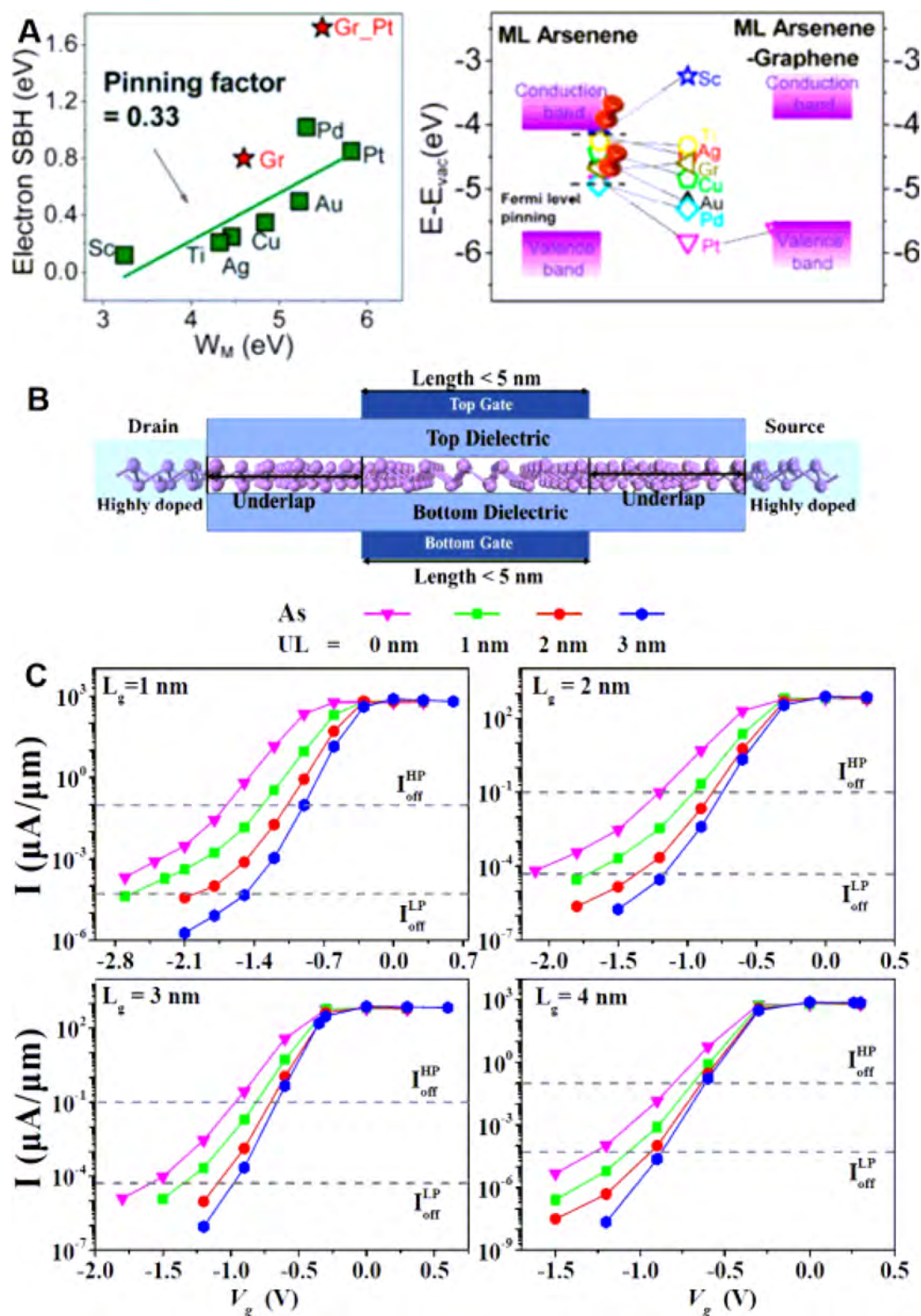


Figure 29. (A) Electrical contacts in monolayer arsenene devices. Reproduced from ref 303. Copyright 2017 American Chemical Society. (B) Schematic view of the sub-5 nm DG ML As/Sb MOSFET. (C) I - V_g characteristics of the sub-5 nm ML As-MOSFETs. Reproduced from ref 304. Copyright 2018 American Chemical Society.

magnetic properties of bismuthene.³⁰⁶ This tunable structure endows bismuthene potential for photodetector applications. In 2018, Huang et al. applied it to construct electrodes for photodetection in a broadband spectrum. The photoelectro-

chemical (PEC) performance of the Bi-based photodetector suggests it is a promising PEC-type photodetector. Further evaluations indicate that its current density can reach 830 nA cm^{-2} , with a drastically improved responsivity of $1.8 \mu\text{A W}^{-1}$.

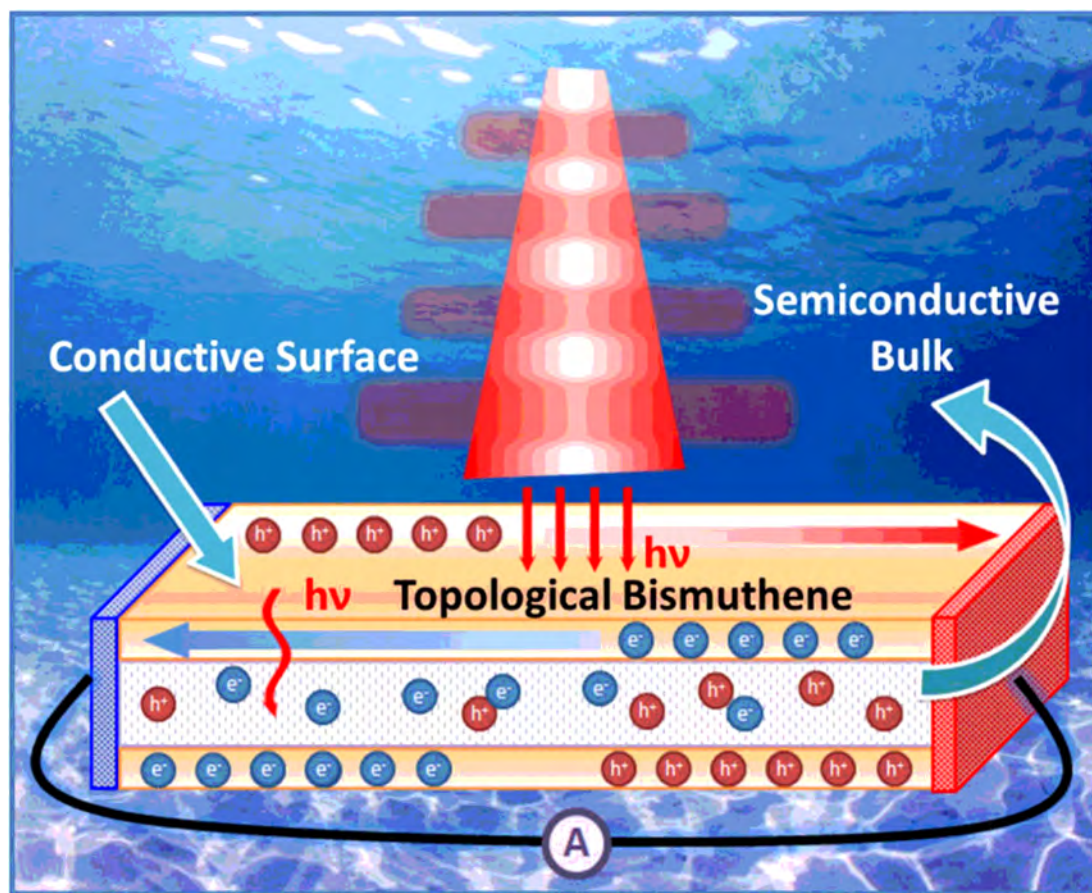


Figure 30. Schematic representation of the photoresponse of a topological Bismuthene photodetector upon sunlight illumination. Reproduced with permission from ref 307. Copyright 2018 IOP Publishing.

This demonstrates great potential for fabricating Bi-based optoelectronic devices in the future (Figure 30).³⁰⁷ Compared to other 2D materials, Bi suffers from low photocurrent density and weak photoresponsivity, inhibiting any large-scale application in working conditions. Chemical modification with other elements would improve this situation. In 2020, Zhang and co-workers successfully prepared bismuth telluride nanoplates, which have enhanced on/off switching stability for Bi/Te based photodetectors and offer effective solutions for rational designs of high-performance optoelectronic devices.³⁰⁸

4.2.4. Tellurene. Wang et al. presented a vdWE-synthesized hexagonal 2D Te nanoplates-based flexible photodetector with high photoresponsivity.³⁰⁹ The device demonstrated high photoresponsivity and excellent stability, as shown in Figure 31A. Under switching of illumination, the measured current exhibited the same levels of both photocurrent and noise, and the photoresponsivity with a value of 162.4 A W^{-1} was achieved, suggesting high photoresponsivity and stability of the 2D Te nanoplates based photodetector. Remarkably, after 100 continuous bending cycles of the device, the measured noise current and photocurrent changed slightly (Figure 31B,C), indicating the device was suitable for flexible and wearable optoelectronic devices. Then, Amani et al. exhibited stable 2D Te nanofilms based near IR photodetectors.³¹⁰ An Au/Al₂O₃ optical-cavity substrate was utilized for improved light absorption. Additionally, by adjusting the Al₂O₃-spacer thickness, the peak photoresponsivity wavelength could be tuned from 1.4 to 2.4 μm (i.e., from 13 to 8 A W^{-1} , respectively), as shown in Figure 31D. To further evaluate the device

performance, the responsivity dependence on various incident laser wavelengths at 78 and 297 K was performed (Figure 31E). The peak responsivity was located at 1.7 μm , showing 27 and 16 A W^{-1} at 78 and 297 K, respectively. Corresponding specific detectivities were calculated to be 2.6×10^{11} and 2.9×10^9 at 78 and 297 K, respectively (Figure 31F). Specific detectivity was enhanced because noise current, which is inversely proportional to specific detectivity, was more efficiently suppressed at 78 K than at room temperature. Results showed that 2D Te nanosheets, solution-synthesized, are promising for high-performance infrared photodetectors. Recently, Xie *et al.* presented a liquid phase epitaxy (LPE)-synthesized 2D nonlayered Te nanoflakes-based high-photoresponse photodetector and the photoelectrochemical measurements on it.³¹¹ Compared with the previous studies, this investigation mainly concentrated on device photoresponses from UV to visible regions. At a fixed potassium hydroxide (KOH) concentration and bias voltage, photocurrents and photoresponses were measured as a function of incident-laser intensity at various wavelengths, as shown in parts G and H, respectively, of Figure 31. As the power of incident laser beams with various wavelengths increased, the measured photocurrents were significantly improved. As a result, the photoresponse was enhanced as well. Additionally, photocurrent stability dependence to KOH concentration was also measured, and results predicted that LPE-synthesized 2D nonlayered Te nanosheets were suitable for application to photodetection in UV–vis regions. Owing to a small and tunable bandgap of 2D Te nanoflakes, this material is promising for MIR photodetector

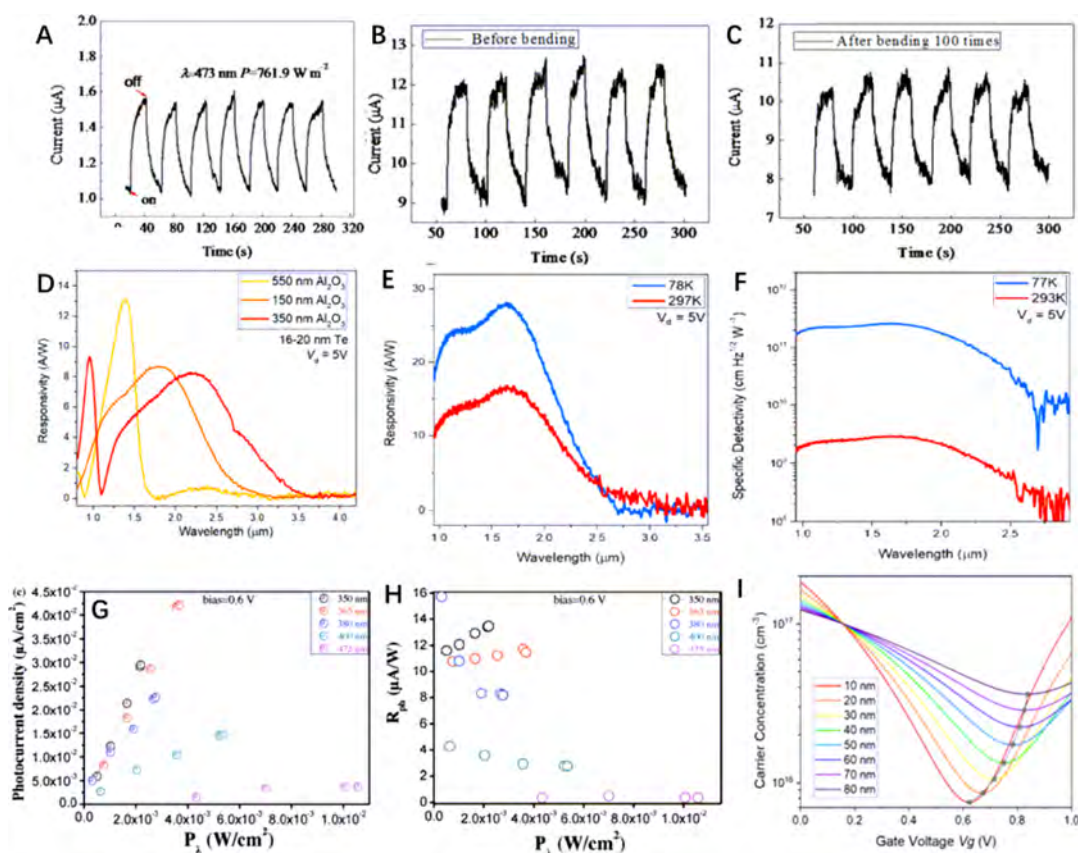


Figure 31. (A) Photoresponse of 2D Te-based photodetector *versus* time with 2 V bias. Photoresponse plotted *versus* time (B) with and (C) without illumination and 100 times bending treatment. Reproduced from ref 309. Copyright 2014 American Chemical Society. (D) IR photoresponse of 2D Te base photodetector with Au/Al₂O₃ optical cavities. (E) Spectral responsivities under an applied gate bias of $V_g = 5$ V and 78 and 297 K. (F) Specific detectivities of optimized thickness Te nanosheet based devices. Reproduced from ref 310. Copyright 2018 American Chemical Society. (G, H) Photoresponse and photocurrent as functions of incident power P_i , respectively. Reproduced with permission from ref 311. Copyright 2018 Wiley-VCH Verlag GmbH and Co. KGaA, Weinheim. (I) Detector NEPs calculated as a function of device length and thickness of the 2D Te sample. Reproduced from ref 312. Copyright 2019 American Chemical Society.

applications. Waveguide integration can improve SNRs more than free-space detectors can. Optical absorption was proportional to the waveguide path length. Moreover, detectable bandwidths of waveguide-integrated devices were wider than those of free-space ones, mainly owing to the reduced carrier-transit times and resistive-capacitive delay. Recently, Jones *et al.* exhibited the 2D Te nanoflakes based waveguide-integrated photodetector.³¹² Small tunable bandgap and low gate-carrier concentration of 2D Te enabled the fabrication of a very low-noise room-temperature photodetector. Figure 31I presents the NEPs of the device based on 2D Te as functions of device length and the thickness of 2D Te nanoflakes. Simulated NEPs were much superior to the best of those previously reported. These outstanding findings suggested that 2D Te holds great potential for on-chip integrated MIR detection applications.

4.3. Catalysis

With a thin-layer structure providing a large specific surface area and abundant anchoring sites for absorbing reagents, 2D materials provide a promising nanoplatform for controllable catalytic properties compared with their corresponding 3D structures. The relatively single reactive environments of 2D materials are very close to the theoretical calculation conditions, leading to a more comprehensive understanding of reaction mechanisms combining experimental results. In recent studies, Xenex have demonstrated promising potentials in electro-

catalysis, photocatalysis, and thermal catalysis. However, current studies on Xenex are still in the initial stage, and more efforts are needed to promote their applications in this direction.

4.3.1. GDY. Due to its unique 2D structure with a highly porous plane, the reactive sites in GDY are increased and thus another catalyst can be dispersed in the pores. This feature endows GDY with great potential to be applied for catalytic applications. So far, a great number of GDY-based materials have been explored for photocatalyst, electrocatalyst, and water-splitting applications.

TiO₂ has been widely applied in photocatalytic degradation of organic contaminants attributed to its extremely low toxicity, low cost, and excellent stability. However, TiO₂ nanoparticles can only employ ultraviolet light because of their large intrinsic bandgap. GDY is found to improve the photocatalytic performance of TiO₂ (Figure 32A).³¹³ Compared to TiO₂, TiO₂-carbon nanotube, and the TiO₂-graphene composite, the TiO₂-GDY nanocomposite exhibits the highest activity for catalyzing the degradation of methylene blue upon UV irradiation. Moreover, the decreased bandgap of TiO₂ after combining with GDY can improve the visible-light-based photocatalytic activity of TiO₂-GDY (Figure 32A2,A3).

When a semiconducting nanomaterial adheres on the basal plane of GDY, recombination of the electron-hole pair can be prevented. The catalytic properties of TiO₂-GDY, 2D carbon-supported TiO₂, and graphene-TiO₂ composites have been

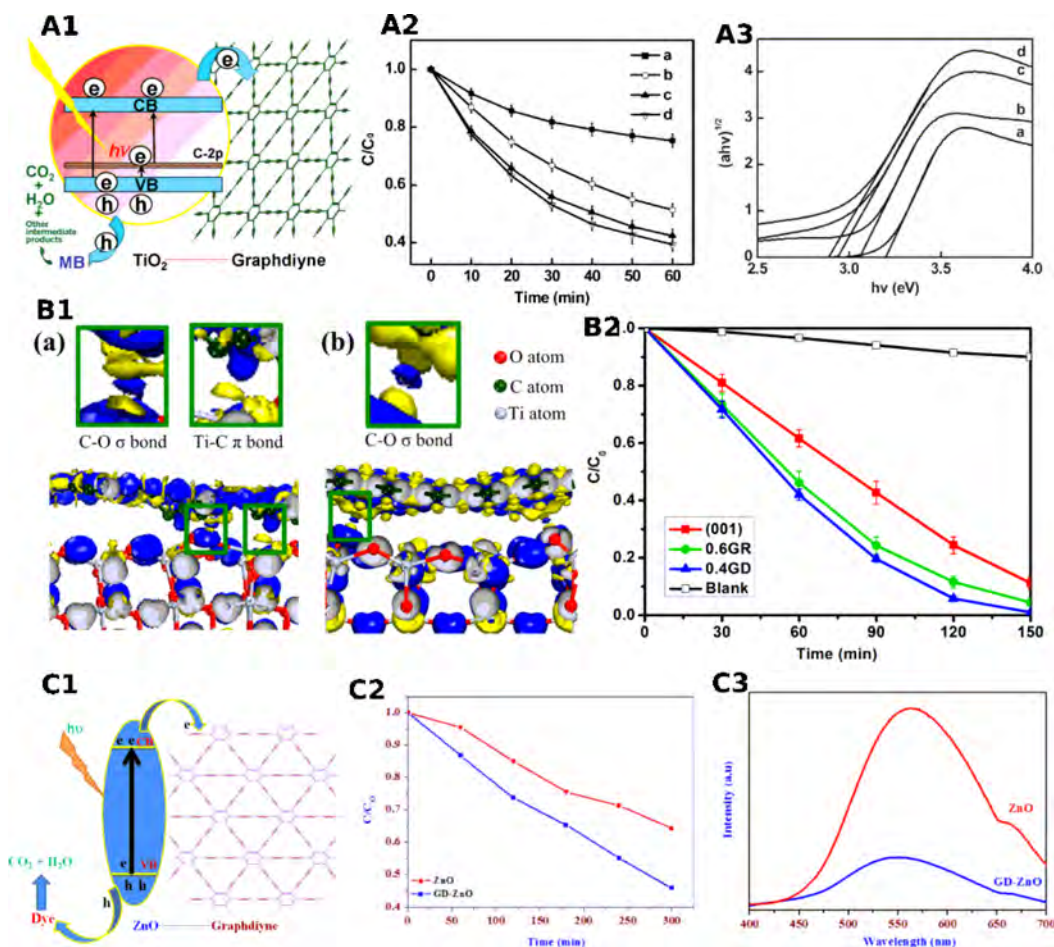


Figure 32. (A1) Schematic processes in the TiO₂-GDY-based photocatalytic degradation of MB. (A2) Visible light-catalytic degradation of MB on (a) pure TiO₂, (b) TiO₂-CNTs, (c) TiO₂-graphene, and (d) TiO₂-GDY. (A3) Tauc plot for determination of bandgap. Reproduced with permission from ref 313. Copyright 2012 Wiley-VCH Verlag GmbH & Co. KGaA, Weinheim. (B1) Different electron density at different composites interfaces: (a) TiO₂-GDY, (b) TiO₂-graphene. Yellow and blue denote the depletion and accumulation of electrons, respectively. (B2) The photocatalytic degradation process of MB through TiO₂(001), TiO₂(001)-GR, TiO₂(001)-GD, and the control. Reproduced from ref 314. Copyright 2013 American Chemical Society. (C1) Schematic photodegradation based on GDY-ZnO. (C2) Degradation rate kinetics of phenol through pure ZnO and GDY-ZnO nanohybrids. (C3) PL spectra of ZnO and GDY-ZnO nanohybrids. Reproduced with permission from ref 315. Copyright 2015 American Chemical Society.

predicted by first-principles DFT (Figure 32B1).³¹⁴ The TiO₂-GDY composite was found to possess excellent charge separation ability, and the photoexcited carriers have the most extended lifetimes among three investigated TiO₂ composites. The prediction is further proved by photocatalytic degradation of methylene blue (Figure 32B2). This strategy is also viable for other semiconductor photocatalysis. Thangavel *et al.* investigated the photocatalytic property of GDY-ZnO nanohybrid on the degradation of rhodamine B and methylene blue (MB) (Figure 32C1).³¹⁵ Enhanced photocatalytic properties can be observed on GDY-ZnO nanohybrids, with a 2-fold higher degradation rate constant of azo dyes than that of pure ZnO nanoparticles (Figure 32C2), which benefits from efficient prevention of the recombination rate of the electron and hole. This mechanism can be proved by the photoluminescence (PL) spectra (Figure 32C3). The PL intensity from pure ZnO is significantly quenched after hybridization with GDY. This PL quenching can be ascribed to the electron-accepting property of GDY. These GDY-based semiconductor hybrid photocatalysis investigations can provide promising ways to overcome the drawback of a single photocatalysis agent for potential environmental treatment. Besides semiconductors, Li *et al.*

reported the first Fe₃O₄-based photocatalyst for nitrogen reduction reactions. The valence state and coordination environment of the iron atoms in Fe₃O₄ can be tuned by incorporating GDY, leading to excellent photocatalytic performances of the GDY@Fe₃O₄ heterojunctions for ammonia synthesis (with the yield up to $1762.35 \pm 153.71 \mu\text{mol h}^{-1}\text{g}_{\text{cat}}^{-1}$).³¹⁶

Besides the application in the photocatalytic field, GDY has also attracted the attention for electrocatalytic applications attributed to the high electrical conductivity and abundant active sites due to plenty of triple bonds. GDY has also been used as a support material to protect electrocatalysts from corrosion. Li's group developed metal-free 3D porous fluorinated GDY on carbon cloth (p-FGDY/CC) and GDY-exfoliated and -sandwiched iron/cobalt-layered double hydroxide (LDH) nanosheet arrays for the electrocatalytic hydrogen-/oxygen-evolution reaction and water splitting.³¹⁷ The high conductivity, abundant active sites, and additional electron-rich character of the strong F-C bond in the p-FGDY/CC electrocatalysis system facilitated high activity, stability, and selectivity in the metal-free catalysis. LDH's electrocatalytic activities and stabilities were dramatically improved with GDY incorporation, because

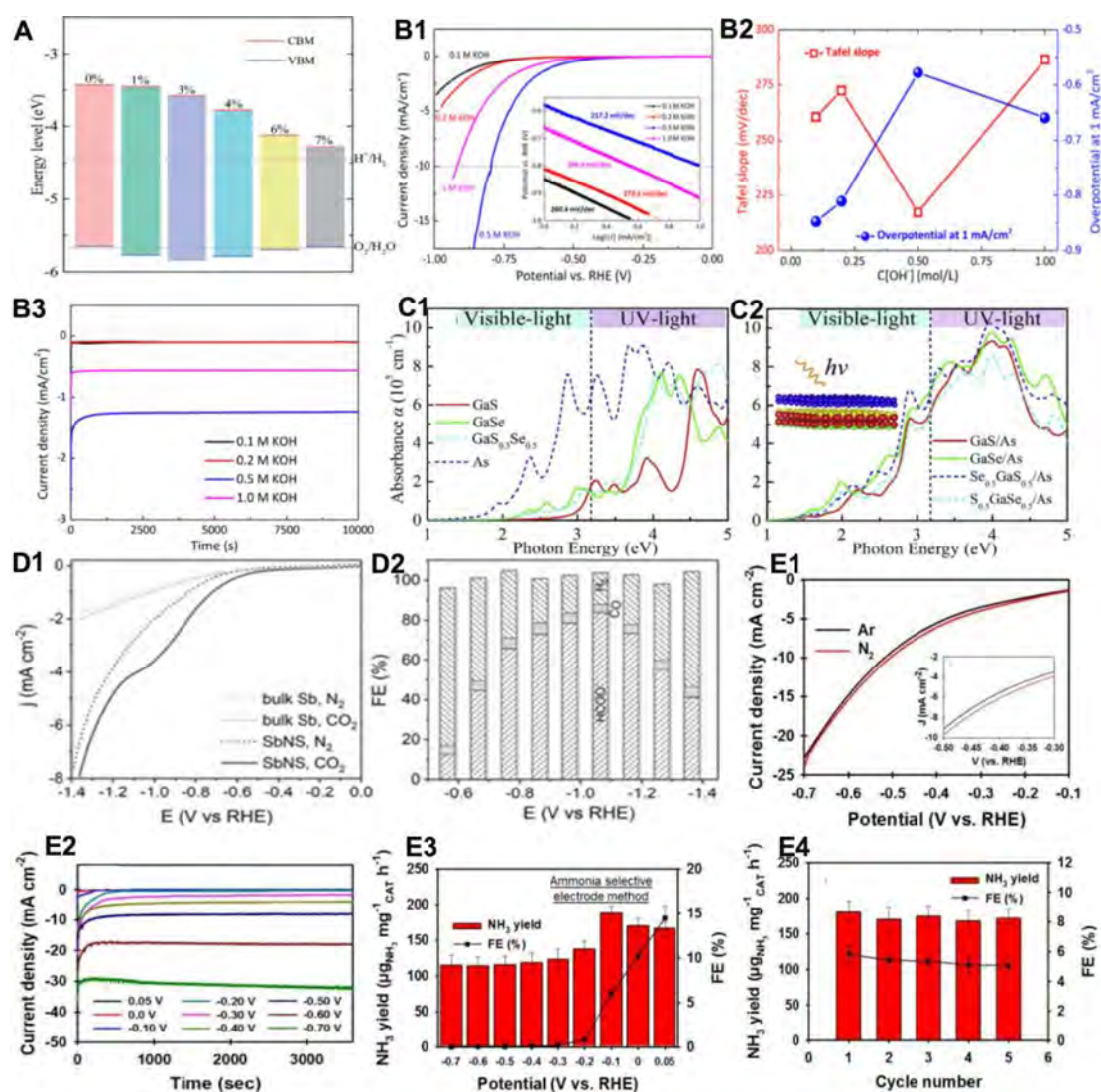


Figure 33. (A) Theoretical band edge positions of the A/C (Sb/carbon) heterostructures as a function of tensile strain (0–7%). Reproduced with permission from ref 330. Copyright 2017 Royal Society of Chemistry. (B1) Polarization curves, inset: Tafel plots of antimonene in KOH electrolyte (B2) Tafel slope and overpotential, and (B3) stability tests of 2D antimonene. Reproduced from ref 331. Copyright 2019 American Chemical Society. Optical absorption spectra of (C1) GaX, arsenene monolayers, and (C2) GaX/As heterostructures using time-dependent Hartree–Fock calculations. Reproduced with permission from ref 190. Copyright 2018, Elsevier, Inc. (D1) Linear sweep voltammetry (LSV) curves of bulk antimony and 2D antimonene nanosheets in nitrogen and carbon dioxide saturated media. (D2) Faradaic efficiency (FE) for formate (bottom), carbon monoxide (middle), and hydrogen gas (upper) over 2D antimonene electrodes at different applied potentials. Reproduced with permission from ref 157. Copyright 2017 Wiley-VCH Verlag GmbH and Co. KGaA, Weinheim. (E1) LSV curves, insert is the enlarged curves ranging from -0.5 to -0.3 V. (E2) Chronoamperometric curves. (E3) NH_3 yield rate and corresponding FE. (E4) NH_3 yield rate and FE. Reproduced with permission from ref 332. Copyright 2020 Royal Society of Chemistry.

GDY provided a number of active sites and a protection capability to the LHD from corrosion. Yu *et al.* integrated the electron-rich GDY into molybdenum disulfide to achieve a new electrocatalyst for water decomposition in the whole pH range.³¹⁸ Fang *et al.* synthesized a free-standing GDY/ Co_2N using GDY nanosheet arrays in situ grown on the surface of Co_2N nanowires with interface bonding modification.³¹⁹ GDY contributes unique π -electron characteristics to optimize surface binding of Co–N compounds. It resulted in ammonia synthesis with high electrocatalytic efficiency and selectivity. Recently, Li's group synthesized charge-transfer complexes of Ni-terephthalic acid nanosheet on GDY, with a strong p–d coupling effect at the interface.³²⁰ Therefore, Ni-terephthalic acid nanosheet/GDY showed record-breaking oxygen evolution reaction in an alkaline electrolyte. Liu's group prepared a 3D GDY scaffold to support

rhodium nanoparticles.³²¹ Keeping the intrinsic properties of GDY, the 3D GDY also exhibits a porous structure and high specific surface area. These Rh@3DGDY composites showed high electrocatalytic activity and good recyclability in the 4-nitrophenol reduction reaction. They also successfully synthesized GDY nanowalls and GDY-based hierarchical architecture to optimize their catalytic properties.^{99,228} Wu *et al.* applied GDY to support cobalt nanoparticles catalysis for oxygen evolution, leading to improved electrocatalytic activity.³²² First, the interaction between the catalysts and the π -conjugated networks of GDY would prevent the nanoparticles from aggregation. Second, the porous structure of GDY possessed a high adsorption energy to stabilize the metal nanoparticles. At last, the good chemical stability and outstanding electrical conductivity allow GDY to serve as support materials for the

catalysts. Zhang's group successfully prepared structure-controlled GDY on arbitrary substrates ranging from 1D to 3D by employing a copper envelope catalysis strategy.⁷⁰ They fabricated the GDY/BiVO₄ photoanode using this method and it presented enhanced photoelectrochemical activity and stability for water splitting. It is because GDY can extract the photogenerated holes from BiVO₄ to decrease the electron–hole recombination rate and thereby improve the stability of BiVO₄.

Metal atom catalysts (AC) are at the research forefront in the field of catalysis. They are fabricated by anchoring single atoms on support materials. A zerovalent metal AC provides a critical approach to utilize every single metal atom. The active sites in the zero-valence metal atom catalyst are homogeneous. Thus, they possess high selectivity, low cost, and high reactivity compared to bulk metal catalysts. However, as the particle size of the catalyst continues to decrease, the surface energy of the metal atom catalyst increases, which is prone to migration and agglomeration, resulting in unstable charge transfer and uneven active sites. This disposition makes it easy to limit the load and affect the mass activity of the ACs. Therefore, the current research focuses on choosing suitable support materials to provide efficient and stable metal AC for a practical application with scalable fabrication. GDY has a high π -conjugation, wide interplanar spacing, in-plane triangular pores, and excellent thermal stability, making it the best candidate as an AC substrate. The previous experimental results successfully demonstrated GDY as a direct support for zerovalent metal ACs. Li's group fabricated well-defined structured metal atom-GDY hybrid (M⁰/GDY) ACs by anchoring isolated zerovalent nickel, iron, molybdenum and palladium atoms at the corners of the triangular pores in GDY and applied them to electrochemical catalysis.^{63,323,324} The isolated nickel, iron, and palladium atoms were anchored on a three-dimensional (3D) GDY electrode formed on carbon cloth surfaces by electrochemical reduction of each metal ion to obtain stable Ni⁰/GDY, Fe⁰/GDY, and Pd⁰/GDY ACs.^{63,324} Mo⁰/GDY was synthesized by solvothermal reduction of molybdenum pentachloride on the 3D GDY electrode.³²³ The ACs revealed that strong chemical interactions and electronic coupling between the zerovalent metal atom and GDY could stabilize the atoms on the GDY substrate separately and permit an efficient charge transport between the active catalytic sites and the substrate, resulting in outstanding catalytic activity for hydrogen evolution reaction (HER) or electrochemical nitrogen reduction reaction (ECNRR).

4.3.2. Group V: Arsenene, Antimonene, and Bismuthene.

4.3.2.1. Electrocatalysis and Photocatalysis. The unique electronic structures of 2D Xenes allow combinations of some modifiers and Xenes for application in photoelectric catalytic processes.³²⁵ Some of these reactions could alleviate energy-related issues, such as water splitting reaction, CO₂ reduction reaction, and nitrogen reduction reaction.

4.3.2.2. Water-Splitting Reaction. Hydrogen gas (H₂), because of its high energy efficiency, safe byproduct, and abundant storage, is proposed to be one crucial type of next-generation clean energy that is developed as an alternative to depleting fossil fuels. In recent years, evolution of H₂ from a water-splitting reaction is one of the most examined processes for which electrocatalytic or photocatalytic approaches are often needed. The water-splitting reaction typically includes two processes: a hydrogen evolution reaction (HER, 2H⁺ + 2e⁻ → H₂) process at the cathode while an oxygen evolution reaction (OER, H₂O → 2H⁺ + 1/2O₂ + 2e⁻) at the anode. This complete

reaction can produce two H₂ and one O₂ by the decomposition of two water molecules. In terms of thermodynamics, a minimum energy of 1.23 eV is required for the water splitting reaction. Thus, the tunable bandgap of the Xenes can be designed and modified for a rational preparation of optimized catalysts, accelerating this process.^{249,326–328} Several factors have been reported to influence the HER and OER processes, such as the dopants, surface sites, and the 2D element itself.³²⁹

Figure 33A illustrates the tensile strain dependent band alignments of a Sb/carbon (A/C) heterostructure with the redox capacity of oxygen evolution (O₂/H₂O) at pH = 0 and hydrogen evolution (H⁺/H₂). It is obvious that for the unstrained system, OER cannot happen under the promotion of the VBM. Therefore, implementing an appropriate tensile strain from 1% to 6% to decrease the VBM is essential for lowering the O₂/H₂O energy, thus making spontaneous photocatalytic water splitting occur. It is noteworthy that when the tensile strains are less than 6%, the VBM location is next to the water oxidation potential, and the heterostructure is beneficial for catalysts to promote the whole water splitting. When the tensile strain is increased above 6%, the VBM location will increase above the oxidation potential of O₂/H₂O, thus preventing the water-splitting reaction from occurring.³³⁰ Using a few-layer Sb, Zhang *et al.* carefully studied the HER and OER performance.²⁵⁰ As shown in Figure 33B, a systematic and comparative HER study was performed for antimonene. The catalytic performance was significantly increased, which was ascribed to a possible reason that the semimetallic electronic structure might accelerate the electron transfer rate and thus enlarge the HER capability. Figure 33B1 shows that the lowest onset potential around -0.27 eV can be obtained, when the KOH concentration is 0.5 M, indicating a low driving voltage for initiating the HER process. The Tafel slopes in the inset of Figure 33B1 also presented that the lowest slope was achieved using 0.5 M KOH, proving that the catalytic activity is enhanced at the alkali concentration. Moreover, Figure 33B2 provides the important factors in HER at different KOH concentrations. It is obvious that the results are in accordance with those in Figure 33B1. The possible reason for the enhanced catalytic performance of antimonene might be due to the semimetallic states of this Xene, which would accelerate electron transfer and thus improve the HER activity. Stability tests in Figure 33B3 demonstrate one step further that antimonene has potential for various applications.

Constructing heterostructures of these Xenes as an effective bandgap engineering strategy is also beneficial for catalytic water splitting reactions. Peng *et al.* investigated the photocatalytic behaviors of Se_{0.5}GaS_{0.5}/As and S_{0.5}GaSe_{0.5}/As heterostructures by DFT calculations and carrier mobility calculations.¹⁹⁰ The formation of heterostructures promotes an indirect bandgap to direct bandgap transition depending on the distances between the layers. These hybrid structures display high carrier mobility without a specific direction, promoting the separation and migration of the photogenerated charge carriers and further speeding up the HER process. Compared with the pure 2D GaX, GaX/As heterostructures possess prominently increased absorption in the visible spectral range and good stability (Figure 33C).

4.3.2.3. CO₂ Reduction. Increasing global energy demand and environmental concern have attracted more attention to CO₂ transformation, which alleviates global warming caused by excessive emission of CO₂, and provides a sustainable solution to reduce fossil fuels consumption. Thus, the catalytic conversion

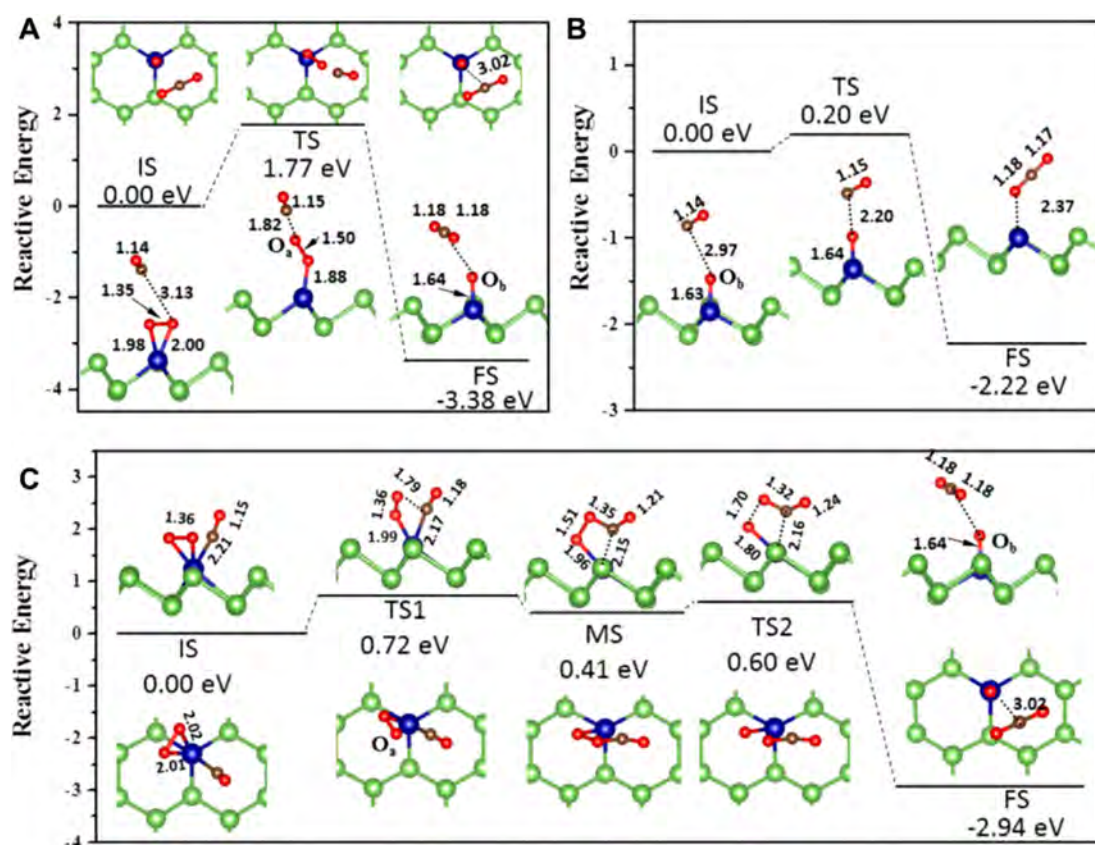


Figure 34. Simulated energetic profiles for the CO oxidation process on transition-metal-doped arsenene catalyst *via* (A) $\text{CO} + \text{O}_2 \rightarrow \text{CO}_2 + \text{O}$ and (B) $\text{CO} + \text{O} \rightarrow \text{CO}_2$ by ER mechanism; (C) $\text{CO} + \text{O}_2 \rightarrow \text{O}-\text{O}-\text{C}-\text{O} \rightarrow \text{CO}_2 + \text{O}$ by LH mechanism. Reproduced with permission from ref 333. Copyright 2019 Elsevier, Inc.

of CO_2 is a promising route. The excellent properties of the 2D materials-supported metal single-atom catalysts has offered a new research direction for CO_2 fixation.

Figure 33D illustrates a recent work that uses antimonene for electrocatalytic CO_2 reduction reaction, where MacFarlane's group successfully applied the as-prepared antimonene nanosheets for highly effective reactions with extraordinarily high selectivity toward formate.¹⁵⁷ As shown in Figure 33D1, a comparative analysis between antimonene and bulk Sb showed that an antimonene electrode exhibited a lower onset potential and better reactive performance. Further, the antimonene electrode showed a peak at -1.06 V in the CO_2 -saturated solution, but the peak disappeared in the N_2 -saturated solution, suggesting CO_2 electroreduction occurred. Figure 33D2 indicates that the applied potential significantly affects the H_2 and formate product distribution. The faradaic efficiency (FE) for formate reached 84% at -1.06 V, while that for CO maintained around 100%, regardless of the implementing potential. A positive correlation between I_{mass} and the lateral size of the antimonene nanosheets provides substantial evidence that the sites located at the edge are intrinsically more active.

4.3.2.4. Nitrogen Reduction Reaction. Ammonia gas (NH_3) has been regarded as one of the most important industrial chemicals for a long time, but the generally employed Haber–Bosch process needs demanding pressure/temperature conditions and thus cannot avoid waste of energy. Therefore, NH_3 synthesis *via* electrocatalysis and photocatalysis under mild conditions is more economical and highly appreciated.

Although theoretical calculations have reported a series of ammonia synthesis over 2D materials, experimental exploration

of this reaction over the Xenes with these three elements has been rarely dealt with. An investigation based on a few-layer Sb nanosheets cathode was recently performed in detail, with the results shown in Figure 33E.³³² No obvious decay in current densities were observed in Figure 33E2, suggesting that antimonene has great stability. The HER is the main process at high electrode potentials, causing current densities improvement. Figure 33E3,4 provided the catalytic performance results, manifesting that the NH_3 yields and FEs are encouraging, which are comparable with the best electrocatalysts so far. This builds up an exciting avenue for developing highly effective and selective Xene catalysts for the mild-condition NH_3 synthesis. Apart from the excellent performance, this catalyst survived five cycles with negligible reactivity, proving its robustness for practical cases.

4.3.2.5. Thermal Catalysis. Existing in the form of nanosheets, these three Xenes have demonstrated great potential for heterogeneous catalytic applications, as evidenced by the discussions above. Apart from energy conversion related catalytic reactions mentioned in Section 4.6, they can also catalyze various thermal catalytic processes, including hydrogenation reactions and oxidation reactions.

However, it must be taken into consideration that pure Xenes are not good candidates for both hydrogenation and oxidation reactions. The reason is that an electron-enriched structure makes it difficult to absorb the H_2 molecule and further split the molecule, which is a key step for hydrogenation reaction. In addition, the Xenes are usually not stable when facing O_2 , so they are not good candidates with high stability. Different modifications that can modulate the electron density, and

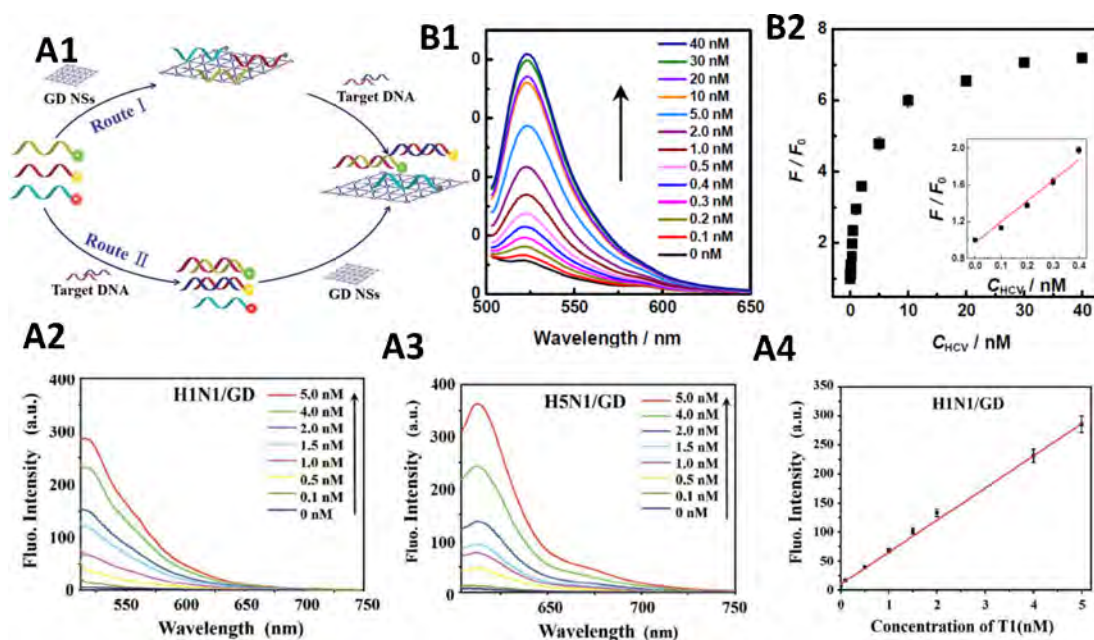


Figure 35. (A1) Schematic DNA detection based on GDY in two different ways. (A2, A3) Fluorescence spectra of fluorophore-labeled single-stranded DNA (ssDNA) when binding with targeted DNA at different concentrations. The target DNAs of H1N1 and H5N1 are the influenza A virus subtype. (A4) Calibration curve for H1N1 detection. Reproduced with permission from ref 338. Copyright 2017 Wiley-VCH Verlag GmbH & Co. KGaA, Weinheim. (B1) Fluorescence spectra of a GDYO probe loading ssDNA of the hepatitis C virus (P_{HCV}) as a function of concentrations of the hepatitis C virus target ssDNA (T_{HCV}) complementary to P_{HCV} . (B2) Plot of fluorescence quenching efficiency with inset showing the calibration curve. (F_0 and F indicate fluorescence intensities before and after mixing with T_{HCV} , respectively.) Reproduced with permission from ref 102. Copyright 2016 Royal Society of Chemistry.

enhance the stability, provide solutions for solving these problems. Taking a benchmark reaction in heterogeneous catalysis, the CO oxidation reaction as an example, a recent theoretical study examined possible catalytic pathways of different transition metal decorated arsenene.³³³ Among different metal modifications, arsenene with Cr as the dopant is calculated to be most favorable for CO oxidation reaction, with the lowest adsorption energies of O_2 molecules, indicating that O_2 adsorbed on Cr-modified arsenene is the most energetically stable configuration. Specifically, the adsorption energy is -1.28 eV for arsenene with Cr as the dopant, while the values for arsenene with Mn, Fe, Co, Ni, and Cu are -0.75 , -1.01 , -0.86 , -0.78 , and -0.36 eV, respectively. Detailed catalytic processes *via* Langmuir–Hinshelwood (LH) and Eley–Rideal (ER) mechanisms are depicted in Figure 34. Comparing the LH and ER mechanisms, the energy barrier for the LH mechanism is 0.72 eV over CO oxidation reaction, which is lower than that (1.77 eV) for the ER mechanism, meaning the LH mechanism is favorable. The Bader charge result reveals that the gained electrons (0.72 e) by O_2 from Cr-doped arsenene under only O_2 adsorption is larger than those (0.70 e) for coadsorption of CO and O_2 molecules, which indicates the coadsorption facilitates the O–Cr bond break to improve catalytic activity for CO oxidation. This example is encouraging because metal decoration endows Xenes with exciting catalytic performance and offers ideal platforms for conducting mechanistic studies. It helps the rational design to fabricate various well-defined Xenes supported single-atom or cluster catalysis with a precise structure–performance relationship.

4.4. Sensors

The unique physical and electrical characteristics make 2D Xenes ideal candidates for biosensors, gas sensors, and chemical sensors. The general principle is to transform molecular binding

characteristics into measurable electronic signals with high sensitivity and selectivity.

4.4.1. GDY. A 2D planar structure with electron-conducting properties endows GDY a promising nanoplatfor for effective detection of a gas or a biomolecule as described below.

4.4.1.1. Biosensor. Homogeneous detections for molecules targeting with fluorogenic probes have aroused great interest owing to their convenient operation.³³⁴ However, epidemic prevention and clinical diagnostics have growing demands for high selectivity, sensitivity, and high-speed sensing devices. Great success has been achieved by employing a novel strategy or new nanomaterial-based fluorogenic probes.^{335,336} 2D nanomaterials have shown their talent to be efficient detection platforms to sense small molecules or deoxyribonucleic acid (DNA) due to their strong adsorption and fluorescence-quenching function toward dye-labeled molecules or DNA.³³⁷

Parvin *et al.* developed a GDY-based novel sensing platform to detect DNA with a high signal-to-noise ratio in real-time (Figure 35A), which shows an outstanding fluorescence quenching ability and different affinities toward double-stranded or single-stranded DNA.³³⁸ The GDY NSs were found to possess high sensitivity toward several DNAs, which could detect minimum 25×10^{-12} M (Figure 35A2–A3). A linear relationship can be obtained (Figure 35A4). Wang *et al.* found a higher quenching ability in GDY oxide (GDYO) than GDY (Figure 35B1, B2).¹⁰² Such excellent properties of GDY and GDYO can be developed for novel biosensing devices to detect DNA in real-time. Besides the detection of DNA, GDY can also be used as a microRNA sensor with remarkable detecting limits of 3.3×10^{-19} M.³³⁹

4.4.1.2. Gas Sensor. Gas sensors can be applied to detect toxic vapors in the atmosphere, with a rapid response. The adsorption behavior of trimethylamine (TMA) and dimethylamine (DMA) vapor molecules on GDY NSs was investigated

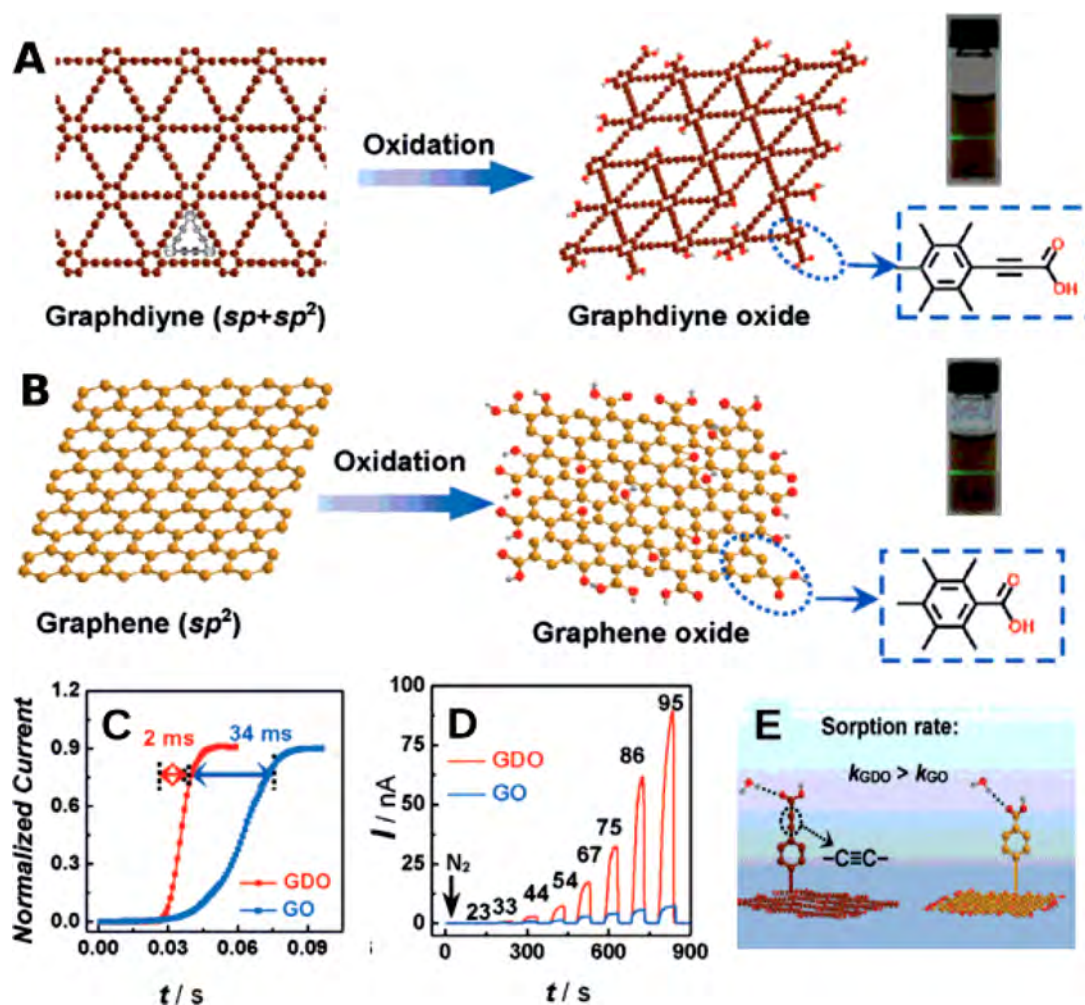


Figure 36. (A, B) Schematic representations for stacking structures of pristine GDY and graphene and their corresponding oxides (GDYO and GO) with insets showing the Tyndall effects of a water dispersion of GDYO and GO NSs. (C) Normalized response of the GO-based (GO, blue) and GDYO-based (GDO, red) humidity sensors. (D) Dynamic response curves of GDYO (GDO, red) and GO-based (GO, blue) shown by the current change when exposed to various relative humidity levels. (E) Schematic water molecular binding model for GDYO and GO. Reproduced with permission from ref 341. Copyright 2018 Wiley-VCH Verlag GmbH & Co. KGaA, Weinheim.

by Nagarajan *et al.*³⁴⁰ The bandgap changes when the TMA/DMA molecule interacts with GDY NSs. Yan *et al.* found that the GDY oxide (GDYO) possesses a rapid water molecular response, which is much quicker than that of graphene oxide (GO) of the same C/O ratio and thickness (Figure 36A–C).³⁴¹ Moreover, the GDYO-based gas sensor (red curve) possesses a much higher response current intensity than that of the GO-based gas sensor (blue curve), indicating a higher sensitivity of the GDYO-based sensor (Figure 36D), which is attributed to the stronger electron-withdrawing property of unique carbon hybridization in GDYO than the ethylenic bonds in GO (Figure 36E).

4.4.2. Borophene. **4.4.2.1. Biosensor.** Rastgou *et al.* studied the electronic sensitivities of borophene NSs with the B36 structure toward four nucleobases through density functional theory calculations.³⁴² The B36 structure is likely a bowl with a central hexagonal hole. It is observed that the attachment of the four nucleobases to borophene NSs will bring a change in electrical conductivity, leading to different electrical signals. Moreover, the reactivity order of nucleobases toward the borophene NSs is as follows: $A > G > C > T$. Cytosine has the largest influence on the conductivity of borophene NSs and will

result in the largest electrical signal; thymine produces the second-largest signal. Therefore, the borophene NSs may play a role in devices that are used to determine the DNA sequence.

4.4.2.2. Gas Sensor. There is a broad application prospect of borophene used as a gas sensor. It has been reported to be used for detecting ethanol,³⁴³ formaldehyde,³⁴⁴ and hydrogen cyanide.³⁴⁵ The electronic properties of borophene changed after gas adsorption, and thus an electronic signal can be generated and detected. The adsorption of ethanol molecules and the formaldehyde molecules on borophene NSs increases the electrical conductivity sharply.³⁴⁴ B36 borophene is sensitive to hydrogen cyanide and the concentration of HCN gas, which can be used to detect these toxic gases. Also, transmission functions change dramatically after the adsorption of CO, NO, NO₂, and NH₃ on the 2-*Pmmn* phase of borophene. Their adsorption strengths are much stronger than those on other 2D materials like graphene, MoS₂, and phosphorene.^{346,347}

4.4.3. Group V: Arsenene, Antimonene, and Bismuthene. Among numerous 2D materials, Xenes, especially pnictogens, have been continuously investigated by researchers for sensor applications due to the structures and properties mentioned above.^{179,348} Considering that pnictogens' electronic

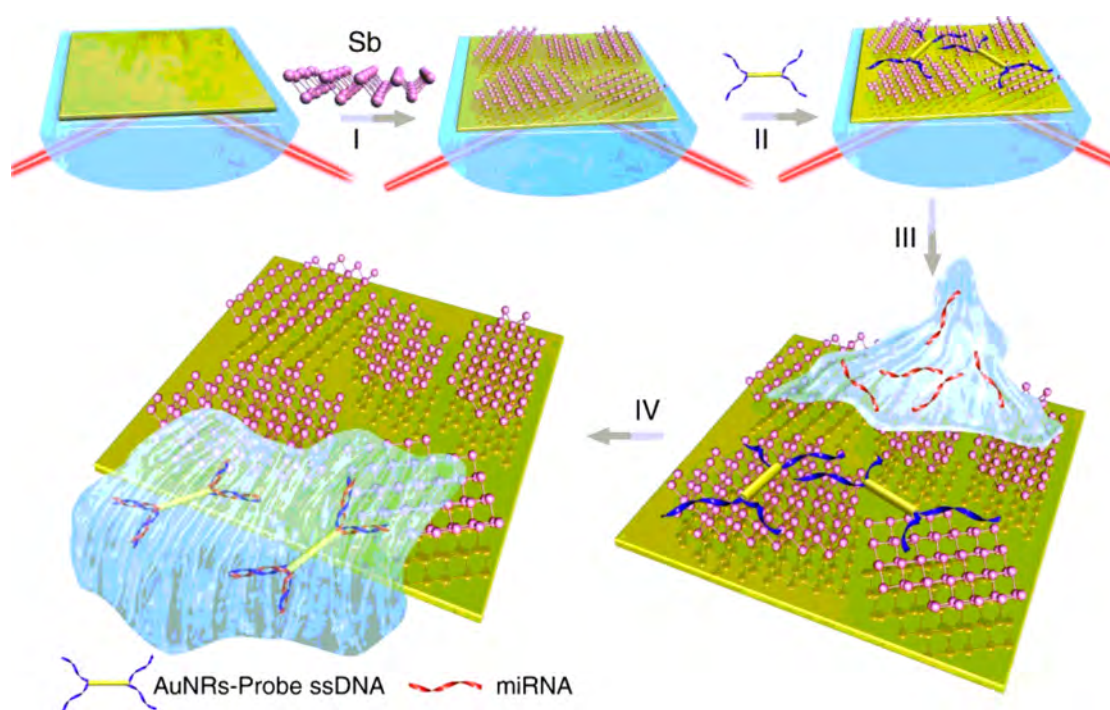


Figure 37. Schematic demonstration of the synthetic process and miRNA detection mechanisms of the antimonene-based system. Reproduced with permission from ref 351. Copyright 2019 Springer Nature.

properties and chemical potentials are sensitive to heteroatom dopants or heterostructures compositions, the interaction of these 2D pnictogens with gaseous molecules or biomolecules will inevitably modulate the conductivity and electrochemical structure.³⁴⁹ Even for the same sensing molecule, the signals would change with the coordinating configurations as well as the environment. Currently, although employing pnictogens for chemical and electronic sensors have made rapid progress, most of the studies are based on DFT calculations, which have laid good theoretical foundations for future exploration. However, more solid evidence obtained from experimental studies are needed before putting Xenes into industrial applications.

4.4.3.1. Biosensors. As a generally accepted biomarker, noncoding microRNA (miRNA) exhibits irregular expression in cancer cells and is therefore usually selected as the target site during treatment. Different 2D material-based nanoplatfoms have all demonstrated sensitive detection of miRNA. Despite broadly investigated fluorescence techniques using dye molecules, conducting molecular-level quantification of miRNA without labeling remains difficult. Employing 2D phosphorene as the fluorescence quenching candidate, our group successfully developed a 2D nanoplatfom for miRNA sensing that linearly responded to miRNA concentrations from 10 to 1000 nM.³⁵⁰ Furthermore, for label-free sensing of miRNA, our group developed a 2D antimonene-based nanosensor using the surface plasma resonance (SPR) technology. However, the existing SPR technique has limited sensitivity to detect genes such as miRNAs. For the higher sensitivity, gold nanorods were employed in the localized SPR technique to amplify optical detection signals, with a detection limit of 10^{-17} M. Simple and accurate detection of highly expressed cancer genes, miRNAs, and ssDNA was realized (Figure 37).³⁵¹

With the development of this new optical genetic detection method, early detection of different cancers is expected to be

achieved, which would significantly reduce the mortality rate of cancer patients by early treatment.

4.4.3.2. Chemical Sensors. Due to pnictogens' uniform and simple structures, several first principle studies have been systematically performed for predicting the possibility of employing these Xenes as specific and highly sensitive gas sensors from the fundamental mechanisms. Previous investigations showed that arsenene, antimonene, and bismuthene all have a special affinity toward nitrogen-containing toxic gases (NO_2 , NH_3 , NO), with great sensitivity.^{352–356} The high sensitivity for detecting these gases originates from the doping configuration of gas molecules onto the Xene surface, which influences the electron density of these Xenes.^{357,251}

Pumera and co-workers synthesized a batch of few-layered arsenene nanosheets *via* the liquid exfoliation approach, which was successfully applied to electrochemical detection of methanol and acetone vapors with high sensitivity (Figure 38A–F).²⁵¹ Based on the electrochemical impedance spectroscopy results shown in Figure 38A, acetone and methanol exhibited different impedance phase spectra from the other organic solvent. At 10 Hz, the phase shift of methanol over arsenene nanosheets was much stronger than for the others (see Figure 38B) and an ultrafast phase change from 0° to 68° within only several seconds (see Figure 38C), indicating that this 2D material is highly sensitive for detecting methanol vapor at such resonance frequency. The same conclusion was drawn from Figure 38D,E that arsenene is a good sensor for acetone at the 0.1 Hz frequency. Further stability examination in Figure 38F suggests that the sensors are stable for at least 3 weeks after continuous measurement without any obvious decay in the signal strength. Besides toxic gases, 2D pnictogens were also reported for effectively detecting phenol based on an enzymatic system. (Figure 38G–I).³⁵⁸ The 2D materials were obtained using shear exfoliation to avoid hydrophilic groups onto the surface that usually appeared for samples prepared using

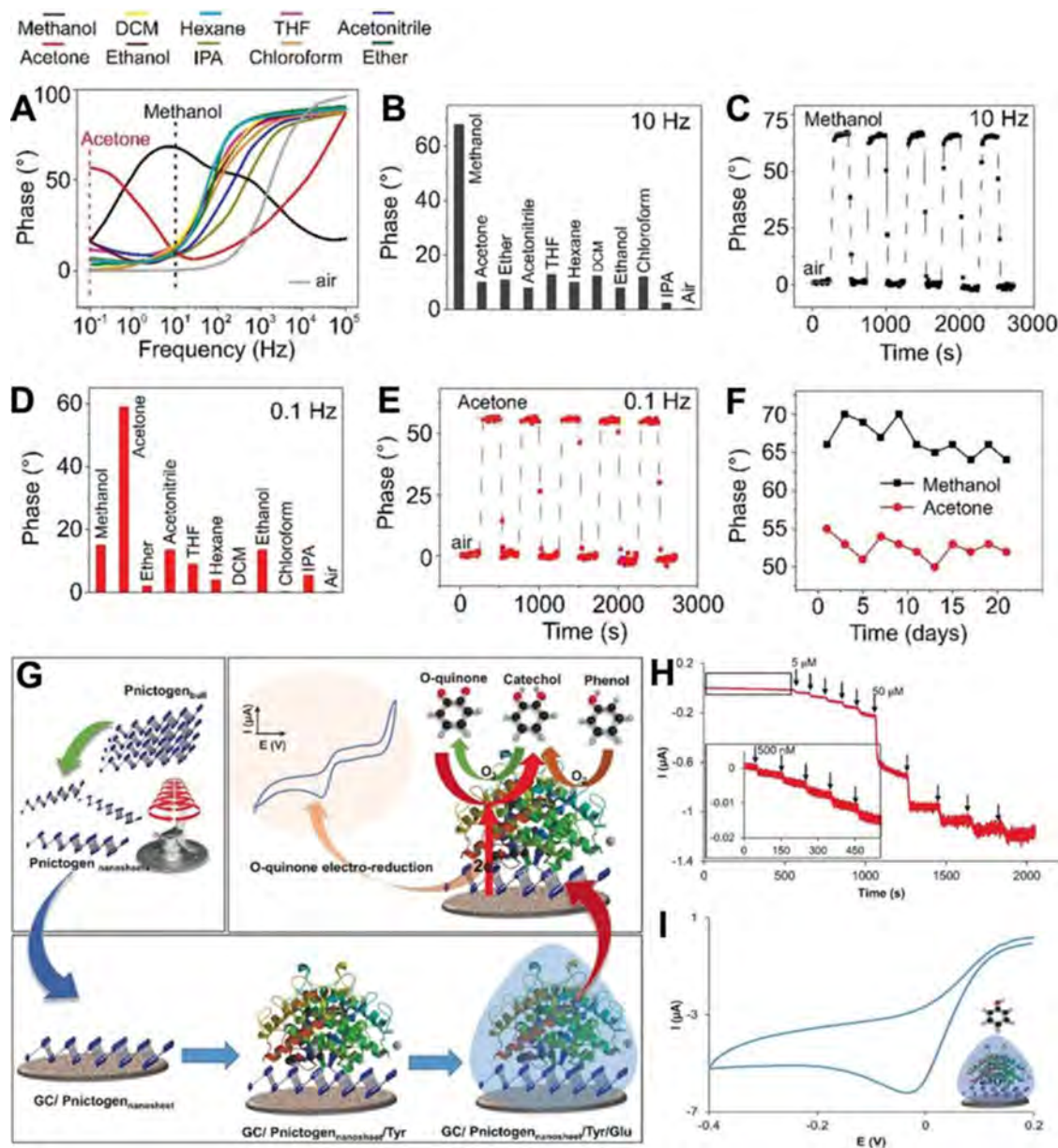


Figure 38. (A–F) The performance of 2D arsenene for sensing vapors: (A) impedance phase spectra in the presence of different organic vapors; (B) impedance phase at 10 Hz under the same treatment as in “A”; (C) phase change at 10 Hz in methanol vapors and in the air for 5 cycles; (D) impedance phase at 0.1 Hz under the same treatment as in “A”; (E) phase change at 0.1 Hz in the presence of acetone vapor and in the air for 5 cycles; (F) stability test for methanol and acetone vapor sensors. Reproduced with permission from ref 251. Copyright 2018 Wiley-VCH Verlag GmbH and Co. KGaA, Weinheim. (G) Schematic of the proposed pnictogens based-biosensor for the detection of phenols: pnictogen nanosheets are obtained *via* shear exfoliation, and the nanosheets-based sensor was constructed by layer stacks of nanosheets, tyrosinase (Tyr) as well as glutaraldehyde (Glu) onto a glassy carbon (GC) electrode; the as-synthesized sensor can detect phenol following the *o*-quinone electron-reduction mechanism. (H) Chronoamperometry response in the presence of different phenol concentrations. (I) Cathodic scan of the antimonene based sensor in phenol. Reproduced with permission from ref 358. Copyright 2018 Wiley-VCH Verlag GmbH and Co. KGaA, Weinheim.

standard liquid exfoliation, which exhibited the most satisfactory sensing results after evaluation in terms of sensitivity, reproducibility, and selectivity. The detection mechanism for phenol originates from electro-reduction of *o*-quinone to catechol over pnictogen nanosheets as depicted in Figure 38G, suggesting that the electro-reduction process preferentially occurs over 2D antimonene among different pnictogens. As shown in Figure 38G (upper right), phenol was converted to catechol by a hydration process after interacting with O₂, and the catechol was oxidized to *o*-quinone by O₂ and tyrosinase. Then the obtained *o*-quinone was electrochemically reduced to

catechol on 2D antimonene, giving a chronoamperometric response. In Figure 38H, the signal response can be observed even at a phenol concentration as low as 500 nM, confirming the high sensitivity of 2D antimonene. The reason for the best performance of antimonene among different pnictogens is illustrated in Figure 38I that the *o*-quinone reduction peak appeared at -0.01 eV, which suggests that the appearance and reduction of *o*-quinone is independent of the electro-oxidation process. Endowed with a facile synthetic approach, enriched unpaired electrons and desirable sensitivity, VA group Xenes are promising for detecting a wide range of chemicals. More

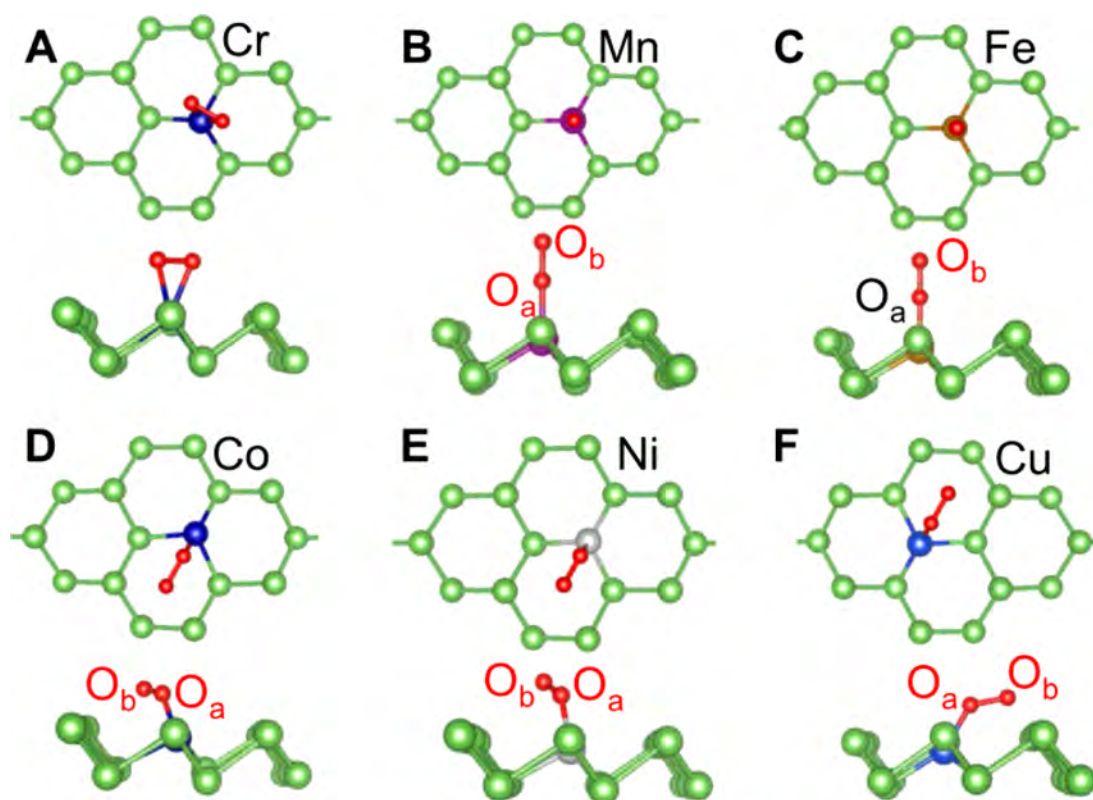


Figure 39. (A–F) Scheme for the most stable oxygen gas adsorption modes on different transition metal-anchored arsenene. Reproduced with permission from ref 333. Copyright 2020 Elsevier, Inc.

importantly, in the field of sensors, the fundamental results are easily transformed into practical products.

Arsenene decorated with heteroatom dopants is promising for sensing applications. Huang and co-workers investigated the adsorption behaviors of O_2 gas in arsenene doped with different transition metals,³³³ and different configurations were obtained after structural optimization based on theoretical calculations from the perspective of both geometric stability and electronic states. As shown in Figure 39, Cr prefers to coordinate with two oxygen atoms, while all the others interact with O_2 molecules *via* a terminal metal–O single bond. Further detailed calculations proved that all metal-doped arsenene absorbed O_2 more strongly than pure arsenene with higher adsorption energies. The enhanced adsorption phenomenon was proposed to result from the interactions between the O_{2p} , metal 3d and As 4d orbitals, making the hybrids of metal species and arsenene promising probes for sensing O_2 . This investigation opens a new window for making the best use of the electrochemical potentials of Xenes by sophisticated tuning of the d orbitals with implemented additional disturbance. Guided by theoretical simulations, various feasible materials, including pure Xenes, heteroatom doped Xenes, and van der Waals heterostructures, can be tested before practical applications in gas sensing.

4.4.4. Tellurene. Although many 2D materials have been reported to be used for sensor devices, there are still some challenges: graphene and most of MXenes lack a bandgap and the sensitivity of TMDs (such as MoS_2) is low, while phosphorene is unstable in air. Comparatively, a NO_2 gas sensor based on tellurene³⁵⁹ has almost all the desirable attributes, that is, an ultralow detection limit (~ 25 ppb), a large detection range, a low baseline noise ($\sim 0.5\%$) (Figure 40A1), and an extraordinary selectivity (Figure 40A2). More-

over, in our recent work,³⁶⁰ NO_2 gas sensors based on liquid-phase exfoliated tellurene NSs possess high linearity of up to 94%, quick response (25 ppb: 83 s; 100 ppb: 26 s), fast recovery time (25 ppb: 458 s; 100 ppb: 290 s) (Figure 40B1, B2), and continuous operation even under high temperature. The sensing mechanism has also been explored, and it is resulted from the electron transfer from tellurene to NO_2 in the interface (Figure 40B3, B4).

4.5. Biomedical Applications

The development of both inorganic and organic nanostructures for imaging, sensing, and targeted delivery of therapeutics has propelled the field of nanomedicine.³⁶¹ This subsection provides examples of biomedical applications of Xenes covered in this review.

4.5.1. Phototherapy. Xenes have aroused increasing interest as theranostic agents used for photothermal imaging (PTI),³⁶² photoacoustic imaging (PAI),³⁶³ and fluorescence imaging (FI)³⁶⁴ as well as for phototherapies (photothermal therapy (PTT) and photodynamic therapy (PDT)).^{175,365–367}

Phototherapy is receiving increasing attention due to its minimal invasion, precise treatment, intelligently controllable doses, lower resistance than chemotherapy, and fewer side effects.³⁶⁸

The introduction of suitable optical materials to construct drug-loading platforms and a combination of traditional therapy with phototherapy might lead to an important advancement in cancer treatment. PTT refers to a therapy that employs a material with photothermal conversion and targeting ability using recognition technology to accumulate in tumor tissue. Upon irradiation by an external light source (generally near-infrared light for deep tissue penetration), local hyperpyrexia can be produced, thus killing cancer cells. In addition to transforming light into heat,

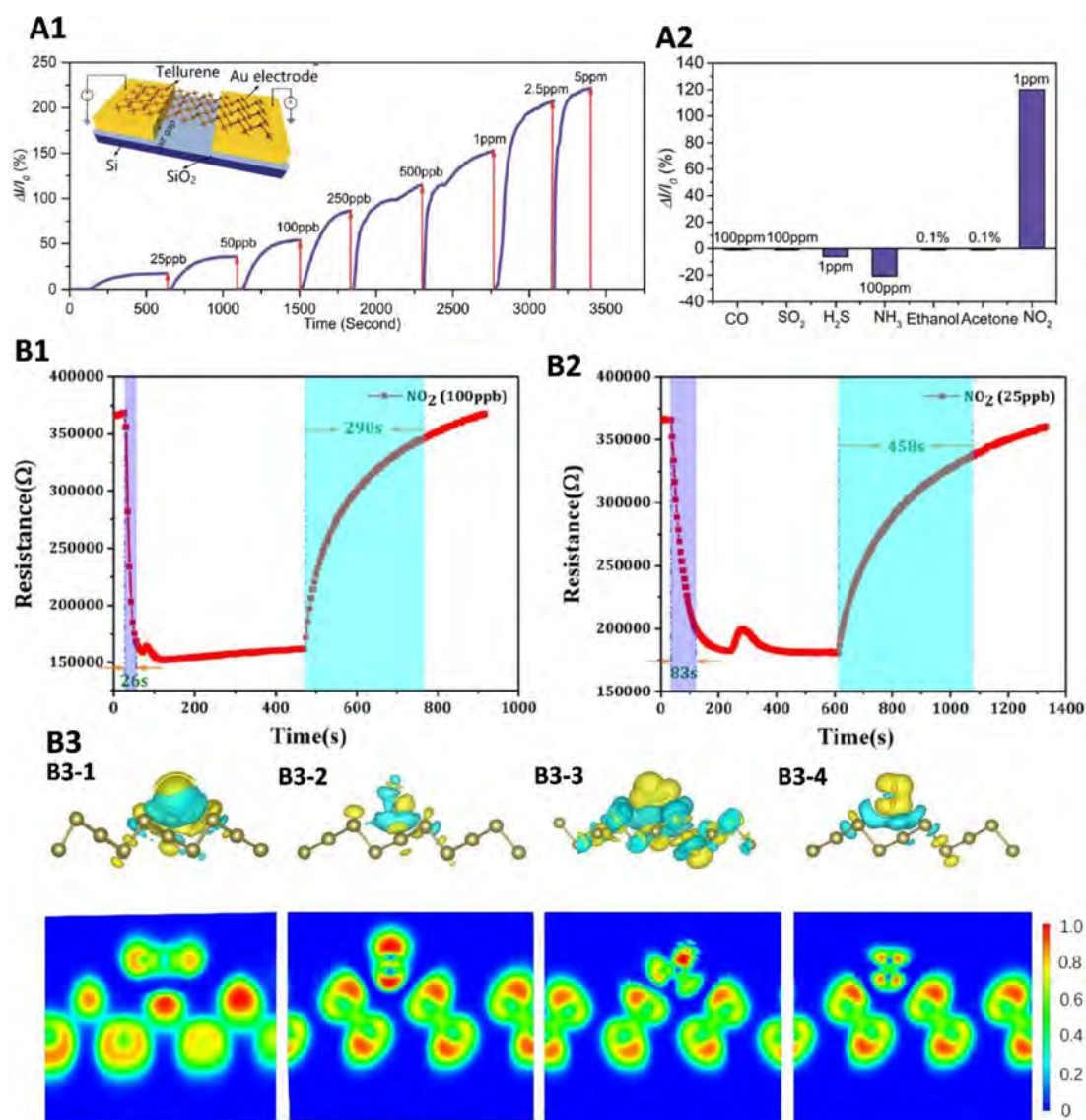


Figure 40. (A1) Concentration/time-dependent NO_2 sensing response of tellurene based gas sensor with inset showing schematic representation of the sensor. (A2) Response of the tellurene sensor toward different kinds of gas. Reproduced with permission from ref 359. Copyright 2019 Royal Society of Chemistry. Response and recovery time of a tellurene sensor under (B1) 100 ppb and (B2) 25 ppb NO_2 ; Pictures of charge density difference (CDD) and electron localization functional (ELF) of (B3-1) CO_2 , (B3-2) N_2 , (B3-3) NO_2 , and (B3-4) O_2 sorption on tellurene. Aquamarine and yellow regions in CDD represent the depletion and accumulation of electrons, respectively. Reproduced from ref 360. Copyright 2020 American Chemical Society.

ideal materials for PTT should also have good biocompatibility and biodegradability, as well as low toxicity.

PDT is a phototherapy that requires photosensitizers and laser activation to deal with tumors. Irradiation of a tumor site using specific wavelengths activates the photosensitizer selectively clustered in the tumor site, inducing a photochemical reaction intended for antitumor effect. Photosensitizers in PDT transfer energy to the surrounding oxygen, generating highly active oxygen species (ROS) such as singlet oxygen, $^1\text{O}_2$. The ROS oxidize the surrounding biomacromolecules to produce cytotoxicity and thus kill tumor cells. Superior to conventional oncology, PDT is more precise and effective with negligible side effects. Traditional PDT has three limitations:

- (1) It is highly limited in the hypoxic environment of tumor cells. Thus, the production of $^1\text{O}_2$ is inefficient and needs to be improved. Further, the $^1\text{O}_2$ molecules cannot move

more than $0.02 \mu\text{m}$ after being generated. Therefore, very high targeting efficiency is required;

- (2) Most commonly used photosensitizers are hydrophobic and lipophilic, resulting in fast aggregation in aqueous solution, which severely restricts their practical use and in vivo applications;
- (3) The wavelength of light employed to generate ROS is usually lower than 700 nm, at which the penetration depth of light into the body is very short, resulting in low photodynamic efficiency. This has greatly limited the clinical application of PDT.

Biocompatible 2D materials provide potential solutions for these limitations. As discussed above, surface modification of hydrophobic 2D Xenes would endow them with good dispersion stability in water. The high surface area of 2D materials offers abundant loading sites for photosensitizers and targeting agents, which are beneficial for targeted therapy. Moreover, many 2D

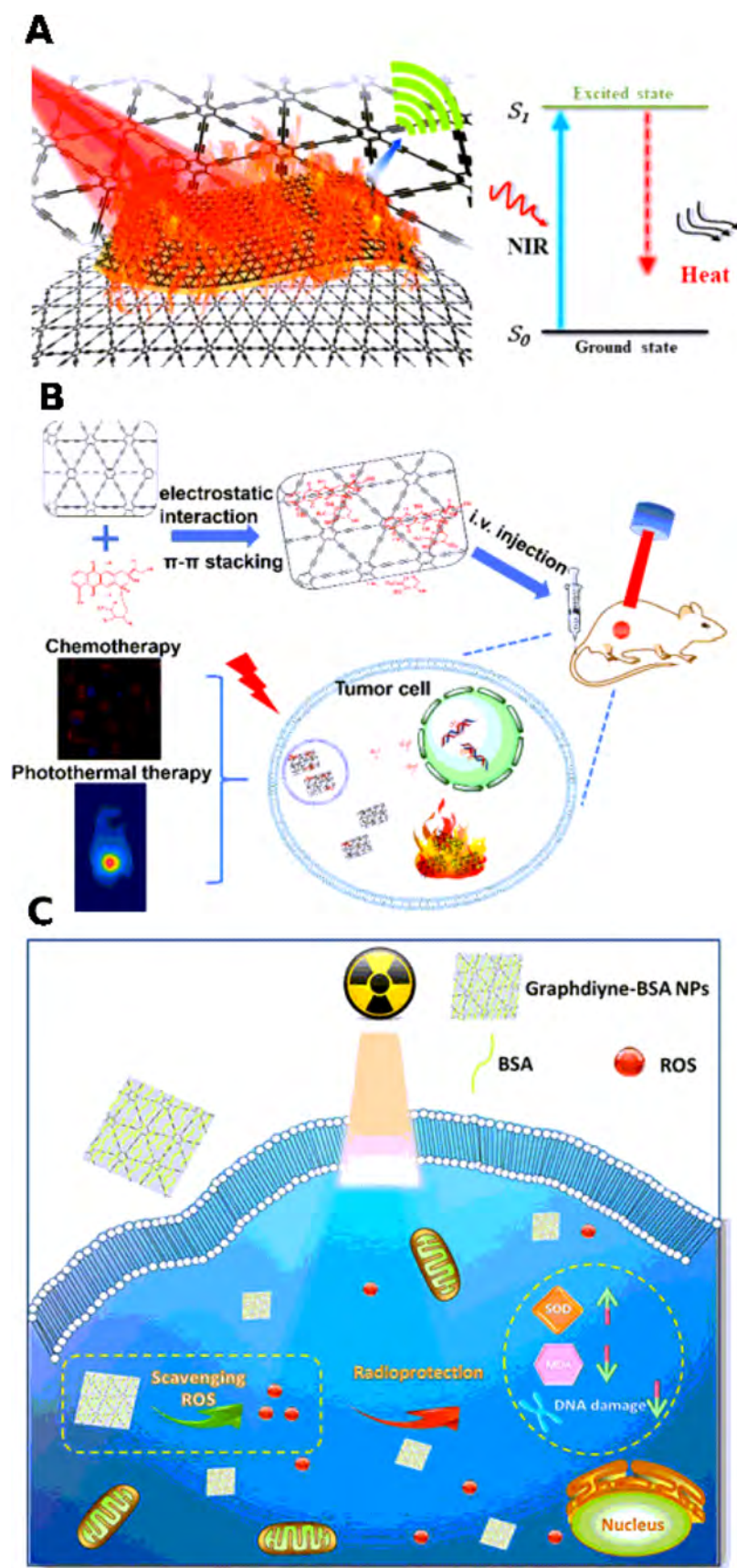


Figure 41. (A) Schematic diagram of the GDY NSs for PAI-guided PTT. Reproduced from ref 101. Copyright 2017 American Chemical Society. (B) Application of GDY NSs in synergistic photothermal-chemotherapy. Reproduced from ref 376. Copyright 2018 American Chemical Society. (C) GDY nanoparticle-based radiation protection for cancer radiotherapy. Reproduced with permission from ref 377. Copyright 2018 American Chemical Society.

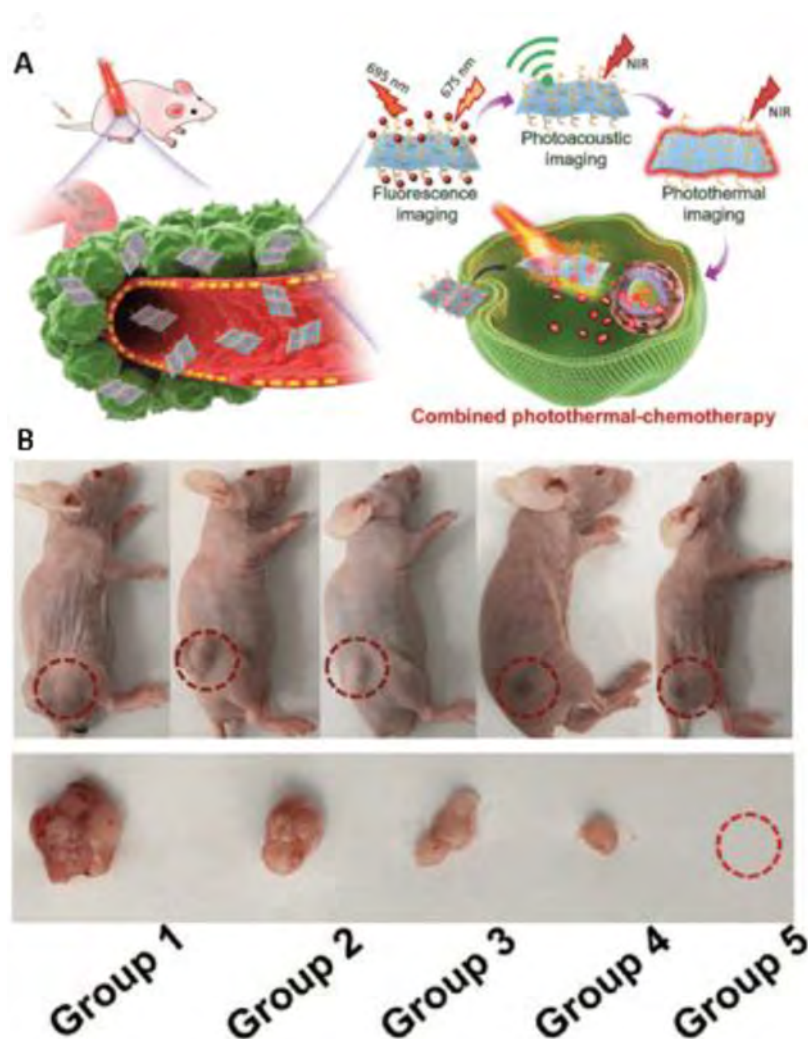


Figure 42. (A) B-PEG/DOX NSs based multimodal imaging-guided cancer therapy. (B) Photographs of representative tumors after 14 days with different treatments (Group 1: treated with saline only, Group 2: treated with DOX alone, Group 3: treated with B-PEG/DOX alone, Group 4: treated with B-PEG NSs under NIR irradiation, and Group 5: treated with B-PEG/DOX NSs under NIR irradiation). Reproduced with permission from ref 378. Copyright 2018 Wiley-VCH Verlag GmbH & Co. KGaA, Weinheim.

material-supported metal species are efficient photocatalysts for splitting water, producing H_2 and O_2 , which could help alleviate hypoxia. Finally, these 2D materials can have remarkable photothermal efficiency as well as drug loading capability for multimodal combination therapy.³⁶⁹ Hypoxia caused by diffusion and perfusion limitations is closely related to tumor development, metastasis, and treatment resistance. Strategies for simultaneously overcoming these two causes of hypoxia to improve cancer treatment efficacy have been lacking. BP has been adopted as a PDT candidate in a number of studies during the past years. In 2015, Xie and co-workers successfully produced a series of BP nanosheets *via* liquid exfoliation and proved BP could perform as a good photosensitizer in converting O_2 to 1O_2 under visible light, with a quantum yield of 0.91.³⁶⁹ Later, the same group found that BP was able to transform H_2O to another reactive oxygen species, $\bullet OH$, under ultraviolet light, suggesting the omnipotent optical behavior of BP.³⁷⁰ However, the photodynamic effect of BP is not obvious under NIR, which is highly appreciated in clinical applications. A more common practice is to anchor another PDT photosensitizers onto BP, forming a hybrid.^{371–374}

The degradable nature of Xenes makes them promising for biomedical applications. The ultralarge specific surface of Xenes enables an extremely high loading efficiency of theranostic molecules.³⁷⁵ Owing to the complex biological environment, surface modifications of biomaterials are usually needed for biomedical applications. First, chemical modification is necessary and important for improving the biocompatibility of inorganic Xenes. Then, the enhanced dispersibility and prolonged blood circulation can be obtained by tuning their surface potential and surface reactivity. Finally, attaching of targeting agents on the surface of Xenes endows the increase of the theranostic efficacy and avoids any side effect to normal organs.

4.5.1.1. GDY. GDY and its derivatives have shown promising potential for biomedical application. The sp-hybridized carbon atoms existing in GDY enhances its ability to remove active oxygen. Recently, Li *et al.* illustrated the application of GDY for PAI and PTT in living mice simultaneously (Figure 41A),¹⁰¹ which has not been reported previously. The photothermal conversion efficiency of GDY was stable and high, which was reported to be 42%. Moreover, GDY possessed an exceptional

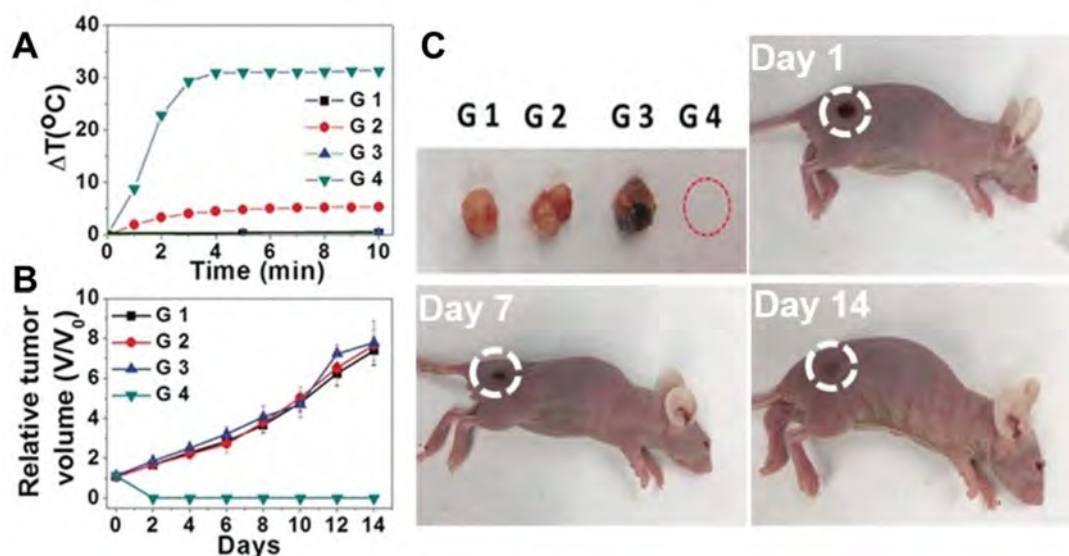


Figure 43. 2D antimonene quantum dots-based photothermal therapy. (A) Relation curve describing the tumor temperature variations with time (G1: saline without irradiation, G2: no material injection under irradiation, G3: antimonene injection without irradiation, and G4: antimonene injection with irradiation). (B) Relative tumor volumes change with the number of days. (C) Images for tumors at different days. Reproduced with permission from ref 384. Copyright 2017 Wiley-VCH Verlag GmbH and Co. KGaA, Weinheim.

photoacoustic (PA) response. Their work broadens the 2D GDY application for cancer treatment.

Originated from the large specific surface of GDY and its strong electrostatic interaction with drug molecules, GDY NSs were also used for delivering drugs (Figure 41B).³⁷⁶ Jin *et al.* used GDY NSs to deliver doxorubicin (DOX) for synergistic photothermal/chemotherapy in living mice. It showed an excellent tumor suppression effect under 808 nm laser irradiation. It was due to the high efficiency of DOX loading on GDY and a high photothermal conversion efficiency.

GDY is also an emerging candidate as a radiation protector. Most recently, a GDY containing composite, bovine serum albumin (BSA)-modified GDY was employed to protect normal tissues from radiation (Figure 41C).³⁷⁷ The BSA-modified GDY nanoparticles possess a favorable ROS scavenging ability in ROS scavenging systems. Furthermore, they could also efficiently decrease cell damage under radiation *in vitro* and *in vivo*.

4.5.1.2. Borophene. Borophene has been shown to be promising for tumor imaging and cancer therapy.³² Ji *et al.* reported a drug delivery platform based on borophene NSs (Figure 42A)³⁷⁸ with a high drug-loading capacity. Under NIR light, its photothermal conversion efficiency reached 42.5%. It could also realize multiple imaging modalities, including photothermal, photoacoustic, and fluorescence imaging. This borophene based drug delivery system accumulates in tumor sites precisely and shows an excellent cancer therapy efficiency with the tumor ablated completely (Figure 42B).

4.3.1.3. Group V: Arsenene, Antimonene, and Bismuthene. Ever since the reports of using BP as an efficient photothermal agent,^{379–383} Xenex-based PTT has become a research frontier, and various Xenexes such as borophene and antimonene have shown admirable potential for antibacteria and anticancer applications. Among them, antimonene stands out due to its high biocompatibility and photothermal conversion efficacy (PTCE). Tao *et al.* designed a 2D antimonene quantum dots-based photothermal agent, as shown in Figure 43. These quantum dots were first obtained *via* the sonic liquid exfoliation method, followed by surface modification with PEG to increase

the stability against water and oxygen and its biosafety. Measured under biological medium, this PTT agent is found to have a high PTCE value of 45.5%, outperforming several other nanomaterials-based photothermal agents such as black phosphorus, graphene, and Au. More encouragingly, the PEG-modified quantum dots degraded rapidly under irradiation of near-infrared light (808 nm). The PEG-coated antimonene quantum dots are effective for cancer treatment *in vitro* and *in vivo* experiments.³⁸⁴ This work has attracted tremendous attention because it expands the range of photothermal agents to other heavier pnictogens, inspiring future investigations of these Xenexes and explorations for BP alternatives with better stability and biocompatibility.

With the distinct features of 2D structures, including large surface area, tunable surface, and satisfactory PTCE, the pnictogens have also been used as theranostic agents. These Xenexes have the potential for multimodal imaging (PTI, PAI, *etc.*) and multifunctional therapy (chemo-therapy, PTT, PDT, *etc.*). In 2017, Li and co-workers successfully prepared Bi nanoparticles (NPs) by rationally reducing a Bi precursor with oleylamine and applied them to the CT/PAI dual-modal imaging-guided PTT/radiotherapy synergistic therapy (Figure 44A–F).³⁸⁵ Before the test, the Bi NPs were modified with PEG and tumor-homing peptide LyP-1 (Figure 44A), forming NPs with an average size between 3 and 4 nm (see Figure 44B) and good tumor targeting ability as well as enhanced biocompatibility. Bi NPs have demonstrated strong adsorption within the second near-infrared window of increased biological transparency (NIR-II, 1000–1350 nm), and absorb ionizing X-ray radiation, which accounts for the excellent ability to apply in the multimodal optical as well as CT imaging using Bi nuclei. Figure 44C proves that the *in vitro* Hounsfield units (HU value) of Bi NPs showed a much higher slope than iohexol, demonstrating prominent improvement of CT imaging. Figure 44D illustrates that Bi NPs are promising for PA imaging enhancement. The intrinsically high PTCE and heavy molar weight are beneficial for highly effective synergistic PTT/radiotherapy (see Figure 44E,F). Besides, the report demonstrated that NPs with low

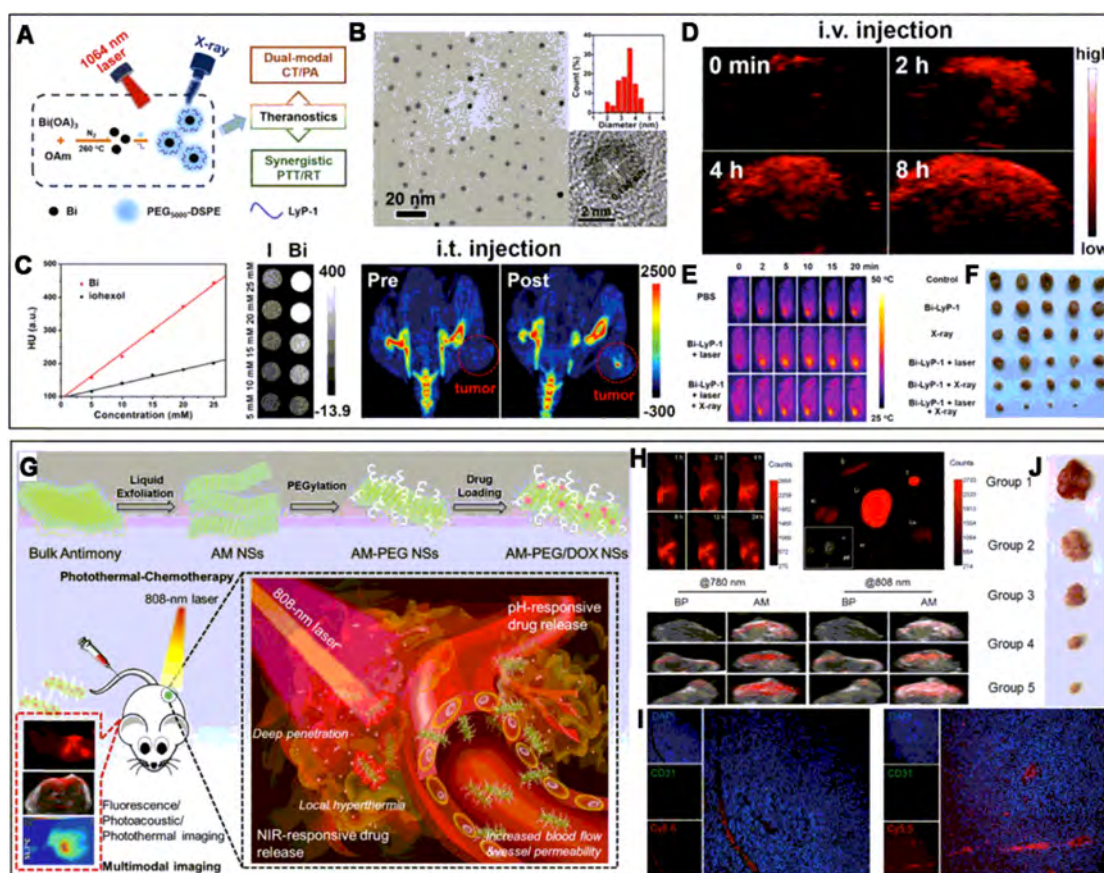


Figure 44. (A–F) Bismuthene nanosheet-based PTT/radiotherapy: (A) schematic illustration of synthesis and applications of bismuthene nanoparticles (Bi NPs); (B) TEM images of Bi NPs; (C) Hounsfield units' values of Bi NPs and iohexol at different concentrations, the X-ray CT images of Bi NPs and tumors; (D) PA images of tumors before and after Bi NPs injection at 700 nm; (E) IR imaging of tumor-bearing mice exposed to irradiation; (F) photos of tumors under different treatments after 2 weeks. Reproduced from ref 385. Copyright 2017 American Chemical Society. (G–J) Antimonene (AM)-based chemo-PTT platform: (G) Schematic illustration of preparation and multifunctioning of therapeutics for treating cancer. (H) Fluorescence imaging of tumor-bearing mice (upper left) and tumors (upper right) and ultrasound and PA imaging of tumors (lower) after injecting antimonene. (I) Fluorescence images of tumors after injecting Cy5.5 modified AM nanosheets. (J) Photograph of tumors in different groups after 14 d treatment (i.v. injection of saline (group 1), DOX (group 2), AM nanosheets/DOX (group 3 and 5), and AM nanosheets (group 4); for group 4 and 5, a NIR (808 nm) laser was used to illuminate for 10 min). Reproduced with permission from ref 386. Copyright 2018 Wiley-VCH Verlag GmbH and Co. KGaA, Weinheim.

toxicity could be quickly and completely cleared. This work offers a promising safe, and multifunctional Bi nano therapeutics platform. In addition to Bi, 2D antimonene is another potential candidate for a theranostic agent due to the above-discussed PTCE and PTT performance. By the liquid exfoliation method, Zhang *et al.*, in 2018, obtained uniformly distributed ultrathin Sb nanosheets (Figure 44G–J).³⁸⁶ Antimonene cannot absorb light as strongly as Bi, and the atomic weight of Sb is lower than that of Bi, which inhibits multimodal imaging and therapy based on the Sb Xene itself. However, a high surface area enables this 2D material to support high loading of fluorescence imaging agents (e.g., Cy5.5) and chemotherapeutic drugs (e.g., DOX), and this hybrid functions as a potent cancer theranostic agent (Figure 44G, H). The researchers found that the Sb nanosheets shared a similar PTCE with the Sb quantum dots mentioned above (41.8% vs 45%), with an extremely high DOX loading capacity of 150%. Interestingly, a smart and controllable drug release is realized by triggering the hybrids' microenvironmental change, and the system is sensitive to both pH and temperature. Noteworthy, antimonene-based nanoplateforms are reported to preferably accumulate in the tumor site, leading to activation by deep penetrating NIR irradiation. Guided by fluorescence

imaging/PAI and PTI (Figure 44H,I), the Sb nanosheet-supported DOX nanoplateform exhibited satisfactory performance in inhibiting the growth of tumor in vivo (Figure 44J), while no apparent side effects were detected throughout the whole treatment process.³⁸⁷

With large surface area and tunable bandgaps, the three pnictogens discussed in this review are also promising for PDT applications, despite the fact that PDT studies on them are lacking. As mentioned above, antimonene has demonstrated exceptional PTT potential for cancer treatment. Intrinsically, with similar chemical properties to BP, antimonene is also worth testing for PDT application. Lu *et al.* developed a type of Sb-based nanoparticles with a size of ~55 nm to overcome the poor stability issue of antimonene NS, which was named cancer cell membrane-camouflaged nanoparticles (CmNPs). As shown in Figure 45A, the stability and the targeting effect toward cancer cells are prominently enhanced compared to Sb nanosheets. Also, this NP system shows promise for multimodal imaging and, more importantly, phototherapy. Specifically, benefiting from the outstanding PTT behavior, the Sb-based nanoparticles showed a good linear relationship of photoacoustic signal-sample concentration, which leads to photothermal/photo-

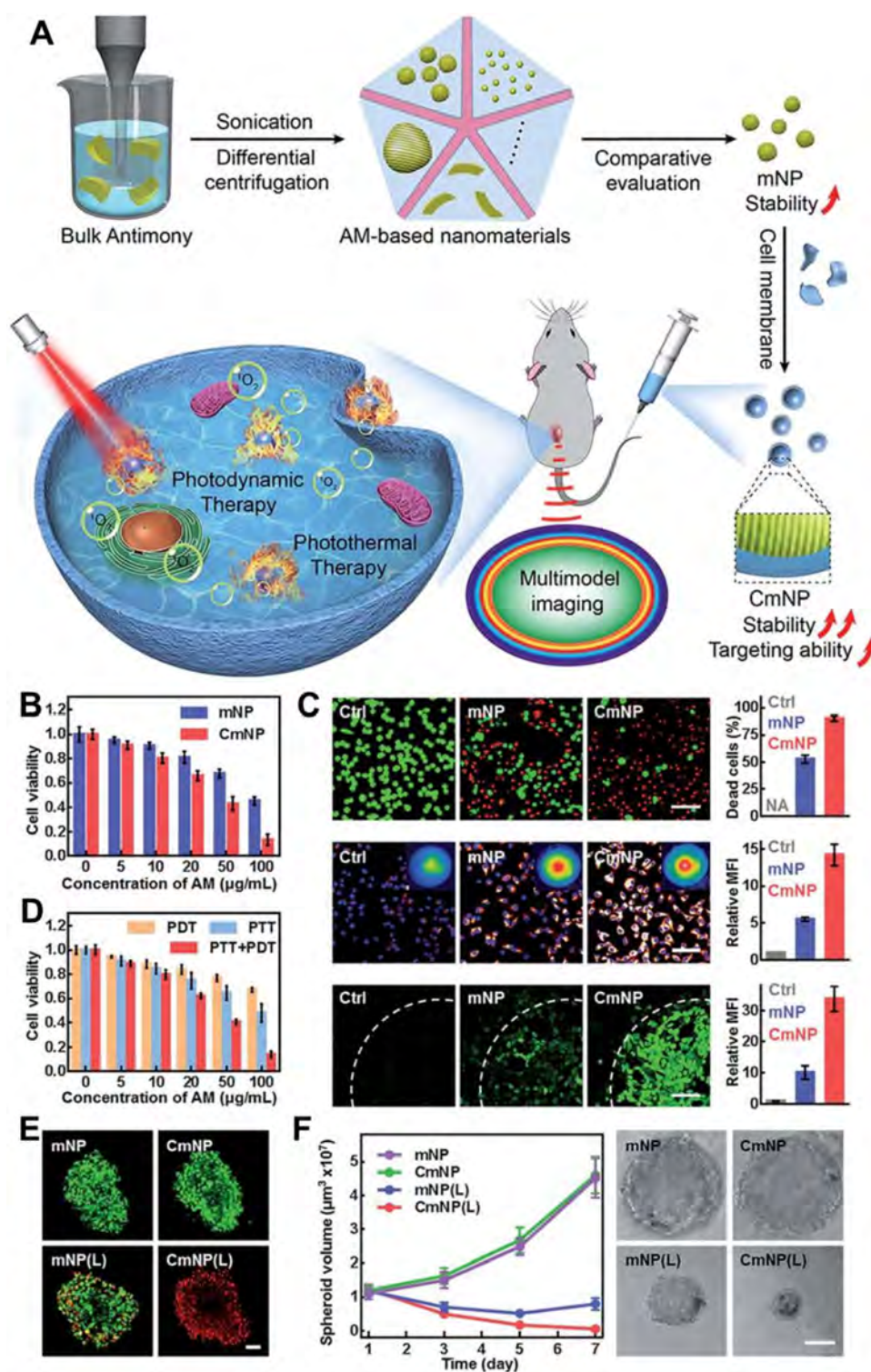


Figure 45. (A) Schematic description of the preparation of cell membrane-camouflaged antimonene nanoparticles (CmNPs) as well as their application; (B–F) *In vitro* experimental results of phototherapy using CmNPs: (B) Cell viabilities after interacting with mNPs (without camouflage) and CmNPs; (C) fluorescence of stained cells treated with CmNPs, (green: live cells, red: dead cells) (upper), immunofluorescence analysis of cells labeled with HSP90 antibody after laser irradiation (glow: HSP90, blue: nuclei) (middle), and intracellular $^1\text{O}_2$ generation (lower); (D) cell viability after PDT, PTT and combination therapy; (E) fluorescent staining of cells before (upper) and after (lower) phototreatment (green fluorescent cells are alive); (F) time-dependent change of multicellular tumor spheroid sizes and corresponding photographs after 7 days' treatment. Reproduced with permission from ref 388. Copyright 2019 Royal Society of Chemistry.

acoustic bimodal imaging. Further, the CmNPs are effective for type-II PDT, converting O_2 to $^1\text{O}_2$ under 808 nm irradiation. Figure 45B shows both CmNPs and antimonene NPs without camouflage (mNP) are good phototherapy agents, and that

CmNPs are more effective due to higher stability and targeting capacity. Figure 45C provides solid evidence for both PTT and PDT resulting from CmNPs. In Figure 45D, both PTT and PDT are consolidated with simultaneous experiments. To confirm

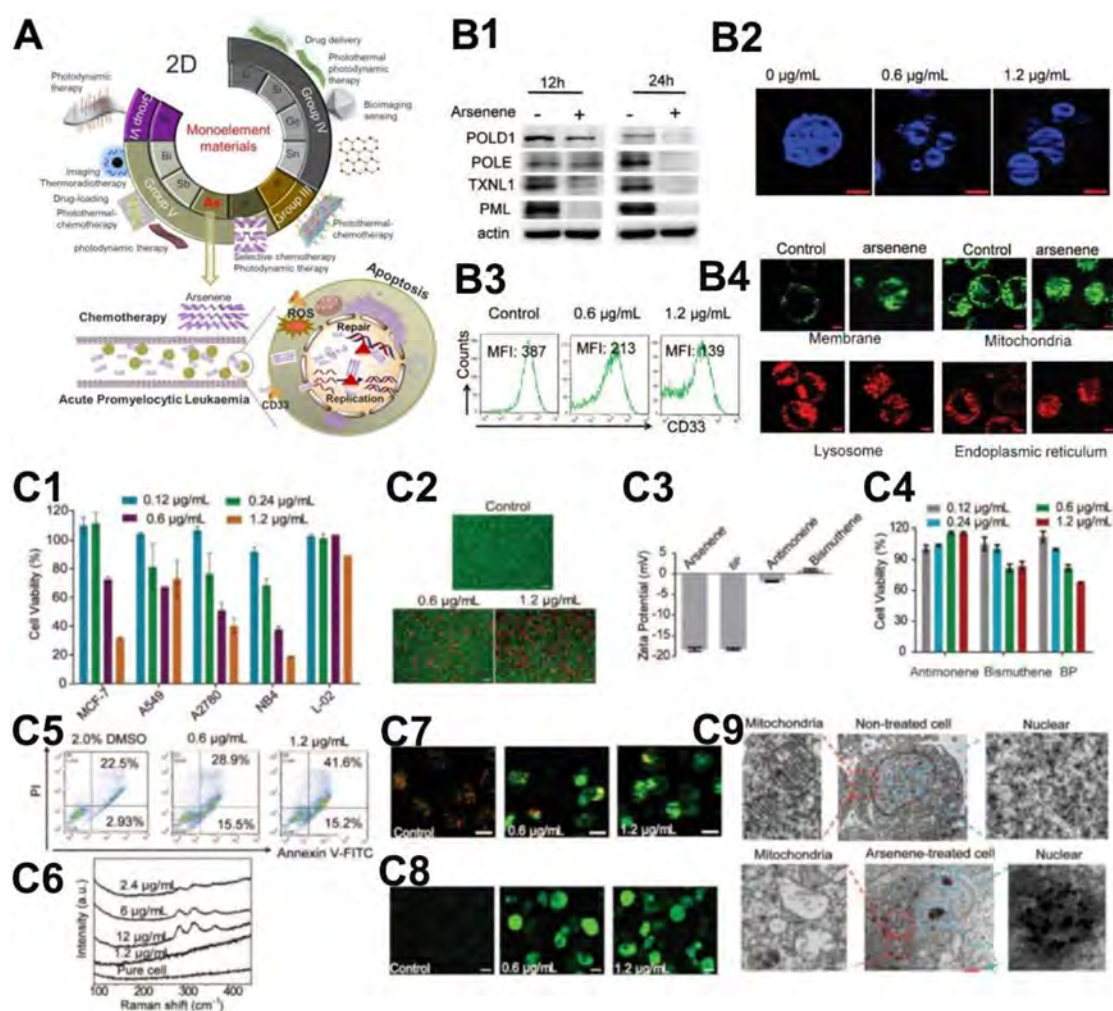


Figure 46. (A) Overview of Xenics for biomedicines and a brief introduction of applying arsenene in acute promyelocytic leukemia (APL). (B) Effect of arsenene nanosheets on cellular proteins and interaction between arsenene and proteins in NB4 cells: (B1) Western blot of differentially expressed nuclear proteins in cells with and without arsenene treatment, (B2) images of the NB4 cell nucleus with and without arsenene treatment, (B3) immunofluorescence detection of CD33 in arsenene-treated NB4 cells by flow cytometry, (B4) images of organelles treated with arsenene. (C) Anticancer activity of arsenene: (C1) Cell viability after treating with arsenene, (C2) fluorescence images of NB4 cells stained with Calcein-AM (live cells, green), and PI (dead cells, red), scale bars: 50 mm, (C3) zeta potential of different Xenics, (C4) cell viability after interacting with antimonene, bismuthene, and BP, (C5) detection of apoptosis detected by flow cytometry, (C6) Raman spectra of arsenene in NB4 cells, (C7) measurement of mitochondrial membrane potential *via* fluorescence after JC-1 staining (red: hyperpolarization; green: depolarization), (C8) fluorescence detection of intracellular ROS generation after DCFH-DA staining, and (C9) TEM images of NB4 cells after treatment. Reproduced with permission from ref 389. Copyright 2020 Wiley-VCH Verlag GmbH and Co. KGaA, Weinheim.

this conclusion one step further, staining and size change measurement of multicellular tumor spheroids after treatment were performed with the same results as above (see Figure 45E,F). This bifunctional phototherapy using the Sb-based system with higher stability and superior efficiency under NIR compared to BP clarified the future development of VA group Xenics for cancer treatment.³⁸⁸

Guo's group recently found that arsenene is a highly efficient PDT candidate for potentially treating acute promyelocytic leukemia (APL).³⁸⁹ 2D arsenene has rarely been employed for biomedical applications due to the toxicity of As³⁺. Excitingly, it has been reported that As nanosheets are less toxic, it suggests the possibility of applying arsenene to biomedicines.³⁹⁰ Figure 46A provides an overview of how arsenene is effective in PDT for APL. Western blot results (see Figure 46B1) suggest that arsenene promotes the degradation of proteins, and the fluorescence cellular imaging (see Figure 46B2) manifested that arsenene damaged the nuclei. Figure 46B3,4 indicates that

arsenene deals with NB4 cells *via* interfering with the cell surface recognition by glycoprotein CD33. Figure 46C provides more details relating to the functioning mechanisms. During the process, arsenene nanosheets were prepared *via* a liquid exfoliation approach, with a zeta potential (−18.0 mV) much higher than bismuthene (0.921 mV) and antimonene (−1.78 mV), which usually leads to better dispersion and easier uptake by cells (see Figure 46C3). Cell viability tests demonstrated that 2D Xenics with a higher zeta potential tend to be more toxic for cancer cells and NB4 cells, but all of the Xenics showed ignorable toxicity toward the normal L-02 cells (see Figure 46C1,2,4). Mechanistic study using flow cytometry Figure 46C5 indicates that 41.6% of cells undergo late apoptosis and Figure 46C7 suggests early apoptosis also exists with the mitochondria depolarization evidence. In addition, the Raman spectra of arsenene in NB4 cells proved that oxidation of low-valence As occurs (see Figure 46C6). Oxidized As leads to overproduction of ROS, as observed in the fluorescence images of NB4 cells

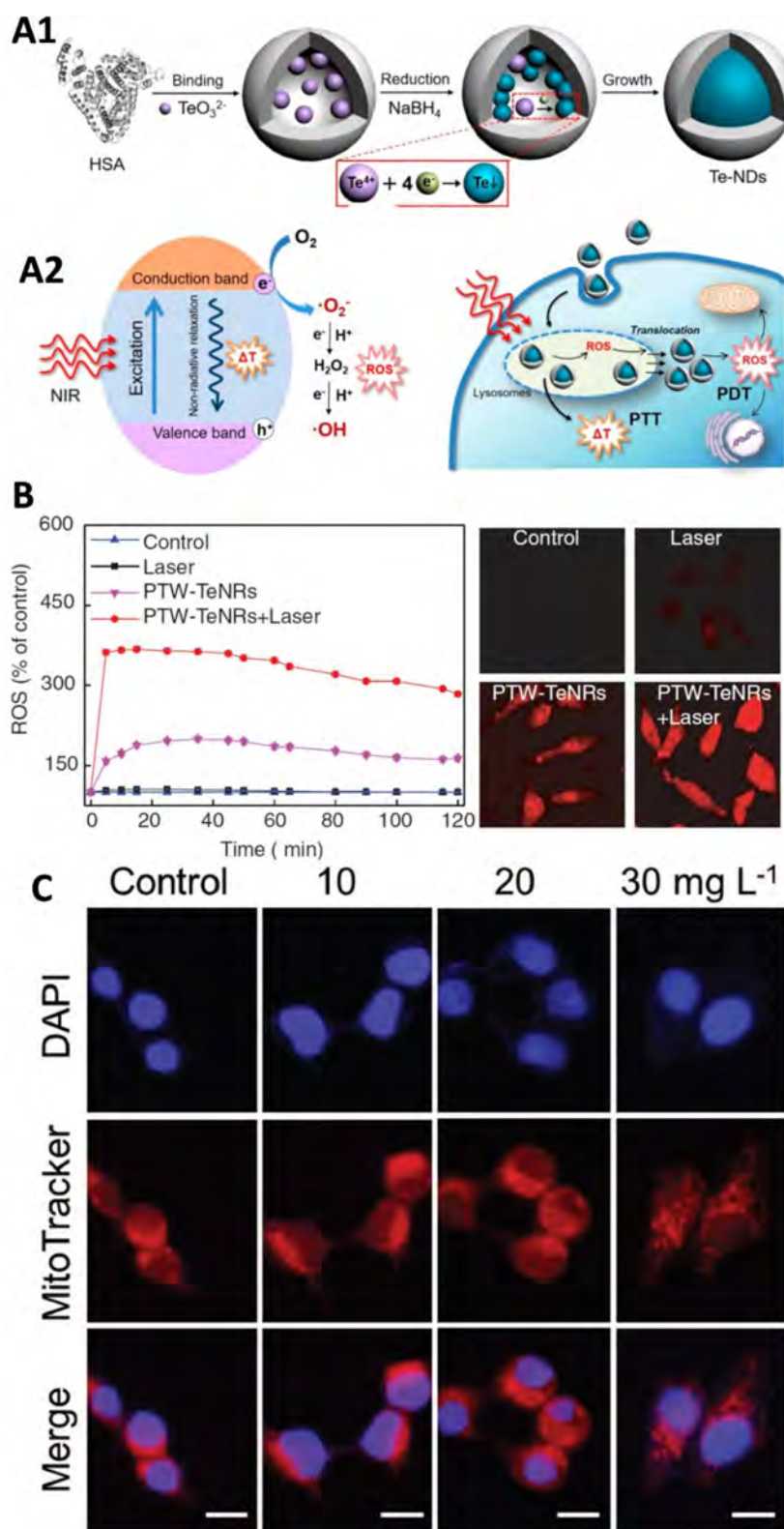


Figure 47. (A1) Schematic diagram of Te nanodots synthesis process through an albumin nanoreactor. (A2) Photoheat and photo-ROS conversion mechanisms of Te nanodots. Reproduced from ref 393. Copyright 2017 American Chemical Society. (B) Laser-induced excessive ROS generation of Te nanorods quantified by the fluorescent intensity. Reproduced with permission from ref 394. Copyright 2017 Wiley-VCH Verlag GmbH & Co. KGaA, Weinheim. (C) Mitochondrial dysfunction of cells when exposed to Te nanoneedles. Reproduced with permission from ref 391. Copyright 2018 Wiley-VCH Verlag GmbH & Co. KGaA, Weinheim.

staining with dichlorofluorescein (see Figure 46C8) that strong green signals appear. ROS generation and gradual depolarization of mitochondrial membrane potential, contribute to apoptosis

and inhibition of NB4 cells, as depicted in Figure 46C9. To further dig into the apoptosis process, binding proteins with As were investigated, suggesting that arsenene would affect the

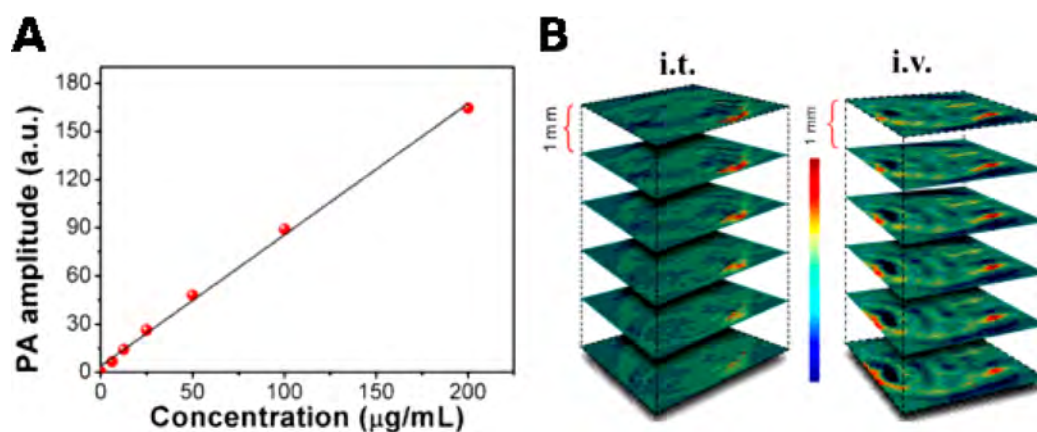


Figure 48. (A) Photoacoustic amplitudes at different concentrations of GDY; (B) PA images of the tumor after intratumoral (i.t.) and intravenous (i.v.) administration of GDY. Reproduced from ref 101. Copyright 2017 American Chemical Society.

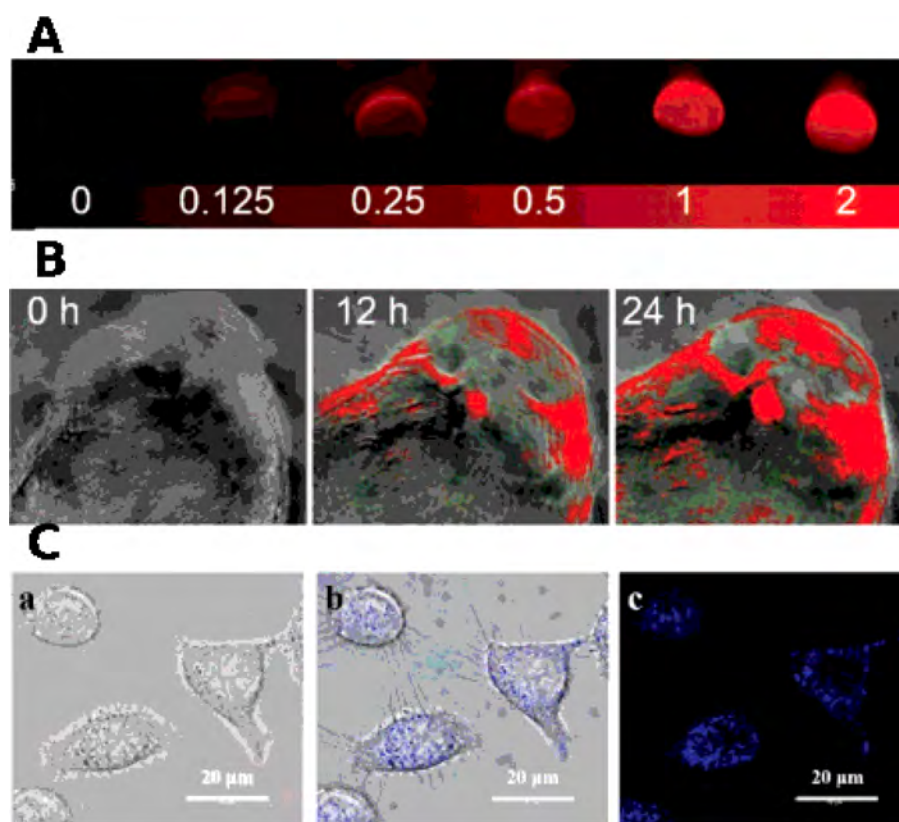


Figure 49. (A) Concentration-dependent in vitro photoacoustic images of PEGylated borophene NSs. (B) PA images of the tumor site at various times after the injection of borophene NSs. Reproduced with permission from ref 378. Copyright 2018 Wiley-VCH Verlag GmbH & Co. KGaA, Weinheim. (C) Bright-field (a), fluorescence (c), and their overlay (b) images of HeLa cells when incubated with borophene NSs. Reproduced with permission from ref 396. Copyright The Royal Society of Chemistry 2020.

pyrimidine metabolism, DNA replication and damage nuclei, which altogether contribute to cell apoptosis.

These exciting results depict a bright future of 2D Xenes in biomedicine, but we have to admit that the investigations on these three Xenes are still in infancy. Although preliminary results have been performed to suggest the potential of Xenes from both experiments and theoretical calculations, the current efforts of researchers are usually focused on material preparation and initial treatment evaluation. With outstanding optical properties, high drug loading capacity, and biocompatibility, more efforts are required to exploit the vast potential of these Xenes, which offers a library for different disease treatments.

4.3.1.4. Tellurene. Weakening cancer cells' antioxidant defense and ROS generation are two mechanisms of anticancer activity of organotellurium compounds and Te nanomaterials.^{391,392} Yang *et al.* introduced well-defined bifunctional Te nanodots using hollow albumin nanoreactor for photoinduced synergistic tumor therapy (Figure 47A1).³⁹³ Upon NIR light irradiation, Te nanodots can lead to efficient photothermal conversion, as well as the production of ROS *via* a type-I photodynamic mechanism, thereby resulting in simultaneous PDT and PTT (Figure 47A2). Huang *et al.* demonstrate a simultaneous chemo-photothermal combination tumor therapy using Te nanorods coated with a polysaccharide-protein

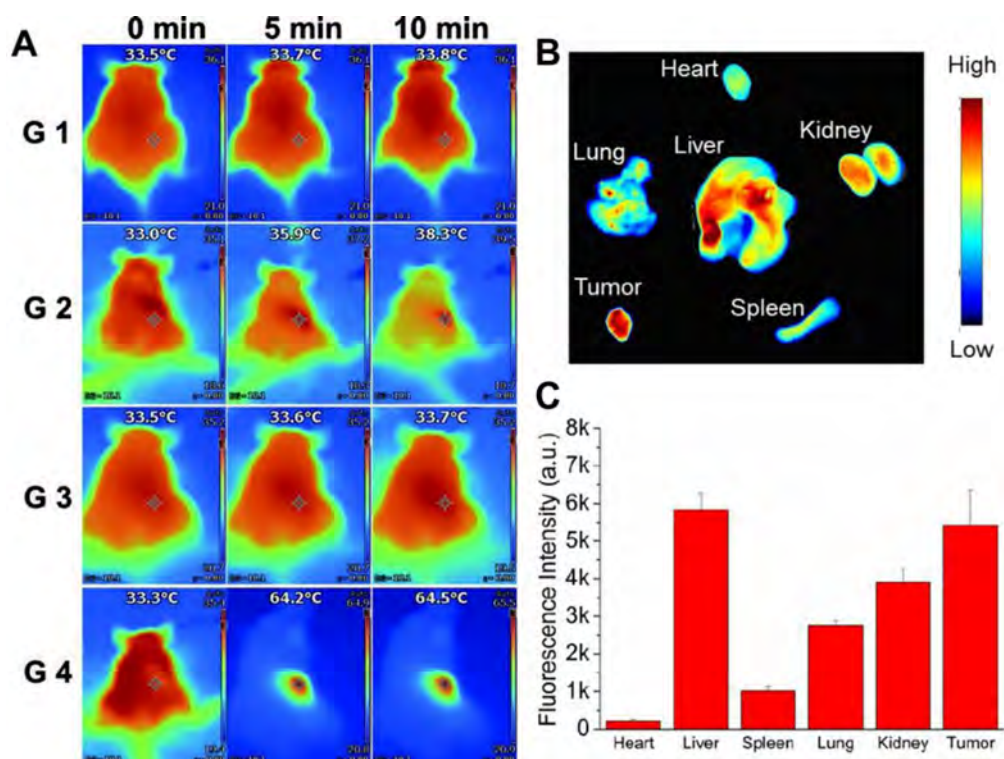


Figure 50. (A) Infrared imaging of tumor-bearing mice with and without 808 nm laser irradiation (G1: saline without irradiation, G2: no material injection under irradiation, G3: antimonene injection without irradiation, and G4: antimonene injection with irradiation). (B) NIR bioimaging of major organs and tumors after 12 h. (C) Biodistribution of materials in nude mice measured by average fluorescence signals based on (B). Reproduced with permission from ref 384. Copyright 2017 Wiley-VCH Verlag GmbH and Co. KGaA, Weinheim.

complex (PTW-TeNRs),³⁹⁴ which shows a high photothermal conversion efficiency based on strong NIR absorbance. Through further induction of ROS (Figure 47B), highly efficient tumor cell killing can be obtained. The ROS production was also found by Lin *et al.*,³⁹⁵ who followed liquid exfoliation synthesis of 2D Te NSs.³⁸ Furthermore, the Te NSs show high photoacoustic imaging ability due to their strong NIR absorbance, which can be designed for photoacoustic imaging-guided PDT.

To prepare Te nanomaterials with high NIR absorption remains a challenge. Blue Te nanoneedles can be obtained through a reduction reaction with a biocompatible size and strong NIR absorbance.³⁹¹ Compared to purple Te nanomaterials, blue Te nanoneedles show more efficient photothermal conversion and laser-induced antioxidative activity in free radicals scavenging. These blue nanoneedles show mitochondrial dysfunction-induced anticancer activity toward different cell-lines (Figure 47C). Furthermore, the blue Te nanoneedles can act as photoacoustic agents. Taken together, image-guided synergistic thermo-chemotherapy can be obtained by blue Te nanoneedles.

4.5.2. Bioimaging. **4.5.2.1. GDY.** Photoacoustic imaging (PAI) provides higher spatial resolution than ultrasonic imaging and larger tissue penetration depth than optical imaging. Li *et al.* investigated the photoacoustic signal intensity of the PEGylated GDY in the NIR region.¹⁰¹ The photoacoustic intensity shows a linear relationship with the concentration (Figure 48A). Figure 48B shows the three-dimensional scanned in vivo PAI images. There existed a clear photoacoustic (PA) signal at the tumor site after intratumoral injection of the PEGylated GDY. Two hours after intravenous injection of PEGylated GDY, the photoacoustic signal started to appear at the tumor site and reached

the strongest signal at 12 h. This also shows a high tumor-targeting efficacy of PEGylated GDY.

4.5.2.2. Borophene. The photothermal effect of PEGylated borophene NSs has been shown, which also makes them potential as PA agents.³⁷⁸ Figure 49A shows a concentration-dependent PA signal at 780 nm with good linearity. For in vivo PA imaging investigation, PEGylated borophene NSs were intravenously (i.v.) injected in the tumor-bearing mice. Then the PA signal was measured periodically. It increased dramatically at the tumor site after 12 h of intravenous injection of PEGylated borophene NSs, which was maintained even at 24 h post-injection (Figure 49B). It demonstrated that PEGylated borophene NSs could be used as PA agents for PAI-guided therapy.

Moreover, borophene showed the potential as a fluorescence imaging agent. First, the 2D ultrathin borophene NSs with a defect nanolayer can be fabricated effectively *via* liquid-phase exfoliation with modification.³⁹⁶ Blue fluorescence characteristics were observed in the as-prepared ultrathin borophene NSs, which had a quantum yield of 10.6%. It was originated from the defective layer with the quantum confinement effect. The ultrathin borophene NSs were then used as a fluorescent probe for cellular bioimaging (Figure 49C).

4.5.2.3. Group VA: Arsenene, Antimonene, and Bismuthene. Apart from serving as biosensors and cancer treatment candidates, Xenes consisting of group VA elements also have potentials for disease diagnosis and targeting identification *via* various imaging types.

4.5.2.3.1. Photothermal Imaging and Photoacoustic Imaging. Compared to optical imaging, PTI and PAI prominently enhanced the imaging depth.^{397,398} As discussed above, antimonene, existing in nanoscale form, shows high

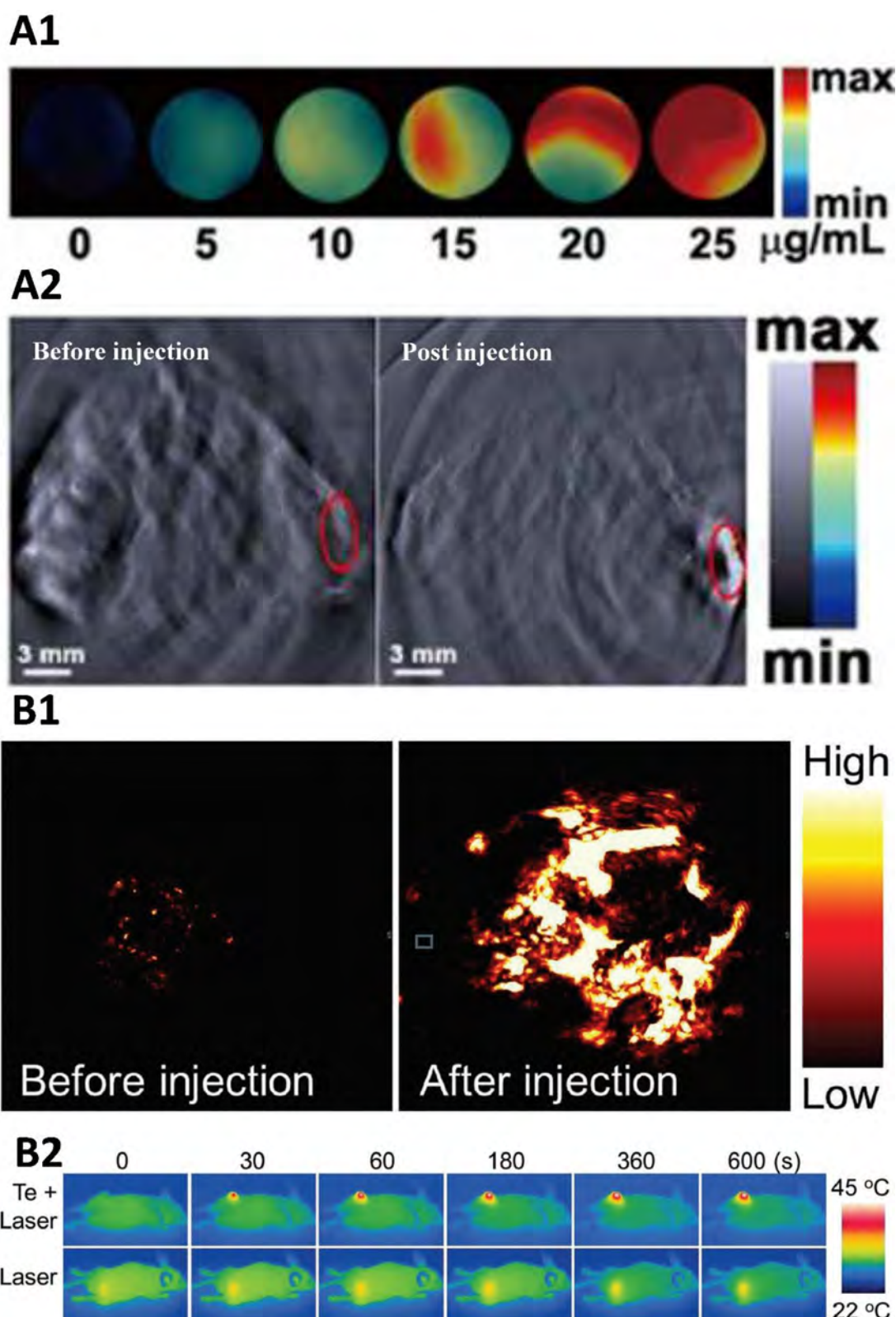


Figure 51. (A1) In vitro PA images depend on the concentration of Te NSs; (A2) In vivo PA images in the tumor site of mice before (left) and after (right) intratumoral administration of Te NSs. Reproduced with permission from ref 395. Copyright The Royal Society of Chemistry 2018. (B1) PA signal in the tumor site when injected the Te nanoneedles. (B2) Comparison of photothermal images of tumor-bearing mice at various times after injection with saline (Laser) and Te nanoneedles (Te + Laser). Reproduced with permission from ref 391. Copyright 2018 Wiley-VCH Verlag GmbH & Co. KGaA, Weinheim.

photothermal conversion efficiency, endowing antimonene as a promising candidate both PT and PA imaging.³⁸⁴ Figure 50A

provides an example for PT imaging of animals, which helps to check the photothermal effect of antimonene.³⁸⁴ Also, for

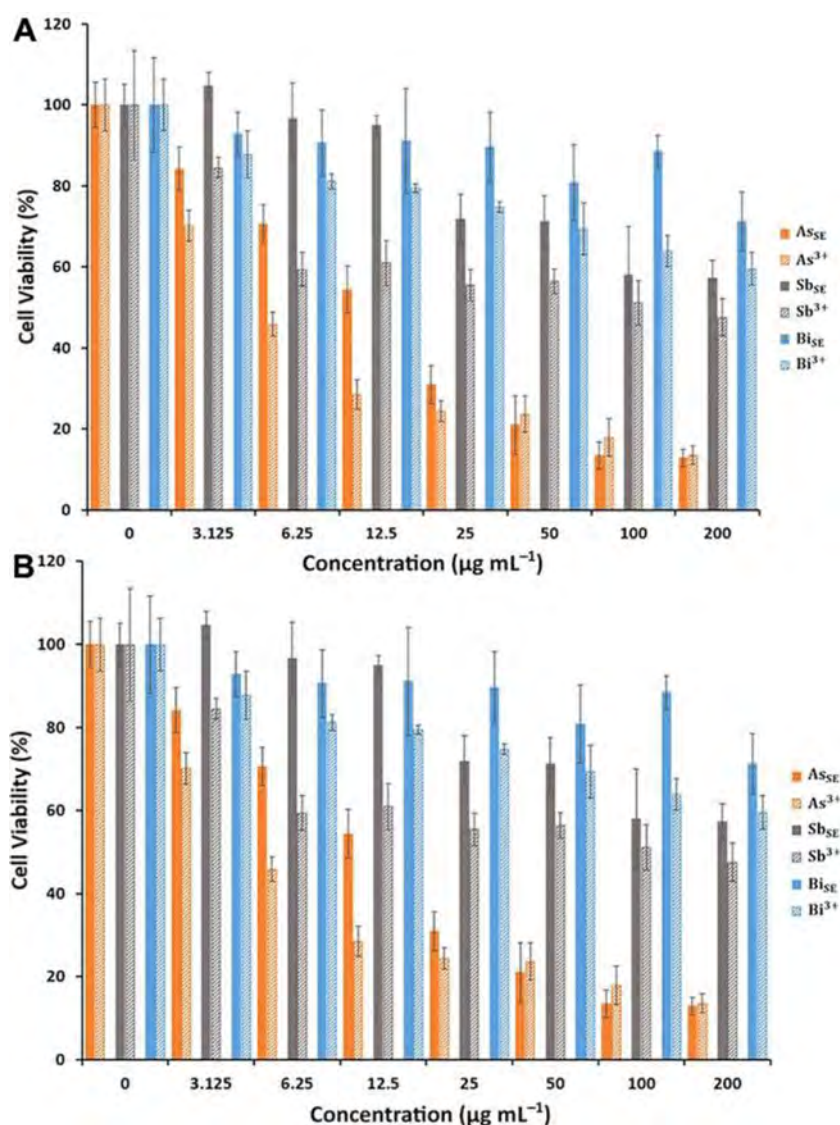


Figure S2. A549 cell viability results from (A) WST-8 and (B) MTT assays in the presence of Xene nanosheets and their +3-valence oxides after 24 h⁺ treatment. Reproduced with permission from ref 390. Copyright 2019 Wiley-VCH Verlag GmbH and Co. KGaA, Weinheim.

antimonene, apart from PT imaging, it has the potential for PA imaging, as proved in Figure 45H, which leads to more precise diagnosis.³⁸⁶

4.5.2.4. Tellurene. Followed by the liquid exfoliation synthesis of 2D Te NSs by Xie *et al.*,³⁸ Lin *et al.*³⁹⁵ observed a high photoacoustic signal from Te NSs@glutathione owing to their near-infrared absorbance. The photoacoustic signal increases as the concentration increases, confirming the potential of Te NSs@glutathione as photoacoustic contrast agents (Figure 51A1). The photoacoustic signals at the tumor site increase remarkably after the Te NSs@glutathione injection (Figure 51A2). The photoacoustic imaging capacity was also investigated in another type of Te nanostructure, the Te nanoneedles.³⁹¹ Upon nanoneedle injection, the tumor site presents an obvious contrast in comparison to the tumor site before injection (Figure 51B1), indicating the nanoneedles' effective photoacoustic imaging capability. Moreover, the thermal images in the tumor site can be recorded (Figure 51B2).

4.5.3. Biosafety. Biosafety issues should never be ignored when discussing the biomedical applications of novel materi-

als.²¹ Here, we provide some biocompatibility and toxicity studies on Xenes.

4.5.3.1. GDY. The physicochemical properties and cytotoxicity of GDY oxide (GDYO) and graphene oxide (GO) were studied by Zheng *et al.*³⁹⁹ GDYO showed higher stability in saline solution than GO, attributable to intermolecular hydrogen bonds. This good dispersity shows its potential for in vivo application. Furthermore, they showed apoptosis of cells due to GO's ROS production, while the GDYO did not influence cell viability. However, in vivo toxicity was observed with mutagenesis in mice when intravenously injected 4 mg kg⁻¹ per day and lasted 5 days. Modified GDY nanostructures were also investigated. When PEG or BSA was attached to GDY, the toxic concentration of GDY was lower than 100^{101,400} or 40 µg mL⁻¹.⁴⁰⁰ No apparent injury was observed for mice experiments that injected 10 mg GDY/kg body weight.⁴⁰⁰

4.5.3.2. Borophene. The cytotoxicity of PEGylated borophene was checked in several kinds of cancer cells.³⁷⁸ After incubation with PEGylated borophene NSs of 500 µg mL⁻¹ at maximum, no apparent cytotoxicity was observed for all tested cell lines. The release of the other two key toxicity indicators of

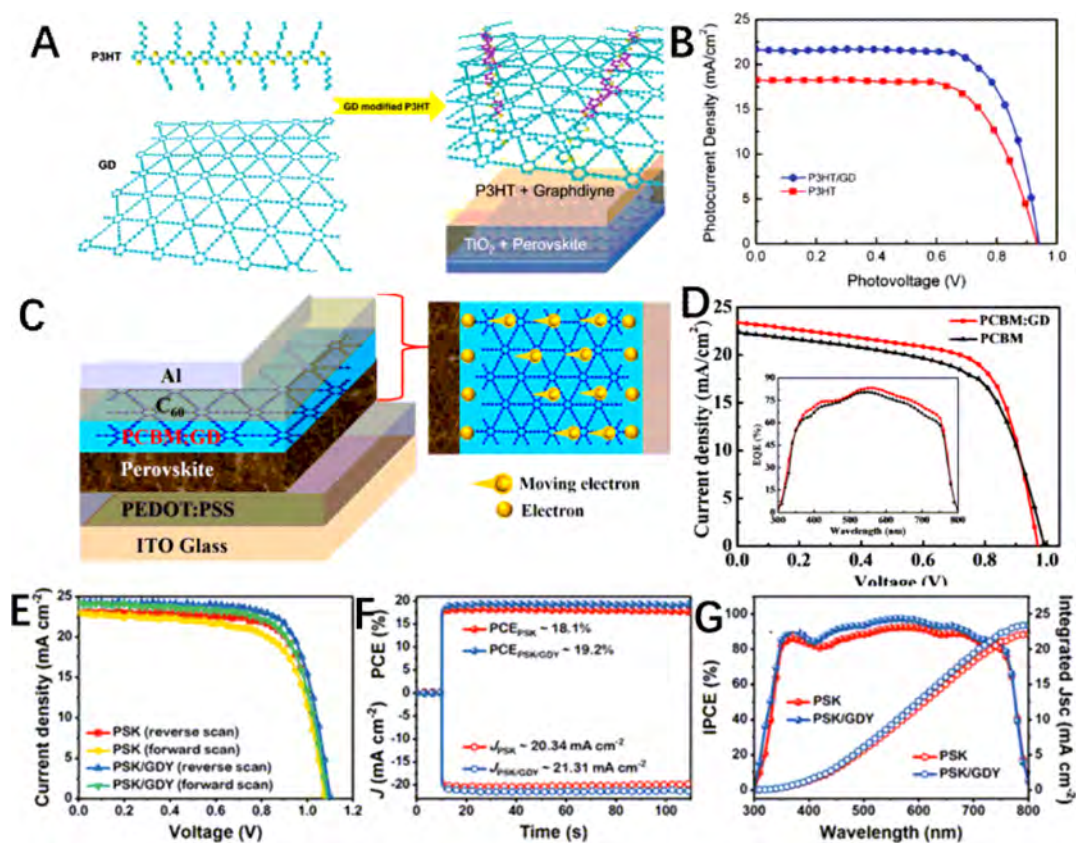


Figure 53. (A) Schematic diagram of perovskite solar cells with the P3HT hole-transporting material modified with GDY and (B) J-V characteristics of the solar cell. Reproduced with permission from ref 413. Copyright 2015 Wiley-VCH Verlag GmbH and Co. KGaA, Weinheim. (C) schematic diagram of perovskite solar cell with doping GDY in the electron-transporting layer; (D) Corresponding J-V characteristic curves. Reproduced from ref 416. Copyright 2015 American Chemical Society. (E) J-V curves under simulated AM 1.5G illumination of 100 mW cm^{-2} in reverse and forward scans. (F) Steady-state output J_{sc} and its corresponding PCE measured at the maximum power point. (G) IPCE spectra together with the integrated J_{sc} of perovskite solar cells introducing GDY between perovskite and hole-transporting layers. Reproduced with permission from ref 423. Copyright 2020 Wiley-VCH Verlag GmbH and Co. KGaA, Weinheim.

nanomaterials, ROS and lactate dehydrogenase (LDH), were also tested. The release of ROS and LDH caused by PEGylated borophene treated cells showed no significant difference with the control group. It proved the high biosafety and promising potential of borophene for biomedical applications.

4.5.3.3. Group VA: Arsenene, Antimonene, and Bismuthene. Side effects and toxicity related to these three elements (As, Sb, and Bi) have long been explored, and toxicity is quite common for VA group elements.^{401–403} The chemical valence of these elements has been proposed and evidenced to dramatically influence the toxicity, and thus, the biosafety issue for Group VA elements must be considered.

The reported Xenos have demonstrated exciting biosafety behaviors under certain concentrations, but the chemistry of why they are safe and what would happen if concentrations increase, has not been deciphered. In 2019, Puma's group conducted a systematic study on the cytotoxicity of arsenene, antimonene, bismuthine, and their corresponding oxides (Figure S2).³⁹⁰ Taking adenocarcinoma human lung epithelial A549 cells as an example, arsenene demonstrated the highest cytotoxicity upon concentration increase, while bismuthene showed good compatibility even when the concentration increased to $100 \mu\text{g mL}^{-1}$, with the cell viability staying above 80%. In Figure S2A,B, a comprehensive comparison is displayed, indicating that the +3 valence salts of these elements generally

induce toxicity than the intrinsically 0 valence Xenos and that arsenene is much more toxic than antimonene and bismuthene.

Inspired by the low toxicity of zero valence Sb and Bi, as well as the advantages of 2D materials mentioned above, antimonene and bismuthene are more promising for large-scale applications in biomedicines.

4.5.3.4. Tellurene. In recent years, innovative applications of Te have emerged with the development of nanotechnology. For example, Te quantum dots (QDs) and Te nanostructures have been used for biosensors, biological labeling, and imaging.⁴⁰⁴ They have also been applied in targeted drug delivery systems. Also, Te nanoparticles show great potential in novel applications, such as free radical scavenging, antioxidant, and lipid-lowering.

The chemistry of tellurium is rich in inorganic substances. Moreover, Te exists in a variety of organisms in the human body. Te has been applied in antibacterial fields for many years, such as atherosclerosis, anti-inflammatory, and antileishmaniasis. It has also been used widely for immuno-modulation. Many of the organotellurides are potential agents with protein inhibition, microorganisms killing, and apoptosis induction in specific cancer cells from a pharmacological perspective.⁴⁰⁵

4.6. Energy Application

4.6.1. GDY. **4.6.1.1. Solar Cell.** GDY has been applied in polymer solar cells,^{406,407} perovskite solar cells,^{408–410} fuel cells,⁴¹¹ and photocatalysis fields.^{315,412} Xiao *et al.* reported

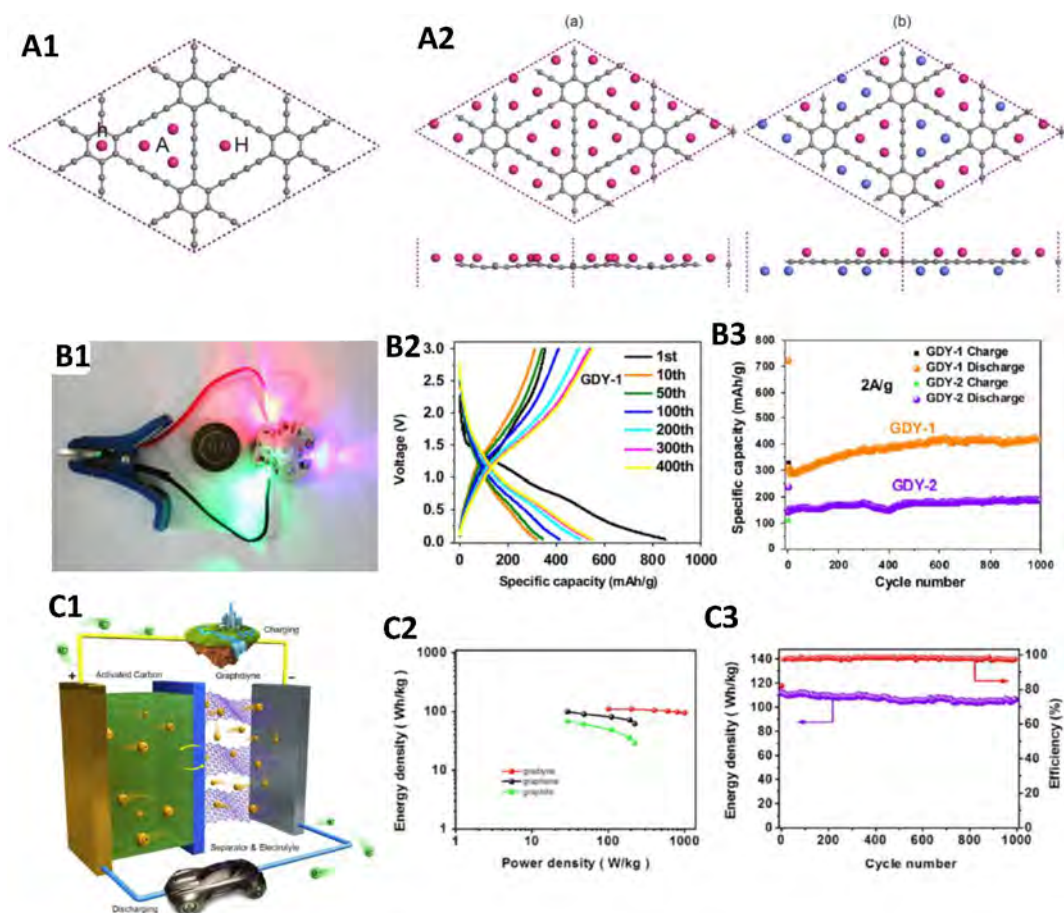


Figure 54. (A1) Schematic of monolayer GDY in a 2×2 supercell and the sites where lithium ions possibly adsorb are shown. (A2) Top and side views of the optimized configuration with lithium atoms adsorption on (a) one side and (b) two sides of GDY. Different colors indicate lithium atoms on different sides of the GDY layer. Reproduced with permission from ref 425. Copyright 2013 American Institute of Physics. (B1) Photo of the Li-ion battery based on GDY and its application in LED lighting. (B2) Charge/discharge profile under constant current of the GDY electrode in the studied voltage range of 5 mV and 3 V (current density: 500 mA g^{-1}). (B3) Cycling stability comparison between the electrodes of GDY-1 and GDY-2 samples from 5 mV to 3 V (current density: 2 A g^{-1}). Reproduced with permission from ref 427. Copyright 2015 Elsevier, Inc. (C1) Schematic of the GDY based Li-ion capacitor. (C2) Ragone plots of GDY/AC Lithium-ion capacitor (LIC), the previously reported graphene and graphite LICs are also shown as references. (C3) Stability of GDY/AC Lithium-ion capacitor (current density: 200 mA g^{-1}). Reproduced with permission from ref 77. Copyright 2016 Elsevier, Inc.

perovskite solar cells using GDY as a dopant in the hole-transporting material (HTM) layer of poly(3-hexylthiophene) (P3HT) (as shown in Figure 53A).⁴¹⁵ The results of Raman spectra and UV electron spectra exhibited that between the GDY particles and P3HT a strong π - π stacking interaction is observed, which is beneficial for hole transport and improved performance. In addition, some GDY aggregates demonstrate scattering properties, which positively contribute to light absorption in the long wavelength band of perovskite solar cells. The PCE is up to 14.58%, which is better than the original device based on P3HT (Figure 53B). Subsequently, Ren *et al.* successfully prepared nanocomposites of GDY nanosheet modified platinum nanoparticles by a simple ion-beam sputtering method.⁴¹⁴ The power conversion efficiency of platinum (Pt) nanoparticle-GDY NSs counter electrode based dye-sensitized solar cells is significantly improved by a special “p-n” junction structure, enhanced electron transferability, and catalytic activity. The experimental results demonstrated that the fabricated solar cells still have a high PCE of 6.35%, which confirmed that the performance is comparable to the Pt foil and is larger than that of the rGO/Pt nanoparticle and Pt nanoparticles composite materials. Jin *et al.* presented PbS

colloidal quantum dots solar cells with the anode buffer layer of GDY.⁴¹⁵ Compared with the reference device, its PCE with GDY is significantly enhanced from 9.49% to 10.64%. Furthermore, the device has excellent long-term stability. Kuang *et al.* reported that GDY was doped into the phenyl- C_{61} -butyric acid methyl ester (PCBM) layer of perovskite-type solar cells (with ITO/PEDOT:PSS/ $\text{CH}_3\text{NH}_3\text{PbI}_{3-x}\text{Cl}_x$ /PCBM:GD/ C_{60} /Al structure for the perovskite solar cells, as shown in Figure 53C).⁴¹⁶ Compared with devices based on PCBM, the average PCE of the devices has increased by 28.7%. The optimized PCE was measured to be 14.8% (as shown in Figure 53D). Zhang *et al.* improved all photovoltaic parameters by dispersing GDY quantum dots in perovskite type solar cells or in a precursor solution or modifying the surface of each flake, the PCE was increased from 17.17% to 19.89%.⁴¹⁷ The enhanced fill factor and J_{SC} are mainly due to the larger Spiro-OMeTAD carrier conductivity, larger MAPbI_3 grains, and carrier recombination suppressed caused by trap states existing at the interface and boundary, thereby increasing the overall solar energy. Li *et al.* introduced GDY into the perovskite flake to establish a perovskite/GDY bulk heterojunction for planar perovskite solar cells.⁴¹⁸ It is indicated that the heterojunction

provides additional channels to promote exciton separation and the extraction of photogenerated electrons. For higher J_{SC} , the electron transport ability has been improved, and the introduced GDY can passivate the grain boundary and interface, effectively inhibiting the recombination of photogenerated carriers, resulting in a relatively high filling rate. A power conversion efficiency of 20.54% is achieved. Li *et al.* reported that GDY is doped in MAPbI₃-based perovskite solar cells.⁴¹⁹ In addition, the stability and J – V hysteresis were also significantly enhanced. The results showed that double-doped GDY improved the conductivity, charge extraction ability, increased the electron mobility in the electron transport layer, enhanced the electron transport layer's film morphology, reduced charge recombination, and increased the fill factor. Li *et al.* demonstrated that GDY could be used as a matrix material of the perovskite active layer.⁴²⁰ In the process of preparation, the optimum molar ratio of PbI₂, MAI, and GDY for active materials is 1:1:0.25. A power conversion efficiency of 21.01% was achieved at maximum. When GDY is used as a matrix material, the film morphology, crystallization, and other photoelectric characteristics of the perovskite active layer are greatly affected. Fewer grain boundaries and larger domain sizes were achieved by introducing GDY. Li *et al.* proposed an effective method to modify P₃CT-K flake by doping GDY to further improve perovskite solar cells' performance. This method can enhance the surface wettability of hole-transport layers and significantly optimize the perovskite morphology by uniformly covering and reducing grain boundaries.⁴²¹ Doping GDY in hole-transport layers can also improve hole extraction mobility and suppress recombination, enhancing device performance. At the same time, GDY-doped devices exhibited significantly improved J – V hysteresis. Liu *et al.* successfully used chlorine-functionalized GDY as a solid additive to modify its morphology, to realize versatility, and to improve the efficiency and productivity of the device.⁴²² Compared with the 15.6% efficiency of the control equipment, it achieved a 17.3% efficiency, of which the certified current was 17.1%, while the J_{SC} and fill factor increased simultaneously. Zhang *et al.* used GDY in the planar perovskite solar cells to modify the pore transport.⁴²³ Using GDY containing chlorobenzene as an antisolvent, GDY can be injected into the upper part of the layered perovskite. It can act as a transport tunnel and a hole collector at the same time, facilitating the diffusion and separation of photogenerated holes and electrons in perovskite. Moreover, after GDY modification, a Schottky barrier was established at the interface between GDY and perovskite, which can guarantee a one-way hole transport behavior from perovskite to GDY. Thus, the photogenerated carriers in the layered perovskite can separate automatically. Therefore, in comparison with a single perovskite based solar cells, the J_{sc} and PCE of the perovskite/GDY solar cells increase, and recombination of dark current and charge is significantly delayed (as shown in Figure 53E–G). The modification with GDY also enhanced the environmental stability of perovskite flakes and perovskite solar cells due to its hydrophobicity.

4.6.1.2. Battery. The atomic structure and chemical property of GDY make it promising for fabricating electrochemical energy storage devices.⁴⁵ GDY has a single-layer two-dimensional planar structure. Its infinitely extending two-dimensional plane is pleated for maintaining the stability of the structure. The sp²-hybridized benzene rings and sp-hybridized butadiyne bonds in GDY form triangular pores, leading to the pores in its layered structure. It endows GDY very high π conjugation, regular and orderly distribution of pore structure, and adjustable electronic

structure. The two-dimensional planar structure and the three-dimensional ordered porous properties of GDY make it beneficial for the storage of molecules and ions, as well as for rapid migration of electrons, which improves the battery performance based on GDY.^{47,424}

In contrast to graphite-based electrodes, the lithiation potentials and specific capacities of GDY can be significantly enhanced. The GDY-based electrodes possess lithiation potentials ranging from 2.1 to 2.7 V. The interlayer spacing of GDY is larger than that of graphite, which is more suitable for lithium-ion insertion without destroying the layered structure. Moreover, the GDY with porous structure is beneficial for both interlayer and intralayer Li⁺ diffusion in GDY with barriers between 0.35 to 0.52 eV, other than the confined in-plane Li⁺ diffusion of graphite (Figure 54A1, A2).⁴²⁵ In the GDY, the lithium atoms are located at three symmetric sites in its pores and have a unique triangular pattern (Figure 54A2). Thus, the Li⁺ intercalation in GDY could be in LiC₃, whose storage capacity can be enhanced to twice of the traditional form of LiC₆ in graphite.⁴²⁶ Therefore, GDY is very suitable to be fabricated as an anode for lithium-ion batteries, attributed to the high mobility and excellent lithium storage ability. Huang *et al.* reported GDY as a Li storage material with high efficiency and clarified the Li storage mechanism in multilayer GDY (Figure 54B1).⁴²⁷ GDY-based batteries have achieved outstanding rate performance, high specific capacity, and long cycle life (Figure 54B2). During 1000 cycles, the specific capacity maintained at 420 mAh g⁻¹ under a high current density of 2A g⁻¹ (Figure 54B3). Li's group prepared 2,4,6-hydrogen-substituted GDY on a copper foil *via* an in situ cross-coupling reaction of 1,3,5-triethynylbenzene in pyridine.⁷⁶ It was applied in a lithium-ion battery, obtaining a large reversible capacity of 1050 mAh g⁻¹. In one crystalline unit, six benzene rings were connected by diacetylene linkages and the hydrogen atoms are located in the pores, resulting in more active binding sites for Li ions storage. Then, they prepared GDY nanostructures, including nanotubes and nanosheets with the Cu nanowires used as catalysts and templates for the in situ growth.⁴²⁸ They achieved a capacity of 1388 mAh g⁻¹, that was almost twice of the theoretical value of GDY, indicating a double side Li ion storing capacity of 2D GDY. Fluorine substituted (on 2,4,6-carbons of benzene) GDY (FGDY) was prepared *via* a C–C coupling reaction.⁴²⁹ Because the C–F semi-ionic bonds transformed to ionic bonds reversibly in the charge–discharge process, FGDY showed a high capacity of 1700 mAh g⁻¹. Normally, organic cathodes in a battery have low conductivity and molecular dissolution. However, when π -conjugated GDY was weaved on the organic cathodes, it led to increased conductivity and suppressed dissolution, resulting in an enhanced energy density of 310 W h kg⁻¹.⁴³⁰ The introduction of GDY to lithium-ion batteries resulted in high rate performance and improved stability.

Lithium-ion capacitor (LIC) is a newly existing hybrid energy storage device that “interleaves” lithium-ion batteries and electric double-layer capacitors. However, a traditional LIC usually has relatively low energy density, which limits its development. Du *et al.* have respectively used activated carbon (AC) and GDY for cathode and anode to fabricate a hybrid LIC (Figure 54C1).⁷⁷ Its energy density was 95.1 Wh kg⁻¹, and the initial specific energy was 112.2 Wh kg⁻¹ with the power density of 1000.4 W kg⁻¹ and 400.1 W kg⁻¹, respectively (Figure 54C2 and C3). Furthermore, the initial specific energy retains 94.7% in the 1000 cycle (Figure 54). That high performance of the GDY anode provides great potential for next-generation batteries.

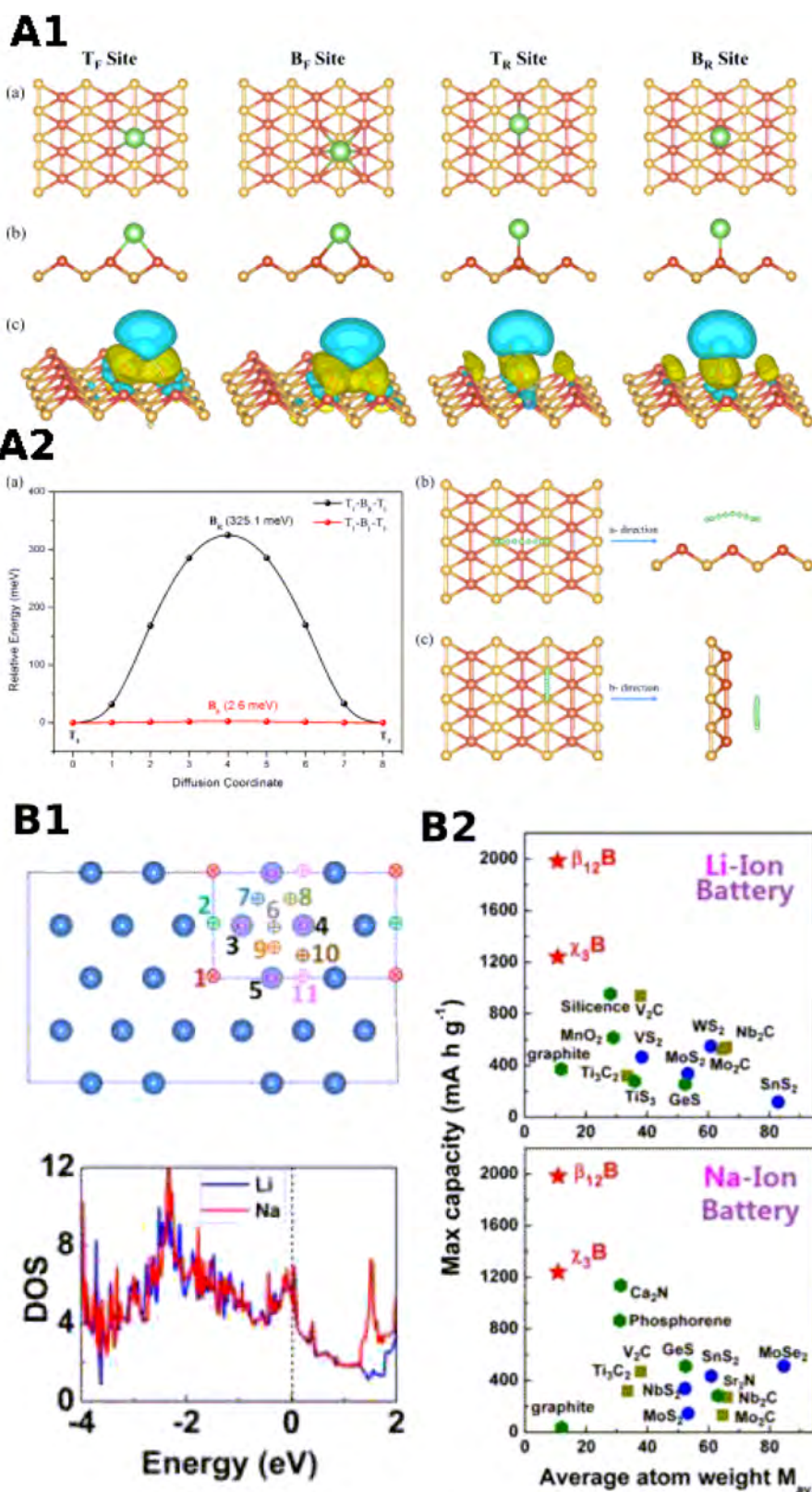


Figure 55. (A1) (a) Top view, (b) side view of four lithium adsorption sites with high symmetry (T_F , B_F , T_R , and B_R sites from left to right) and (c) their charge density difference plots correspondingly (The yellow and blue areas represent electron losses and gains, respectively. The green ball represents a lithium atom). (A2) (a) Comparison of the energy distribution diagrams between lithium diffusion along $T_F-B_R-T_F$ and $T_F-B_F-T_F$ paths and (b) top and (c) side view of lithium diffusion along $T_F-B_R-T_F$ and $T_F-B_F-T_F$ pathways, respectively. $T_F-B_F-T_F$ is along the furrowed path, and $T_F-B_R-T_F$ is perpendicular to the furrow. Reproduced with permission from ref 441. Copyright 2016 Elsevier, Inc. (B1) Considered Li adsorption sites and Na adsorption sites on the surface of β_{12} borophene (top) and their density of states (DOS, bottom). (B2) Comparisons between the electrode capacities based on borophene and typical 2D materials in Lithium and sodium-ion batteries. Reproduced with permission from ref 439. Copyright 2016 Royal Society of Chemistry.

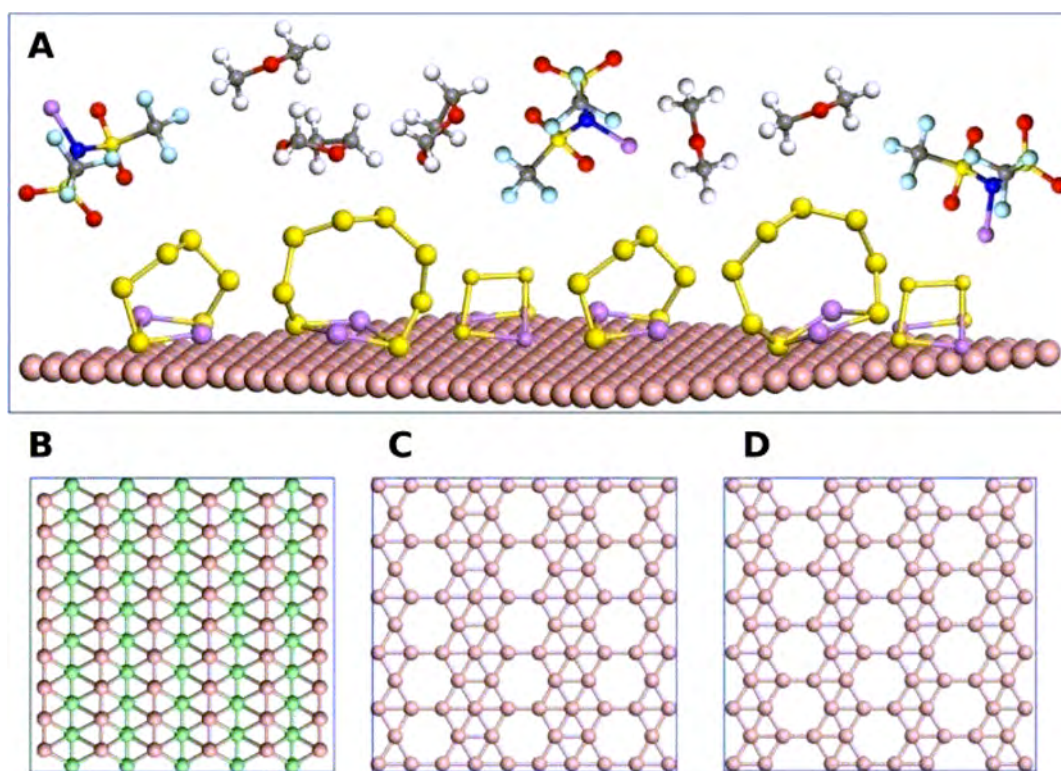


Figure 56. (A) Adsorption of polysulfides on borophene in competition with the electrolyte. Different colors of balls represent different elements: pink, boron; yellow, sulfur; purple, lithium; gray, carbon; red, oxygen; light blue, fluorine; white, hydrogen; and dark, nitrogen. (B–D) Structure diagrams of triangular, β_{12} - and γ_3 -borophene, respectively. The pink balls represent the groove B atoms, while the green balls in (B) represent bulge B atoms. Reproduced with permission from ref 443. Copyright 2019 The Royal Society of Chemistry.

The low cost and abundance of sodium make sodium-ion batteries (SIBs) widely studied. However, the sodium ion (Na^+) has a larger diameter than Li^+ ; thus, Na^+ is hard to intercalate in graphite. However, with a triangular porous structure and asymmetrically conjugated π electrons, GDY can provide 3D channels for Na^+ diffusion. Like Li atoms, a model showing the Na^+ occupation in GDY was built, and the intercalation form could also be NaC_3 .⁴³¹ Na^+ can easily diffuse in GDY planes, as the energy barrier is rather low (0.4 eV).⁴³² Since GDY possesses outstanding Na^+ storage and diffusion performances, it is considered a promising electrode in SIBs. Li *et al.* constructed a 3D structured GDY *via* the Glaser–Hay coupling reaction with a modification, which was used first as the anode material in the SIBs. Glaser coupling is a traditional method to synthesize 1,3-diynes. Glaser–Hay coupling is a technique modified by Hay, demonstrating that the nitrogen ligand *N,N,N',N'*-tetramethylethylenediamine (TMEDA) addition promoted the coupling reaction in other nonalkaline solution such as acetone.²² Their sodium storage properties and stability are excellent, with a high reversible capacity of about 812 mAh g^{-1} .⁸¹ The result is originated from (i) the porous 3D architecture of the GDY assembly optimizing the sodium storage and diffusion behavior and (ii) the generation of a stable solid electrolyte interface with the diacetylene linkages increasing the stability. Boron-GDY (BGDY) is a structure of hexagonal fused rings composed of diacetylene bridges and the boron atom, replacing the benzene rings in GDY.⁴³³ In addition to GDY incorporating abundant carbyne ligands in its pores as the Na ion binding sites, BGDY provides extra binding sites on the electronegative boron atoms, resulting in a more stable affinity to Na ions. Furthermore, the hexagonal pores in the BGDY molecular plane are larger than

those in pristine GDY, which is beneficial for the Na ion (larger than Li ion) transfer in the perpendicular direction.

Besides the traditional LIBs and SIBs, GDY was also applied in next generation batteries, *i.e.*, metal–sulfur batteries. Sulfide GDY reserving short sulfur molecules (S_{2-4}) was synthesized by splitting S_8 rings and anchoring in the triangular pores of GDY by chemically bonding to carbon–carbon triple bonds.⁴³⁴ It resulted in a conductive carbon skeleton with short sulfur energy storage and high lithium ion mobility. Therefore, using sulfide GDY in lithium–sulfur (Li–S) batteries and magnesium–sulfur (Mg–S) batteries greatly improved their electrochemical performances. A polyanion (Nafion) embedded GDY was developed to tune the mass transfer behavior in a core–shell nanostructure, thus ameliorating the phase transformation process in the cathodic reaction.⁴³⁵ In Nafion-GDY, GDY plays a role of sulfur reservoir with good conductivity and is applied to catalyze the cathodic reactions. As the Nafion-GDY was incorporated in the Li–S battery, the volume capacity of the battery could be enhanced to 1832 Ah L^{-1} , and the stability was also improved due to their complementary effects.

Lithium dendrite growth is a critical issue that affects the stability and safety of lithium-based batteries.^{436–438} Zuo *et al.* discovered evenly distributed Cu quantum dots (CuQDs) on GDY nanosheets were ideal substrates for uniform lithium plating with the suppression of lithium dendrite formation.⁴³⁶ When studying the influence of the copper substrate on the growth of GDY, they found that polycrystalline copper nanowires can spontaneously split into a large number of CuQDs during the growth of GDY, and then the QDs blocked the GDY growth with long-range order. The obtained CuQDs were evenly distributed on the surface of less ordered GDY

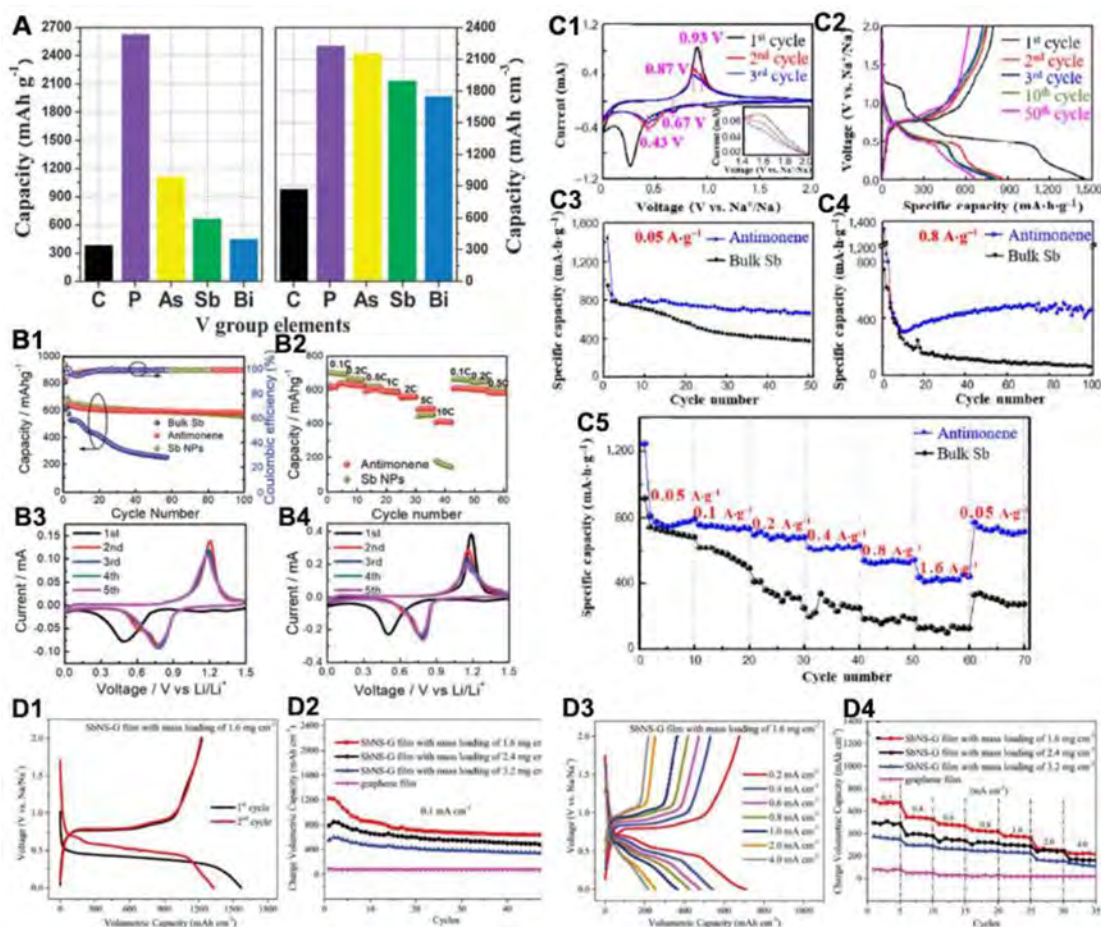


Figure 57. (A) Gravimetric (left) and volumetric (right) capacities for different elements. Reproduced with permission from ref 449. Copyright 2010 Royal Society of Chemistry. (B1) Cycling and (B2) rate performances of bulk Sb, 2D Sb, and Sb NPs. CV curves of (B3) 2D Sb and (B4) Sb NPs. Reproduced with permission from ref 448. Copyright 2019 Royal Society of Chemistry. (C) Electrochemical performance of antimonene: (C1) CV curves, (C2) discharge–charge behavior, (C3) cycling performance, (C4) long-term cycling life, and (C5) rate performance. Reproduced with permission from ref 252. Copyright 2018 Springer Nature. (D) Electrochemical performance of antimonene nanosheet-graphene film: (D1) first-two charge–discharge profiles, (D2) cyclic performances, (D3) influence of current densities on charging–discharging profiles, and (4) rate performance. Reproduced with permission from ref 156. Copyright 2017 Wiley-VCH Verlag GmbH and Co. KGaA, Weinheim.

nanosheets. The CuQD-GDY showed extremely high lithiophilicity, resulting in the increased binding energy between the Li atom and GDY from -2.56 eV to -3.17 eV, attributable to a charge transfer from CuQD to GDY. At the same time, a large number of pores on the less ordered GDY efficiently disturbed the lithium dendrite growth, while a long-range ordered GDY grown on the Cu foil could not avoid ultralong growth of the dendrite. It was beneficial for the development of the Li–S batteries.

4.6.2. Borophene. The low atomic weight, metallic feature, and structural channels for fast ion migration make borophene promising for fabricating the anode in metal-ion batteries. The metallic borophenes have a capacity up to 1984 mAh g^{-1} for both Li- and Na-ion batteries, while in calcium-ion batteries (CIBs) and magnesium-ion batteries (MIBs) it can be 800 and 1960 mAh g^{-1} , respectively.^{439,440}

Jiang *et al.* studied theoretically the potential of borophene applied for the anode in lithium-ion batteries.⁴⁴¹ The adsorption energy of borophene to Li atom is -1.12 eV, ensuring high binding stability of Li-borophene batteries during the lithiation process (Figure 55A1). The specific capacity of a commercial graphite anode is 372 mAh g^{-1} . For comparison, the specific capacity of a borophene anode is five times larger (1860 mA h

g^{-1}), due to its fully lithiated form of $\text{Li}_{0.75}\text{B}$. The energy barriers in different directions of corrugated borophene are dramatically different, resulting in anisotropic Li^+ diffusion in borophene. Moreover, it is just 2.6 meV along the groove of corrugated borophene, while other 2D materials-based anodes, such as the Ti_3C_2 and phosphorene, have much higher energy barriers of 70 and 80 meV, respectively (Figure 55A2). It leads to ultrafast Li^+ diffusion in borophene. These suggest that a borophene anode in LIBs is promising to enhance batteries' power density drastically.

Moreover, Zhang *et al.* predicted that borophene could be used for electrode fabrication in LIBs and SIBs.⁴³⁹ The simulations are conducted on the two experimentally stable borophene structures of χ_3 and β_{12} . The good electric conductivity of borophene remains after Li^+ and Na^+ adsorption, and their optimized sites on borophene are determined (Figure 55B1). Besides advantages including low average open-circuit voltages and small diffusion barriers, the storage capacity can be up to 1240 mAh g^{-1} in the χ_3 structure and 1984 mAh g^{-1} in the β_{12} structure for both lithium and sodium ions. These are the highest in the ever-discovered 2D materials, and it is also much higher than those of the commercial barriers with graphite electrode (Figure 55B2). These results strongly suggest that

borophene is attractive for fabricating anodes in both LIBs and SIBs.

4.6.2.1. Lithium–Sulfur Battery (LSB). Lithium–sulfur battery (LSB) is promising for energy storage with a higher energy density than the current lithium-ion batteries. The main challenge for LSB is the polysulfide shuttle, low discharge capacity, and rapid capacity decay. Host materials with excellent polysulfide absorbability and high conductivity are preferred for scaffolds to load sulfur in LSB.⁴⁴² The porous and wave-type configuration in borophene makes it ideal to confine Li_2S_n . Recently, few theoretical studies on Li_2S_n adsorption are explored. For instance, three types of borophenes are theoretically investigated as host agents for sulfur cathodes (Figure 56).⁴⁴³ They possess light masses and good conductivities. The larger binding energies of polysulfides on the borophenes than those on the commonly used electrolytes, reduce the polysulfide dissolution in the electrolytes. Moreover, the polarization of surfaces in borophenes can provide appropriate sites to immobilize polysulfides. Thus, borophene-based or B-doped materials benefit from the hindered shuttle effect of polysulfides. These properties of borophene and its derivatives endow them as promising host materials for LBS.

4.6.3. Group V: Arsenene, Antimonene, and Bismuthene. Bulk 3D Sb and Bi have been found to have great potential for sodium ions storage, with the theoretical values for Na_3Sb and Na_3Bi being 660 and 385 mAh g^{-1} , respectively. Benefiting from a transition from semiconductive to metallic properties after being exfoliated as 2D nanosheets, antimonene, and bismuthene, together with their heterostructures with other 2D materials, exhibit more attractive charge storage performances in K^+ , Na^+ , Li^+ , and Mg^{2+} batteries with high energy density.^{156,252,444–446} As depicted in Figure 57A, elements As, Sb, and Bi all show performances superior to the widely applied carbon in gravimetric and volumetric capacities. These elements generally exhibit low atomic packing factors, suggesting that incorporating Li ions into crystals consisting of these elements is feasible. Furthermore, the three elements all tend to form alloys with Li, demonstrating vast potential for storing Li.

Using the first principle studies, Ye *et al.* found that the Mg storage performance of arsenene is mainly dependent on the layer numbers and compositions.⁴⁴⁷ With the theoretical adsorption energy tuned from 0.82 to 2.48 eV, Mg ions could be anchored onto As nanosheets with different layer numbers and heterostructures. Among different cases, theoretical results revealed that monolayer arsenene has a much higher specific capacity than the bilayer structure as well as the arsenene/graphene heterostructure, but a much lower open-circuit voltage on the average. The lowest diffusion barrier ranging from 0.08 to 0.33 eV for Mg ions is also found for monolayer arsenene, indicating the intrinsically intriguing charge/discharge performances, with good recycling reversibility observed. Among As, Sb, and Bi, antimonene has been most intensively studied for ion storage. As shown in Figure 57B, a detailed comparison among the Sb nanosheet, bulk Sb and Sb nanoparticles have been conducted to examine their capacity to store Li-ions.⁴⁴⁸ The results suggest that even without additional agents, dimension engineering could serve as a helpful strategy to achieve high stability because of the promising cost-effective electrode fabrication for scale-up production. The result demonstrated that antimonene performed much better than the Sb nanoparticles in terms of reaction rates. Moreover, the nanosheets even performed better than the reported Sb NPs or Sb/carbon heterostructures. CVs of nanosheets and nanoparticles were

collected to gain deep insight into the mechanism, which manifests a good alloying/dealloying process for all the Sb samples, regardless of the configurations. To confirm the generality of antimonene for ion storage, Lin's group examined the Na^+ storage capability of Sb by a similar comparison study over the 2D nanosheet and bulk Sb, with the electrochemical properties shown in Figure 57C.²⁵² As can be seen, there is a two-step pathway for the alloy/dealloy process, where Sb, NaSb , and Na_3Sb transform gradually under the influence of the electronic field. Bulk Sb exhibits a poor cyclability, whereas the 2D antimonene demonstrates excellent stability (Figure 57C1). Figure 57C2–C4 show the cycling performances under different current density, which display that antimonene outperformed bulk Sb, regardless of the density (664 vs 381 mAh g^{-1} at 50 mA/g after 50 cycles, 458 vs 63 mAh g^{-1} at 800 mA/g after 100 cycles). The detailed process is depicted in Figure 57C5, indicating that antimonene has prominently high speed and cycling performances, thus gaining an advantage over bulk Sb. To a step closer to practical applications, Yang and co-workers constructed a compacted film based on antimonene nanosheets-graphene (SbNS-G). It is concluded that an antimonene based film is superior to other materials, which opens a window toward building up supercapacitors.¹⁵⁶

Xenes are promising candidates for superconductors and supercapacitors. Kong *et al.* employed DFT calculations to explore feasible phonon-mediated superconductivity in arsenene nanosheets under electron doping. Strong superconducting pairing interaction was found to be a consequence, mainly of the p_z -like electrons of As atoms and the A_1 phonon mode near the K point. More surprisingly, the superconducting transition temperature reaches 30.8 K in arsenene with the doped electron density of 0.2 e/cell and additional application of 12% biaxial tensile strain. It is worth noting that the calculated transition temperature outperforms much better than the bulk arsenene and is the highest one compared with other simulated values for electron-doped 2D Xene superconductors. This sheds light on the application of arsenene and similar elemental 2D materials such as Sb, Bi, and the like for superconductors.³⁰²

Banks's group employed antimonene nanosheets for such applications.⁴⁵⁰ Based on a carbon electrode, Sb demonstrates to prominently enhance the energy storage performance of this electrode in cyclic voltammetry and constant current charging. Electrochemical measurements come at a capacitance of 1578 F g^{-1} as well as at a charging current density of 14 A g^{-1} for this antimonene. Thus, antimonene can be regarded as a potential 2D material for supercapacitor applications. This platform also conveys the power and energy densities of 4.8 kW kg^{-1} and 20 mWh kg^{-1} , which are highly competitive compared with other 2D materials. More encouragingly, this antimonene based system exhibits great cycling performances for more than 1000 cycles.

As a pioneering VA group 2D material, black phosphorus (BP) has demonstrated its admirable electronic and optical advantages resulting from the readily modulated bandgaps *via* changing the layer numbers. Like BP, the VA group Xenes also have direct bandgaps, and thus bandgap engineering makes it possible to realize the transformation of a given 2D Xene from a conductor to a semiconductor. Harnessing this feature, Song and co-workers prepared a batch of semiconductive indirect-bandgap antimonene nanosheets (SANs). Such SANs are an excellent candidate in planar inverted perovskite solar cells for the hole extraction layer and drastically improve the performance of the whole system because of quick hole extraction and

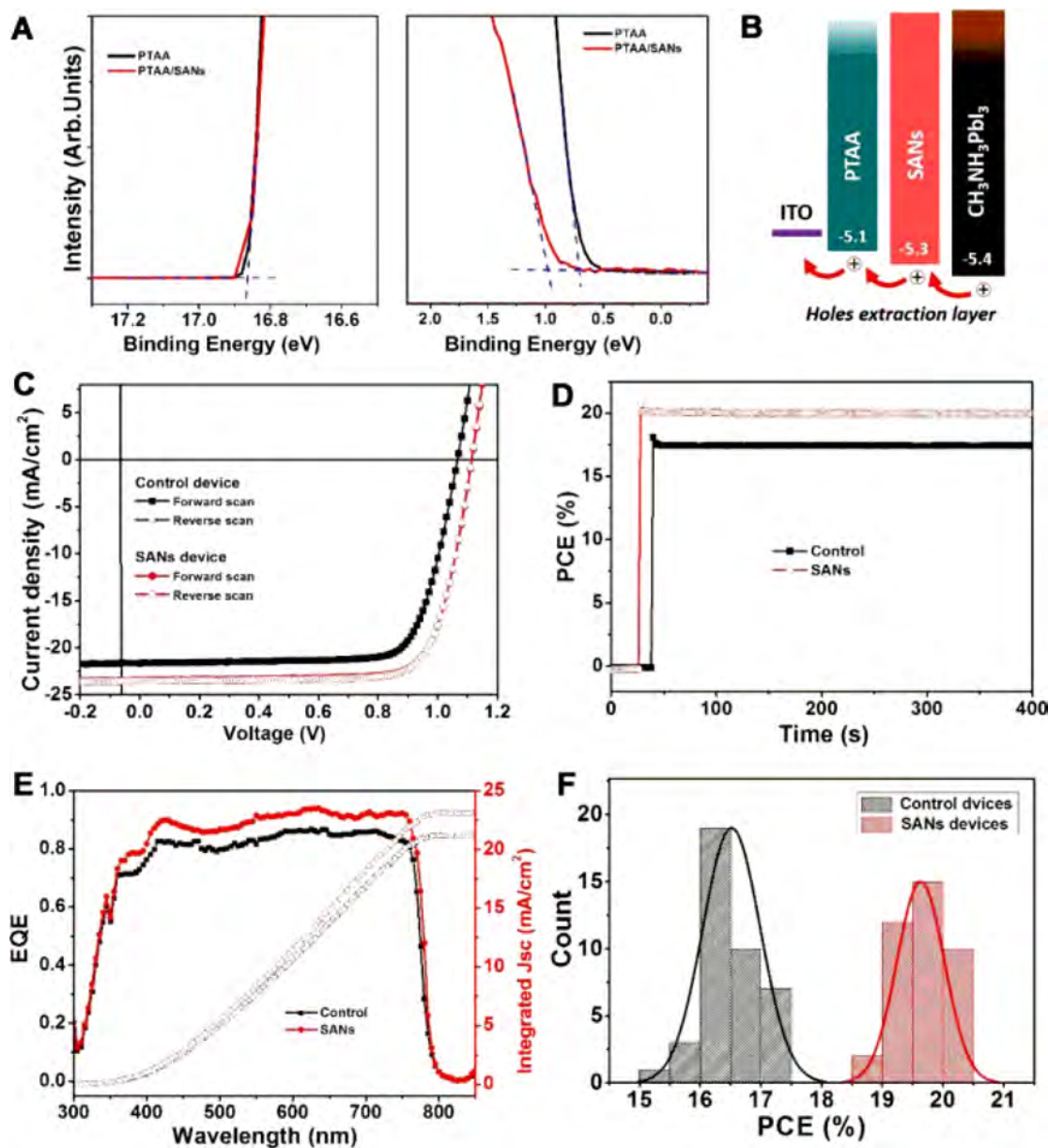


Figure 58. (A) UPS spectra showing secondary electron cutoff region (left) and valence band region (right) (PTAA: poly[bis(4-phenyl)(2,4,6-trimethylphenyl)amine]; SANS: semiconductive antimonene nanosheets). (B) Explication of hole transfer from perovskite to PTAA/SANS. (C) J - V curves of the control and SANS with the most favorable performance. (D) Steady power conversion efficiencies (PCE) curves. (E) External quantum efficiency (EQE) plots at the maximum power point. (F) Statistical PCE results of perovskite solar cells without (control) and with SANS. Reproduced with permission from ref 451. Copyright 2018 Wiley-VCH Verlag GmbH and Co. KGaA, Weinheim.

highly effective hole transfer at the interface of perovskite/hole transport layer.⁴⁵¹ As shown in Figure 58A, the binding energy values indicate that SANS have direct charge transfer with the stabilizer PTAA, which is a key for maintaining stability in various applications. Figure 58B implies that the stabilized SANS have intrinsically high electrical conductivity and good compatibility with the perovskite film, which all together promotes hole transfer, suggesting SANS are an ideal hole extraction layer for hot planar inverted perovskite solar cells (PVSCs). The performance and stability test in Figure 58C–F suggests that the as-prepared PVSCs exhibited enhanced power conversion efficiency within the range from 17.58% to 20.05%. All these experimental results provide substantial evidence that antimonene is an up-and-coming candidate for energy conversion. It has to be admitted that most of the solar cell

studies based on the Xenon are mostly relying on theoretical calculations. Although DFT calculations have put forward numerous ideas, they are not easy to realize due to the assumed simplified and optimized factors.^{452,453}

4.6.4. Tellurene. Lithium–sulfur batteries (LSB) have aroused great attention, attributed to the high specific capacity whose theoretical value is 1675 mAh g⁻¹, and sulfur is abundant in nature.^{454–456} The lithiation process of tellurium, which locates in the same sulfur group, shows a behavior similar to sulfur but has a higher electronic conductivity. It ensures efficient utilization of tellurium cathode with a higher theoretical capacity of 2621 mAh cm⁻³^{457–459} and efficient battery packing for practical portable devices.^{457,460} Therefore, tellurium is viewed to be a promising candidate as a cathode material. Liu *et al.* have designed a kind of lithium tellurium battery (LTB) with

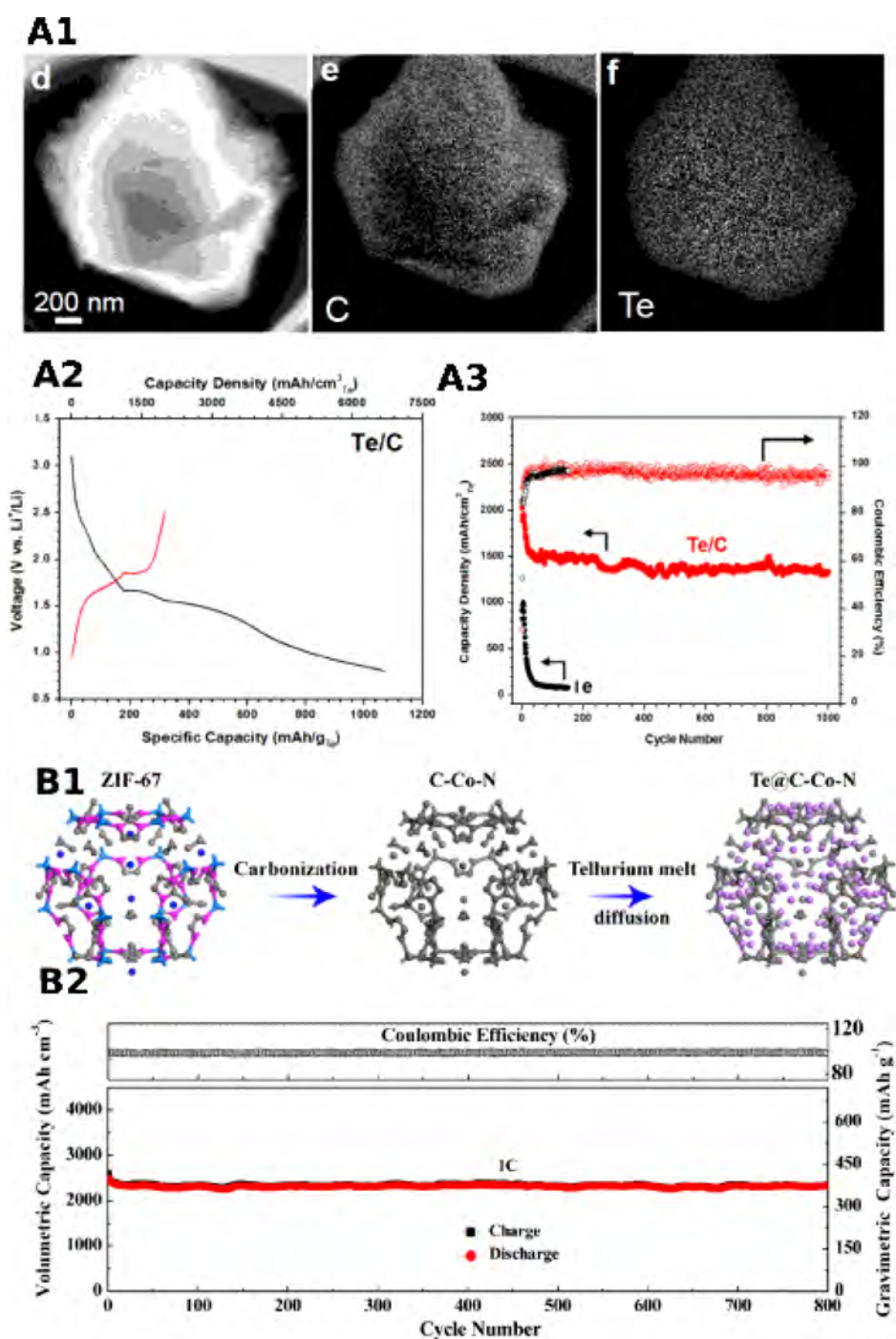


Figure 59. (A1) TEM image (left) and element mapping of C (middle) and Te (right) in the Te/C composite; (A2) charge/discharge profiles; (A3) comparison of the cycling performance and Coulombic efficiency between the pristine Te electrode and Te/C composite. Reproduced with permission from ref 457. Copyright 2014 Royal Society of Chemistry. (B1) Schematic diagram of the Te@C-Co-N cathode preparation process. (B2) Stability performance of Te@C-Co-N composite used as a cathode at 1C during 800 cycles. Reproduced with permission from ref 462. Copyright 2017 American Chemical Society.

the cathode fabricated with the hybrid tellurium and porous carbon materials (Te/C) (Figure 59A1).⁴⁵⁷ The confinement effect exists in the porous carbon matrix. A reversible volumetric capacity of $1400 \text{ mAh}/\text{cm}^3$ can be achieved at a current of $312 \text{ mA}/\text{cm}^3$ by the Te/C cathode (Figure 59A2), and it remains 87% after 1000 cycles (Figure 59A3). All these merits endow the Te/C composite as a promising material for LIB cathodes.

There are some investigations on improving the performance of the tellurium cathode by using a conductive carbonaceous

matrix.^{457–460} However, it is still difficult to achieve an electrode with enhanced conductivity and Te volume expansion ($\Delta V = 104\%$) suppression through confining tellurium in a conductive electrode framework.⁴⁶¹ He *et al.* employed nanoporous carbon polyhedral doped with nitrogen (N) and cobalt (Co) (C-Co-N) for the Te host in Li-Te batteries (Figure 59B1).⁴⁶² Here, 77.2 wt % of Te can be loaded in the Te@C-Co-N cathode, resulting in high capacity ($2615.2 \text{ mAh}/\text{cm}^3$) close to Te's theoretical value. Excellent cycling stability is also obtained, with

as high as 93.6% of capacity retained after 800 cycles (Figure S9B2). The C–Co–N matrix with high conductivity and plenty of micropores offers effective ionic diffusion channels and electron transfer channels. It is worth noting that these investigated Li–Te batteries are not based on the 2D tellurene, which needs further investigations with more promising expectations because of more electronic-active sites in tellurene NSs.

5. CONCLUSIONS AND PERSPECTIVES

We have presented a systematic and comprehensive status of the features, fabrication, and diverse applications of the emerging Xenes. The progress has already provided some critical insights into their physics and potential applications.

The rich material properties in pristine and functionalized Xenes make the design of on-demand devices more promising for electronic, magnetic, photonic, thermal, biological, and sensor nanoplatforms. However, many technical issues are yet to be solved. This section provides our subjective opinion on challenges remaining and opportunities that exist for multidisciplinary research.

Most importantly, to truly advance practical applications, the benefits of Xenes relative to the 3D counterpart and other 2D materials need to be explicitly investigated experimentally and confirmed. Given the advantages of 2D materials on a high surface to volume ratio, flexibility, high storage capacities, and long spin lifetimes, significant research is required to realize commercialization advantage over mature 3D materials and other low-dimensional materials. However, despite facing significant challenges, the unique characteristics of these emerging materials will affect any future technical application bringing revolution in electronics, photonics, sensing, biomedical applications, catalysis, and energy systems.

An issue to be addressed is determination of the influencing factors of such nanoplatforms for different applications. The electro-optic properties, bandgap variations, varied carrier mobility, how the defects or heterostructures modulate electronic and optical structures, and whether morphology and size affect the properties, remain to be deciphered. Furthermore, in the field of biomedical applications, side-effects and cytotoxicity of Xenes during the biological process are yet to be comprehensively determined, particularly in their long-term effects. Regarding phototherapeutic applications, light penetration and safety issues for both PTT and PDT cannot be ignored. PTT has been realized under irradiation by NIR-I light; however, it would be more beneficial to achieve effective PTT in other optical windows (NIR-II and NIR-III) with deeper penetration and reduced scattering. In terms of catalysis, near-neighbor and coupling interactions of multicomponents in heterogeneous catalytic reactions, trigger synergistic catalytic effect, but the strategic design and precise construction of these composite systems remain a challenge. With respect to energy applications, Xenes are suitable for fabricating capacitors and anodes of batteries because of their excellent mechanical properties, excellent conductivity, and high specific surface area. Their use as cathode materials and water purification based on green technology are also main research directions. The application of Xenes improves the overall performance of solar cells as well. However, their demonstrated performance is not as expected, which needs to be improved further. The stability issue of Xenes might result in a nonuniform surface with multiple valences, yielding more complicated catalytic pathways and

byproducts; thus, the surface chemistry of Xenes should also be highlighted in catalytic applications.

5.1. Challenges

5.1.1. Synthesis, Fabrication, and Characterization.

Multitudes of unique properties of Xenes have been theoretically predicted. However, they need to be verified by experiments which require the development of more precise synthetic approaches and advanced characterization techniques. The synthesis of Xenes must be efficient with a high yield from their bulk phase to guarantee the reliability for mass production, which may be more feasible for Xenes than multielemental 2D materials. The fabrication strategies must also be application-oriented. For example, a biomedical application prefers a green and nontoxic fabrication process. Second, depending on a specific application, different strategies must be adopted to mitigate the degradation of the materials, especially for Xenes which lack a layered bulk allotrope. Due to the limitations of the present technique, the expenses for fabricating high-quality, large-scale Xenes with expected functions are still high. More economical and scalable approaches under mild conditions need to be developed.

So far, only layered Xenes structures have been fabricated. Novel fabrication may produce other morphologies such as nanotubes and nanospheres. Graphene has been widely used in 3D print nanocomposites.^{463,464} A combination of additive manufacturing technology and graphene reinforcement offers an efficient way for fast manufacturing of multifunctional 3D systems with enhanced characteristic. As yet, there is no report of 3D print manufacturing for the other Xenes. The storage and the postprocessing of Xenes used in functional devices are also challenging.

Novel approaches are in high demand, and characterizations revealing local properties for specific sites, instead of averaged bulk material attributes, are likewise required. Most of the current characterization methods employed are general techniques such as Raman and FTIR, which provide averaged information, instead of site-specific scenarios, limiting any deep insight into the most desired morphology and effective units, hindering further understanding on the structure–property relationship investigations on Xenes. Although techniques such as STM make it possible to identify the exact structure of obtained 2D nanoplatforms, their applications are not widely applied due to complicated manipulation, limited scope, and relatively high costs.

5.1.2. Database for Opto-Electro-Magnetic-Biomedical Properties.

The Xenes and their heterostructures are multivariate systems as they involve dangling bonds, covalent and noncovalent interactions, etc. It requires multiscale theory and informatics tools to treat them comprehensively. These predictive models can be valuable in exploring new types of Xenes and their based heterostructures. Current achievements in understanding and manipulating opto-electro-magnetic-biomedical properties of Xenes reported so far are still limited, thus the database is limited for utilizing machine learning, artificial intelligence, and data mining for the improvement of this field. A complication is also posed by the repeatability and reliability of all the published data. Another area lacking in reported studies is the magnetic properties of Xenes. Even though the monoelemental 2D materials discussed here are diamagnetic in their pristine form, doping, surface grafting, and heterostructures with other 2D magnetic materials may be useful approaches to produce next-generation magnetic 2D materials.

5.2. Opportunities

This subsection presents our views on the huge opportunities for the progress of this field. It is intended to stimulate future multidisciplinary research.

5.2.1. Multiscale Modeling and Materials Informatics.

The design and synthesis of materials compositionally modified, surface grafted, and manipulated at the interface in a heterostructure can be significantly benefited by combining materials informatics and multiscale modeling. This comprehensive approach can be highly effective in time and resources and can make useful predictions on composition, structure, and interfaces, thus accelerating the discovery of new materials.

Multiscale modeling invokes interactions processing at various time- and length- scales, such as quantum mechanics/density functional theory (DFT) for local chemical interactions containing up to hundreds of atoms; parametrized molecular mechanics for weaker longer length scale interactions; the surrounding ambient media being treated as a polarizable dielectric continuum. Advanced quantum theories, such as solid-state and quantum chemistry-based theories, can be implemented into the modern computer architecture with hybrid processor unit, involving graphical cards, bringing simulation to the exascale computational regime. Combining multiscale modeling and the real-time response theory can address the response of the material to strongly confined local fields for large complex environments and is a promising approach to compute the nonlinear optical response of Xenes and any other low-dimensional materials in ultrashort and ultrastrong pulsed electromagnetic fields.

Materials informatics is an emerging branch of informatics, being inspired by bioinformatics development, which combines statistical, computational, and machine learning methods to forecast and optimize structure, processing, and composition of materials to obtain the required properties. Virtual high-throughput approaches can be combined with multiscale modeling to develop a comprehension of structure–property relationships. Machine learning combining artificial intelligence, together with a recent extension to deep learning, brings a technology revolution with a potential to transform new materials discovery radically.

5.2.2. Photonic Structures. 2D structures can be novel photonic nanocomponents in various forms of optical cavities such as (a) Fabry–Perot cavity; (b) photonic crystal cavity; (c) whispering gallery mode cavity and (d) distributed Bragg reflector cavity.⁴⁶⁵ Xenes can also be an important class of materials for photonics devices and nonlinear optical applications. Fabrication and study of photonic cavities using nanostructured and nanopatterned Xenes for high-quality photonic devices are another area of opportunity, but need more detailed theoretical and experimental studies of their linear and nonlinear optical properties. Plasmonically coupled Xenes can also be another opportunity to enhance optical interactions, such as boosting electron/photon interactions for useful photonic and optoelectronic devices.

Included in nonlinear optical applications are high-speed optical computing, optical power limiting, nonlinear diffraction of light, optical imaging and all-optical signal processing. Only limited experimental studies of nonlinear optical properties exist, mostly as mode-locker or Q-switcher in lasers for ultrashort pulse generation. Thus, great opportunity exists to expand systematic studies to explore other nonlinear optical applications using surface grafted, morphologically varied, and heterostructure configurations.

5.2.3. Magnetic 2-D Xenes. As pointed earlier, the magnetic characteristics of monoelemental 2D materials can be manipulated by doping and vacancies, surface grafting, and heterostructure formation with other 2D magnetic materials to produce novel magnetic 2D materials.

For next-generation information technologies, the emergence of 2D Xenes with a half-metallicity state is highly desired. In this regard, combining with substitutional magnetic doping and in-plane bending treatment in a zigzag direction, the half-metallicity 2D Xene nanoribbons with stability in long-range magnetic order was theoretically suggested.⁴⁶⁶ For the 2D Xenes without intrinsic magnetism, magnetism inducing processes, such as introduction of a vacancy, external fields, doping, and strain, should be explored, which are beneficial for novel electronic and spintronic device applications.⁴⁶⁷ To effectively extend bandgap without damaging the extraordinary electronic properties of 2D Xenes, the functionalization process, mainly the magnetic modification process, should focus on controlling and tailoring desired properties, reversibility of functionalization, and so forth. Through these structural and morphological modifications, both the optical and magnetic properties can be judiciously tailored to yield a new generation of magneto-optic materials, possibly with a very large Verdet constant which quantifies the magneto-optic effect (Faraday rotation).

5.2.4. Phase Change Materials, ENZ Materials, Quantum Materials, and Metasurfaces. Phase change materials have drawn considerable attentions since different phases of the same material may possess varied magnetic, electric, or optical property. Combined with light, local heating, pressure, exposure to a chemical specie, electric pulse or pressure treatment, a phase transition process can be induced, which can change its optical, electric or magnetic property. For example, light-induced refractive index variation from one phase to another in a dielectric is suitable for optical switching device applications. Xenes offer mesoscopic engineering of morphology, surface grafting, ease of heterostructure fabrication, and compositional variability of material and thus hold great potential to develop emerging phase change materials.

Epsilon-near-zero (ENZ) materials are another exciting class of materials within a certain spectral range, possess a near-zero dielectric permittivity value ($\epsilon \sim 0$). This can lead to novel optical phenomena by the unusual behavior of wave propagation and giant enhancement of local electric field. In Xenes, the ENZ property can be realized by using manipulation of morphologies, surface termination, and variability of composition. Utilizing composites or Xenes nanosheets integrated with a negative epsilon plasmonic structure can be another approach to achieve ENZ behavior. To our best of knowledge, no Xenes with ENZ property has been currently reported.

Quantum materials exhibit electron correlations intensively to macroscopic length scale and manifest quantum effects at finite (room) temperature. These materials are characterized by layer-dependent bandgaps and, consequently, optical properties. Xenes can thus be explored as quantum materials.

Metasurfaces are nanoengineered optically thin structures with optical properties (refraction, transmission, reflection) widely different from their naturally occurring bulk form. Metasurfaces can play an essential role in metaphotonics, a rapidly developing field in electro-magnetic fields manipulation within the nanoengineered material to control the light propagation.⁴⁶⁸ There is a great role for metasurfaces as flat optics for versatile applications ranging from solar energy harvesting, to optical communications, to biophotonics and

sensor technology. Metasurfaces enable unprecedented control of electromagnetic waves within short time and space scales, including transmission, refraction, reflection, dispersion, steering, interference, and radiation. Because of their mesoscopic engineering of morphology and compositional variability, Xenes offer a cost-effective “bottom-up” means to produce large scale and high-quality metasurfaces. Additionally, heterostructures can be formed by integrating various 2D materials with Xenes, which can break the mirror symmetry and fabricate chiral metasurfaces. All these advanced properties enable metasurfaces to be considered as a promising candidate in spintronic and spin-controlled photonic applications.

5.2.5. Organic–Inorganic Hybrid Heterostructures.

Modification of Xenes with π -conjugated organic compounds decorated with various functionalities is also worth investigating. The bonding structures of 2D materials generally include covalent or metal–metal bonds and van der Waals interactions, both of which can help tune the electronic and optical properties rationally. Thus, surface conjugation of Xenes with π -electron enriched compounds can modulate the chemical and physical properties by altering the bonding structures.

In a novel heterostructure design, the interlayers between the Xene multilayers can be connected by simultaneously conjugating with the ending functional groups of the same π -electron enriched organic compounds.^{469,168,470} The coupling between the electrons in Xene layers and conjugated organic compounds would produce hybridization of their quantum states, which enhances the DOS, endowing such Xene-organic structure hybrids more superior nonlinear optical performance. The coupling of Xenes with an organic structure of asymmetry containing electron acceptor and donor groups can induce charge transfer that can impact their optoelectronic and nonlinear optical properties. Additionally, organic structures containing thiol groups can bond to metal species to introduce plasmonic coupling. It is also anticipated that the interface between the organic compounds and Xenes will promote the electron transfer and charge separation. Thus, surface engineering of Xenes and chemical modifications of organic compounds offer a promising research direction for modulating the hybrids. The wide variety of functional organic compounds (oligomers, polymers, or supramolecular compounds), which can be conjugated or simply adsorbed on Xenes, provide abundant resources for constructing hybrid heterostructures, reinforcing the Xene-based heterostructures, and achieving versatile applications.

5.2.6. Biomedical Applications. As covered in section 4.5, Xenes have already shown promise for various biomedical applications. The scope of biomedical applications can be further expanded by making the best of the optical properties, induced magnetic characteristics of Xenes, and rational surface modification with drugs, photosensitizers, imaging, and sensing agents. Coupling the Xene surfaces with therapeutic molecules will yield synergetic theranostic 2D platforms, enabling imaging and sensing directed multimode synergetic therapy and real-time monitoring. For clinical applications, both *in vitro* biocompatibility and long-term *in vivo* biosafety need to be evaluated. The design and selection of Xenes responsive to IR light source for deeper penetration and lower incident power will further advance phototherapy.

It still may require some time for phototherapy using Xenes to be directly applied to clinical applications, and researchers have to work mainly on the following aspects. First, we have to admit that even the laser whose wavelength is located within the NIR-

II region can only penetrate around 1 cm, let alone the materials responding at visible light or NIR-I range. Therefore, it might be more meaningful to focus the phototherapy studies involving Xenes and their heterostructures on superficial diseases. Second, constructing Xene-based nanozymes, which can function as peroxidase or glucose oxidase under tumor microenvironment without light irradiation, is a promising direction. In tumor cells, the slightly acidic conditions require higher stability of Xenes than neutral conditions, so certain modifications of Xenes are worth exploring. Third, the costs for obtaining these Xenes are still very high, which limits their applications compared to nitrogen-doped carbon or other cheap materials. How to optimize the synthetic procedure and decrease the expenses is demanding attention. Finally, cross-discipline should always be kept in mind. For example, if we try to apply Xenes in treating lung cancer *via* phototherapy, we can locate the Xene-based laser fiber close to the tumor treatment site, further making the best of the phototherapy potential of Xenes. Dealing with diseases is a never-ending topic, and developing novel materials, especially Xenes-based materials, which are advantageous in many aspects, is always in high demand.

AUTHOR INFORMATION

Corresponding Authors

Paras N. Prasad – *Institute for Lasers, Photonics, and Biophotonics and Department of Chemistry, University at Buffalo, State University of New York, Buffalo 14260-3000, United States*; orcid.org/0000-0002-0905-7084; Email: pnprasad@buffalo.edu

Han Zhang – *Key Laboratory of Optoelectronic Devices and Systems of Ministry of Education and Guangdong Province, Institute of Microscale Optoelectronics, and Otolaryngology Department of the First Affiliated Hospital, Shenzhen Second People's Hospital, Health Science Center, Shenzhen University, Shenzhen 518060, P.R. China*; orcid.org/0000-0002-0166-1973; Email: hzhang@szu.edu.cn

Authors

Zhongjian Xie – *Institute of Pediatrics, Shenzhen Children's Hospital, Shenzhen 518038 Guangdong, P.R. China*; *Key Laboratory of Optoelectronic Devices and Systems of Ministry of Education and Guangdong Province, Institute of Microscale Optoelectronics, and Otolaryngology Department of the First Affiliated Hospital, Shenzhen Second People's Hospital, Health Science Center, Shenzhen University, Shenzhen 518060, P.R. China*

Bin Zhang – *Key Laboratory of Optoelectronic Devices and Systems of Ministry of Education and Guangdong Province, Institute of Microscale Optoelectronics, and Otolaryngology Department of the First Affiliated Hospital, Shenzhen Second People's Hospital, Health Science Center, Shenzhen University, Shenzhen 518060, P.R. China*

Yanqi Ge – *Key Laboratory of Optoelectronic Devices and Systems of Ministry of Education and Guangdong Province, Institute of Microscale Optoelectronics, and Otolaryngology Department of the First Affiliated Hospital, Shenzhen Second People's Hospital, Health Science Center, Shenzhen University, Shenzhen 518060, P.R. China*

Yao Zhu – *Shenzhen Medical Ultrasound Engineering Center, Department of Ultrasonography, Shenzhen People's Hospital, Second Clinical Medical College of Jinan University, First Clinical Medical College of Southern University of Science and Technology, Shenzhen 518020, China*

Guohui Nie – Key Laboratory of Optoelectronic Devices and Systems of Ministry of Education and Guangdong Province, Institute of Microscale Optoelectronics, and Otolaryngology Department of the First Affiliated Hospital, Shenzhen Second People's Hospital, Health Science Center, Shenzhen University, Shenzhen 518060, P.R. China

YuFeng Song – Key Laboratory of Optoelectronic Devices and Systems of Ministry of Education and Guangdong Province, Institute of Microscale Optoelectronics, and Otolaryngology Department of the First Affiliated Hospital, Shenzhen Second People's Hospital, Health Science Center, Shenzhen University, Shenzhen 518060, P.R. China

Chang-Keun Lim – Department of Chemical and Materials Engineering, School of Engineering and Digital Sciences, Nazarbayev University, Nur-Sultan City 010000, Kazakhstan; orcid.org/0000-0003-1306-5770

Complete contact information is available at:

<https://pubs.acs.org/10.1021/acs.chemrev.1c00165>

Author Contributions

[†]Z.X., B.Z., Y.G., Y.Z., G.N., Y.S., and C.-K.L. contributed equally to this work. The manuscript was written through contributions of all authors. All authors have given approval to the final version of the manuscript.

Notes

The authors declare no competing financial interest.

Biographies

Zhongjian Xie received his Ph.D. from the University of Lyon, France, in 2016. Then he joined Prof. Han Zhang's lab at Shenzhen University as a postdoc. Now he is a full professor at Shenzhen Children's Hospital. He has published over 50 peer-reviewed papers with total citations of 2100 and an H-index of 22. His research interests focus on the application of nanomaterials in biological applications.

Bin Zhang is a research professor of Shenzhen Second People's Hospital (First Affiliated Hospital of Shenzhen University). He received his B.S. degree from Peking University (2013) and his Ph.D. degree from the National University of Singapore (2018). His Ph.D. research focused on investigating the synthesis, characterization, and catalytic application of 2D material-supported noble metal single-atom catalysts. His research interest is to fabricate 2D materials supported single-atom catalysts and apply them to biophotonics and nanozymes. He has published more than 40 academic papers in decent journals such as *Nature Communications*, *Journal of the American Chemical Society*, *Angewandte Chemie*, and the like, with a total citation of >2300 times.

Yanqi Ge was born in Jiangsu Province, China. She received her Ph.D. degree in optical engineering from Shenzhen University, Shenzhen, China, in 2018. She is currently researching two-dimensional materials, nonlinear optics, optoelectronics technology, and mode-locked fiber lasers at Shenzhen University.

Zhu Yao received her Ph.D. degree from INSA de Lyon (France, 2016). She is now an Assistant Researcher and Supervisor of Master in Shenzhen People's Hospital (Second Clinical Medical College of Jinan University, First Clinical Medical College of Southern University of Science and Technology). Her research direction focuses on multi-functional nanotheranostic systems based on two-dimensional materials.

Guohui Nie is the director of the Shenzhen Second People's Hospital (First Affiliated Hospital of Shenzhen University), a chief physician, and a full professor. Guohui Nie has been engaged in fundamental and

clinical research on otolaryngology. His research focuses on developing diagnostic methods and nanomedicine based on tumor microenvironment investigation for nasopharyngeal carcinoma. In addition to three professional books, he has also published more than 70 high-quality academic papers in decent, well-reputed international journals such as *Cell Metabolism*, *Nature Communications*, and *PNAS* as the corresponding author.

YuFeng Song received his bachelor's degree from Tianjin University, China in 2008 and Ph.D. from Nanyang Technological University, Singapore, in 2014. He is currently working at Shenzhen University as an Associate Professor. His research interest includes nonlinear fiber optics, ultrafast fiber lasers, optical solitons, and high-speed optical signal processing.

Chang-Keun Lim is an assistant professor of the Department of Chemical and Materials Engineering, Nazarbayev University, and a principal investigator of the Photonic Materials and Biophotonics Laboratory. He obtained his Ph.D. in Materials Science and Engineering at Seoul National University and then developed his professional career at Korea Institute of Science and Technology and SUNY at Buffalo. His research background and interest are based on photoactive organic and organic–inorganic hybrid materials for biomedical and optoelectronic applications.

Han Zhang is a full Professor and Director of Shenzhen Engineering Laboratory of phosphorene and optoelectronics, Shenzhen University. He is an expert on low-dimensional optoelectronic devices and applications. He has published over 400 peer-review research and invited review articles in the last 10 years. The related works have been published in many prestigious journals such as *PNAS*, *Physics Reports*, *Nature Communications*, etc. His publications have received >46000 citations, with an H-index of 121. He has been awarded as Highly Cited Researcher by Clarivate Analytics at 2018, 2019 and 2020, and OSA Fellow.

Paras N Prasad currently holds the unique multidisciplinary position of SUNY Distinguished Professor of Chemistry, Physics, Electrical Engineering, and Medicine (four departments spanning three schools). He is the Samuel P. Capen Chair of Chemistry and the Executive Director of the multidisciplinary Institute for Lasers, Photonics and Biophotonics, which he founded in 1999. His pioneering contributions in interdisciplinary research at the interface of photonics, nanotechnology, and biomedicine have broadly impacted healthcare, energy, and optical technologies. Scientific American named him among the world's top 50 science and technology leaders. He has authored 870 scientific papers: four field-defining monographs, widely used in teaching worldwide, in nonlinear optics, biophotonics, nanophotonics, and nanomedicine; eight edited books; and numerous patents. His Google Scholar h-Index is 130, with ~75,000 citations. His many awards for research excellence include 2021 IEEE Photonics Society William Streifer Scientific Achievement Award; IEEE Pioneer Award in Nanotechnology; the American Chemical Society Peter Debye Award, the Morley Medal and the Schoellkopf Medal; SPIE's highest honor of Gold medal; Optical Society Michael Feld Biophotonics award; Western New York Health Care Industries Technology/Discovery Award; SUNY Excellence in the Pursuit of Knowledge award; UB's first Innovation Impact award; UB President's Medal; Guggenheim Fellowship; Sloan Fellowship. He is an elected foreign fellow of the National Academy of Sciences, India, and a fellow of the National Academy of Inventors. He is a fellow of the APS, OSA, SPIE, and IEEE and was listed among Thompson Reuters "Highly Cited Researchers" for 2014 and 2016. He has Honorary Doctorates from KTH in Sweden, the Aix-Marseille University in France, MEPHI in Russia, and the Federal University of Pernambuco in Brazil. Globally, his technologies

have produced nine spin-off companies, including publicly traded Nanobiotix, now in advanced clinical trials for cancer therapy.

ACKNOWLEDGMENTS

This work was financially supported by China Postdoctoral Science Foundation Funded Project (Grant No. 2019M660212); Guangdong Natural Science Foundation of China (2020A151501787); and Science and Technology Innovation Commission of Shenzhen (Grant No. JCYJ20190806163805286). The Science and Technology Project of Shenzhen (JCYJ20180508152903208), Guangdong Basic and Applied Basic Research Foundation (2019B1515120043 and 2019A151511132), Natural Science Foundation of Guangdong Province (Grant Nos. 2020A151501612) and Longhua District Science and Innovation Commission Project Grants of Shenzhen (JCYJ201904) are grateful acknowledged. We also acknowledge the support from Instrumental Analysis Center of Shenzhen University (Xili Campus). The work at the Institute for Lasers, Photonics and Biophotonics at The University at Buffalo was supported by funds provided by the office of Vice President for Research and Economic Development. The work at Nazarbayev University was supported by the Faculty Development Competitive Research Grant Program of Nazarbayev University (Grant No. 021220FD0151).

REFERENCES

- (1) Moreno, C.; Vilas-Varela, M.; Kretz, B.; Garcia-Lekue, A.; Costache, M. V.; Paradinas, M.; Panighel, M.; Ceballos, G.; Valenzuela, S. S.; Peña, D.; et al. Bottom-up Synthesis of Multifunctional Nanoporous Graphene. *Science* **2018**, *360*, 199–203.
- (2) Zhu, F. F.; Chen, W. J.; Xu, Y.; Gao, C. L.; Guan, D. D.; Liu, C. H.; Qian, D.; Zhang, S. C.; Jia, J. F. Epitaxial Growth of Two-Dimensional Stanene. *Nat. Mater.* **2015**, *14*, 1020–1025.
- (3) Acun, A.; Zhang, L.; Bampoulis, P.; Farmanbar, M.; Van Houselt, A.; Rudenko, A. N.; Lingensfelder, M.; Brocks, G.; Poelsema, B.; Katsnelson, M. I.; et al. Germanene: The Germanium Analogue of Graphene. *J. Phys.: Condens. Matter* **2015**, *27*, 443002.
- (4) Zhao, J.; Liu, H.; Yu, Z.; Quhe, R.; Zhou, S.; Wang, Y.; Liu, C. C.; Zhong, H.; Han, N.; Lu, J.; et al. Rise of Silicene: A Competitive 2D Material. *Prog. Mater. Sci.* **2016**, *83*, 24–151.
- (5) Mayorga-Martinez, C. C.; Gusmao, R.; Sofer, Z.; Pumera, M. Pnictogens Based Biosensor: Phosphorene, Arsenene, Antimonene, and Bismuthene. *Angew. Chem., Int. Ed.* **2019**, *58*, 134–138.
- (6) Pumera, M.; Sofer, Z. 2D Monoelemental Arsenene, Antimonene, and Bismuthene: Beyond Black Phosphorus. *Adv. Mater.* **2017**, *29*, 1605299.
- (7) Xiao, C.; Wang, F.; Yang, S. A.; Lu, Y.; Feng, Y.; Zhang, S. Elemental Ferroelectricity and Antiferroelectricity in Group-V Monolayer. *Adv. Funct. Mater.* **2018**, *28*, 1707383.
- (8) Zhang, S.; Guo, S.; Chen, Z.; Wang, Y.; Gao, H.; Gómez-Herrero, J.; Ares, P.; Zamora, F.; Zhu, Z.; Zeng, H. Recent Progress in 2D Group-VA Semiconductors: From Theory to Experiment. *Chem. Soc. Rev.* **2018**, *47*, 982–1021.
- (9) Xing, C.; Huang, W.; Xie, Z.; Zhao, J.; Ma, D.; Fan, T.; Liang, W.; Ge, Y.; Dong, B.; Li, J.; et al. Ultrasmall Bismuth Quantum Dots: Facile Liquid-Phase Exfoliation, Characterization, and Application in High-Performance UV-Vis Photodetector. *ACS Photonics* **2018**, *5*, 621–629.
- (10) Zhu, Y.; Xie, Z.; Li, J.; Liu, Y.; Li, C.; Liang, W.; Huang, W.; Kang, J.; Cheng, F.; Kang, L.; et al. From Phosphorus to Phosphorene: Applications in Disease Theranostics. *Coord. Chem. Rev.* **2021**, *446*, 214110.
- (11) Zhu, Y.; Liu, Y.; Xie, Z.; He, T.; Su, L.; Guo, F.; Arkin, G.; Lai, X.; Xu, J.; Zhang, H. Magnetic Black Phosphorus Microbubbles for Targeted Tumor Theranostics. *Nanophotonics* **2021**, *10*, 3339–3358.
- (12) Zhang, X.; Hu, J.; Cheng, Y.; Yang, H. Y.; Yao, Y.; Yang, S. A. Borophene as an Extremely High Capacity Electrode Material for Li-Ion and Na-Ion Batteries. *Nanoscale* **2016**, *8*, 15340–15347.
- (13) Jiang, H. R.; Lu, Z.; Wu, M. C.; Ciucci, F.; Zhao, T. S. Borophene: A Promising Anode Material Offering High Specific Capacity and High Rate Capability for Lithium-Ion Batteries. *Nano Energy* **2016**, *23*, 97–104.
- (14) Feng, B.; Sugino, O.; Liu, R. Y.; Zhang, J.; Yukawa, R.; Kawamura, M.; Iimori, T.; Kim, H.; Hasegawa, Y.; Li, H.; et al. Dirac Fermions in Borophene. *Phys. Rev. Lett.* **2017**, *118*, 096401.
- (15) Li, W.; Kong, L.; Chen, C.; Gou, J.; Sheng, S.; Zhang, W.; Li, H.; Chen, L.; Cheng, P.; Wu, K. Experimental Realization of Honeycomb Borophene. *Sci. Bull.* **2018**, *63*, 282–286.
- (16) Chen, Y.; Yu, G.; Chen, W.; Liu, Y.; Li, G. D.; Zhu, P.; Tao, Q.; Li, Q.; Liu, J.; Shen, X.; et al. Highly Active, Nonprecious Electrocatalyst Comprising Borophene Subunits for the Hydrogen Evolution Reaction. *J. Am. Chem. Soc.* **2017**, *139*, 12370–12373.
- (17) Zhai, H. J.; Kiran, B.; Li, J.; Wang, L. S. Hydrocarbon Analogues of Boron Clusters Planarity, Aromaticity and Antiaromaticity. *Nat. Mater.* **2003**, *2*, 827–833.
- (18) Wang, L. S. Photoelectron Spectroscopy of Size-Selected Boron Clusters: From Planar Structures to Borophenes and Borospherenes. *Int. Rev. Phys. Chem.* **2016**, *35*, 69–142.
- (19) Gao, M.; Li, Q. Z.; Yan, X. W.; Wang, J. Prediction of Phonon-Mediated Superconductivity in Borophene. *Phys. Rev. B: Condens. Matter Mater. Phys.* **2017**, *95*, 1–9.
- (20) Li, W. L.; Chen, Q.; Tian, W. J.; Bai, H.; Zhao, Y. F.; Hu, H. S.; Li, J.; Zhai, H. J.; Li, S. D.; Wang, L. S. The B₃₅ cluster with a Double-Hexagonal Vacancy: A New and More Flexible Structural Motif for Borophene. *J. Am. Chem. Soc.* **2014**, *136*, 12257–12260.
- (21) Peng, B.; Zhang, H.; Shao, H.; Xu, Y.; Zhang, R.; Zhu, H. The Electronic, Optical, and Thermodynamic Properties of Borophene from First-Principles Calculations. *J. Mater. Chem. C* **2016**, *4*, 3592–3598.
- (22) Sergeeva, A. P.; Popov, I. A.; Piazza, Z. A.; Li, W. L.; Romanescu, C.; Wang, L. S.; Boldyrev, A. I. Understanding Boron through Size-Selected Clusters: Structure, Chemical Bonding, and Fluxionality. *Acc. Chem. Res.* **2014**, *47*, 1349–1358.
- (23) Kong, X.; Liu, Q.; Zhang, C.; Peng, Z.; Chen, Q. Elemental Two-Dimensional Nanosheets beyond Graphene. *Chem. Soc. Rev.* **2017**, *46*, 2127–2157.
- (24) Qiu, M.; Ren, W. X.; Jeong, T.; Won, M.; Park, G. Y.; Sang, D. K.; Liu, L.-P.; Zhang, H.; Kim, J. S. Omnipotent Phosphorene: A next-Generation, Two-Dimensional Nanoplatfor for Multidisciplinary Biomedical Applications. *Chem. Soc. Rev.* **2018**, *47*, 5588–5601.
- (25) Baughman, R. H.; Eckhardt, H.; Kertesz, M. Structure-property Predictions for New Planar Forms of Carbon: Layered Phases Containing Sp² and Sp Atoms. *J. Chem. Phys.* **1987**, *87*, 6687–6699.
- (26) Li, G.; Li, Y.; Liu, H.; Guo, Y.; Li, Y.; Zhu, D. Architecture of Graphdiyne Nanoscale Films. *Chem. Commun.* **2010**, *46*, 3256–3258.
- (27) Gay-Lussac, J. L.; Thénard, L. J. Sur La Décomposition et La Recomposition de l'acide Boracique. *Ann. Chim. Phys.* **1808**, *68*, 169–174.
- (28) Sands, D. E.; Hoard, J. L. Rhombohedral Elemental Boron. *J. Am. Chem. Soc.* **1957**, *79*, 5582–5583.
- (29) Boustani, I. New Quasi-Planar Surfaces of Bare Boron. *Surf. Sci.* **1997**, *370*, 355–363.
- (30) Mannix, A. J.; Alducin, D.; Myers, B. D.; Liu, X.; Fisher, B. L.; Zhou, X.-F.; Kiraly, B.; Wood, J. D.; Alducin, D.; Myers, B. D.; et al. Synthesis of Borophenes: Anisotropic, Two-Dimensional Boron Polymorphs. *Science* **2015**, *350*, 1513–1516.
- (31) Xie, Z.; Meng, X.; Li, X.; Liang, W.; Huang, W.; Chen, K.; Chen, J.; Xing, C.; Qiu, M.; Zhang, B.; et al. Two-Dimensional Borophene: Properties, Fabrication, and Promising Applications. *Research* **2020**, *2020*, 2624617.
- (32) Duo, Y.; Xie, Z.; Wang, L.; Mahmood Abbasi, N.; Yang, T.; Li, Z.; Hu, G.; Zhang, H. Borophene-Based Biomedical Applications: Status and Future Challenges. *Coord. Chem. Rev.* **2021**, *427*, 213549.

- (33) Tao, W.; Kong, N.; Ji, X.; Zhang, Y.; Sharma, A.; Ouyang, J.; Qi, B.; Wang, J.; Xie, N.; Kang, C.; et al. Emerging Two-Dimensional Monoelemental Materials (Xenes) for Biomedical Applications. *Chem. Soc. Rev.* **2019**, *48*, 2891–2912.
- (34) Yu, X.; Liang, W.; Xing, C.; Chen, K.; Chen, J.; Huang, W.; Xie, N.; Qiu, M.; Yan, X.; Xie, Z.; et al. Emerging 2D Pnictogens for Catalytic Applications: Status and Challenges. *J. Mater. Chem. A* **2020**, *8*, 12887–12927.
- (35) Aktürk, E.; Aktürk, O. Ü.; Ciraci, S. Single and Bilayer Bismuthene: Stability at High Temperature and Mechanical and Electronic Properties. *Phys. Rev. B: Condens. Matter Mater. Phys.* **2016**, *94*, 14115.
- (36) Zhu, Z.; Cai, X.; Yi, S.; Chen, J.; Dai, Y.; Niu, C.; Guo, Z. Multivalency-Driven Formation of Te-Based Monolayer Materials: A Combined First-Principles and Experimental Study. *Phys. Rev. Lett.* **2017**, *119*, 106101–106106.
- (37) Wang, Y.; Qiu, G.; Wang, R.; Huang, S.; Wang, Q.; Liu, Y.; Du, Y.; Goddard, W. A.; Kim, M. J.; Xu, X.; et al. Field-Effect Transistors Made from Solution-Grown Two-Dimensional Tellurene. *Nat. Electron.* **2018**, *1*, 228–236.
- (38) Xie, Z.; Xing, C.; Huang, W.; Fan, T.; Li, Z.; Zhao, J.; Xiang, Y.; Guo, Z.; Li, J.; Yang, Z. Ultrathin 2D Nonlayered Tellurium Nanosheets: Facile Liquid-Phase Exfoliation, Characterization, and Photoresponse with High Performance and Enhanced Stability. *Adv. Funct. Mater.* **2018**, *28*, 1705833.
- (39) Molle, A.; Goldberger, J.; Houssa, M.; Xu, Y.; Zhang, S.-C.; Akinwande, D. Buckled Two-Dimensional Xene Sheets. *Nat. Mater.* **2017**, *16*, 163–169.
- (40) Mannix, A. J.; Kiraly, B.; Hersam, M. C.; Guisinger, N. P. Synthesis and Chemistry of Elemental 2D Materials. *Nat. Rev. Chem.* **2017**, *1*, 0014.
- (41) Kamal, C.; Ezawa, M. Arsenene: Two-Dimensional Buckled and Puckered Honeycomb Arsenic Systems. *Phys. Rev. B: Condens. Matter Mater. Phys.* **2015**, *91*, 85423–85433.
- (42) Zhu, Z.; Cai, X.; Yi, S.; Chen, J.; Dai, Y.; Niu, C.; Guo, Z.; Xie, M.; Liu, F.; Cho, J.-H. Multivalency-Driven Formation of Te-Based Monolayer Materials: A Combined First-Principles and Experimental Study. *Phys. Rev. Lett.* **2017**, *119*, 106101.
- (43) Tai, G.; Hu, T.; Zhou, Y.; Wang, X.; Kong, J.; Zeng, T.; You, Y.; Wang, Q. Synthesis of Atomically Thin Boron Films on Copper Foils. *Angew. Chem., Int. Ed.* **2015**, *54*, 15473–15477.
- (44) Kistanov, A. A.; Khadiullin, S. K.; Zhou, K.; Dmitriev, S. V.; Korznikova, E. A. Environmental Stability of Bismuthene: Oxidation Mechanism and Structural Stability of 2D Pnictogens. *J. Mater. Chem. C* **2019**, *7*, 9195–9202.
- (45) Gao, X.; Liu, H.; Wang, D.; Zhang, J. Graphdiyne: Synthesis, Properties, and Applications. *Chem. Soc. Rev.* **2019**, *48*, 908–936.
- (46) Du, Y.; Zhou, W.; Gao, J.; Pan, X.; Li, Y. Fundament and Application of Graphdiyne in Electrochemical Energy. *Acc. Chem. Res.* **2020**, *53*, 459–469.
- (47) Huang, C.; Li, Y.; Wang, N.; Xue, Y.; Zuo, Z.; Liu, H.; Li, Y. Progress in Research into 2D Graphdiyne-Based Materials. *Chem. Rev.* **2018**, *118*, 7744–7803.
- (48) Li, J.; Gao, X.; Zhu, L.; Ghazzal, M. N.; Zhang, J.; Tung, C.-H.; Wu, L.-Z. Graphdiyne for Crucial Gas Involved Catalytic Reactions in Energy Conversion Applications. *Energy Environ. Sci.* **2020**, *13*, 1326–1346.
- (49) Zuo, Z.; Li, Y. Emerging Electrochemical Energy Applications of Graphdiyne. *Joule* **2019**, *3*, 899–903.
- (50) Balch, A. L.; Winkler, K. Two-Component Polymeric Materials of Fullerenes and the Transition Metal Complexes: A Bridge between Metal–Organic Frameworks and Conducting Polymers. *Chem. Rev.* **2016**, *116*, 3812–3882.
- (51) Terrones, M.; Botello-Méndez, A. R.; Campos-Delgado, J.; López-Urías, F.; Vega-Cantú, Y. I.; Rodríguez-Macías, F. J.; Elías, A. L.; Muñoz-Sandoval, E.; Cano-Márquez, A. G.; Charlier, J.-C. Graphene and Graphite Nanoribbons: Morphology, Properties, Synthesis, Defects and Applications. *Nano Today* **2010**, *5*, 351–372.
- (52) Allen, M. J.; Tung, V. C.; Kaner, R. B. Honeycomb Carbon: A Review of Graphene. *Chem. Rev.* **2010**, *110*, 132–145.
- (53) Niu, T. Carbon Nanotubes Advance Next-Generation Electronics. *Nano Today* **2020**, *35*, 100992.
- (54) Cranford, S. W.; Brommer, D. B.; Buehler, M. J. Extended Graphynes: Simple Scaling Laws for Stiffness, Strength and Fracture. *Nanoscale* **2012**, *4*, 7797–7809.
- (55) Chen, X.; Cheng, M. J.; Wu, S. Q.; Zhu, Z. Z. First-Principle Study of Structure Stability and Electronic Structures of γ Graphyne Derivatives. *Wuli Xuebao* **2017**, *66*, 1071021–1071028.
- (56) Bu, H.; Zhao, M.; Zhang, H.; Wang, X.; Xi, Y.; Wang, Z. Isoelectronic Doping of Graphdiyne with Boron and Nitrogen: Stable Configurations and Band Gap Modification. *J. Phys. Chem. A* **2012**, *116*, 3934–3939.
- (57) Chen, Y.; Xie, Y.; Yan, X.; Cohen, M. L.; Zhang, S. Topological Carbon Materials: A New Perspective. *Phys. Rep.* **2020**, *868*, 1–32.
- (58) Luo, G.; Qian, X.; Liu, H.; Qin, R.; Zhou, J.; Li, L.; Gao, Z.; Wang, E.; Mei, W.-N.; Lu, J.; et al. Quasiparticle Energies and Excitonic Effects of the Two-Dimensional Carbon Allotrope Graphdiyne: Theory and Experiment. *Phys. Rev. B: Condens. Matter Mater. Phys.* **2011**, *84*, 75439.
- (59) Guo, S.; Jiang, Y.; Wu, F.; Yu, P.; Liu, H.; Li, Y.; Mao, L. Graphdiyne-Promoted Highly Efficient Photocatalytic Activity of Graphdiyne/Silver Phosphate Pickering Emulsion Under Visible-Light Irradiation. *ACS Appl. Mater. Interfaces* **2019**, *11*, 2684–2691.
- (60) Lv, J. X.; Zhang, Z. M.; Wang, J.; Lu, X. L.; Zhang, W.; Lu, T. B. In Situ Synthesis of CdS/Graphdiyne Heterojunction for Enhanced Photocatalytic Activity of Hydrogen Production. *ACS Appl. Mater. Interfaces* **2019**, *11*, 2655–2661.
- (61) Dong, Y.; Zhao, Y.; Chen, Y.; Feng, Y.; Zhu, M.; Ju, C.; Zhang, B.; Liu, H.; Xu, J. Graphdiyne-Hybridized N-Doped TiO₂ Nanosheets for Enhanced Visible Light Photocatalytic Activity. *J. Mater. Sci.* **2018**, *53*, 8921–8932.
- (62) Si, H.-Y.; Mao, C.-J.; Zhou, J.-Y.; Rong, X.-F.; Deng, Q.-X.; Chen, S.-L.; Zhao, J.-J.; Sun, X.-G.; Shen, Y.; Feng, W.-J.; et al. Z-Scheme Ag₃PO₄/Graphdiyne/g-C₃N₄ Composites: Enhanced Photocatalytic O₂ Generation Benefiting from Dual Roles of Graphdiyne. *Carbon* **2018**, *132*, 598–605.
- (63) Xue, Y.; Huang, B.; Yi, Y.; Guo, Y.; Zuo, Z.; Li, Y.; Jia, Z.; Liu, H.; Li, Y. Anchoring zero valence single atoms of nickel and iron on graphdiyne for hydrogen evolution. *Nat. Commun.* **2018**, *9*, 1460.
- (64) Lv, Q.; Si, W.; Yang, Z.; Wang, N.; Tu, Z.; Yi, Y.; Huang, C.; Jiang, L.; Zhang, M.; He, J. Nitrogen-Doped Porous Graphdiyne: A Highly Efficient Metal-Free Electrocatalyst for Oxygen Reduction Reaction. *ACS Appl. Mater. Interfaces* **2017**, *9*, 29744–29752.
- (65) Yu, H.; Xue, Y.; Lan, H.; Chao, Z.; Zhao, Y.; Li, Z.; Li, Y. Controlled Growth of MoS₂ Nanosheets on 2D N-Doped Graphdiyne Nanolayers for Highly Associated Effects on Water Reduction. *Adv. Funct. Mater.* **2018**, *28*, 1707564.
- (66) Yin, X. P.; Wang, H. J.; Ta Ng, S. F.; Lu, X. L.; Shu, M. Engineering the Coordination Environment of Single-Atom Platinum Anchored on Graphdiyne for Optimizing Electrocatalytic Hydrogen Evolution. *Angew. Chem., Int. Ed.* **2018**, *57*, 9382–9386.
- (67) Kuang, P.; Zhu, B.; Li, Y.; Liu, H.; Yu, J.; Fan, K. Graphdiyne: A Superior Carbon Additive to Boost the Activity of Water Oxidation Catalysts. *Nanoscale Horiz.* **2018**, *3*, 317–326.
- (68) Hui, L.; Jia, D.; Yu, H.; Xue, Y.; Li, Y. Ultrathin Graphdiyne-Wrapped Iron Carbonate Hydroxide Nanosheets toward Efficient Water Splitting. *ACS Appl. Mater. Interfaces* **2019**, *11*, 2618–2625.
- (69) Han, Y.-Y.; Lu, X.-L.; Tang, S.-F.; Yin, X.-P.; Wei, Z.-W.; Lu, T.-B. Metal-Free 2D/2D Heterojunction of Graphitic Carbon Nitride/Graphdiyne for Improving the Hole Mobility of Graphitic Carbon Nitride. *Adv. Energy Mater.* **2018**, *8*, 1702992.
- (70) Gao, X.; Li, J.; Du, R.; Zhou, J.; Huang, M.-Y.; Liu, R.; Li, J.; Xie, Z.; Wu, L.-Z.; Liu, Z.; et al. Direct Synthesis of Graphdiyne Nanowalls on Arbitrary Substrates and Its Application for Photoelectrochemical Water Splitting Cell. *Adv. Mater.* **2017**, *29*, 1605308.
- (71) Chen, Z. W.; Wen, Z.; Jiang, Q. Rational Design of Ag₃₈ Cluster Supported by Graphdiyne for Catalytic CO Oxidation. *J. Phys. Chem. C* **2017**, *121*, 3463–3468.

- (72) Seif, A.; López, M. J.; Granja-Delrío, A.; Azizi, K.; Alonso, J. A. Adsorption and Growth of Palladium Clusters on Graphdiyne. *Phys. Chem. Chem. Phys.* **2017**, *19*, 19094–19102.
- (73) He, J.; Bao, K.; Cui, W. C.; Yu, J. Y.; Huang, C.; Shen, X.; Cui, Z.; Wang, N. Construction of Large-Area Uniform Graphdiyne Film for High-Performance Lithium-Ion Batteries. *Chem. - Eur. J.* **2018**, *24*, 1187–1192.
- (74) Kim, J.; Kang, S.; Lim, J.; Kim, W. Y. Study of Li Adsorption on Graphdiyne Using Hybrid DFT Calculations. *ACS Appl. Mater. Interfaces* **2019**, *11*, 2677–2683.
- (75) Wang, N.; He, J.; Tu, Z.; Yang, Z.; Zhao, F.; Li, X.; Huang, C.; Wang, K.; Jiu, T.; Yi, Y.; Li, Y. Synthesis of Chlorine-Substituted Graphdiyne and Applications for Lithium-Ion Storage. *Angew. Chem., Int. Ed.* **2017**, *56*, 10740–10745.
- (76) He, J.; Wang, N.; Cui, Z.; Du, H.; Fu, L.; Huang, C.; Yang, Z.; Shen, X.; Yi, Y.; Tu, Z. Hydrogen Substituted Graphdiyne as Carbon-Rich Flexible Electrode for Lithium and Sodium Ion Batteries. *Nat. Commun.* **2017**, *8*, 1172.
- (77) Du, H.; Yang, H.; Huang, C.; He, J.; Liu, H.; Li, Y. Graphdiyne Applied for Lithium-Ion Capacitors Displaying High Power and Energy Densities. *Nano Energy* **2016**, *22*, 615–622.
- (78) Shen, X.; Yang, Z.; Wang, K.; Wang, N.; He, J.; Du, H.; Huang, C. Nitrogen-Doped Graphdiyne as High-Capacity Electrode Materials for Both Lithium-Ion and Sodium-Ion Capacitors. *ChemElectroChem* **2018**, *5*, 1435–1443.
- (79) Zhang, S.; He, J.; Zheng, J.; Huang, C.; Lv, Q.; Wang, K.; Wang, N.; Lan, Z. Porous Graphdiyne Applied for Sodium Ion Storage. *J. Mater. Chem. A* **2017**, *5*, 2045–2051.
- (80) Farokh Niaei, A. H.; Hussain, T.; Hankel, M.; Searles, D. J. Sodium-Intercalated Bulk Graphdiyne as an Anode Material for Rechargeable Batteries. *J. Power Sources* **2017**, *343*, 354–363.
- (81) Wang, K.; Wang, N.; He, J.; Yang, Z.; Shen, X.; Huang, C. Preparation of 3D Architecture Graphdiyne Nanosheets for High-Performance Sodium-Ion Batteries and Capacitors. *ACS Appl. Mater. Interfaces* **2017**, *9*, 40604–40613.
- (82) Huang, C. S.; Li, Y. Structure of 2D Graphdiyne and Its Application in Energy Fields. *Wuli Huaxue Xuebao* **2016**, *32*, 1314–1329.
- (83) Li, J.; Jiu, T.; Chen, S.; Liu, L.; Yao, Q.; Bi, F.; Zhao, C.; Wang, Z.; Zhao, M.; Zhang, G. Graphdiyne as Host Active Material for Perovskite Solar Cell Application. *Nano Lett.* **2018**, *18*, 6941–6947.
- (84) Li, J.; Zhao, M.; Zhao, C.; Jian, H.; Wang, N.; Yao, L.; Huang, C.; Zhao, Y.; Jiu, T. Graphdiyne-Doped P₃CT-K as an Efficient Hole-Transport Layer for MAPbI₃ Perovskite Solar Cells. *ACS Appl. Mater. Interfaces* **2019**, *11*, 2626–2631.
- (85) Liu, J.; Chen, C.; Zhao, Y. Progress and Prospects of Graphdiyne-Based Materials in Biomedical Applications. *Adv. Mater.* **2019**, *31*, 1804386.
- (86) Zhou, X.; You, M.; Wang, F.; Wang, Z.; Gao, X.; Jing, C.; Liu, J.; Guo, M.; Li, J.; Luo, A. Multifunctional Graphdiyne–Cerium Oxide Nanozymes Facilitate MicroRNA Delivery and Attenuate Tumor Hypoxia for Highly Efficient Radiotherapy of Esophageal Cancer. *Adv. Mater.* **2021**, *33*, 2100556.
- (87) Min, H.; Qi, Y.; Zhang, Y.; Han, X.; Li, Y. A Graphdiyne Oxide-Based Iron Sponge with Photothermally Enhanced Tumor-specific Fenton Chemistry. *Adv. Mater.* **2020**, *32*, 2000038.
- (88) Xie, J.; Wang, C.; Wang, N.; Zhu, S.; Mei, L.; Zhang, X.; Yong, Y.; Li, L.; Chen, C.; Huang, C.; et al. Graphdiyne Nanoradioprotector with Efficient Free Radical Scavenging Ability for Mitigating Radiation-Induced Gastrointestinal Tract Damage. *Biomaterials* **2020**, *244*, 119940.
- (89) Xie, J.; Ning, W.; Dong, X.; Wang, C.; Zhao, Y. Graphdiyne Nanoparticles with High Free Radical Scavenging Activity for Radiation Protection. *ACS Appl. Mater. Interfaces* **2019**, *11*, 2579–2590.
- (90) Onida, G.; Reining, L.; Rubio, A. Electronic Excitations: Density-Functional versus Many-Body Green's-Function Approaches. *Rev. Mod. Phys.* **2002**, *74*, 601–659.
- (91) Sheng, X.-L.; Chen, C.; Liu, H.; Chen, Z.; Yu, Z.-M.; Zhao, Y. X.; Yang, S. A. Two-Dimensional Second-Order Topological Insulator in Graphdiyne. *Phys. Rev. Lett.* **2019**, *123*, 256402.
- (92) Qian, X.; Liu, H.; Huang, C.; Chen, S.; Zhang, L.; Li, Y.; Wang, J.; Li, Y. Self-Catalyzed Growth of Large-Area Nanofilms of Two-Dimensional Carbon. *Sci. Rep.* **2015**, *5*, 1–7.
- (93) Qian, X.; Ning, Z.; Li, Y.; Liu, H.; Ouyang, C.; Chen, Q.; Li, Y. Construction of Graphdiyne Nanowires with High-Conductivity and Mobility. *Dalt. Trans.* **2012**, *41*, 730–733.
- (94) Ge, C.; Chen, J.; Tang, S.; Du, Y.; Tang, N. Review of the Electronic, Optical, and Magnetic Properties of Graphdiyne: From Theories to Experiments. *ACS Appl. Mater. Interfaces* **2019**, *11*, 2707–2716.
- (95) Muz, İ.; Göktaş, F.; Kurban, M. Size Dependence in the Electronic and Optical Properties of a BN Analogue of Two-Dimensional Graphdiyne: A Theoretical Study. *Chem. Phys.* **2020**, *539*, 110929.
- (96) Zheng, Q.; Luo, G.; Liu, Q.; Quhe, R.; Zheng, J.; Tang, K.; Gao, Z.; Nagase, S.; Lu, J. Structural and Electronic Properties of Bilayer and Trilayer Graphdiyne. *Nanoscale* **2012**, *4*, 3990–3996.
- (97) Cui, H.-J.; Sheng, X.-L.; Yan, Q.-B.; Zheng, Q.-R.; Su, G. Strain-Induced Dirac Cone-like Electronic Structures and Semiconductor–Semimetal Transition in Graphdiyne. *Phys. Chem. Chem. Phys.* **2013**, *15*, 8179–8185.
- (98) Luo, G.; Zheng, Q.; Mei, W.-N.; Lu, J.; Nagase, S. Structural, Electronic, and Optical Properties of Bulk Graphdiyne. *J. Phys. Chem. C* **2013**, *117*, 13072–13079.
- (99) Zhou, J.; Gao, X.; Liu, R.; Xie, Z.; Yang, J.; Zhang, S.; Zhang, G.; Liu, H.; Li, Y.; Zhang, J. Synthesis of Graphdiyne Nanowalls Using Acetylenic Coupling Reaction. *J. Am. Chem. Soc.* **2015**, *137*, 7596–7599.
- (100) Li, Y.; Heo, J.; Lim, C.-K.; Pliss, A.; Kachynski, A. V.; Kuzmin, A. N.; Kim, S.; Prasad, P. N. Organelle Specific Imaging in Live Cells and Immuno-Labeling Using Resonance Raman Probe. *Biomaterials* **2015**, *53*, 25–31.
- (101) Li, S.; Chen, Y.; Liu, H.; Wang, Y.; Liu, L.; Lv, F.; Li, Y.; Wang, S. Graphdiyne Materials as Nanotransducer for in Vivo Photoacoustic Imaging and Photothermal Therapy of Tumor. *Chem. Mater.* **2017**, *29*, 6087–6094.
- (102) Wang, C.; Yu, P.; Guo, S.; Mao, L.; Liu, H.; Li, Y. Graphdiyne Oxide as a Platform for Fluorescence Sensing. *Chem. Commun.* **2016**, *52*, 5629–5632.
- (103) Ferrari, A.; Robertson, J. Interpretation of Raman Spectra of Disordered and Amorphous Carbon. *Phys. Rev. B: Condens. Matter Mater. Phys.* **2000**, *61*, 14095–14107.
- (104) Zhang, S.; Wang, J.; Li, Z.; Zhao, R.; Tong, L.; Liu, Z.; Zhang, J.; Liu, Z. Raman Spectra and Corresponding Strain Effects in Graphyne and Graphdiyne. *J. Phys. Chem. C* **2016**, *120*, 10605–10613.
- (105) Trusovas, R.; Raikaitis, G.; Niaura, G.; Barkauskas, J.; Valušis, G.; Pauliukaite, R. Recent Advances in Laser Utilization in the Chemical Modification of Graphene Oxide and Its Applications. *Adv. Opt. Mater.* **2016**, *4*, 37–65.
- (106) Wu, L.; Dong, Y.; Zhao, J.; Ma, D.; Huang, W.; Zhang, Y.; Wang, Y.; Jiang, X.; Xiang, Y.; Li, J.; et al. Kerr Nonlinearity in 2D Graphdiyne for Passive Photonic Diodes. *Adv. Mater.* **2019**, *31*, 1807981.
- (107) Zhao, Y.; Guo, P.; Li, X.; Jin, Z. Ultrafast Photonics Application of Graphdiyne in the Optical Communication Region. *Carbon* **2019**, *149*, 336–341.
- (108) Zhang, F.; Liu, G.; Yuan, J.; Wang, Z.; Tang, T.; Fu, S.; Zhang, H.; Man, Z.; Xing, F.; Xu, X. 2D Graphdiyne: An Excellent Ultraviolet Nonlinear Absorption Material. *Nanoscale* **2020**, *12*, 6243–6249.
- (109) Marder, S. R.; Beratan, D. N.; Cheng, L.-T. Approaches for Optimizing the First Electronic Hyperpolarizability of Conjugated Organic Molecules. *Science* **1991**, *252*, 103–106.
- (110) Marder, S. R.; Perry, J. W. Molecular Materials for Second-Order Nonlinear Optical Applications. *Adv. Mater.* **1993**, *5*, 804–815.
- (111) Li, X. Design of Novel Graphdiyne-Based Materials with Large Second-Order Nonlinear Optical Properties. *J. Mater. Chem. C* **2018**, *6*, 7576–7583.

- (112) Li, X.; Li, S. Investigations of Electronic and Nonlinear Optical Properties of Single Alkali Metal Adsorbed Graphene, Graphyne and Graphdiyne Systems by First-Principles Calculations. *J. Mater. Chem. C* **2019**, *7*, 1630–1640.
- (113) Li, X. Graphdiyne: A Promising Nonlinear Optical Material Modulated by Tetrahedral Alkali-Metal Nitrides. *J. Mol. Liq.* **2019**, *277*, 641–645.
- (114) Li, X.; Lu, J. Giant Enhancement of Electronic Polarizability and the First Hyperpolarizability of Fluoride-Decorated Graphene versus Graphyne and Graphdiyne: Insights from Ab Initio Calculations. *Phys. Chem. Chem. Phys.* **2019**, *21*, 13165–13175.
- (115) Li, X.; Zhang, Y.; Lu, J. Remarkably Enhanced First Hyperpolarizability and Nonlinear Refractive Index of Novel Graphdiyne-Based Materials for Promising Optoelectronic Applications: A First-Principles Study. *Appl. Surf. Sci.* **2020**, *512*, 145544.
- (116) Yu, H.; Xue, Y.; Hui, L.; He, F.; Zhang, C.; Liu, Y.; Fang, Y.; Xing, C.; Li, Y.; Liu, H.; et al. Graphdiyne-Engineered Heterostructures for Efficient Overall Water-Splitting. *Nano Energy* **2019**, *64*, 103928.
- (117) Hui, L.; Xue, Y.; He, F.; Jia, D.; Li, Y. Efficient Hydrogen Generation on Graphdiyne-Based Heterostructure. *Nano Energy* **2019**, *55*, 135–142.
- (118) Penev, E. S.; Bhowmick, S.; Sadzadeh, A.; Jakobson, B. I. Polymorphism of Two-Dimensional Boron. *Nano Lett.* **2012**, *12*, 2441–2445.
- (119) Zhang, Z.; Yang, Y.; Penev, E. S.; Jakobson, B. I. Elasticity, Flexibility, and Ideal Strength of Borophenes. *Adv. Funct. Mater.* **2017**, *27*, 1605059.
- (120) Zhang, Z.; Mannix, A. J.; Hu, Z.; Kiraly, B.; Guisinger, N. P.; Hersam, M. C.; Jakobson, B. I. Substrate-Induced Nanoscale Undulations of Borophene on Silver. *Nano Lett.* **2016**, *16*, 6622–6627.
- (121) Penev, E. S.; Kutana, A.; Jakobson, B. I. Can Two-Dimensional Boron Superconduct? *Nano Lett.* **2016**, *16*, 2522–2526.
- (122) Zhao, Y.; Zeng, S.; Ni, J. Superconductivity in Two-Dimensional Boron Allotropes. *Phys. Rev. B: Condens. Matter Mater. Phys.* **2016**, *93*, 1–6.
- (123) Adamska, L.; Sadasivam, S.; Foley, J. J.; Darancet, P.; Sharifzadeh, S. First-Principles Investigation of Borophene as a Monolayer Transparent Conductor. *J. Phys. Chem. C* **2018**, *122*, 4037–4045.
- (124) Liu, Y.; Penev, E. S.; Jakobson, B. I. Probing the Synthesis of Two-Dimensional Boron by First-Principles Computations. *Angew. Chem., Int. Ed.* **2013**, *52*, 3156–3159.
- (125) Wu, X.; Dai, J.; Zhao, Y.; Zhuo, Z.; Yang, J.; Zeng, X. Two-Dimensional Boron Monolayer Sheets. *ACS Nano* **2012**, *6* (8), 7443–7453.
- (126) Tsafack, T.; Jakobson, B. I. Thermomechanical Analysis of Two-Dimensional Boron Monolayers. *Phys. Rev. B: Condens. Matter Mater. Phys.* **2016**, *93*, 165434.
- (127) Xie, S. Y.; Wang, Y.; Li, X. Flat Boron: A New Cousin of Graphene. *Adv. Mater.* **2019**, *31*, 1900392.
- (128) Zhang, Z.; Yang, Y.; Gao, G.; Jakobson, B. I. Two-dimensional Boron Monolayers Mediated by Metal Substrates. *Angew. Chem., Int. Ed.* **2015**, *54*, 13022–13026.
- (129) Ma, F.; Jiao, Y.; Gao, G.; Gu, Y.; Bilic, A.; Chen, Z.; Du, A. Graphene-like Two-Dimensional Ionic Boron with Double Dirac Cones at Ambient Condition. *Nano Lett.* **2016**, *16*, 3022–3028.
- (130) Tang, H.; Ismail-Beigi, S. Novel Precursors for Boron Nanotubes: The Competition of Two-Center and Three-Center Bonding in Boron Sheets. *Phys. Rev. Lett.* **2007**, *99*, 115501.
- (131) Feng, B.; Zhang, J.; Liu, R.-Y.; Iimori, T.; Lian, C.; Li, H.; Chen, L.; Wu, K.; Meng, S.; Komori, F.; et al. Direct Evidence of Metallic Bands in a Monolayer Boron Sheet. *Phys. Rev. B: Condens. Matter Mater. Phys.* **2016**, *94*, 41408.
- (132) Mannix, A. J.; Zhou, X.-F.; Kiraly, B.; Wood, J. D.; Alducin, D.; Myers, B. D.; Liu, X.; Fisher, B. L.; Santiago, U.; Guest, J. R.; et al. Synthesis of Borophenes: Anisotropic, Two-Dimensional Boron Polymorphs. *Science* **2015**, *350*, 1513–1516.
- (133) Feng, B.; Zhang, J.; Zhong, Q.; Li, W.; Li, S.; Li, H.; Cheng, P.; Meng, S.; Chen, L.; Wu, K. Experimental Realization of Two-Dimensional Boron Sheets. *Nat. Chem.* **2016**, *8*, 563–568.
- (134) Adamska, L.; Sadasivam, S.; Foley, J. J.; Darancet, P.; Sharifzadeh, S. First-Principles Investigation of Borophene as a Monolayer Transparent Conductor. *J. Phys. Chem. C* **2018**, *122*, 4037–4045.
- (135) Lherbier, A.; Botello-Méndez, A. R.; Charlier, J.-C. Electronic and Optical Properties of Pristine and Oxidized Borophene. *2D Mater.* **2016**, *3*, 45006.
- (136) Shen, J.; Yang, Z.; Wang, Y.; Xu, L.-C.; Liu, R.; Liu, X. The Gas Sensing Performance of Borophene/MoS₂ Heterostructure. *Appl. Surf. Sci.* **2020**, *504*, 144412.
- (137) Liu, X.; Hersam, M. C. Borophene-Graphene Heterostructures. *Sci. Adv.* **2019**, *5*, No. eaax6444.
- (138) Liu, X.; Wei, Z.; Balla, L.; Mannix, A. J.; Guisinger, N. P.; Luijten, E.; Hersam, M. C. Self-Assembly of Electronically Abrupt Borophene/Organic Lateral Heterostructures. *Sci. Adv.* **2017**, *3*, No. e1602356.
- (139) Jiang, J. W.; Wang, X. C.; Song, Y.; Mi, W. B. Tunable Schottky Barrier and Electronic Properties in Borophene/g-C₂N van Der Waals Heterostructures. *Appl. Surf. Sci.* **2018**, *440*, 42–46.
- (140) Zhang, S.; Yan, Z.; Li, Y.; Chen, Z.; Zeng, H. Atomically Thin Arsenene and Antimonene: Semimetal-Semiconductor and Indirect-Direct Band-Gap Transitions. *Angew. Chem., Int. Ed.* **2015**, *54*, 3112–3115.
- (141) Hu, Y.; Shu, T.; Mao, C.; Xue, L.; Yan, Z.; Wu, Y. Arsenene and Antimonene Doped by Group-VA Atoms: First-Principles Studies of the Geometric Structures, Electronic Properties and STM Images. *Phys. B* **2019**, *553*, 195–201.
- (142) Kang, J.; Noh, S. H.; Han, B. First-Principles Computational Design of Unknown Flat Arsenene Epitaxially Grown on Copper Substrate. *Appl. Surf. Sci.* **2019**, *467–468*, 561–566.
- (143) Ares, P.; Palacios, J. J.; Abellán, G.; Gómez-Herrero, J.; Zamora, F. Recent Progress on Antimonene: A New Bidimensional Material. *Adv. Mater.* **2018**, *30*, 1–27.
- (144) Wang, X.; Song, J.; Qu, J. Antimonene: From Experimental Preparation to Practical Application. *Angew. Chem., Int. Ed.* **2019**, *57*, 2–13.
- (145) Lu, L.; Tang, X.; Cao, R.; Wu, L.; Li, Z.; Jing, G.; Dong, B.; Lu, S.; Li, Y.; Xiang, Y.; et al. Broadband Nonlinear Optical Response in Few-Layer Antimonene and Antimonene Quantum Dots: A Promising Optical Kerr Media with Enhanced Stability. *Adv. Opt. Mater.* **2017**, *5*, 1700301.
- (146) Reis, F.; Li, G.; Dudy, L.; Bauernfeind, M.; Glass, S.; Hanke, W.; Thomale, R. Bismuthene on a SiC Substrate: A Candidate for a High-Temperature Quantum Spin Hall Material. *Science* **2017**, *357*, 287–290.
- (147) Lu, L.; Wang, W.; Wu, L.; Jiang, X.; Xiang, Y.; Li, J.; Fan, D.; Zhang, H. All-Optical Switching of Two Continuous Waves in Few Layer Bismuthene Based on Spatial Cross-Phase Modulation. *ACS Photonics* **2017**, *4*, 2852–2861.
- (148) Song, Y.; Liang, Z.; Jiang, X.; Chen, Y.; Li, Z.; Lu, L.; Ge, Y.; Wang, K.; Zheng, J.; Lu, S.; et al. Few-Layer Antimonene Decorated Microfiber: Ultra-Short Pulse Generation and All-Optical Thresholding with Enhanced Long Term Stability. *2D Mater.* **2017**, *4*, 45010.
- (149) Wang, Y.; Huang, P.; Ye, M.; Quhe, R.; Pan, Y.; Zhang, H.; Zhong, H.; Shi, J.; Lu, J. Many-Body Effect, Carrier Mobility, and Device Performance of Hexagonal Arsenene and Antimonene. *Chem. Mater.* **2017**, *29*, 2191–2201.
- (150) Gupta, S. K.; Sonvane, Y.; Wang, G.; Pandey, R. Size and Edge Roughness Effects on Thermal Conductivity of Pristine Antimonene Allotropes. *Chem. Phys. Lett.* **2015**, *641*, 169–172.
- (151) Lee, J.; Tian, W. C.; Wang, W. L.; Yao, D. X. Two-Dimensional Pnictogen Honeycomb Lattice: Structure, on-Site Spin-Orbit Coupling and Spin Polarization. *Sci. Rep.* **2015**, *5*, 11512.
- (152) Gibaja, C.; Rodríguez-San-Miguel, D.; Ares, P.; Gómez-Herrero, J.; Varela, M.; Gillen, R.; Maultzsch, J.; Hauke, F.; Hirsch, A.; Abellán, G.; et al. Few-Layer Antimonene by Liquid-Phase Exfoliation. *Angew. Chem., Int. Ed.* **2016**, *55*, 14345–14349.

- (153) Ares, P.; Aguilar-Galindo, F.; Rodríguez-San-Miguel, D.; Aldave, D. A.; Díaz-Tendero, S.; Alcamí, M.; Martín, F.; Gómez-Herrero, J.; Zamora, F. Mechanical Isolation of Highly Stable Antimonene under Ambient Conditions. *Adv. Mater.* **2016**, *28*, 6332–6336.
- (154) Wu, X.; Shao, Y.; Liu, H.; Feng, Z.; Wang, Y. L.; Sun, J. T.; Liu, C.; Wang, J. O.; Liu, Z. L.; Zhu, S. Y.; et al. Epitaxial Growth and Air-Stability of Monolayer Antimonene on PdTe₂. *Adv. Mater.* **2017**, *29*, 1605407.
- (155) Ji, J.; Song, X.; Liu, J.; Yan, Z.; Huo, C.; Zhang, S.; Su, M.; Liao, L.; Wang, W.; Ni, Z.; et al. Two-Dimensional Antimonene Single Crystals Grown by van Der Waals Epitaxy. *Nat. Commun.* **2016**, *7*, 1–9.
- (156) Gu, J.; Du, Z.; Zhang, C.; Ma, J.; Li, B.; Yang, S. Liquid-Phase Exfoliated Metallic Antimony Nanosheets toward High Volumetric Sodium Storage. *Adv. Energy Mater.* **2017**, *7*, 1700447.
- (157) Li, F.; Xue, M.; Li, J.; Ma, X.; Chen, L.; Zhang, X.; MacFarlane, D. R.; Zhang, J. Unlocking the Electrocatalytic Activity of Antimony for CO₂ Reduction by Two-Dimensional Engineering of the Bulk Material. *Angew. Chem., Int. Ed.* **2017**, *56*, 14718–14722.
- (158) Martínez-Periñán, E.; Down, M. P.; Gibaja, C.; Lorenzo, E.; Zamora, F.; Banks, C. E. Antimonene: A Novel 2D Nanomaterial for Supercapacitor Applications. *Adv. Energy Mater.* **2018**, *8*, 1702606.
- (159) Castellanos-Gomez, A.; Vicarelli, L.; Prada, E.; Island, J. O.; Narasimha-Acharya, K. L.; Blanter, S. I.; Groenendijk, D. J.; Buscema, M.; Steele, G. A.; Alvarez, J. V.; et al. Isolation and Characterization of Few-Layer Black Phosphorus. *2D Mater.* **2014**, *1*, 25001.
- (160) Şahin, H.; Cahangirov, S.; Topsakal, M.; Bekaroglu, E.; Akturk, E.; Senger, R. T.; Ciraci, S. Monolayer Honeycomb Structures of Group-IV Elements and III-V Binary Compounds: First-Principles Calculations. *Phys. Rev. B: Condens. Matter Mater. Phys.* **2009**, *80*, 155453.
- (161) Peng, X.; Wei, Q.; Copple, A. Strain-Engineered Direct-Indirect Band Gap Transition and Its Mechanism in Two-Dimensional Phosphorene. *Phys. Rev. B: Condens. Matter Mater. Phys.* **2014**, *90*, 85402.
- (162) Wang, G.; Pandey, R.; Karna, S. P. Atomically Thin Group V Elemental Films: Theoretical Investigations of Antimonene Allotropes. *ACS Appl. Mater. Interfaces* **2015**, *7*, 11490–11496.
- (163) Zhang, S.; Xie, M.; Li, F.; Yan, Z.; Li, Y.; Kan, E.; Liu, W.; Chen, Z.; Zeng, H. Semiconducting Group 15 Monolayers: A Broad Range of Band Gaps and High Carrier Mobilities. *Angew. Chem., Int. Ed.* **2016**, *55*, 1666–1669.
- (164) Wang, S.; Wang, W.; Zhao, G. Thermal Transport Properties of Antimonene: An Ab Initio Study. *Phys. Chem. Chem. Phys.* **2016**, *18*, 31217–31222.
- (165) Zhang, S.; Zhou, W.; Ma, Y.; Ji, J.; Cai, B.; Yang, S. A.; Zhu, Z.; Chen, Z.; Zeng, H. Antimonene Oxides: Emerging Tunable Direct Bandgap Semiconductor and Novel Topological Insulator. *Nano Lett.* **2017**, *17*, 3434–3440.
- (166) Zhang, S.; Yan, Z.; Li, Y.; Chen, Z.; Zeng, H. Atomically Thin Arsenene and Antimonene: Semimetal–Semiconductor and Indirect–Direct Band-Gap Transitions. *Angew. Chem., Int. Ed.* **2015**, *54*, 3112–3115.
- (167) Mannix, A. J.; Kiraly, B.; Hersam, M. C.; Guisinger, N. P. Synthesis and Chemistry of Elemental 2D Materials. *Nat. Rev. Chem.* **2017**, *1*, 14.
- (168) Guo, Y.; Xu, K.; Wu, C.; Zhao, J.; Xie, Y. Surface Chemical-Modification for Engineering the Intrinsic Physical Properties of Inorganic Two-Dimensional Nanomaterials. *Chem. Soc. Rev.* **2015**, *44*, 637–646.
- (169) Liu, Y.; Xiao, C.; Li, Z.; Xie, Y. Vacancy Engineering for Tuning Electron and Phonon Structures of Two-Dimensional Materials. *Adv. Energy Mater.* **2016**, *6*, 1600436.
- (170) Wang, H.; Yu, X.-F. Few-Layered Black Phosphorus: From Fabrication and Customization to Biomedical Applications. *Small* **2018**, *14*, 1702830.
- (171) Qiu, M.; Ren, W. X.; Jeong, T.; Won, M.; Park, G. Y.; Sang, D. K.; Liu, L. P.; Zhang, H.; Kim, J. S. Omnipotent Phosphorene: A next-Generation, Two-Dimensional Nanoplatform for Multidisciplinary Biomedical Applications. *Chem. Soc. Rev.* **2018**, *47*, 5588–5601.
- (172) Sturlac, J.; Sofer, Z.; Pummer, M. Chemistry of Layered Pnictogens: Phosphorus, Arsenic, Antimony, and Bismuth. *Angew. Chem., Int. Ed.* **2019**, *58*, 7551–7557.
- (173) Ersan, F.; Kecik, D.; Özçelik, V. O.; Kadioglu, Y.; Aktürk, O. Ü.; Durgun, E.; Aktürk, E.; Ciraci, S. Two-Dimensional Pnictogens: A Review of Recent Progresses and Future Research Directions. *Appl. Phys. Rev.* **2019**, *6*, 21308.
- (174) Zhu, Z.; Tománek, D. Semiconducting Layered Blue Phosphorus: A Computational Study. *Phys. Rev. Lett.* **2014**, *112*, 176802.
- (175) Tao, W.; Kong, N.; Ji, X.; Zhang, Y.; Sharma, A. Emerging Two-Dimensional Monoelemental Materials (Xenes) for Biomedical Applications. *Chem. Soc. Rev.* **2019**, *48*, 2891–2912.
- (176) Mannix, A. J.; Kiraly, B.; Hersam, M. C.; Guisinger, N. P. Synthesis and Chemistry of Elemental 2D Materials. *Nat. Rev. Chem.* **2017**, *1*, 14.
- (177) Wang, Y.; Huang, P.; Ye, M.; Quhe, R.; Pan, Y.; Zhang, H.; Zhong, H.; Shi, J.; Lu, J. Many-Body Effect, Carrier Mobility, and Device Performance of Hexagonal Arsenene and Antimonene. *Chem. Mater.* **2017**, *29*, 2191–2201.
- (178) Wang, X.; Song, J.; Qu, J. Antimonene: From Experimental Preparation to Practical Application. *Angew. Chem., Int. Ed.* **2019**, *58*, 1574–1584.
- (179) Zhang, S.; Guo, S.; Chen, Z.; Wang, Y.; Gao, H.; Gómez-Herrero, J.; Ares, P.; Zamora, F.; Zhu, Z.; Zeng, H. Recent Progress in 2D Group-VA Semiconductors: From Theory to Experiment. *Chem. Soc. Rev.* **2018**, *47*, 982–1021.
- (180) Kecik, D.; Özçelik, V. O.; Durgun, E.; Ciraci, S. Structure Dependent Optoelectronic Properties of Monolayer Antimonene, Bismuthene and Their Binary Compound. *Phys. Chem. Chem. Phys.* **2019**, *21*, 7907–7917.
- (181) Zhang, F.; Wang, M.; Wang, Z.; Han, K.; Liu, X.; Xu, X. Excellent Nonlinear Absorption Properties of β -Antimonene Nanosheets. *J. Mater. Chem. C* **2018**, *6*, 2848–2853.
- (182) Lu, L.; Liang, Z.; Wu, L.; Chen, Y. X.; Song, Y.; Dhanabalan, S. C.; Ponraj, J. S.; Dong, B.; Xiang, Y.; Xing, F. Few-layer Bismuthene: Sonochemical Exfoliation, Nonlinear Optics and Applications for Ultrafast Photonics with Enhanced Stability. *Laser Photon. Rev.* **2018**, *12*, 1700221.
- (183) Yang, Q.-Q.; Liu, R.-T.; Huang, C.; Huang, Y.-F.; Gao, L.-F.; Sun, B.; Huang, Z.-P.; Zhang, L.; Hu, C.-X.; Zhang, Z.-Q.; et al. 2D Bismuthene Fabricated via Acid-Intercalated Exfoliation Showing Strong Nonlinear near-Infrared Responses for Mode-Locking Lasers. *Nanoscale* **2018**, *10*, 21106–21115.
- (184) Liao, W.; Huang, Y.; Wang, H.; Zhang, H. Van Der Waals Heterostructures for Optoelectronics: Progress and Prospects. *Appl. Mater. Today* **2019**, *16*, 435–455.
- (185) Novoselov, K. S.; Mishchenko, A.; Carvalho, A.; Castro Neto, A. H. 2D Materials and van Der Waals Heterostructures. *Science* **2016**, *353*, No. aac9439.
- (186) Geim, A. K.; Grigorieva, I. V. Van Der Waals Heterostructures. *Nature* **2013**, *499*, 419.
- (187) Zeng, H.; Zhao, J.; Cheng, A.-Q.; Zhang, L.; He, Z.; Chen, R.-S. Tuning Electronic and Optical Properties of Arsenene/C₃N van Der Waals Heterostructure by Vertical Strain and External Electric Field. *Nanotechnology* **2018**, *29*, 75201.
- (188) Li, W.; Wang, T.-X.; Dai, X.-Q.; Wang, X.-L.; Ma, Y.-Q.; Chang, S.-S.; Tang, Y.-N. Tuning the Schottky Barrier in the Arsenene/Graphene van Der Waals Heterostructures by Electric Field. *Phys. E* **2017**, *88*, 6–10.
- (189) Liu, J.; Xue, M.; Wang, J.; Sheng, H.; Tang, G.; Zhang, J.; Bai, D. Tunable Electronic and Optical Properties of Arsenene/MoTe₂ van Der Waals Heterostructures. *Vacuum* **2019**, *163*, 128–134.
- (190) Peng, Q.; Guo, Z.; Sa, B.; Zhou, J.; Sun, Z. New Gallium Chalcogenides/Arsenene van Der Waals Heterostructures Promising for Photocatalytic Water Splitting. *Int. J. Hydrogen Energy* **2018**, *43*, 15995–16004.

- (191) Song, Y.; Li, D.; Mi, W.; Wang, X.; Cheng, Y. Electric Field Effects on Spin Splitting of Two-Dimensional van Der Waals Arsenene/FeCl₂ Heterostructures. *J. Phys. Chem. C* **2016**, *120*, 5613–5618.
- (192) Chen, X.; Yang, Q.; Meng, R.; Jiang, J.; Liang, Q.; Tan, C.; Sun, X. The Electronic and Optical Properties of Novel Germanene and Antimonene Heterostructures. *J. Mater. Chem. C* **2016**, *4*, 5434–5441.
- (193) Zhao, J.; Zeng, H. Chemical Functionalization of Pentagermanene Leads to Stabilization and Tunable Electronic Properties by External Tensile Strain. *ACS Omega* **2017**, *2*, 171–180.
- (194) Li, W.; Wang, T.; Dai, X.; Ma, Y.; Tang, Y. Effects of Electric Field on the Electronic Structures of MoS₂/Arsenene van Der Waals Heterostructure. *J. Alloys Compd.* **2017**, *705*, 486–491.
- (195) Tan, C.; Cao, X.; Wu, X.-J.; He, Q.; Yang, J.; Zhang, X.; Chen, J.; Zhao, W.; Han, S.; Nam, G.-H.; et al. Recent Advances in Ultrathin Two-Dimensional Nanomaterials. *Chem. Rev.* **2017**, *117*, 6225–6331.
- (196) Sun, Q.; Dai, Y.; Ma, Y.; Yin, N.; Wei, W.; Yu, L.; Huang, B. Design of Lateral Heterostructure from Arsenene and Antimonene. *2D Mater.* **2016**, *3* (3), 35017.
- (197) Huang, W.; Huang, Y.; You, Y.; Nie, T.; Chen, T. High-Yield Synthesis of Multifunctional Tellurium Nanorods to Achieve Simultaneous Chemo-Photothermal Combination Cancer Therapy. *Adv. Funct. Mater.* **2017**, *27*, 1701388.
- (198) Yang, T.; Ke, H.; Wang, Q.; Tang, Y.; Deng, Y.; Yang, H.; Yang, X.; Yang, P.; Ling, D.; Chen, C.; et al. Bifunctional Tellurium Nanodots for Photo-Induced Synergistic Cancer Therapy. *ACS Nano* **2017**, *11*, 10012–10024.
- (199) Agapito, L. A.; Kioussis, N.; Rd, G. W.; Ong, N. P. Novel Family of Chiral-Based Topological Insulators: Elemental Tellurium under Strain. *Phys. Rev. Lett.* **2013**, *110*, 176401.
- (200) Peng, H.; Kioussis, N.; Snyder, G. J. Elemental Tellurium as a Chiral P-Type Thermoelectric Material. *Phys. Rev. B: Condens. Matter Mater. Phys.* **2014**, *89*, 195206.
- (201) Bottom, V. E. The Hall Effect and Electrical Resistivity of Tellurium. *Science* **1952**, *115*, 570–571.
- (202) Wang, Y.; Qiu, G.; Wang, R.; Huang, S.; Wang, Q.; Liu, Y.; Du, Y.; Goddard, W. A.; Kim, M. J.; Xu, X.; et al. Field-Effect Transistors Made from Solution-Grown Two-Dimensional Tellurene. *Nat. Electron.* **2018**, *1*, 228–236.
- (203) He, Z.; Yang, Y.; Liu, J. W.; Yu, S. H. Emerging Tellurium Nanostructures: Controllable Synthesis and Their Applications. *Chem. Soc. Rev.* **2017**, *46*, 2732–2753.
- (204) Wu, W.; Qiu, G.; Wang, Y.; Wang, R.; Ye, P. Tellurene: Its Physical Properties, Scalable Nanomanufacturing, and Device Applications. *Chem. Soc. Rev.* **2018**, *47*, 7203–7212.
- (205) Wang, Q.; Safdar, M.; Xu, K.; Mirza, M.; Wang, Z.; He, J. Van Der Waals Epitaxy and Photoresponse of Hexagonal Tellurium Nanoplates on Flexible Mica Sheets. *ACS Nano* **2014**, *8*, 7497–7505.
- (206) Peng, J.; Pan, Y.; Yu, Z.; Wu, J.; Zhou, Y.; Guo, Y.; Wu, X.; Wu, C.; Xie, Y. Two-dimensional Tellurium Nanosheet Exhibiting Anomalous Switchable Photoresponse with Thickness Dependence. *Angew. Chem., Int. Ed.* **2018**, *57*, 13533–13537.
- (207) Cao, W.; Wang, L.; Xu, H. Selenium/Tellurium Containing Polymer Materials in Nanobiotechnology. *Nano Today* **2015**, *10*, 717–736.
- (208) Cao, W.; Gu, Y.; Meineck, M.; Li, T.; Xu, H. Tellurium-Containing Polymer Micelles: Competitive-Ligand-Regulated Coordination Responsive Systems. *J. Am. Chem. Soc.* **2014**, *136*, 5132–5137.
- (209) Li, F.; Li, T.; Cao, W.; Wang, L.; Xu, H. Near-Infrared Light Stimuli-Responsive Synergistic Therapy Nanoplatfoms Based on the Coordination of Tellurium-Containing Block Polymer and Cisplatin for Cancer Treatment. *Biomaterials* **2017**, *133*, 208–218.
- (210) Fan, F.; Wang, L.; Li, F.; Fu, Y.; Xu, H. Stimuli-Responsive Layer-by-Layer Tellurium-Containing Polymer Films for the Combination of Chemotherapy and Photodynamic Therapy. *ACS Appl. Mater. Interfaces* **2016**, *8*, 17004–17010.
- (211) Qiao, J.; Pan, Y.; Yang, F.; Wang, C.; Yang, C.; Wei, J. Few-Layer Tellurium: One-Dimensional-like Layered Elementary Semiconductor with Striking Physical Properties. *Sci. Bull.* **2018**, *63*, 159–168.
- (212) Chen, J.; Dai, Y.; Ma, Y.; Dai, X.; Ho, W.; Xie, M. Ultrathin I²-Tellurium Layers Grown on Highly Oriented Pyrolytic Graphite by Molecular-Beam Epitaxy. *Nanoscale* **2017**, *9*, 15945–15948.
- (213) Huang, X.; Guan, J.; Lin, Z.; Liu, B.; Xing, S.; Wang, W.; Guo, J. Epitaxial Growth and Band Structure of Te Film on Graphene. *Nano Lett.* **2017**, *17*, 4619–4623.
- (214) Wu, L.; Huang, W.; Wang, Y.; Zhao, J.; Ma, D.; Xiang, Y.; Li, J.; Ponraj, J. S.; Dhanabalan, S. C.; Zhang, H. 2D Tellurium Based High-Performance All-Optical Nonlinear Photonic Devices. *Adv. Funct. Mater.* **2019**, *29*, 1806346.
- (215) Zhang, F.; Liu, G.; Wang, Z.; Tang, T.; Wang, X.; Wang, C.; Fu, S.; Xing, F.; Han, K.; Xu, X. Broadband Nonlinear Absorption Properties of Two-Dimensional Hexagonal Tellurene Nanosheets. *Nanoscale* **2019**, *11*, 17058–17064.
- (216) Fang, H.; Yang, H.; Wu, Y. Thermoelectric Properties of Silver Telluride–Bismuth Telluride Nanowire Heterostructure Synthesized by Site-Selective Conversion. *Chem. Mater.* **2014**, *26*, 3322–3327.
- (217) Fang, H.; Yang, H.; Wu, Y.; Ruan, X.; Wu, Y. Synthesis and Thermoelectric Properties of Compositional-Modulated Lead Telluride–Bismuth Telluride Nanowire Heterostructures. *Nano Lett.* **2013**, *13*, 2058–2063.
- (218) Hu, W.; Yang, J. First-Principles Study of Two-Dimensional van Der Waals Heterojunctions. *Comput. Mater. Sci.* **2016**, *112*, 518–526.
- (219) Huang, W.; Zhang, Y.; You, Q.; Huang, P.; Wang, Y.; Huang, Z. N.; Ge, Y.; Wu, L.; Dong, Z.; Dai, X.; et al. Enhanced Photodetection Properties of Tellurium@Selenium Roll-to-Roll Nanotube Heterojunctions. *Small* **2019**, *15*, 1900902.
- (220) Wu, K.; Ma, H.; Gao, Y.; Hu, W.; Yang, J. Highly-Efficient Heterojunction Solar Cells Based on Two-Dimensional Tellurene and Transition Metal Dichalcogenides. *J. Mater. Chem. A* **2019**, *7*, 7430–7436.
- (221) Li, C.; Lu, X.; Han, Y.; Tang, S.; Ding, Y.; Liu, R.; Bao, H.; Li, Y.; Luo, J.; Lu, T. Direct Imaging and Determination of the Crystal Structure of Six-Layered Graphdiyne. *Nano Res.* **2018**, *11*, 1714–1721.
- (222) Gao, X.; Zhu, Y.; Yi, D.; Zhou, J.; Zhang, S.; Yin, C.; Ding, F.; Zhang, S.; Yi, X.; Wang, J.; et al. Ultrathin Graphdiyne Film on Graphene through Solution-Phase van Der Waals Epitaxy. *Sci. Adv.* **2018**, *4*, No. eaat6378.
- (223) Liu, R.; Gao, X.; Zhou, J.; Xu, H.; Li, Z.; Zhang, S.; Xie, Z.; Zhang, J.; Liu, Z. Chemical Vapor Deposition Growth of Linked Carbon Monolayers with Acetylenic Scaffoldings on Silver Foil. *Adv. Mater.* **2017**, *29*, 1604665.
- (224) Zhou, J.; Xie, Z.; Liu, R.; Gao, X.; Li, J.; Xiong, Y.; Tong, L.; Zhang, J.; Liu, Z. Synthesis of Ultrathin Graphdiyne Film Using a Surface Template. *ACS Appl. Mater. Interfaces* **2019**, *11*, 2632–2637.
- (225) Yang, Z.; Shen, X.; Wang, N.; He, J.; Li, X.; Wang, X.; Hou, Z.; Wang, K.; Gao, J.; Jiu, T.; et al. Graphdiyne Containing Atomically Precise N Atoms for Efficient Anchoring of Lithium Ion. *ACS Appl. Mater. Interfaces* **2019**, *11*, 2608–2617.
- (226) Matsuoka, R.; Sakamoto, R.; Hoshiko, K.; Sasaki, S.; Masunaga, H.; Nagashio, K.; Nishihara, H. Crystalline Graphdiyne Nanosheets Produced at a Gas/Liquid or Liquid/Liquid Interface. *J. Am. Chem. Soc.* **2017**, *139*, 3145–3152.
- (227) Li, G.; Li, Y.; Qian, X.; Liu, H.; Lin, H.; Chen, N.; Li, Y. Construction of Tubular Molecule Aggregations of Graphdiyne for Highly Efficient Field Emission. *J. Phys. Chem. C* **2011**, *115*, 2611–2615.
- (228) Gao, X.; Ren, H.; Zhou, J.; Du, R.; Yin, C.; Liu, R.; Peng, H.; Tong, L.; Liu, Z.; Zhang, J. Synthesis of Hierarchical Graphdiyne-Based Architecture for Efficient Solar Steam Generation. *Chem. Mater.* **2017**, *29*, 5777–5781.
- (229) Tang, H.; Ismail-Beigi, S. Novel Precursors for Boron Nanotubes: The Competition of Two-Center and Three-Center Bonding in Boron Sheets. *Phys. Rev. Lett.* **2007**, *99*, 115501.
- (230) Yang, X.; Yi, D.; Ni, J. Ab Initio Prediction of Stable Boron Sheets and Boron Nanotubes: Structure, Stability, and Electronic Properties. *Phys. Rev. B: Condens. Matter Mater. Phys.* **2008**, *77*, 41402.

- (231) Liu, H.; Gao, J.; Zhao, J. From Boron Cluster to Two-Dimensional Boron Sheet on Cu(111) Surface: Growth Mechanism and Hole Formation. *Sci. Rep.* **2013**, *3*, 3238.
- (232) Feng, B.; Zhang, J.; Zhong, Q.; Li, W.; Li, S.; Li, H.; Cheng, P.; Meng, S.; Chen, L.; Wu, K. Experimental Realization of Two-Dimensional Boron Sheets. *Nat. Chem.* **2016**, *8*, 563–568.
- (233) Wu, R.; Drozdov, I. K.; Eltinge, S.; Zahl, P.; Ismail-Beigi, S.; Božović, I.; Gozar, A. Large-Area Single-Crystal Sheets of Borophene on Cu (111) Surfaces. *Nat. Nanotechnol.* **2019**, *14*, 44–49.
- (234) Li, W.; Kong, L.; Chen, C.; Gou, J.; Sheng, S.; Zhang, W. Experimental Realization of Honeycomb Borophene. *Sci. Bull.* **2018**, *63*, 282–286.
- (235) Mannix, A. J.; Zhang, Z.; Guisinger, N. P.; Yakobson, B. I.; Hersam, M. C. Borophene as a Prototype for Synthetic 2D Materials Development. *Nat. Nanotechnol.* **2018**, *13*, 444–450.
- (236) Ji, X.; Kong, N.; Wang, J.; Li, W.; Xiao, Y.; Gan, S. T.; Zhang, Y.; Li, Y.; Song, X.; Xiong, Q.; et al. A Novel Top-Down Synthesis of Ultrathin 2D Boron Nanosheets for Multimodal Imaging-Guided Cancer Therapy. *Adv. Mater.* **2018**, *30*, 1803031–1803042.
- (237) Ranjan, P.; Sahu, T. K.; Bhushan, R.; Yamijala, S. S.; Late, D. J.; Kumar, P.; Vinu, A. Freestanding Borophene and Its Hybrids. *Adv. Mater.* **2019**, *31*, 1900353.
- (238) Campbell, G. P.; Mannix, A. J.; Emery, J. D.; Lee, T.-L.; Guisinger, N. P.; Hersam, M. C.; Bedzyk, M. J. Resolving the Chemically Discrete Structure of Synthetic Borophene Polymorphs. *Nano Lett.* **2018**, *18*, 2816–2821.
- (239) Kiraly, B.; Liu, X.; Wang, L.; Zhang, Z.; Mannix, A. J.; Fisher, B. L.; Yakobson, B. I.; Hersam, M. C.; Guisinger, N. P. Borophene Synthesis on Au(111). *ACS Nano* **2019**, *13*, 3816–3822.
- (240) Yao, Y.; Ye, F.; Qi, X.-L.; Zhang, S.-C.; Fang, Z. Spin-Orbit Gap of Graphene: First-Principles Calculations. *Phys. Rev. B: Condens. Matter Mater. Phys.* **2007**, *75*, 41401.
- (241) Kolmogorov, A. N.; Curtarolo, S. Prediction of New Crystal Structure Phases in Metal Borides: A Lithium Monoboride Analog to MgB₂. *Phys. Rev. B: Condens. Matter Mater. Phys.* **2006**, *73*, 180501–180505.
- (242) Carenco, S.; Portehault, D.; Boissière, C.; Mézailles, N.; Sanchez, C. Nanoscaled Metal Borides and Phosphides: Recent Developments and Perspectives. *Chem. Rev.* **2013**, *113*, 7981–8065.
- (243) Kolmogorov, A. N.; Curtarolo, S. Theoretical Study of Metal Borides Stability. *Phys. Rev. B: Condens. Matter Mater. Phys.* **2006**, *74*, 4070–4079.
- (244) Wu, R.; Drozdov, I. K.; Eltinge, S.; Zahl, P.; Ismail-Beigi, S.; Božović, I.; Gozar, A. Large-Area Single-Crystal Sheets of Borophene on Cu(111) Surfaces. *Nat. Nanotechnol.* **2019**, *14*, 44–49.
- (245) Gibaja, C.; Rodríguez-San-Miguel, D.; Ares, P.; Gómez-Herrero, J.; Varela, M.; Gillen, R.; Maultzsch, J.; Hauke, F.; Hirsch, A.; Abellán, G.; et al. Few-Layer Antimonene by Liquid-Phase Exfoliation. *Angew. Chem., Int. Ed.* **2016**, *55*, 14345–14349.
- (246) Wang, X.; He, J.; Zhou, B.; Zhang, Y.; Wu, J.; Hu, R.; Liu, L.; Song, J.; Qu, J. Bandgap-Tunable Preparation of Smooth and Large Two-Dimensional Antimonene. *Angew. Chem.* **2018**, *130*, 8804–8809.
- (247) Qi, Z.-H.; Hu, Y.; Jin, Z.; Ma, J. Tuning the Liquid-Phase Exfoliation of Arsenic Nanosheets by Interaction with Various Solvents. *Phys. Chem. Chem. Phys.* **2019**, *21*, 12087–12090.
- (248) Vishnoi, P.; Mazumder, M.; Pati, S. K.; R. Rao, C. N. Arsenene Nanosheets and Nanodots. *New J. Chem.* **2018**, *42*, 14091–14095.
- (249) Zhang, B.; Fan, T.; Xie, N.; Nie, G.; Zhang, H. Versatile Applications of Metal Single-Atom @ 2D Material Nanoplatfoms. *Adv. Sci.* **2019**, *6*, 1901787.
- (250) Xiao, Q.; Hu, C.-X.; Wu, H.-R.; Ren, Y.-Y.; Li, X.-Y.; Yang, Q.-Q.; Dun, G.-H.; Huang, Z.-P.; Peng, Y.; Yan, F.; et al. Antimonene-Based Flexible Photodetector. *Nanoscale Horizons* **2020**, *5*, 124–130.
- (251) Beladi-Mousavi, S. M.; Pourrahimi, A. M.; Sofer, Z.; Pumera, M. Atomically Thin 2D-Arsenene by Liquid-Phased Exfoliation: Toward Selective Vapor Sensing. *Adv. Funct. Mater.* **2018**, *29*, 1807004.
- (252) Lin, W.; Lian, Y.; Zeng, G.; Chen, Y.; Wen, Z.; Yang, H. A Fast Synthetic Strategy for High-Quality Atomically Thin Antimonene with Ultrahigh Sonication Power. *Nano Res.* **2018**, *11*, 5968–5977.
- (253) Lu, L.; Tang, X.; Cao, R.; Wu, L.; Li, Z.; Jing, G.; Dong, B.; Lu, S.; Li, Y.; Xiang, Y.; et al. Broadband Nonlinear Optical Response in Few-Layer Antimonene and Antimonene Quantum Dots: A Promising Optical Kerr Media with Enhanced Stability. *Adv. Opt. Mater.* **2017**, *5*, 1700301.
- (254) Ares, P.; Aguilar-Galindo, F.; Rodríguez-San-Miguel, D.; Aldave, D. A.; Díaz-Tendero, S.; Alcamí, M.; Martín, F.; Gómez-Herrero, J.; Zamora, F. Mechanical Isolation of Highly Stable Antimonene under Ambient Conditions. *Adv. Mater.* **2016**, *28*, 6332–6336.
- (255) Shao, Y.; Liu, Z.-L.; Cheng, C.; Wu, X.; Liu, H.; Liu, C.; Wang, J.-O.; Zhu, S.-Y.; Wang, Y.-Q.; Shi, D.-X.; et al. Epitaxial Growth of Flat Antimonene Monolayer: A New Honeycomb Analogue of Graphene. *Nano Lett.* **2018**, *18*, 2133–2139.
- (256) Qiu, M.; Wang, D.; Liang, W.; Liu, L.; Zhang, Y.; Chen, X.; Sang, D. K.; Xing, C.; Li, Z.; Dong, B.; et al. Novel Concept of the Smart NIR-Light-Controlled Drug Release of Black Phosphorus Nanostructure for Cancer Therapy. *Proc. Natl. Acad. Sci. U. S. A.* **2018**, *115*, 501–506.
- (257) Xing, C.; Chen, S.; Qiu, M.; Liang, X.; Liu, Q.; Zou, Q.; Li, Z.; Xie, Z.; Wang, D.; Dong, B.; et al. Conceptually Novel Black Phosphorus/Cellulose Hydrogels as Promising Photothermal Agents for Effective Cancer Therapy. *Adv. Healthcare Mater.* **2018**, *7*, 1701510.
- (258) Guo, Z.; Chen, S.; Wang, Z.; Yang, Z.; Liu, F.; Xu, Y.; Wang, J.; Yi, Y.; Zhang, H.; Liao, L.; et al. Metal-Ion-Modified Black Phosphorus with Enhanced Stability and Transistor Performance. *Adv. Mater.* **2017**, *29*, 1703811.
- (259) Zhao, Y.; Wang, H.; Huang, H.; Xiao, Q.; Xu, Y.; Guo, Z.; Xie, H.; Shao, J.; Sun, Z.; Han, W. Surface Coordination of Black Phosphorus for Robust Air and Water Stability. *Angew. Chem., Int. Ed.* **2016**, *55*, 5003–5007.
- (260) Liu, Y.; Gao, P.; Zhang, T.; Zhu, X.; Zhang, M.; Chen, M.; Du, P.; Wang, G.-W.; Ji, H.; Yang, J.; et al. Azide Passivation of Black Phosphorus Nanosheets: Covalent Functionalization Affords Ambient Stability Enhancement. *Angew. Chem., Int. Ed.* **2019**, *58*, 1479–1483.
- (261) Sun, C.; Wen, L.; Zeng, J.; Wang, Y.; Sun, Q.; Deng, L.; Zhao, C.; Li, Z. One-Pot Solventless Preparation of PEGylated Black Phosphorus Nanoparticles for Photoacoustic Imaging and Photothermal Therapy of Cancer. *Biomaterials* **2016**, *91*, 81–89.
- (262) Abellán, G.; Ares, P.; Wild, S.; Nuin, E.; Neiss, C.; Miguel, D. R.-S.; Segovia, P.; Gibaja, C.; Michel, E. G.; Görling, A.; et al. Noncovalent Functionalization and Charge Transfer in Antimonene. *Angew. Chem., Int. Ed.* **2017**, *56*, 14389–14394.
- (263) Liang, X.; Ng, S.-P.; Ding, N.; Wu, C.-M. L. Characterization of Point Defects in Monolayer Arsenene. *Appl. Surf. Sci.* **2018**, *443*, 74–82.
- (264) Su, J.; Feng, L.; Liu, Z. Heterostructure Consists of Monolayer MoS₂ and Arsenene with Novel Electronic and Optical Conductivity. *RSC Adv.* **2016**, *6*, 59633–59638.
- (265) Ren, K.; Tang, W.; Sun, M.; Cai, Y.; Cheng, Y.; Zhang, G. A Direct Z-Scheme PtS₂/Arsenene van Der Waals Heterostructure with High Photocatalytic Water Splitting Efficiency. *Nanoscale* **2020**, *12*, 17281–17289.
- (266) Hogan, C.; Holtgrewe, K.; Ronci, F.; Colonna, S.; Sanna, S.; Moras, P.; Sheverdyeva, P. M.; Mahatha, S.; Papagno, M.; Aliev, Z. S.; et al. Temperature Driven Phase Transition at the Antimonene/Bi₂Se₃ van Der Waals Heterostructure. *ACS Nano* **2019**, *13*, 10481–10489.
- (267) Xie, Z.; Sun, F.; Yao, R.; Zhang, Y.; Zhang, Y.; Zhang, Z.; Fan, J.; Ni, L.; Duan, L. Tuning Electronic Properties of InSe/Arsenene Heterostructure by External Electric Field and Uniaxial Strain. *Appl. Surf. Sci.* **2019**, *475*, 839–846.
- (268) Barrio, J.; Gibaja, C.; Tzadikov, J.; Shalom, M.; Zamora, F. 2D/2D Graphitic Carbon Nitride/Antimonene Heterostructure: Structural Characterization and Application in Photocatalysis. *Adv. Sustain. Syst.* **2019**, *3*, 1800138.
- (269) Fang, Y.; Xue, Y.; Hui, L.; Yu, H.; Liu, Y.; Xing, C.; Lu, F.; He, F.; Liu, H.; Li, Y. In Situ Growth of Graphdiyne Based Heterostructure: Toward Efficient Overall Water Splitting. *Nano Energy* **2019**, *59*, 591–597.

- (270) Niu, X.; Li, Y.; Zhou, Q.; Shu, H.; Wang, J. Arsenene-Based Heterostructures: Highly Efficient Bifunctional Materials for Photovoltaics and Photocatalysis. *ACS Appl. Mater. Interfaces* **2017**, *9*, 42856–42861.
- (271) Yu, Y.; Cao, C.; Liu, H.; Li, P.; Wei, F.; Jiang, Y.; Song, W. A Bi/BiOCl Heterojunction Photocatalyst with Enhanced Electron–Hole Separation and Excellent Visible Light Photodegrading Activity. *J. Mater. Chem. A* **2014**, *2*, 1677–1681.
- (272) Liang, C.; Niu, C.-G.; Zhang, L.; Wen, X.-J.; Yang, S.-F.; Guo, H.; Zeng, G.-M. Construction of 2D Heterojunction System with Enhanced Photocatalytic Performance: Plasmonic Bi and Reduced Graphene Oxide Co-Modified Bi₂SO₇ with High-Speed Charge Transfer Channels. *J. Hazard. Mater.* **2019**, *361*, 245–258.
- (273) He, W.; Sun, Y.; Jiang, G.; Li, Y.; Zhang, X.; Zhang, Y.; Zhou, Y.; Dong, F. Defective Bi₄MoO₉/Bi Metal Core/Shell Heterostructure: Enhanced Visible Light Photocatalysis and Reaction Mechanism. *Appl. Catal., B* **2018**, *239*, 619–627.
- (274) Sun, D.; Huang, L.; Li, L.; Yu, Y.; Du, G.; Xu, B. Plasma Enhanced Bi/Bi₂O₂CO₃ Heterojunction Photocatalyst via a Novel in-Situ Method. *J. Colloid Interface Sci.* **2020**, *571*, 80–89.
- (275) Patil, R. A.; Wei, M.-K.; Yeh, P.-H.; Liang, J.-B.; Gao, W.-T.; Lin, J.-H.; Liou, Y.; Ma, Y.-R. Size-Controllable Synthesis of Bi/Bi₂O₃ Heterojunction Nanoparticles Using Pulsed Nd:YAG Laser Deposition and Metal–Semiconductor–Heterojunction-Assisted Photoluminescence. *Nanoscale* **2016**, *8*, 3565–3571.
- (276) Bao, Q.; Zhang, H.; Wang, Y.; Ni, Z.; Yan, Y.; Shen, Z. X.; Loh, K. P.; Tang, D. Y. Atomic-Layer Graphene as a Saturable Absorber for Ultrafast Pulsed Lasers. *Adv. Funct. Mater.* **2009**, *19*, 3077–3083.
- (277) Liao, Y.; Song, C.; Xiang, Y.; Dai, X. Recent Advances in Spatial Self-Phase Modulation with 2D Materials and Its Applications. *Ann. Phys.* **2020**, *532*, 2000322.
- (278) Guo, J.; Wang, Z.; Shi, R.; Zhang, Y.; He, Z.; Gao, L.; Wang, R.; Shu, Y.; Ma, C.; Ge, Y. Graphdiyne as a Promising Mid-Infrared Nonlinear Optical Material for Ultrafast Photonics. *Adv. Opt. Mater.* **2020**, *8*, 2000067.
- (279) Wu, J.-J.; Tao, Y.-R.; Wu, X.-C.; Chun, Y. Nonlinear Optical Absorption of SnX₂ (X = S, Se) Semiconductor Nanosheets. *J. Alloys Compd.* **2017**, *713*, 38–45.
- (280) Shi, Z.; Li, X.; Zhang, Y.; Li, H.; Zhao, Y.; Guo, P.; Guo, Y. Graphdiyne for Ultrashort Pulse Generation in an Erbium-Doped Hybrid Mode-Locked Fiber Laser. *Front. Phys.* **2019**, *7*, 150.
- (281) Song, Y.; Liang, Z.; Jiang, X.; Chen, Y.; Li, Z.; Lu, L.; Ge, Y.; Wang, K.; Zheng, J.; Lu, S. Few-Layer Antimonene Decorated Microfiber: Ultra-Short Pulse Generation and All-Optical Thresholding with Enhanced Long Term Stability. *2D Mater.* **2017**, *4*, 045010.
- (282) Tian, X.; Wei, R.; Qiu, J. A Broadband Pulsed Optical Switch from Near-Infrared to Mid-Infrared Employing Multilayer Antimonene. In *2018 Asia Communications and Photonics Conference (ACP)* **2018**, 1–3.
- (283) Liu, G.; Zhang, F.; Wu, T.; Li, Z.; Zhang, W.; Han, K.; Xing, F.; Man, Z.; Ge, X.; Fu, S. Single- and Dual-Wavelength Passively Mode-Locked Erbium-Doped Fiber Laser Based on Antimonene Saturable Absorber. *IEEE Photonics J.* **2019**, *11*, 1–11.
- (284) Wang, M.; Zhang, F.; Wang, Z.; Wu, Z.; Xu, X. Passively Q-Switched Nd³⁺ Solid-State Lasers with Antimonene as Saturable Absorber. *Opt. Express* **2018**, *26*, 4085–4095.
- (285) Wang, Y.; Huang, W.; Wang, C.; Guo, J.; Zhang, F.; Song, Y.; Ge, Y.; Wu, L.; Liu, J.; Li, J.; et al. An All-Optical, Actively Q-Switched Fiber Laser by an Antimonene-Based Optical Modulator. *Laser Photonics Rev.* **2019**, *13*, 1800313.
- (286) Luo, H.; Tian, X.; Gao, Y.; Wei, R.; Li, J.; Qiu, J.; Liu, Y. Antimonene: A Long-Term Stable Two-Dimensional Saturable Absorption Material under Ambient Conditions for the Mid-Infrared Spectral Region. *Photonics Res.* **2018**, *6*, 900–907.
- (287) Zhang, G.; Tang, X.; Fu, X.; Chen, W.; Shabbir, B.; Zhang, H.; Liu, Q.; Gong, M. 2D Group-VA Fluorinated Antimonene: Synthesis and Saturable Absorption. *Nanoscale* **2019**, *11*, 1762–1769.
- (288) Song, Y.; Chen, Y.; Jiang, X.; Liang, W.; Wang, K.; Liang, Z.; Ge, Y.; Zhang, F.; Wu, L.; Zheng, J.; et al. Nonlinear Few-Layer Antimonene-Based All-Optical Signal Processing: Ultrafast Optical Switching and High-Speed Wavelength Conversion. *Adv. Opt. Mater.* **2018**, *6*, 1701287.
- (289) Hu, X.; Wang, A.; Zeng, M.; Long, Y.; Zhu, L.; Gui, C.; Fu, L.; Shen, L.; Wang, J. Graphene-Assisted Multiple-Input High-Base Optical Computing. In *2016 15th International Conference on Optical Communications and Networks (ICOON)* **2016**, 1–3.
- (290) Lu, L.; Wang, W.; Wu, L.; Jiang, X.; Xiang, Y.; Li, J.; Fan, D.; Zhang, H. All-Optical Switching of Two Continuous Waves in Few Layer Bismuthene Based on Spatial Cross-Phase Modulation. *ACS Photonics* **2017**, *4*, 2852–2861.
- (291) Reis, F.; Li, G.; Dudy, L.; Bauernfeind, M.; Glass, S.; Hanke, W.; Thomale, R.; Schäfer, J.; Claessen, R. Bismuthene on a SiC Substrate: A Candidate for a High-Temperature Quantum Spin Hall Material. *Science* **2017**, *357*, 287–290.
- (292) Chai, T.; Li, X.; Feng, T.; Guo, P.; Song, Y.; Chen, Y.; Zhang, H. Few-Layer Bismuthene for Ultrashort Pulse Generation in a Dissipative System Based on an Evanescent Field. *Nanoscale* **2018**, *10*, 17617–17622.
- (293) Guo, B.; Wang, S.-H.; Wu, Z.-X.; Wang, Z.-X.; Wang, D.-H.; Huang, H.; Zhang, F.; Ge, Y.-Q.; Zhang, H. Sub-200 fs Soliton Mode-Locked Fiber Laser Based on Bismuthene Saturable Absorber. *Opt. Express* **2018**, *26*, 22750–22760.
- (294) Singh, D.; Gupta, S. K.; Sonvane, Y.; Lukačević, I. Antimonene: A Monolayer Material for Ultraviolet Optical Nanodevices. *J. Mater. Chem. C* **2016**, *4*, 6386–6390.
- (295) Zhang, S.; Hu, Y.; Hu, Z.; Cai, B.; Zeng, H. Hydrogenated Arsenenes as Planar Magnet and Dirac Material. *Appl. Phys. Lett.* **2015**, *107*, 22102.
- (296) Wang, K.; Zhang, X.; Kislyakov, I. M.; Dong, N.; Zhang, S.; Wang, G.; Fan, J.; Zou, X.; Du, J.; Leng, Y.; et al. Bacterially Synthesized Tellurium Nanostructures for Broadband Ultrafast Nonlinear Optical Applications. *Nat. Commun.* **2019**, *10*, 3985.
- (297) Li, Y.; Kuang, D.; Gao, Y.; Cheng, J.; Yu, Z. Titania:Graphdiyne Nanocomposites for High-Performance Deep Ultraviolet Photodetectors Based on Mixed-Phase MgZnO. *J. Alloys Compd.* **2020**, *825*, 153882.
- (298) Jin, Z.; Zhou, Q.; Chen, Y.; Mao, P.; Li, H.; Liu, H.; Wang, J.; Li, Y. Graphdiyne:ZnO Nanocomposites for High-Performance UV Photodetectors. *Adv. Mater.* **2016**, *28*, 3697–3702.
- (299) Zhang, Y.; Huang, P.; Guo, J.; Shi, R.; Huang, W.; Shi, Z.; Wu, L.; Zhang, F.; Gao, L.; Li, C.; et al. Graphdiyne-Based Flexible Photodetectors with High Responsivity and Detectivity. *Adv. Mater.* **2020**, *32*, 2001082.
- (300) Ma, D.; Wang, R.; Zhao, J.; Chen, Q.; Wu, L.; Li, D.; Su, L.; Jiang, X.; Luo, Z.; Ge, Y. A Self-Powered Photodetector Based on Two-Dimensional Boron Nanosheets. *Nanoscale* **2020**, *12*, 5313–5323.
- (301) Zhao, J.; Qi, Z.-H.; Xu, Y.; Dai, J.; Zeng, X. C.; Guo, W.; Ma, J. Theoretical Studies on Tunable Electronic Structures and Potential Applications of Two-Dimensional Arsenene-Based Materials. *Wiley Interdiscip. Rev.: Comput. Mol. Sci.* **2019**, *9*, No. e1387.
- (302) Kong, X.; Gao, M.; Yan, X.-W.; Lu, Z.-Y.; Xiang, T. Superconductivity in Electron-Doped Arsenene. *Chin. Phys. B* **2018**, *27*, 46301.
- (303) Wang, Y.; Ye, M.; Weng, M.; Li, J.; Zhang, X.; Zhang, H.; Guo, Y.; Pan, Y.; Xiao, L.; Liu, J.; et al. Electrical Contacts in Monolayer Arsenene Devices. *ACS Appl. Mater. Interfaces* **2017**, *9*, 29273–29284.
- (304) Sun, X.; Song, Z.; Liu, S.; Wang, Y.; Li, Y.; Wang, W.; Lu, J. Sub-5 nm Monolayer Arsenene and Antimonene Transistors. *ACS Appl. Mater. Interfaces* **2018**, *10*, 22363–22371.
- (305) Jafari, M.; Ansari, R.; Rouhi, S. First-Principle Investigation of the Elastic and Plastic Properties of the Bismuthene: Effect of the External Electric Field. *Superlattices Microstruct.* **2020**, *140*, 106476.
- (306) Qi, M.; Dai, S.; Wu, P. Prediction of Electronic and Magnetic Properties in 3d-Transition-Metal X-Doped Bismuthene (X = V, Cr, Mn and Fe). *Appl. Surf. Sci.* **2019**, *486*, 58–64.
- (307) Huang, H.; Ren, X.; Li, Z.; Wang, H.; Huang, Z.; Qiao, H.; Tang, P.; Zhao, J.; Liang, W.; Ge, Y.; et al. Two-Dimensional Bismuth

Nanosheets as Prospective Photo-Detector with Tunable Optoelectronic Performance. *Nanotechnology* **2018**, *29*, 235201.

(308) Zhang, Y.; You, Q.; Huang, W.; Hu, L.; Ju, J.; Ge, Y.; Zhang, H. Few-Layer Hexagonal Bismuth Telluride (Bi_2Te_3) Nanoplates with High-Performance UV-Vis Photodetection. *Nanoscale Adv.* **2020**, *2*, 1333–1339.

(309) Wang, Q.; Safdar, M.; Xu, K.; Mirza, M.; Wang, Z.; He, J. Van Der Waals Epitaxy and Photoresponse of Hexagonal Tellurium Nanoplates on Flexible Mica Sheets. *ACS Nano* **2014**, *8*, 7497–7505.

(310) Amani, M.; Tan, C.; Zhang, G.; Zhao, C.; Bullock, J.; Song, X.; Kim, H.; Shrestha, V. R.; Gao, Y.; Crozier, K. B. Solution-Synthesized High-Mobility Tellurium Nanoflakes for Short-Wave Infrared Photodetectors. *ACS Nano* **2018**, *12*, 7253–7263.

(311) Xie, Z.; Xing, C.; Huang, W.; Fan, T.; Li, Z.; Zhao, J.; Xiang, Y.; Guo, Z.; Li, J.; Yang, Z.; et al. Ultrathin 2D Nonlayered Tellurium Nanosheets: Facile Liquid-Phase Exfoliation, Characterization, and Photoresponse with High Performance and Enhanced Stability. *Adv. Funct. Mater.* **2018**, *28*, 1705833.

(312) Deckoff-Jones, S.; Wang, Y.; Lin, H.; Wu, W.; Hu, J. Tellurene: A Multifunctional Material for Midinfrared Optoelectronics. *ACS Photonics* **2019**, *6*, 1632–1638.

(313) Wang, S.; Yi, L.; Halpert, J. E.; Lai, X.; Liu, Y.; Cao, H.; Yu, R.; Wang, D.; Li, Y. A Novel and Highly Efficient Photocatalyst Based on P25–Graphdiyne Nanocomposite. *Small* **2012**, *8*, 265–271.

(314) Yang, N.; Liu, Y.; Wen, H.; Tang, Z.; Zhao, H.; Li, Y.; Wang, D. Photocatalytic Properties of Graphdiyne and Graphene Modified TiO_2 : From Theory to Experiment. *ACS Nano* **2013**, *7*, 1504–1512.

(315) Thangavel, S.; Krishnamoorthy, K.; Krishnaswamy, V.; Raju, N.; Kim, S. J.; Venugopal, G. Graphdiyne–ZnO Nanohybrids as an Advanced Photocatalytic Material. *J. Phys. Chem. C* **2015**, *119*, 22057–22065.

(316) Fang, Y.; Xue, Y.; Hui, L.; Yu, H.; Li, Y. Graphdiyne@ Janus Magnetite for Photocatalytic Nitrogen Fixation. *Angew. Chem.* **2021**, *133*, 3207–3211.

(317) Xing, C.; Xue, Y.; Huang, B.; Yu, H.; Hui, L.; Fang, Y.; Liu, Y.; Zhao, Y.; Li, Z.; Li, Y. Fluorographdiyne: A Metal-Free Catalyst for Applications in Water Reduction and Oxidation. *Angew. Chem.* **2019**, *131*, 14035–14041.

(318) Yu, H.; Xue, Y.; Hui, L.; Zhang, C.; Li, Y.; Zuo, Z.; Zhao, Y.; Li, Z.; Li, Y. Efficient Hydrogen Production on a 3D Flexible Heterojunction Material. *Adv. Mater.* **2018**, *30*, 1707082.

(319) Fang, Y.; Xue, Y.; Li, Y.; Yu, H.; Hui, L.; Liu, Y.; Xing, C.; Zhang, C.; Zhang, D.; Wang, Z.; Chen, X.; Gao, Y.; Huang, B.; Y, L. Graphdiyne Interface Engineering: Highly Active and Selective Ammonia Synthesis. *Angew. Chem., Int. Ed.* **2020**, *132*, 13021–13027.

(320) Liu, Y.; Xue, Y.; Yu, H.; Hui, L.; Huang, B.; Li, Y. Graphdiyne Ultrathin Nanosheets for Efficient Water Splitting. *Adv. Funct. Mater.* **2021**, *31*, 2010112.

(321) Li, J.; Xu, J.; Xie, Z.; Gao, X.; Zhou, J.; Xiong, Y.; Chen, C.; Zhang, J.; Liu, Z. Diatomite-Templated Synthesis of Freestanding 3D Graphdiyne for Energy Storage and Catalysis Application. *Adv. Mater.* **2018**, *30*, 1800548.

(322) Li, J.; Gao, X.; Jiang, X.; Li, X. B.; Liu, Z.; Zhang, J.; Tung, C. H.; Wu, L. Z. Graphdiyne: A Promising Catalyst–Support To Stabilize Cobalt Nanoparticles for Oxygen Evolution. *ACS Catal.* **2017**, *7*, 5209–5213.

(323) Hui, L.; Xue, Y.; Yu, H.; Liu, Y.; Fang, Y.; Xing, C.; Huang, B.; Li, Y. Highly Efficient and Selective Generation of Ammonia and Hydrogen on a Graphdiyne-Based Catalyst. *J. Am. Chem. Soc.* **2019**, *141*, 10677–10683.

(324) Yu, H.; Xue, Y.; Hui, L.; Zhang, C.; Fang, Y.; Liu, Y.; Chen, X.; Zhang, D.; Huang, B.; Li, Y. Graphdiyne Based Metal Atomic Catalysts for Synthesizing Ammonia. *Natl. Sci. Rev.* **2021**, *8*, No. nwa213.

(325) Yu, X.; Liang, W.; Xing, C.; Chen, K.; Chen, J.; Huang, W.; Xie, N.; Qiu, M.; Yan, X.; Xie, Z.; et al. Rising 2D Pnictogens for Catalytic Applications: Status and Challenges. *J. Mater. Chem. A* **2020**, *6*, 4883–5230.

(326) Zhang, B.; Asakura, H.; Zhang, J.; Zhang, J.; De, S.; Yan, N. Stabilizing a Platinum Single-Atom Catalyst on Supported Phospho-

molybdenic Acid without Compromising Hydrogenation Activity. *Angew. Chem., Int. Ed.* **2016**, *55*, 8319–8323.

(327) Chen, X.; Zhang, B.; Wang, Y.; Yan, N. Valorization of Renewable Carbon Resources for Chemicals. *Chimia* **2015**, *69*, 120–124.

(328) Fang, J.; Li, J.; Zhang, B.; Yuan, X.; Asakura, H.; Tanaka, T.; Teramura, K.; Xie, J.; Yan, N. The Support Effect on the Size and Catalytic Activity of Thiolated Au₂₅ Nanoclusters as Precatalysts. *Nanoscale* **2015**, *7*, 6325–6333.

(329) Som, N. N.; Mankad, V.; Jha, P. K. Hydrogen Evolution Reaction: The Role of Arsenene Nanosheet and Dopant. *Int. J. Hydrogen Energy* **2018**, *43*, 21634–21641.

(330) Li, X.-H.; Wang, B.-J.; Cai, X.-L.; Yu, W.-Y.; Zhang, L.-W.; Wang, G.-D.; Ke, S.-H. Arsenene/ $\text{Ca}(\text{OH})_2$ van Der Waals Heterostructure: Strain Tunable Electronic and Photocatalytic Properties. *RSC Adv.* **2017**, *7*, 44394–44400.

(331) Ren, X.; Li, Z.; Qiao, H.; Liang, W.; Liu, H.; Zhang, F.; Qi, X.; Liu, Y.; Huang, Z.; Zhang, D.; et al. Few-Layer Antimonene Nanosheet: A Metal-Free Bifunctional Electrocatalyst for Effective Water Splitting. *ACS Appl. Energy Mater.* **2019**, *2*, 4774–4781.

(332) Bat-Erdene, M.; Xu, G.-R.; Batmunkh, M.; Bati, A.; White, J.; Nine, M. J.; Losic, D.; Chen, Y.; Wang, Y.; Ma, T.; et al. Surface Oxidized Two-Dimensional Antimonene Nanosheets for Electrochemical Ammonia Synthesis under Ambient Conditions. *J. Mater. Chem. A* **2020**, *8*, 4735–4739.

(333) Wu, P.; Huang, M. Transition Metal Doped Arsenene: Promising Materials for Gas Sensing, Catalysis and Spintronics. *Appl. Surf. Sci.* **2020**, *506*, 144660.

(334) Li, D.; Song, S.; Fan, C. Target-Responsive Structural Switching for Nucleic Acid-Based Sensors. *Acc. Chem. Res.* **2010**, *43*, 631–641.

(335) Freeman, R.; Willner, I. Optical Molecular Sensing with Semiconductor Quantum Dots (QDs). *Chem. Soc. Rev.* **2012**, *41*, 4067–4085.

(336) Yoon, S.; Miller, E. W.; He, Q.; Do, P. H.; Chang, C. J. A Bright and Specific Fluorescent Sensor for Mercury in Water, Cells, and Tissue. *Angew. Chem., Int. Ed.* **2007**, *46*, 6658–6661.

(337) Chen, X.; Gao, P.; Guo, L.; Zhang, S. Graphdiyne as a Promising Material for Detecting Amino Acids. *Sci. Rep.* **2015**, *5*, 16720.

(338) Parvin, N.; Jin, Q.; Wei, Y.; Yu, R.; Zheng, B.; Huang, L.; Zhang, Y.; Wang, L.; Zhang, H.; Gao, M.; et al. Few-Layer Graphdiyne Nanosheets Applied for Multiplexed Real-Time DNA Detection. *Adv. Mater.* **2017**, *29*, 1606755.

(339) Li, Y.; Li, X.; Meng, Y.; Hun, X. Photoelectrochemical Platform for MicroRNA Let-7a Detection Based on Graphdiyne Loaded with AuNPs Modified Electrode Coupled with Alkaline Phosphatase. *Biosens. Bioelectron.* **2019**, *130*, 269–275.

(340) Nagarajan, V.; Srimathi, U.; Chandiramouli, R. First-Principles Insights on Detection of Dimethyl Amine and Trimethyl Amine Vapors Using Graphdiyne Nanosheets. *Comput. Theor. Chem.* **2018**, *1123*, 119–127.

(341) Yan, H.; Guo, S.; Wu, F.; Yu, P.; Liu, H.; Li, Y.; Mao, L. Carbon Atom Hybridization Matters: Ultrafast Humidity Response of Graphdiyne Oxides. *Angew. Chem.* **2018**, *130*, 3986–3990.

(342) Rastgou, A.; Soleymanabadi, H.; Bodaghi, A. DNA Sequencing by Borophene Nanosheet via an Electronic Response: A Theoretical Study. *Microelectron. Eng.* **2017**, *169*, 9–15.

(343) Nagarajan, V.; Chandiramouli, R. Borophene Nanosheet Molecular Device for Detection of Ethanol – A First-Principles Study. *Comput. Theor. Chem.* **2017**, *1105*, 52–60.

(344) Shahbazi Kootenaei, A.; Ansari, G. B36 Borophene as an Electronic Sensor for Formaldehyde: Quantum Chemical Analysis. *Phys. Lett. A* **2016**, *380*, 2664–2668.

(345) Omidvar, A. Borophene: A Novel Boron Sheet with a Hexagonal Vacancy Offering High Sensitivity for Hydrogen Cyanide Detection. *Comput. Theor. Chem.* **2017**, *1115*, 179–184.

(346) Chandiramouli, R.; Nagarajan, V. Borospherene Nanostructure as CO and NO Sensor – A First-Principles Study. *Vacuum* **2017**, *142*, 13–20.

- (347) Shukla, V.; Wärnå, J.; Jena, N. K.; Grigoriev, A.; Ahuja, R. Toward the Realization of 2D Borophene Based Gas Sensor. *J. Phys. Chem. C* **2017**, *121*, 26869–26876.
- (348) Beladi-Mousavi, S. M.; Pumera, M. 2D-Pnictogens: Alloy-Based Anode Battery Materials with Ultrahigh Cycling Stability. *Chem. Soc. Rev.* **2018**, *47*, 6964–6989.
- (349) Üzengi Aktürk, O.; Aktürk, E.; Ciraci, S. Effects of Adatoms and Physisorbed Molecules on the Physical Properties of Antimonene. *Phys. Rev. B: Condens. Matter Mater. Phys.* **2016**, *93*, 35450.
- (350) Zhou, J.; Li, Z.; Ying, M.; Liu, M.; Wang, X.; Wang, X.; Cao, L.; Zhang, H.; Xu, G. Black Phosphorus Nanosheets for Rapid MicroRNA Detection. *Nanoscale* **2018**, *10*, S060–S064.
- (351) Xue, T.; Liang, W.; Li, Y.; Sun, Y.; Xiang, Y.; Zhang, Y.; Dai, Z.; Duo, Y.; Wu, L.; Qi, K.; et al. Ultrasensitive Detection of miRNA with an Antimonene-Based Surface Plasmon Resonance Sensor. *Nat. Commun.* **2019**, *10*, 28–37.
- (352) Liu, C.; Liu, C.-S.; Yan, X. Arsenene as a Promising Candidate for NO and NO₂ Sensor: A First-Principles Study. *Phys. Lett. A* **2017**, *381*, 1092–1096.
- (353) Snehha, P.; Nagarajan, V.; Chandiramouli, R. Novel Bismuthene Nanotubes to Detect NH₃, NO₂ and PH₃ Gas Molecules – A First-Principles Insight. *Chem. Phys. Lett.* **2018**, *712*, 102–111.
- (354) Khan, M. S.; Srivastava, A.; Pandey, R. Electronic Properties of a Pristine and NH₃/NO₂ Adsorbed Buckled Arsenene Monolayer. *RSC Adv.* **2016**, *6*, 72634–72642.
- (355) Bhuvaneswari, R.; Nagarajan, V.; Chandiramouli, R. Nitrogen Mustard Gas Molecules and α -Arsenene Nanosheet Interaction Studies – A DFT Insight. *J. Mol. Graphics Modell.* **2019**, *92*, 65–73.
- (356) Srivastava, A.; Khan, M. S.; Ahuja, R. Electron Transport in NH₃/NO₂ Sensed Buckled Antimonene. *Solid State Commun.* **2018**, *272*, 1–7.
- (357) Chen, X.; Wang, L.; Sun, X.; Meng, R.; Xiao, J.; Ye, H.; Zhang, G. Sulfur Dioxide and Nitrogen Dioxide Gas Sensor Based on Arsenene: A First-Principle Study. *IEEE Electron Device Lett.* **2017**, *38*, 661–664.
- (358) Mayorga-Martinez, C. C.; Gusmão, R.; Sofer, Z.; Pumera, M. Pnictogen-Based Enzymatic Phenol Biosensors: Phosphorene, Arsenene, Antimonene, and Bismuthene. *Angew. Chem., Int. Ed.* **2019**, *58*, 134–138.
- (359) Wang, D.; Yang, A.; Lan, T.; Fan, C.; Pan, J.; Liu, Z.; Chu, J.; Yuan, H.; Wang, X.; Rong, M. Tellurene Based Chemical Sensor. *J. Mater. Chem. A* **2019**, *7*, 26326–26333.
- (360) Cui, H.; Zheng, K.; Xie, Z.; Yu, J.; Zhu, X.; Ren, H.; Wang, Z.; Zhang, F.; Li, X.; Tao, L.-Q.; et al. Tellurene Nanoflake-Based NO₂ Sensors with Superior Sensitivity and a Sub-Parts-per-Billion Detection Limit. *ACS Appl. Mater. Interfaces* **2020**, *12*, 47704–47713.
- (361) Chen, G.; Roy, I.; Yang, C.; Prasad, P. N. Nanochemistry and Nanomedicine for Nanoparticle-Based Diagnostics and Therapy. *Chem. Rev.* **2016**, *116*, 2826–2885.
- (362) Tao, W.; Ji, X.; Xu, X.; Islam, M. A.; Li, Z.; Chen, S.; Saw, P. E.; Zhang, H.; Bharwani, Z.; Guo, Z.; et al. Antimonene Quantum Dots: Synthesis and Application as Near-Infrared Photothermal Agents for Effective Cancer Therapy Communications Angewandte. *Angew. Chem., Int. Ed.* **2017**, *100049*, 11896–11900.
- (363) Xie, Z.; Chen, S.; Duo, Y.; Zhu, Y.; Fan, T.; Zou, Q.; Qu, M.; Lin, Z.; Zhao, J.; Li, Y.; et al. Biocompatible Two-Dimensional Titanium Nanosheets for Multimodal Imaging-Guided Cancer Theranostics. *ACS Appl. Mater. Interfaces* **2019**, *11*, 22129–22140.
- (364) Tao, W.; Zhu, X.; Yu, X.; Zeng, X.; Xiao, Q.; Zhang, X.; Ji, X.; Wang, X.; Shi, J.; Zhang, H.; et al. Black Phosphorus Nanosheets as a Robust Delivery Platform for Cancer Theranostics. *Adv. Mater.* **2017**, *29*, 1603276.
- (365) Chen, J.; Fan, T.; Xie, Z.; Zeng, Q.; Xue, P.; Zheng, T.; Chen, Y.; Luo, X.; Zhang, H. Advances in Nanomaterials for Photodynamic Therapy Applications: Status and Challenges. *Biomaterials* **2020**, *237*, 119827.
- (366) Wu, X.; Jiang, X.; Fan, T.; Zheng, Z.; Liu, Z.; Chen, Y.; Cao, L.; Xie, Z.; Zhang, D.; Zhao, J. Recent Advances in Photodynamic Therapy Based on Emerging Two-Dimensional Layered Nanomaterials. *Nano Res.* **2020**, *13*, 1485–1508.
- (367) Xiong, S.; Li, Z.; Liu, Y.; Wang, Q.; Luo, J.; Chen, X.; Xie, Z.; Zhang, Y.; Zhang, H.; Chen, T. Brain-Targeted Delivery Shuttled by Black Phosphorus Nanostructure to Treat Parkinson's Disease. *Biomaterials* **2020**, *260*, 120339.
- (368) Xie, Z.; Fan, T.; An, J.; Choi, W.; Duo, Y.; Ge, Y.; Zhang, B.; Nie, G.; Xie, N.; Zheng, T.; et al. Emerging Combination Strategies with Phototherapy in Cancer Nanomedicine. *Chem. Soc. Rev.* **2020**, *49*, 8065–8087.
- (369) Wang, H.; Yang, X.; Shao, W.; Chen, S.; Xie, J.; Zhang, X.; Wang, J.; Xie, Y. Ultrathin Black Phosphorus Nanosheets for Efficient Singlet Oxygen Generation. *J. Am. Chem. Soc.* **2015**, *137*, 11376–11382.
- (370) Wang, H.; Jiang, S.; Shao, W.; Zhang, X.; Chen, S.; Sun, X.; Zhang, Q.; Luo, Y.; Xie, Y. Optically Switchable Photocatalysis in Ultrathin Black Phosphorus Nanosheets. *J. Am. Chem. Soc.* **2018**, *140*, 3474–3480.
- (371) Li, Y.; Liu, Z.; Hou, Y.; Yang, G.; Fei, X.; Zhao, H.; Guo, Y.; Su, C.; Wang, Z.; Zhong, H.; et al. Multifunctional Nanoplatfrom Based on Black Phosphorus Quantum Dots for Bioimaging and Photodynamic/Photothermal Synergistic Cancer Therapy. *ACS Appl. Mater. Interfaces* **2017**, *9*, 25098–25106.
- (372) Zhang, D.; Lin, X.; Lan, S.; Sun, H.; Wang, X.; Liu, X.; Zhang, Y.; Zeng, Y. Localized Surface Plasmon Resonance Enhanced Singlet Oxygen Generation and Light Absorption Based on Black Phosphorus@AuNPs Nanosheet for Tumor Photodynamic/Thermal Therapy. *Part. Part. Syst. Charact.* **2018**, *35*, 1800010.
- (373) Yang, D.; Yang, G.; Yang, P.; Lv, R.; Gai, S.; Li, C.; He, F.; Lin, J. Assembly of Au Plasmonic Photothermal Agent and Iron Oxide Nanoparticles on Ultrathin Black Phosphorus for Targeted Photothermal and Photodynamic Cancer Therapy. *Adv. Funct. Mater.* **2017**, *27*, 1700371.
- (374) Ouyang, J.; Deng, Y.; Chen, W.; Xu, Q.; Wang, L.; Liu, Z.; Tang, F.; Deng, L.; Liu, Y.-N. Marriage of Artificial Catalase and Black Phosphorus Nanosheets for Reinforced Photodynamic Antitumor Therapy. *J. Mater. Chem. B* **2018**, *6*, 2057–2064.
- (375) Xie, Z.; Wang, D.; Fan, T.; Xing, C.; Li, Z.; Tao, W.; Liu, L.; Bao, S.; Fan, D.; Zhang, H. Black Phosphorus Analogue Tin Sulfide Nanosheets: Synthesis and Application as near-Infrared Photothermal Agents and Drug Delivery Platforms for Cancer Therapy. *J. Mater. Chem. B* **2018**, *6*, 4747–4755.
- (376) Jin, J.; Guo, M.; Liu, J.; Liu, J.; Zhou, H.; Li, J.; Wang, L.; Liu, H.; Li, Y.; Zhao, Y.; et al. Graphdiyne Nanosheet-Based Drug Delivery Platform for Photothermal/Chemotherapy Combination Treatment of Cancer. *ACS Appl. Mater. Interfaces* **2018**, *10*, 8436–8442.
- (377) Xie, J.; Wang, N.; Dong, X.; Wang, C.; Du, Z.; Mei, L.; Yong, Y.; Huang, C.; Li, Y.; Gu, Z.; et al. Graphdiyne Nanoparticles with High Free Radical Scavenging Activity for Radiation Protection. *ACS Appl. Mater. Interfaces* **2019**, *11*, 2579–2590.
- (378) Ji, X.; Kong, N.; Wang, J.; Li, W.; Xiao, Y.; Gan, S. T.; Zhang, Y.; Li, Y.; Song, X.; Xiong, Q.; et al. A Novel Top-Down Synthesis of Ultrathin 2D Boron Nanosheets for Multimodal Imaging-Guided Cancer Therapy. *Adv. Mater.* **2018**, *30*, 1803031.
- (379) Liang, X.; Ye, X.; Wang, C.; Xing, C.; Miao, Q.; Xie, Z.; Chen, X.; Zhang, X.; Zhang, H.; Mei, L. Photothermal Cancer Immunotherapy by Erythrocyte Membrane-Coated Black Phosphorus Formulation. *J. Controlled Release* **2019**, *296*, 150–161.
- (380) Xing, C.; Chen, S.; Qiu, M.; Liang, X.; Liu, Q.; Zou, Q.; Li, Z.; Xie, Z.; Wang, D.; Dong, B.; et al. Conceptually Novel Black Phosphorus/Cellulose Hydrogels as Promising Photothermal Agents for Effective Cancer Therapy. *Adv. Healthcare Mater.* **2018**, *7*, 1701510.
- (381) An, D.; Fu, J.; Xie, Z.; Xing, C.; Zhang, B.; Wang, B.; Qiu, M. Progress in the Therapeutic Applications of Polymer-Decorated Black Phosphorus and Black Phosphorus Analog Nanomaterials in Biomedicine. *J. Mater. Chem. B* **2020**, *8*, 7076–7120.
- (382) Xie, Z.; Peng, M.; Lu, R.; Meng, X.; Liang, W.; Li, Z.; Qiu, M.; Zhang, B.; Nie, G.; Xie, N.; et al. Black Phosphorus-Based Photothermal Therapy with ACD47-Mediated Immune Checkpoint Block-

- ade for Enhanced Cancer Immunotherapy. *Light: Sci. Appl.* **2020**, *9*, 161.
- (383) Peng, L.; Abbasi, N.; Xiao, Y.; Xie, Z. Black Phosphorus: Degradation Mechanism, Passivation Method, and Application for In Situ Tissue Regeneration. *Adv. Mater. Interfaces* **2020**, *7*, 2001538.
- (384) Tao, W.; Ji, X.; Xu, X.; Islam, M. A.; Li, Z.; Chen, S.; Saw, P. E.; Zhang, H.; Bharwani, Z.; Guo, Z.; et al. Antimonene Quantum Dots: Synthesis and Application as Near-Infrared Photothermal Agents for Effective Cancer Therapy. *Angew. Chem., Int. Ed.* **2017**, *56*, 11896–11900.
- (385) Yu, X.; Li, A.; Zhao, C.; Yang, K.; Chen, X.; Li, W. Ultrasmall Semimetal Nanoparticles of Bismuth for Dual-Modal Computed Tomography/Photoacoustic Imaging and Synergistic Thermoradiotherapy. *ACS Nano* **2017**, *11*, 3990–4001.
- (386) Tao, W.; Ji, X.; Zhu, X.; Li, L.; Wang, J.; Zhang, Y.; Saw, P. E.; Li, W.; Kong, N.; Islam, M. A.; et al. Two-Dimensional Antimonene-Based Photonic Nanomedicine for Cancer Theranostics. *Adv. Mater.* **2018**, *30*, 1802061.
- (387) Lei, P.; An, R.; Zhang, P.; Yao, S.; Song, S.; Dong, L.; Xu, X.; Du, K.; Feng, J.; Zhang, H. Ultrafast Synthesis of Ultrasmall Poly-(Vinylpyrrolidone)-Protected Bismuth Nanodots as a Multifunctional Theranostic Agent for In Vivo Dual-Modal CT/Photothermal-Imaging-Guided Photothermal Therapy. *Adv. Funct. Mater.* **2017**, *27*, 1702018.
- (388) Lu, G.; Lv, C.; Bao, W.; Li, F.; Zhang, F.; Zhang, L.; Wang, S.; Gao, X.; Zhao, D.; Wei, W.; et al. Antimonene with Two-Orders-of-Magnitude Improved Stability for High-Performance Cancer Theranostics. *Chem. Sci.* **2019**, *10*, 4847–4853.
- (389) Wang, X.; Hu, Y.; Mo, J.; Zhang, J.; Wang, Z.; Wei, W.; Li, H.; Ma, J.; Zhao, J.; Jin, Z.; et al. Arsenene: A Potential Therapeutic Agent for Acute Promyelocytic Leukaemia Cells by Acting on Nuclear Proteins. *Angew. Chem., Int. Ed.* **2020**, *59*, 5151–5158.
- (390) Chia, H. L.; Latiff, N. M.; Gusmão, R.; Sofer, Z.; Pumera, M. Cytotoxicity of Shear Exfoliated Pnictogen (As, Sb, Bi) Nanosheets. *Chem. - Eur. J.* **2019**, *25*, 2242–2249.
- (391) Yu, N.; Li, J.; Wang, Z.; Yang, S.; Liu, Z.; Wang, Y.; Zhu, M.; Wang, D.; Chen, Z. Blue Te Nanoneedles with Strong NIR Photothermal and Laser-Enhanced Anticancer Effects as “All-in-One” Nanoagents for Synergistic Thermo-Chemotherapy of Tumors. *Adv. Healthcare Mater.* **2018**, *7*, 1800643.
- (392) Wang, H.; Chai, L.; Xie, Z.; Zhang, H. Recent Advance of Tellurium for Biomedical Applications. *Chem. Res. Chin. Univ.* **2020**, *36*, 551–559.
- (393) Yang, T.; Ke, H.; Wang, Q.; Tang, Y.; Deng, Y.; Yang, H.; Yang, X.; Yang, P.; Ling, D.; Chen, C.; et al. Bifunctional Tellurium Nanodots for Photo-Induced Synergistic Cancer Therapy. *ACS Nano* **2017**, *11*, 10012–10024.
- (394) Huang, W.; Huang, Y.; You, Y.; Nie, T.; Chen, T. High-Yield Synthesis of Multifunctional Tellurium Nanorods to Achieve Simultaneous Chemo-Photothermal Combination Cancer Therapy. *Adv. Funct. Mater.* **2017**, *27*, 1701388.
- (395) Lin, Y.; Wu, Y.; Wang, R.; Tao, G.; Luo, P.-F.; Lin, X.; Huang, G.; Li, J.; Yang, H.-H. Two-Dimensional Tellurium Nanosheets for Photoacoustic Imaging-Guided Photodynamic Therapy. *Chem. Commun.* **2018**, *54*, 8579–8582.
- (396) Ma, D.; Zhao, J.; Xie, J.; Zhang, F.; Wang, R.; Wu, L.; Liang, W.; Li, D.; Ge, Y.; Li, J. Ultrathin Boron Nanosheets as an Emerging Two-Dimensional Photoluminescence Material for Bioimaging. *Nanoscale Horiz.* **2020**, *5*, 705–713.
- (397) Lyu, Y.; Li, J.; Pu, K. Second Near-Infrared Absorbing Agents for Photoacoustic Imaging and Photothermal Therapy. *Small Methods* **2019**, *3*, 1900553.
- (398) Jiang, Y.; Pu, K. Advanced Photoacoustic Imaging Applications of Near-Infrared Absorbing Organic Nanoparticles. *Small* **2017**, *13*, 1700710.
- (399) Tang, Y.; Zhao, Z.; Hu, H.; Liu, Y.; Wang, X.; Zhou, S.; Qiu, J. Highly Stretchable and Ultrasensitive Strain Sensor Based on Reduced Graphene Oxide Microtubes–Elastomer Composite. *ACS Appl. Mater. Interfaces* **2015**, *7*, 27432–27439.
- (400) Min, H.; Qi, Y.; Chen, Y.; Zhang, Y.; Han, X.; Xu, Y.; Liu, Y.; Hu, J.; Liu, H.; Li, Y.; et al. Synthesis and Imaging of Biocompatible Graphdiyne Quantum Dots. *ACS Appl. Mater. Interfaces* **2019**, *11*, 32798–32807.
- (401) Titma, T.; Shimmo, R.; Siigur, J.; Kahru, A. Toxicity of Antimony, Copper, Cobalt, Manganese, Titanium and Zinc Oxide Nanoparticles for the Alveolar and Intestinal Epithelial Barrier Cells in Vitro. *Cytotechnology* **2016**, *68*, 2363–2377.
- (402) Egodawatta, L. P.; Holland, A.; Koppel, D.; Jolley, D. F. Influence of Soil Phosphate on the Accumulation and Toxicity of Arsenic and Antimony in Choy Sum Cultivated in Individually and Co-Contaminated Soils. *Environ. Toxicol. Chem.* **2020**, *39*, 1233–1243.
- (403) Jain, C. K.; Ali, I. Arsenic: Occurrence, Toxicity and Speciation Techniques. *Water Res.* **2000**, *34*, 4304–4312.
- (404) Zare, B.; Nami, M.; Shahverdi, A.-R. Tracing Tellurium and Its Nanostructures in Biology. *Biol. Trace Elem. Res.* **2017**, *180*, 171–181.
- (405) Ba, L. A.; Döring, M.; Jamier, V.; Jacob, C. Tellurium: An Element with Great Biological Potency and Potential. *Org. Biomol. Chem.* **2010**, *8*, 4203–4216.
- (406) Li, J.; Jian, H.; Chen, Y.; Liu, H.; Liu, L.; Yao, Q.; Bi, F.; Zhao, C.; Tan, X.; Jiang, J. Studies of Graphdiyne-ZnO Nanocomposite Material and Application in Polymer Solar Cells. *Sol. RRL* **2018**, *2*, 1800211.
- (407) Jian, H.; Li, J.; Zhao, M.; Zhang, H.; He, L.; Tao, G.; Jiu, T. The Influence of Ionic Radius of Interfacial Molecule on Device Performances of Polymer Solar Cells. *Sol. Energy* **2018**, *170*, 906–912.
- (408) Tsai, H.; Nie, W.; Blancon, J.-C.; Stoumpos, C. C.; Asadpour, R.; Harutyunyan, B.; Neukirch, A. J.; Verduzco, R.; Crochet, J. J.; Tretiak, S. High-Efficiency Two-Dimensional Ruddlesden–Popper Perovskite Solar Cells. *Nature* **2016**, *536*, 312–316.
- (409) Cao, D. H.; Stoumpos, C. C.; Farha, O. K.; Hupp, J. T.; Kanatzidis, M. G. 2D Homologous Perovskites as Light-Absorbing Materials for Solar Cell Applications. *J. Am. Chem. Soc.* **2015**, *137*, 7843–7850.
- (410) Ke, W.; Mao, L.; Stoumpos, C. C.; Hoffman, J.; Spanopoulos, I.; Mohite, A. D.; Kanatzidis, M. C. Compositional and Solvent Engineering in Dion–Jacobson 2D Perovskites Boosts Solar Cell Efficiency and Stability. *Adv. Energy Mater.* **2019**, *9*, 1803384.
- (411) Wang, F.; Zuo, Z.; Li, L.; Li, K.; He, F.; Jiang, Z.; Li, Y. Large-Area Aminated-Graphdiyne Thin Films for Direct Methanol Fuel Cells. *Angew. Chem., Int. Ed.* **2019**, *58*, 15010–15015.
- (412) Pan, Q.; Liu, H.; Zhao, Y.; Chen, S.; Xue, B.; Kan, X.; Huang, X.; Liu, J.; Li, Z. Preparation of N-Graphdiyne Nanosheets at Liquid/Liquid Interface for Photocatalytic NADH Regeneration. *ACS Appl. Mater. Interfaces* **2019**, *11*, 2740–2744.
- (413) Xiao, J.; Shi, J.; Liu, H.; Xu, Y.; Lv, S.; Luo, Y.; Li, D.; Meng, Q.; Li, Y. Efficient CH₃NH₃PbI₃ Perovskite Solar Cells Based on Graphdiyne (GD)-Modified P3HT Hole-Transporting Material. *Adv. Energy Mater.* **2015**, *5*, 1401943.
- (414) Ren, H.; Shao, H.; Zhang, L.; Guo, D.; Jin, Q.; Yu, R.; Wang, L.; Li, Y.; Wang, Y.; Zhao, H.; et al. A New Graphdiyne Nanosheet/Pt Nanoparticle-Based Counter Electrode Material with Enhanced Catalytic Activity for Dye-Sensitized Solar Cells. *Adv. Energy Mater.* **2015**, *5*, 1500296.
- (415) Jin, Z.; Yuan, M.; Li, H.; Yang, H.; Zhou, Q.; Liu, H.; Lan, X.; Liu, M.; Wang, J.; Sargent, E. H.; et al. Graphdiyne: An Efficient Hole Transporter for Stable High-Performance Colloidal Quantum Dot Solar Cells. *Adv. Funct. Mater.* **2016**, *26*, 5284–5289.
- (416) Kuang, C.; Tang, G.; Jiu, T.; Yang, H.; Liu, H.; Li, B.; Luo, W.; Li, X.; Zhang, W.; Lu, F.; et al. Highly Efficient Electron Transport Obtained by Doping PCBM with Graphdiyne in Planar-Heterojunction Perovskite Solar Cells. *Nano Lett.* **2015**, *15*, 2756–2762.
- (417) Zhang, X.; Wang, Q.; Jin, Z.; Chen, Y.; Liu, H.; Wang, J.; Li, Y.; Liu, S. (Frank). Graphdiyne Quantum Dots for Much Improved Stability and Efficiency of Perovskite Solar Cells. *Adv. Mater. Interfaces* **2018**, *5*, 1701117.
- (418) Li, H.; Zhang, R.; Li, Y.; Li, Y.; Liu, H.; Shi, J.; Zhang, H.; Wu, H.; Luo, Y.; Li, D.; et al. Graphdiyne-Based Bulk Heterojunction for

Efficient and Moisture-Stable Planar Perovskite Solar Cells. *Adv. Energy Mater.* **2018**, *8*, 1802012.

(419) Li, J.; Jiu, T.; Duan, C.; Wang, Y.; Zhang, H.; Jian, H.; Zhao, Y.; Wang, N.; Huang, C.; Li, Y. Improved Electron Transport in MAPbI₃ Perovskite Solar Cells Based on Dual Doping Graphdiyne. *Nano Energy* **2018**, *46*, 331–337.

(420) Li, J.; Jiu, T.; Chen, S.; Liu, L.; Yao, Q.; Bi, F.; Zhao, C.; Wang, Z.; Zhao, M.; Zhang, G.; et al. Graphdiyne as a Host Active Material for Perovskite Solar Cell Application. *Nano Lett.* **2018**, *18*, 6941–6947.

(421) Li, J.; Zhao, M.; Zhao, C.; Jian, H.; Wang, N.; Yao, L.; Huang, C.; Zhao, Y.; Jiu, T. Graphdiyne-Doped P3CT-K as an Efficient Hole-Transport Layer for MAPbI₃ Perovskite Solar Cells. *ACS Appl. Mater. Interfaces* **2019**, *11*, 2626–2631.

(422) Liu, L.; Kan, Y.; Gao, K.; Wang, J.; Zhao, M.; Chen, H.; Zhao, C.; Jiu, T.; Jen, A.-K.-Y.; Li, Y. Graphdiyne Derivative as Multifunctional Solid Additive in Binary Organic Solar Cells with 17.3% Efficiency and High Reproducibility. *Adv. Mater.* **2020**, *32*, 1907604.

(423) Zhang, J.; Tian, J.; Fan, J.; Yu, J.; Ho, W. Graphdiyne: A Brilliant Hole Accumulator for Stable and Efficient Planar Perovskite Solar Cells. *Small* **2020**, *16*, 1907290.

(424) Wang, F.; Zuo, Z.; Shang, H.; Zhao, Y.; Li, Y. Ultrafast Interweaving Graphdiyne Nanochain on Arbitrary Substrates and Its Performance as a Supercapacitor Electrode. *ACS Appl. Mater. Interfaces* **2019**, *11*, 2599–2607.

(425) Zhang, H.; Xia, Y.; Bu, H.; Wang, X.; Zhang, M.; Luo, Y.; Zhao, M. Graphdiyne: A Promising Anode Material for Lithium Ion Batteries with High Capacity and Rate Capability. *J. Appl. Phys.* **2013**, *113*, 44309.

(426) Zhang, H.; Zhao, M.; He, X.; Wang, Z.; Zhang, X.; Liu, X. High Mobility and High Storage Capacity of Lithium in sp–sp² Hybridized Carbon Network: The Case of Graphyne. *J. Phys. Chem. C* **2011**, *115*, 8845–8850.

(427) Huang, C.; Zhang, S.; Liu, H.; Li, Y.; Cui, G.; Li, Y. Graphdiyne for High Capacity and Long-Life Lithium Storage. *Nano Energy* **2015**, *11*, 481–489.

(428) Shang, H.; Zuo, Z.; Li, L.; Wang, F.; Liu, H.; Li, Y.; Li, Y. Ultrathin Graphdiyne Nanosheets Grown In Situ on Copper Nanowires and Their Performance as Lithium-Ion Battery Anodes. *Angew. Chem., Int. Ed.* **2018**, *57*, 774–778.

(429) He, J.; Wang, N.; Yang, Z.; Shen, X.; Wang, K.; Huang, C.; Yi, Y.; Tu, Z.; Li, Y. Fluoride Graphdiyne as a Free-Standing Electrode Displaying Ultra-Stable and Extraordinary High Li Storage Performance. *Energy Environ. Sci.* **2018**, *11*, 2893–2903.

(430) Li, L.; Zuo, Z.; Wang, F.; Gao, J.; Cao, A.; He, F.; Li, Y. In Situ Coating Graphdiyne for High-Energy-Density and Stable Organic Cathodes. *Adv. Mater.* **2020**, *32*, 2000140.

(431) Zhang, S.; He, J.; Zheng, J.; Huang, C.; Lv, Q.; Wang, K.; Wang, N.; Lan, Z. Porous Graphdiyne Applied for Sodium Ion Storage. *J. Mater. Chem. A* **2017**, *5*, 2045–2051.

(432) Xu, Z.; Lv, X.; Li, J.; Chen, J.; Liu, Q. A Promising Anode Material for Sodium-Ion Battery with High Capacity and High Diffusion Ability: Graphyne and Graphdiyne. *RSC Adv.* **2016**, *6*, 25594–25600.

(433) Wang, N.; Li, X.; Tu, Z.; Zhao, F.; He, J.; Guan, Z.; Huang, C.; Yi, Y.; Li, Y. Synthesis and Electronic Structure of Boron-Graphdiyne with an sp-Hybridized Carbon Skeleton and Its Application in Sodium Storage. *Angew. Chem.* **2018**, *130*, 4032–4037.

(434) Du, H.; Zhang, Z.; He, J.; Cui, Z.; Chai, J.; Ma, J.; Yang, Z.; Huang, C.; Cui, G. A Delicately Designed Sulfide Graphdiyne Compatible Cathode for High-Performance Lithium/Magnesium–Sulfur Batteries. *Small* **2017**, *13*, 1702277.

(435) Wang, F.; Zuo, Z.; Li, L.; He, F.; Li, Y. Graphdiyne Nanostructure for High-Performance Lithium-Sulfur Batteries. *Nano Energy* **2020**, *68*, 104307.

(436) Zuo, Z.; He, F.; Wang, F.; Li, L.; Li, Y. Spontaneously Splitting Copper Nanowires into Quantum Dots on Graphdiyne for Suppressing Lithium Dendrites. *Adv. Mater.* **2020**, *32*, 2004379.

(437) Jana, A.; Woo, S. I.; Vikrant, K. S. N.; Garcia, R. E. Electrochemomechanics of Lithium Dendrite Growth. *Energy Environ. Sci.* **2019**, *12*, 3595–3607.

(438) Jana, A.; Garcia, R. E. Lithium Dendrite Growth Mechanisms in Liquid Electrolytes. *Nano Energy* **2017**, *41*, 552–565.

(439) Zhang, X.; Hu, J.; Cheng, Y.; Yang, H. Y.; Yao, Y.; Yang, S. A. Borophene as an Extremely High Capacity Electrode Material for Li-Ion and Na-Ion Batteries. *Nanoscale* **2016**, *8*, 15340–15347.

(440) Mortazavi, B.; Dianat, A.; Rahaman, O.; Cuniberti, G.; Rabczuk, T. Borophene as an Anode Material for Ca, Mg, Na or Li Ion Storage: A First-Principle Study. *J. Power Sources* **2016**, *329*, 456–461.

(441) Jiang, H. R.; Lu, Z.; Wu, M. C.; Ciucci, F.; Zhao, T. S. Borophene: A Promising Anode Material Offering High Specific Capacity and High Rate Capability for Lithium-Ion Batteries. *Nano Energy* **2016**, *23*, 97–104.

(442) Peng, H.-J.; Zhang, G.; Chen, X.; Zhang, Z.-W.; Xu, W.-T.; Huang, J.-Q.; Zhang, Q. Enhanced Electrochemical Kinetics on Conductive Polar Mediators for Lithium–Sulfur Batteries. *Angew. Chem., Int. Ed.* **2016**, *55*, 12990–12995.

(443) Rao, D.; Liu, X.; Yang, H.; Zhang, L.; Qiao, G.; Shen, X.; Xiaohong, Y.; Wang, G.; Lu, R. Interfacial Competition between a Borophene-Based Cathode and Electrolyte for the Multiple-Sulfide Immobilization of a Lithium Sulfur Battery. *J. Mater. Chem. A* **2019**, *7*, 7092–7098.

(444) Li, X.; Ni, J.; Savilov, S. V.; Li, L. Materials Based on Antimony and Bismuth for Sodium Storage. *Chem. - Eur. J.* **2018**, *24*, 13719–13727.

(445) Lei, K.; Wang, C.; Liu, L.; Luo, Y.; Mu, C.; Li, F.; Chen, J. A Porous Network of Bismuth Used as the Anode Material for High-Energy-Density Potassium-Ion Batteries. *Angew. Chem., Int. Ed.* **2018**, *57*, 4687–4691.

(446) Yu, J.; Zhou, J.; Yao, P.; Xie, H.; Zhang, M.; Ji, M.; Liu, H.; Liu, Q.; Zhu, C.; Xu, J. Antimonene Engineered Highly Deformable Freestanding Electrode with Extraordinarily Improved Energy Storage Performance. *Adv. Energy Mater.* **2019**, *9*, 1902462.

(447) Ye, X.-J.; Zhu, G.-L.; Liu, J.; Liu, C.-S.; Yan, X.-H. Monolayer, Bilayer, and Heterostructure Arsenene as Potential Anode Materials for Magnesium-Ion Batteries: A First-Principles Study. *J. Phys. Chem. C* **2019**, *123*, 15777–15786.

(448) Gao, Y.; Tian, W.; Huo, C.; Zhang, K.; Guo, S.; Zhang, S.; Song, X.; Jiang, L.; Huo, K.; Zeng, H. Tailoring Natural Layered β -Phase Antimony into Few Layer Antimonene for Li Storage with High Rate Capabilities. *J. Mater. Chem. A* **2019**, *7*, 3238–3243.

(449) Park, C.-M.; Kim, J.-H.; Kim, H.; Sohn, H.-J. Li-Alloy Based Anode Materials for Li Secondary Batteries. *Chem. Soc. Rev.* **2010**, *39*, 3115–3141.

(450) Martínez-Periñán, E.; Down, M. P.; Gibaja, C.; Lorenzo, E.; Zamora, F.; Banks, C. E. Antimonene: A Novel 2D Nanomaterial for Supercapacitor Applications. *Adv. Energy Mater.* **2018**, *8*, 1702606.

(451) Zhang, F.; He, J.; Xiang, Y.; Zheng, K.; Xue, B.; Ye, S.; Peng, X.; Hao, Y.; Lian, J.; Zeng, P.; et al. Semimetal–Semiconductor Transitions for Monolayer Antimonene Nanosheets and Their Application in Perovskite Solar Cells. *Adv. Mater.* **2018**, *30*, 1803244.

(452) Zhao, J.; Li, Y.; Ma, J. Quantum Spin Hall Insulators in Functionalized Arsenene (AsX, X = F, OH and CH₃) Monolayers with Pronounced Light Absorption. *Nanoscale* **2016**, *8*, 9657–9666.

(453) Wang, Z.; Zhang, R.; Zhao, M.; Wang, Z.; Wei, B.; Zhang, X.; Feng, S.; Cao, H.; Liu, P.; Hao, Y.; et al. High-Yield Production of Stable Antimonene Quantum Sheets for Highly Efficient Organic Photovoltaics. *J. Mater. Chem. A* **2018**, *6*, 23773–23779.

(454) He, J.; Chen, Y.; Li, P.; Fu, F.; Wang, Z.; Zhang, W. Three-Dimensional CNT/Graphene–Sulfur Hybrid Sponges with High Sulfur Loading as Superior-Capacity Cathodes for Lithium–Sulfur Batteries. *J. Mater. Chem. A* **2015**, *3*, 18605–18610.

(455) He, J.; Chen, Y.; Lv, W.; Wen, K.; Xu, C.; Zhang, W.; Li, Y.; Qin, W.; He, W. From Metal–Organic Framework to Li₂S@C–Co–N Nanoporous Architecture: A High-Capacity Cathode for Lithium–Sulfur Batteries. *ACS Nano* **2016**, *10*, 10981–10987.

(456) Chung, S.-H.; Chang, C.-H.; Manthiram, A. A Carbon-Cotton Cathode with Ultrahigh-Loading Capability for Statically and Dynamically Stable Lithium–Sulfur Batteries. *ACS Nano* **2016**, *10*, 10462–10470.

(457) Liu, Y.; Wang, J.; Xu, Y.; Zhu, Y.; Bigio, D.; Wang, C. Lithium–Tellurium Batteries Based on Tellurium/Porous Carbon Composite. *J. Mater. Chem. A* **2014**, *2*, 12201–12207.

(458) Zhang, J.; Yin, Y.-X.; You, Y.; Yan, Y.; Guo, Y.-G. A High-Capacity Tellurium@Carbon Anode Material for Lithium-Ion Batteries. *Energy Technol.* **2014**, *2*, 757–762.

(459) Xu, J.; Xin, S.; Liu, J.-W.; Wang, J.-L.; Lei, Y.; Yu, S.-H. Elastic Carbon Nanotube Aerogel Meets Tellurium Nanowires: A Binder- and Collector-Free Electrode for Li-Te Batteries. *Adv. Funct. Mater.* **2016**, *26*, 3580–3588.

(460) He, J.; Chen, Y.; Lv, W.; Wen, K.; Wang, Z.; Zhang, W.; Li, Y.; Qin, W.; He, W. Three-Dimensional Hierarchical Reduced Graphene Oxide/Tellurium Nanowires: A High-Performance Freestanding Cathode for Li–Te Batteries. *ACS Nano* **2016**, *10*, 8837–8842.

(461) Ding, N.; Chen, S.-F.; Geng, D.-S.; Chien, S.-W.; An, T.; Hor, T. S. A.; Liu, Z.-L.; Yu, S.-H.; Zong, Y. Tellurium@Ordered Macroporous Carbon Composite and Free-Standing Tellurium Nanowire Mat as Cathode Materials for Rechargeable Lithium–Tellurium Batteries. *Adv. Energy Mater.* **2015**, *5*, 1401999.

(462) He, J.; Lv, W.; Chen, Y.; Wen, K.; Xu, C.; Zhang, W.; Li, Y.; Qin, W.; He, W. Tellurium-Impregnated Porous Cobalt-Doped Carbon Polyhedra as Superior Cathodes for Lithium–Tellurium Batteries. *ACS Nano* **2017**, *11*, 8144–8152.

(463) Ponnamma, D.; Yin, Y.; Salim, N.; Parameswaranpillai, J.; Hameed, N. Recent Progress and Multifunctional Applications of 3D Printed Graphene Nanocomposites. *Composites, Part B* **2021**, *204*, 108493.

(464) Zhu, C.; Han, T. Y.-J.; Duoss, E. B.; Golobic, A. M.; Kuntz, J. D.; Spadaccini, C. M.; Worsley, M. A. Highly Compressible 3D Periodic Graphene Aerogel Microlattices. *Nat. Commun.* **2015**, *6*, 6962.

(465) Zhang, Y.; Lim, C.-K.; Dai, Z.; Yu, G.; Haus, J. W.; Zhang, H.; Prasad, P. N. Photonics and Optoelectronics Using Nano-Structured Hybrid Perovskite Media and Their Optical Cavities. *Phys. Rep.* **2019**, *795*, 1–51.

(466) Shi, J. L.; Zhao, X. J.; Seifert, G.; Wei, S. H.; Zhang, D. B. Unconventional Deformation Potential and Half-Metallicity in Zigzag Nanoribbons of 2D-Xenes. *Phys. Chem. Chem. Phys.* **2020**, *22*, 7294–7299.

(467) Wei, S.; Tang, X.; Liao, X.; Ge, Y.; Wei, Y. Recent Progress of Spintronics Based on Emerging 2D Materials: CrI₃ and Xenes. *Mater. Res. Express* **2019**, *6*, 122004.

(468) Baev, A.; Prasad, P. N.; Gren, H.; Samo, M.; Wegener, M. Metaphotonics: An Emerging Field with Opportunities and Challenges. *Phys. Rep.* **2015**, *594*, 1–60.

(469) Huang, Y. L.; Zheng, Y. J.; Song, Z.; Chi, D.; Quek, S. Y. The Organic–2D Transition Metal Dichalcogenide Heterointerface. *Chem. Soc. Rev.* **2018**, *47*, 3241–3264.

(470) Gobbi, M.; Orgiu, E.; Samori, P. When 2D Materials Meet Molecules: Opportunities and Challenges of Hybrid Organic/Inorganic van Der Waals Heterostructures. *Adv. Mater.* **2018**, *30*, 1706103.